TECHNISCHE UNIVERSITÄT MÜNCHEN

Physik-Department
Lehrstuhl für Funktionelle Materialien

Ordered maghemite nanoparticles in diblock copolymer films

Yuan Yao

Vollständiger Abdruck der von der Fakultät für Physik der Technischen Universität München zur Erlangung des akademischen Grades eines

Doktors der Naturwissenschaften (Dr. rer. nat.)

genehmigten Dissertation.

Vorsitzender:	Univ.-Prof. Dr. Martin Zacharias
Prüfer der Dissertation:	1. apl. Prof. Dr. Peter Müller-Buschbaum
	2. Univ.-Prof. Dr. Peter Böni

Die Dissertation wurde am 28.12.2015 bei der Technischen Universität München eingereicht und durch die Fakultät für Physik am 16.02.2016 angenommen.

Abstract

In the present thesis, the alignment of PS-coated maghemite ($\gamma - Fe_2O_3$) nanoparticles (NPs) within varied diblock copolymer (DBC) templates was investigated with regard to potential magnetic applications. The main focus lies on the effects of several control parameters on the morphology of the nanoparticles-diblock copolymer hybrid films, including the type of DBC, the thickness of the films, and the concentration of incorporated NPs. On a wide range of length scales microscopic imaging and scattering techniques provide a thorough understanding of the surface and inner structures of the films, which are compared to their corresponding magnetic properties. The depth profiles of films are probed for selected hybrid systems employing Time-of-Flight neutron scattering. The versatile structures of all investigated NPs-DBC hybrid film systems are tuned using different treatment procedures and environmental conditions driving the film preparation. These variations lead to different arrays of NPs and thus result in different magnetic properties. Thereby, the present thesis introduces several possibilities to establish diverse nanostructures for different potential applications.

Zusammenfassung

In dieser Dissertation wird die Ausrichtung von PS-beschichteten Maghemit ($\gamma - Fe_2O_3$)-Nanopartikeln (NPs) innerhalb verschiedener Diblockcopolymer (DBC) Template hinsichtlich potentieller magnetischer Anwendungen untersucht. Hierbei liegt ein besonderes Augenmerk auf dem Einfluss verschiedener experimenteller Parameter auf die Morphologie der NPs-DBC Hybridfilme, wie beispielsweise dem Typ des verwendeten DBC, der Filmdicke und der Konzentration eingebauter NPs. Auf verschiedenen Größenskalen ermöglichen Mikroskopie- und Beugungsmethoden ein tiefgreifendes Verständnis der Strukturen an der Oberfläche sowie im Inneren der Filme, welche wiederum mit den magnetischen Eigenschaften verglichen werden. Die Filmtiefenprofile ausgewählter Hybridsysteme werden durch Verwendung von Flugzeit Neutronenstreuung erforscht. Die vielfältigen Strukturen aller untersuchter NPs-DBC Hybridfilme werden optimiert, indem verschiedene Bearbeitungsverfahren und Präparationsbedingungen während der Herstellung der Filme variiert werden. Diese Veränderungen führen zu verschiedenen Anordnungen von NPs und somit zu verschiedenen magnetischen Eigenschaften. Damit führt die vorliegende Arbeit mehrere Möglichkeiten ein, verschiedenartige Nanostrukturen für unterschiedliche Anwendungsgebiete herzustellen.

Contents

List of abbreviations

D ..... periodic domain distance

H_c ..... coercivity

M_r ..... remanence

M_s ..... saturation magnetization

N ..... degree of polymerization

R_g ..... radius of gyration of polymer chain

T_g ..... glass transition temperature

χ ..... Flory-Huggins parameter

$\gamma - Fe_2O_3$ ..... maghemite

d ..... film thickness

f ..... volume fraction

1D ..... one dimension

AFM ..... atomic force microscopy

BC ..... block copolymer

BCC ..... body centered cubic

DBC ..... diblock copolymer

DI water ..... deionized water

DWBA ..... distorted wave Born approximation

FWHM ..... full width at half maximum

GISANS ..... grazing incidence small angle neutron scattering

GISAXS ..... grazing incidence small angle x-ray scattering

H_2SO_4 ..... sulphuric acid

hex ..... hexagonal

IUPAC ..... International Union of Pure and Applied Chemistry

lam ..... lamellar

LMA ..... local monodisperse approximation

MPMS ..... magnetic property measurement system

NP ..... nanoparticle

ODT ..... order disorder transition

OM ..... optical microscopy

OOT ..... order order transition

PBMA ..... poly(n-butyl methacrylate)

PMMA ..... poly(methyl methacrylate), $(C_5H_8O_2)_n$

PNIPAM ..... poly(N-isopropyl acrylamide)

SAXS ..... small angle x-ray scattering

SCFT ..... self consistent field theory

SDD ..... sample-detector distance

SEM ..... scanning electron microscopy

SLD ..... scattering length density

SQUID ..... superconducting quantum interference device

SSL ..... strong segregation limit

TOF ..... time-of-flight

WSL ..... weak segregation limit

XRD ..... x-ray diffraction

XRR ..... x-ray reflectivity

Chapter 1

Introduction

Hybrid nanocomposites, comprising a block copolymer (BC) structural template and incorporated inorganic functional nanoparticles (NPs), have attracted great interests due to the considerable potential of tailoring their properties for plentiful applications. The incorporation of versatile functional NP fillers endows the hybrid nanocomposites with specific advantageous optical, mechanical, electric, thermal, or magnetic properties, rendering them interesting materials for many fields of applications, such as sensors, packaging, photonic band gap materials, solar cells, spin-dependent electron transport devices, thermoplastic resins, thermo-responsible materials, high-frequency loss-free switching, biomedical imaging, medical diagnosis and therapy, catalysis, drug delivery, and high-density magnetic storage devices. [1–24]

In general, the superiority of NPs originates from their physical and chemical properties due to the large ratio of surface area to volume. [25] Particularly, maghemite (γ-Fe_2O_3) NPs have the potential applications in medical field and magnetic data storage device. Compared to bulk magnetic material, the low magnetic remanence and coercivity of the magnetic NPs are typically beneficial. [26]

It has been widely investigated that periodic ordered templates in nanoscale can be established via self-assembly microphase separation of diblock copolymers (DBCs), which consist of two chemically incompatible blocks linked by a covalent bond. By selecting different chemical blocks, changing their molecular weights, and tuning the polymer block ratios, versatile morphologies of spheres, cylinders, gyroids, and lamella can be fabricated with a characteristic length scale ranging from 10 to 100 nm. [27–29] For DBC thin films, besides the microphase separation induced nanostructures, the orientation with respect to the film/air interface, which can be parallel, perpendicular, or randomly arranged, is crucial for practical applications as well. Therefore, producing an appropriately oriented, highly periodic ordered DBC matrix is of the most interest for fabricating well defined NPs-DBC hybrid nanocomposites. [30, 31]

The control of the NP arrays within the provided DBC template is a challenge for our targeted NPs-DBC nanopatterns. It can be realized by combing a guiding DBC matrix [32, 33] and an external field force, such as an electrical field [34, 35] or a magnetic field [36–38], which profits the desired structures.

The finalized morphologies are equilibrious results of the joint interplays, including enthalpic and entropic interactions between DBC blocks, between NPs, and between DBC to NPs. [39, 40] Normally, Using several different approaches, such as vapor deposition, plasma deposition, electrophoresis, dip-coating, and wet coating, can help control the arrangement of the NPs inside the DBC matrix to some extent. [41] Particular interests are wet chemical approaches, which use ink-type mixtures of NPs and DBCs, and allow for large scale fabrication methods such as printing or spray coating. [42] A prerequisite of the approach is the use of functionalized NPs to promote a preferential affinity to one of the DBC blocks. [43] Properly functionalized NPs exhibit an enthalpic driving force for the selective deposition of the NPs inside one domain of the microphase separated structure during the self-assembly process of the NPs-DBC mixture. [44, 45] Moreover, self-aggregation of the NPs in polymer phase can be prohibited to a certain degree with such proper coating. [46]

Several studies on the magnetic NP arrays within homopolymers have been demonstrated previously. [47,48] Compared to homopolymers, DBCs enhance the complexity of the system structure and the formation of hierarchically ordered structures. Moreover, a DBC template incorporated with magnetic NPs allows for creating diverse morphologies. [49,50] On one hand, the versatile ordered nano-patterns for the arrangement of the NPs can be provided by guiding DBC templates. [51] On the other hand, the fundamental DBC morphologies can be also modified by the incorporated NPs due to a change of the free energy density. [52] Related investigations have been reported in literature. For example, Lo et al. have studied that NPs were well-dispersed in ordered PS domains in case the ratio of the NP diameter, d, to the PS domain size, D, fulfills $d/D \leq 0.3$. [53] When the NP size equals or is bigger than the domain size of the DBC, a phase transition of a lamella to a cylinder morphology was found. [53] Zhang group reported that poly(ethylene oxide) (PEO)-functionalized CdSe nanorods were successfully assembled into the channels and pores in varied polystyrene-*block*-polymethyl methacrylate (PS-*b*-PMMA) DBC templates, Because the surface of the nanorods are covered with PEO ligand. However, other alkane-covered CdSe nanorods cannot be compatible with this assembly process. [54] Furthermore, the comprehensive effects of the surface modified NPs on the morphology of self-assembled polystyrene-*block*-poly 2-vinylpyridine (PS-*b*-PVP) DBC, including nanorods length, NP size, NP concentration and molecular properties of DBC, were systematically investigated by the Lo group. [46, 53, 55] For a similar hybrid system, the magnetic

pyridine-grafted Fe_2P nanorods, at short rod lengths, are selectively deposited into PVP domains because of the preferential interaction between pyridine-tethered nanorods and PVP, and they align parallel to the interfaces between PS and PVP domains. However, extensive rod aggregation and macrophase separation appear with long lengths and high nanorod concentration. [55]
The following Chapter 2 briefly presents important fundamental theoretical backgrounds related to this thesis, which mainly consist of polymer, magnetism, and scattering basics. The later Chapter 3 describes all employed experimental techniques in this thesis. Surface profilometry and X-ray reflectivity (XRR) have been used to examine the film thickness. The surface topography has been imaged with scanning electron microscopy (SEM) and atomic force microscopy (AFM) on a small area in nanometer or sub-micrometer scales. In addition, optical microscopy (OM) also has been employed for measuring large regions with micrometer scale. Grazing incidence small-angle x-ray scattering (GISAXS) and time-of-flight mode grazing incidence small-angle neutron scattering (TOF-GISANS) have been applied as the most important characterization technique for probing the inner nanostructures located underneath the surface over a large illuminated area. Besides, the chemical identity and the size of the employed maghemite NPs have been determined with Mössbauer, x-ray diffraction (XRD) and small-angle x-ray scattering (SAXS) measurements. The normal sample preparations are described in Chapter 4. Other specifics of the investigated samples are detailed in the beginning of the corresponding result and discussion chapters.

In the present thesis, the investigations mainly focus on the effect of NPs concentration on the morphological evolution of the metal-oxide NPs-DBC hybrid films and the corresponding magnetic properties. The thorough understanding of basic principle is of most important for the realization of highly ordered, well oriented NP arrays. In Figure 1.1, a schematic representation summarizes all the hybrid film systems investigated in this thesis. All the related questions arise whether it is possible to control the arrangement of NPs via an easy low-temperature, low-energy cost process by combining the methods of self-assembly, microphase separation of DBC and wet-chemical surface modified NPs. On the route to achieve the desired morphologies of hybrid films, several important questions need to be figured out. What is the critical NP concentration for the formation of NP-aggregates? Can the structures originated from microphase separation remain, when any NP-aggregate exists? Is there a correlation between any interfaces, e.g., the interface of film/substrate, film/air, NP-aggregate enrichment layer/substrate, and NP-aggregate enrichment layer/air? Is there a limit of the NP incorporation? In particular related to applications: What is the interrelation between the established structures and the magnetic properties? All these questions are addressed in the Chapter 5, 6, 7 and 8 for four

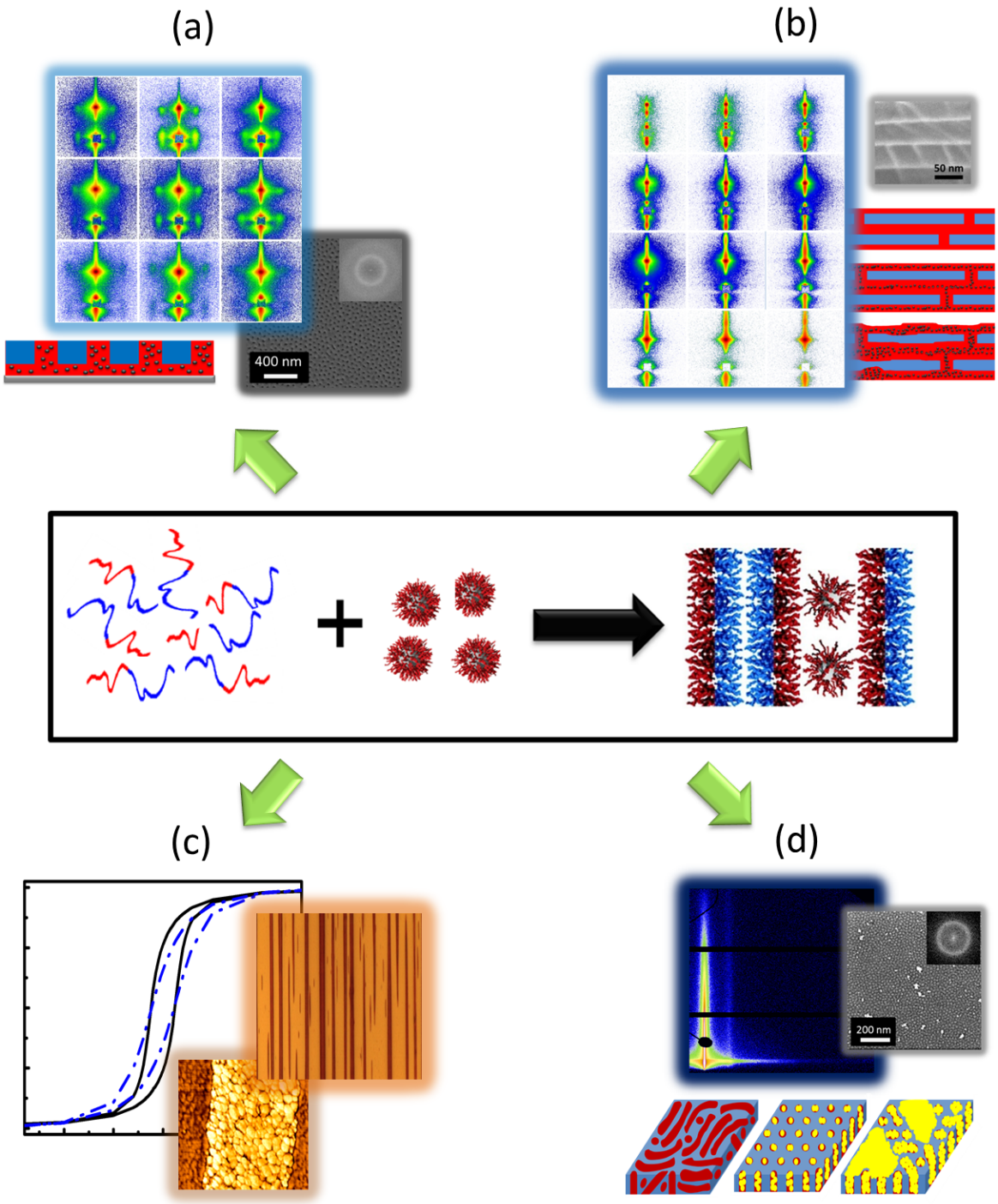

Figure 1.1: Overview about different hybrid film systems investigated in the present thesis: films with structures of (a) a perforated lamella with an enrichment layer and (b) a parallel lamella, which are containing maghemite NPs created via self-assembly of PSd-*b*-PBMA DBC with respective preparation method, (c) nano- and micro-structures of magnetic field guided maghemite NPs in PS-*b*-PMMA DBC films, and (d) arrangement of maghemite NPs via wet chemical self-assembly in PS-*b*-PNIPAM DBC films.

different hybrid film systems (in Figure 1.1). Chapter 5 (in Figure 1.1a) and Chapter 6 (in Figure 1.1b) represent two types of films with structures of a perforated lamella with an enrichment layer and a parallel lamellar, which contain maghemite NPs created via self-assembly of PSd-*b*-PBMA DBC with respective preparation method. Chapter 7 (in Figure 1.1c) mainly focuses on the nano- and micro-structures of magnetic field guided maghemite NPs in PS-*b*-PMMA DBC films. Chapter 8 (in Figure 1.1d) shows the arrangement of maghemite NPs via wet chemical self-assembly in PS-*b*-PNIPAM DBC films.

The thesis ends with a concise summary and a short outlook in the Chapter 9.

Chapter 2

Theoretical aspects

The investigated systems are used for magnetic related applications, e.g., high-density magnetic memory devices and magnetic sensors. The aimed functionality is in a close relation to the structural properties. Our goal is to investigate the nano-morphology of DBC films with incorporated γ-Fe_2O_3 NPs. For this purpose, the involved theoretical background of the experiment investigations and interpretations are presented in this chapter. In the first section, the polymer basics are described with the focus on microphase separation of DBC. Afterwards, basic magnetic properties are addressed with emphasis on superparamagnetic behaviors. For the investigation of inner film structure, the final section introduces a crucial aspect of x-ray and neutron scattering mainly emphasizing on the grazing incident scattering techniques.

2.1 Polymer

As mentioned in the introduction chapter, the control of arrangement of maghemite NPs mainly relies on the highly periodic ordered DBC templates. Such ordered structures originate from microphase separation of DBC. Therefore, the understanding of the polymer basics in both physics and chemistry aspects are presented in Section 2.1.1, since they are essential to fabricate the targeted nanostructures. Remarks on microphase separation of DBC are presented in Section 2.1.2. The most practical film regime of DBC regarding interface-induced preferential polymer block segregation is described in the final Section 2.1.3.

2.1.1 Polymer basics

General definitions of polymer

In Greek, the meaning of poly and meros is many and part, respectively, which interprets that the polymer is a large molecule consisted of a large number of identical basic repeating units. The units are named monomer and are typically connected together by covalent bonds. [56] The commonly used International Union of Pure and Applied Chemistry (IUPAC) regulation defines that *polymer is a substance composed of macromolecules. A macromolecule is a molecule having high relative molar mass, the structure of which essentially comprises the multiple repetitions of units derived, actually or conceptually, from molecules of low relative molecular mass.* [57] Generally, molecules are classified according to their molecular mass, M_W, as below: [58]

- micromolecule: M_W <1000 g/mol
- oligomer: $1000 \leq M_W \leq 10000$g/mol
- polymer macromolecule: M_W >1000 g/mol

Polymer is artificially synthesis by a so-called polymerization process, which is a chemical reaction to covalently bind monomers in order to form a long chain-like molecule, as

$$\mathrm{A} + \mathrm{A} + \mathrm{A}\ldots \Rightarrow \mathrm{AAA}\ldots \tag{2.1}$$

Since there is no possibility to obtain just one defined chain length of the polymer with an absolutely identical degree of polymerization, but always with statistical information, all the definitions regarding polymer are with respect to statistics. The number of repeated monomeric units in a single polymer chain or a macromolecule is defined as degree of polymerization, denoted *N*. Due to the presence of different degree of polymerization, the most accurate molar mass of polymer can be described by a molar mass distribution function. In case certain polymer sample contains macromolecules of n moles, the total weight of the polymer is w. For the component i ($1 \leq i \leq n$), the molar mass, the number of macromolecules, and the weight are M_i, n_i, and w_i, respectively. The relations of them are given as following:

$$\sum_i n_i = n \tag{2.2}$$

$$\sum_i w_i = w \tag{2.3}$$

$$w_i = \sum n_i M_i \tag{2.4}$$

However, the average molar mass is more commonly used. Here simply introduces two widely accepted definition of average molar mass. Firstly, the number average molar mass is defined as:

$$\overline{M_n} = \frac{\sum n_i M_i}{\sum n_i} \tag{2.5}$$

The other commonly used weight average molar mass is defined as:

$$\overline{M_w} = \frac{\sum w_i \cdot M_i}{\sum w_i} = \frac{\sum n_i \cdot M_i^2}{\sum n_i \cdot M_i} \tag{2.6}$$

Besides, another important parameter of polydispersity (denoted P), which defines the width of the distribution, is in relation to both mentioned average molar mass and is described as:

$$\mathrm{P} = \frac{\overline{M_w}}{\overline{M_n}} = \mathrm{U}{+}1 \tag{2.7}$$

where P is the polydispersity index and U is the inconsistency. Both of P and U characterize the width of the distribution function. The polydispersity of polymers strongly depends on the polymerization process. Since all artificial synthesized polymers are polydispersed, P is always >1. The monodisperse ($P = 1$) behavior can be only found in natural or biopolymer regions, e.g., proteins and enzymes. For normal industrial applications, the control over narrow polydisperse distribution is not quite strict since the production of polymers with small polydispersity requires high cost investment. However, a narrow distribution is essential for scientific investigations, because the change of molecular weight has a large effect on properties of employed polymers.

Constitution, configuration and conformation

As mentioned in last section, polymers are built up with a great number of small, chemically bonded monomers. For a better understanding of the polymers, more knowledge of monomer and polymer are required. They are presented here: constitution, configuration and conformation of polymer chains.

The constitution of a polymer describes the type and the order of the monomers' arrangement in the backbone chain, which presents the molecular architecture. For clarity, selected typical simplified formulae of different types of polymers are shown in the Figure 2.1. In the case of only one type of monomer involving, the polymer is defined as homopolymer (Figure 2.1a), e.g., Polystyrene (PS) and Polymethyl methacrylate (PMMA). In the case of more than one type of monomers including, the resulting polymer is defined as copolymer. There are several different possibilities for the architecture of copolymers.

When monomers randomly distributed among a polymer chain, such copolymer is called random copolymer (Figure 2.1b). If monomers alternatively distributed, it is called alternating copolymer (Figure 2.1c). In case long sequences well-defined numbers of different monomers (homopolymer) are bonded together in block style, the resulting copolymer is called block copolymer. When there are two different monomer blocks involved in block copolymer, it is called diblock copolymer (Figure 2.1d) and written as polyA-*block*-polyB, denoted PA-*b*-PB, e.g., polystyrene-*block*-poly(methyl methacrylate), PS-*b*-PMMA, polystyrene-*block*-poly(n-butyl methacrylate), PSd-*b*-PBMA, and polystyrene-*block*-poly(N-isopropyl acrylamide), PS-*b*-PNIPAM, which are investigated in the present thesis. In the case of three blocks involved, the resulting block copolymer is called triblock copolymer (Figure 2.1e).

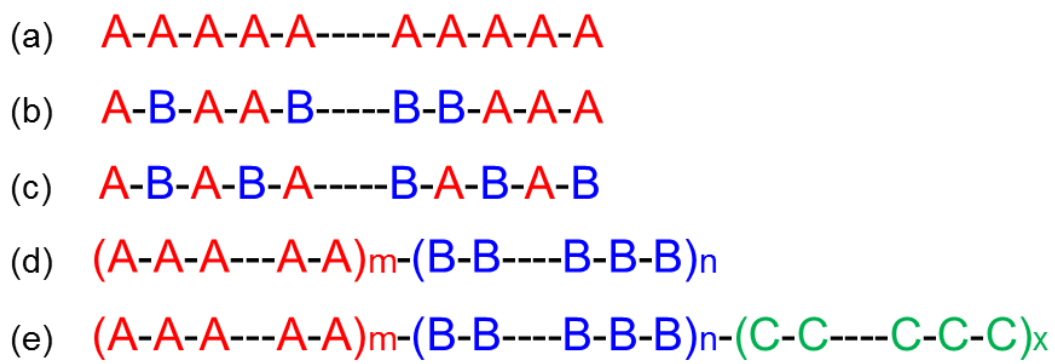

Figure 2.1: Formulae of (a) homopolymer, polyA, (b) random copolymer, polyA-*ran*-polyB, (c) alternating copolymer, polyA-*alt*-polyB, (d) diblock copolymer, polyA-*b*-polyB, and (e) triblock copolymer, polyA-*b*-polyB-*b*-polyC. The red, blue and green represent different types of monomers.

The configuration describes the spatial location of side groups with respect to the polymer main chain. This geometrical architecture resulted from the arrangement of atoms is determined by chemical bonds, which can only be changed when chemical bonds are broken or reformed. The side groups can be atoms or molecules with free bonds, e.g., O, H, S, benzen, etc. For the carbon-carbon double bond (-C=C-), there is no possibility to change its configuration, because the rotation around double bond cannot be realized. The properties of polymers are greatly influenced by the regularity and the symmetry of the side groups. When side groups are on the same side of a double bond, the resulting configuration is called *cis*; In contrast, the *trans* configuration arises when the side groups are sited on the opposite sides of the double bond. The orderliness of the succession of configurationally repeating units in the polymer main chain is defined as *tacticity*, which is an important factor in polymer thermodynamics. [59] If the repeated monomeric units

are always arranged in the same order, the resulting configuration is called *isotactic* (in Figure 2.2a); When the position of them regularly locates at alternative sides of the main chain, the corresponding configuration is called *syndiotactic* (in Figure 2.2b); If they are arranged in a totally random order, the configuration of *atactic* is obtained (in Figure 2.2c). Figure 2.2 shows the schematics of these different polymer configurations.

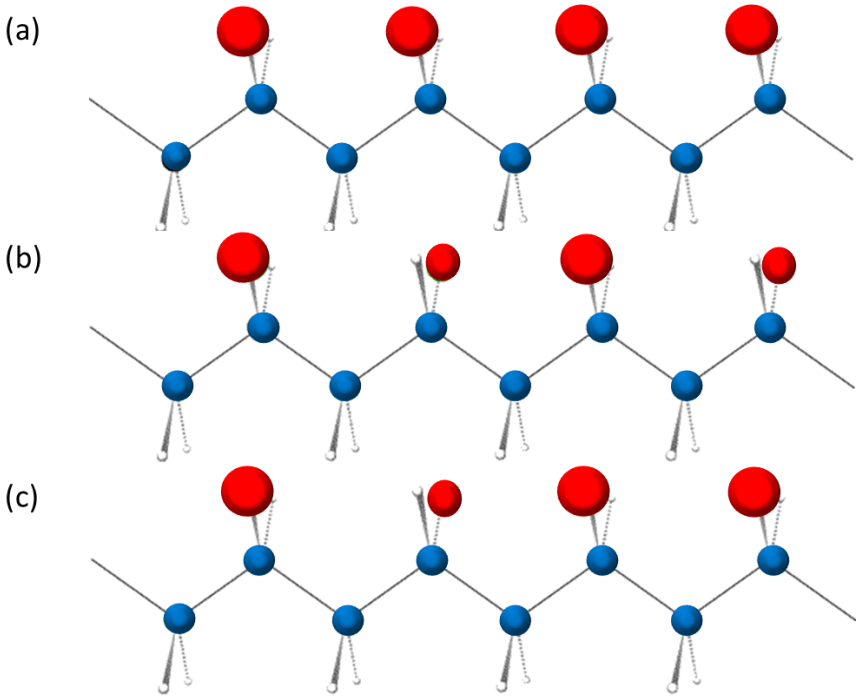

Figure 2.2: Schematics of polymer configurations of (a) isotactic, (b) syndiotactic, and (c) atactic. The blue solid spheres represent the carbon atoms connected by double bonds, which functions as a polymer main chain. The red solid spheres represent side groups. Image modified from reference [60].

The order resulted from the rotation of molecules with respect to the single bonds is defined as *conformation*, which brings the diverse construction of a complete polymer chain because the rotations around carbon-carbon single bond are well possible. For the single bond, thermal fluctuation of the length and offset angle are small at room temperature. However, the surrounding of the polymer has effects on the chain conformations. For examples, in a good solvent, open chain conformation (with more stretched chains) can be achieved because the Gibb's free energy favors the mixing of solvent and polymer; In contrast, in a bad solvent, tightly coiled conformation (with Gaussian-like coils) is obtained since the Gibb's free energy favors phase separation between solvent and polymer. Therefore, the selection of appropriate solvent to the investigated polymer is crucial. Based on the potential energy as a function of torsional angle, three typical conformations

are observed: trans, gauche +, and gauche -, as depicted in Figure 2.3. Torsion angle describes the angle of rotation offset from the trans-conformation.

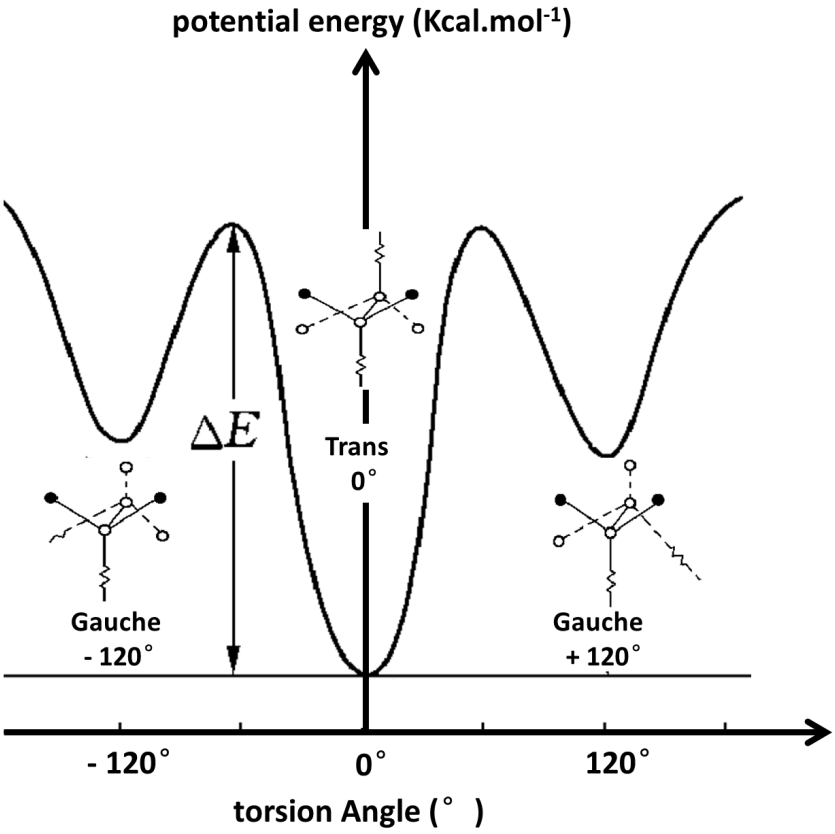

Figure 2.3: Potential energy of different conformations as a function of torsional angle. Image modified from reference [61].

The glass transition temperature

The glass transition temperature, denoted T_g, is one of the most important physical characterized temperature for the investigated amorphous polymers in current thesis. T_g describes such a critical transitional temperature, above which the polymer starts to behave like the soft rubber; below which the polymer starts freezing like the hard glass. [59] The commonly used examined method for T_g is differential scanning calorimetry (DSC). The distinct polymer transition between glassy and rubbery state can be interpreted with two different theories: free-volume theory and molecular theory. [62] The free-volume theory describes: when the conformation of polymer backbone deforms, there are extra free spaces squeezed out for setting in other molecular segments. When the temperature is well above T_g, molecular segments can be reorganized so that the free volume is reduced.

In contrast, when the temperature is lower than T_g, the movement of molecular segments becomes rather slow and can be considered as a frozen state with respect to the experimental time-scale, so that they act like a solid. Based on the other molecular theory, with the temperature well above T_g, the polymer segments have plenty of mobilizable freedom to reach all possible conformation via the rotation around flexible single bonds; when the temperature is lower than T_g, polymer segments are frozen as pre-established states, so that they behavior like a glassy solid. In a word, T_g can be considered as a characterization that describes the melting degree of freedom for the polymer. [59] Since heating annealing is a widely used post-treatment method to equilibrate the polymer morphology, the determination of the temperature for heating annealing is essential. The equilibration process requires the polymer in a mobile state thus, the heating temperature must be higher than the T_g of the employed polymers, but it also shouldn't be too high to destroy the pre-established ordered structures.
Several factors, including molar mass, chain branching, degree of crosslinking and structures of repeating unit, the presence of side groups and their size, length and tacticity, etc., influence the T_g of polymers. Based on the well acknowledged *Flory-Fox relationship*, [63] T_g of a polymer blend can be calculated from the T_g of individual, pure polymer components and their corresponding volume fraction, which is represented in Equation 2.8 :

$$\frac{1}{T_g} = \frac{\phi_A}{T_g^A} + \frac{\phi_B}{T_g^B} \tag{2.8}$$

where ϕ_A and ϕ_B represent the volume fraction of component A and B in the entire polymer, respectively, T_g^A and T_g^B represent the T_g of pure polymer A and B components, respectively. In current thesis, the Equation 2.8 is applied to estimate the approximate T_g of the investigated DBCs with leaving out of the consideration regarding the chemical bond between two blocks.

2.1.2 Phase separation

The behavior of the phase separation has been interpreted in this section based on several text books. [59, 64, 65] For a polymer blend consisting of two different homopolymers, the behavior of either phase separation or a homogeneous mixture will be observed in the case of the different miscibility of homopolymers, which can be explained with Gibb's free energy. [64, 65] Here, a mean-field theory regarding polymer blends was introduced by Huggins and later was developed by Flory. [64, 65] It defines the interaction of a single body and its external field, which summarizes all the interactions from the else bodies, to

replace the theory of many-body interactions with a more complicated system. According to thermodynamics, the change of Gibb's free energy ($\triangle G$) describes the condition of miscibility, which consists of enthalpic and entropic components:

$$\triangle G = \triangle H - T \triangle S \tag{2.9}$$

where $\triangle H$ is the enthalpy, T is the temperature, and $\triangle S$ is the entropy. $\triangle S$ originates from a lattice model, in which every site of the lattice can only be engaged once. For a blend consisting of two polymers (polymer A and polymer B), based on the construction of the former Flory-Huggins theory, the Gibb's free energy was developed to

$$\triangle G_m = RT(\frac{\phi_a}{N_a} ln\phi_a + \frac{\phi_b}{N_b} ln\phi_b + \chi\phi_a\phi_b) \tag{2.10}$$

$$\mathrm{R} = k_B N_A \tag{2.11}$$

Where R is the gas constant, k_B is the Boltzmann's constant, N_A is the Avogadro's number. In Equation 2.10 , ϕ_a and ϕ_b represent the volume fraction of polymer A and B, and N_a and N_b represent the degree of polymerization of polymer A and B, respectively. The first two components in Equation 2.10 describe the entropic contribution. Moreover, the enthalpic contribution is written in the last part, which includes the interaction between polymers via employing the Flory-Huggins interaction parameter χ. Further, χ also can be distributed to entropic (χ_S) and enthalpic (χ_H) parts:

$$\chi = \chi_S + \frac{\chi_H}{T} \tag{2.12}$$

In case a symmetric blend consists of two polymers A and B with equal degree of polymerization, $N_a = N_b = N$, a theoretical phase diagram is predicted as shown in Figure 2.4.

The presence of phase separation happens thermodynamically, with the minimization of the Gibb's free energy. Therefore, the status of a polymer blend, either a homogeneous blend or a phase separation, is determined by the minimization of the Gibb's free energy. In Figure 2.4 , the binodal (indicated with solid curve) describes the boundary between a homogeneous blend and a phase separation region. The critical value of χ is provided with the second derivative of $\triangle G_m$ (Equation 2.10):

$$\chi_c = (2N_b)^{-1}(1 + \sqrt{\frac{N_b}{N_a}})^2 \tag{2.13}$$

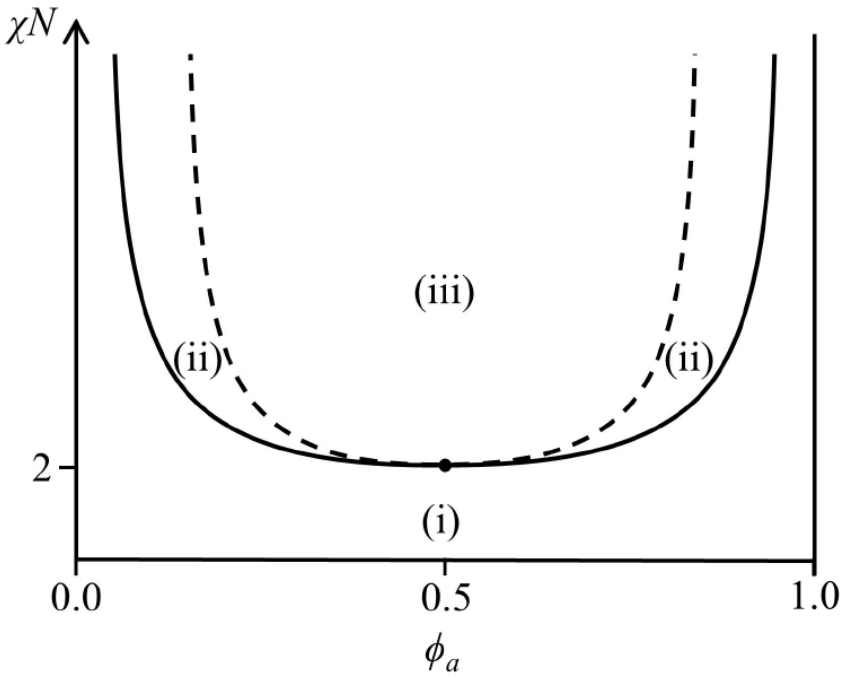

Figure 2.4: Phase diagram of a symmetric polymer blend of two polymers A and B with equal degree of polymerization $N_a = N_b = N$ at different χN. (i) a homogeneous polymer blend, (ii) a metastable and (iii) an unstable phase separated polymer region are indicated. The solid curve and dashed curve are the binodal and spinodal, respectively. The solid dot is the critical point. Image taken from reference [59].

Besides, in case the polymer blend consists of two polymers A and B with unequal degree of polymerization, $N_a \neq N_b$, an asymmetric phase diagram is arisen. Either nucleation and growth, or spinodal decomposition can direct to the demixing process of polymer blends. [59, 66]

Microphase separation behavior of DBC

For the diblock copolymers consisted of two chemically incompatible polymer blocks and connected with a chemical covalent bond, the new average material characteristics benefited from the advantages of the both blocks are arisen. Although the repulsive interaction between the chemically different blocks intends to lead them to segregate, the strong chemical bond prevents them from a demixing and macro-phase separation. As a compromise, a characteristic separation occurs to DBCs with a domain size in a mesoscopic scale, which mainly depends on the lengths of the both blocks. Since all segregated domains possess a

homogeneous dimension, they can form a periodic manner fabricating ordered mesoscopic structures. Such resulted characteristic separation is called microphase separation.

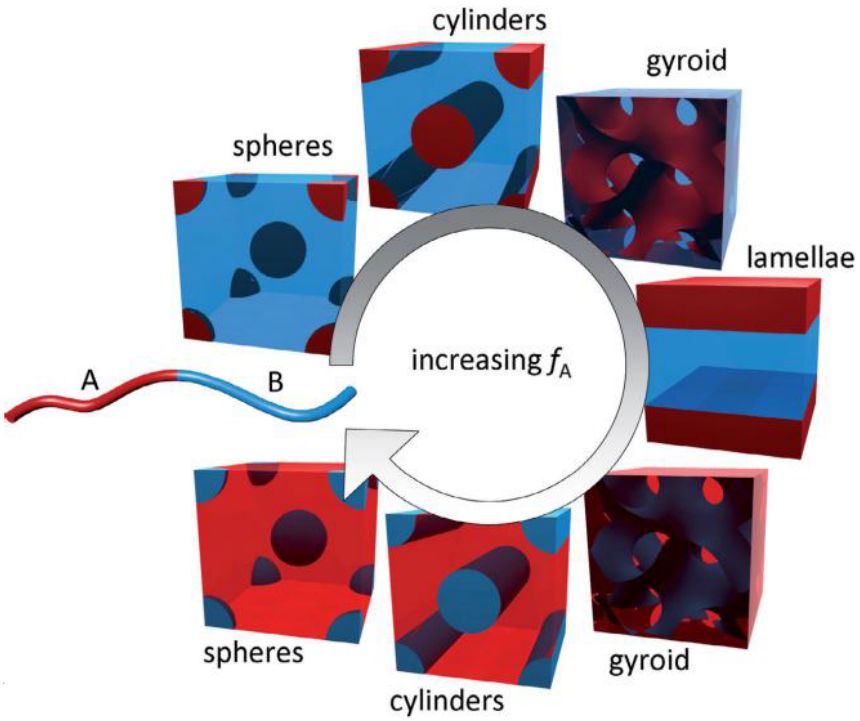

Figure 2.5: Illustrations of the typical equilibrium morphologies created via microphase separation in DBC systems with the increase of the volume fraction of the block A. Image taken from reference [67, 68].

Bates et al. first reviewed the theoretical prediction and experimental results of the microphase separation behavior in BC systems. [69] The typical equilibrium morphologies created via microphase separation in DBC systems are shown in Figure 2.5. Depending on the volume fractions of the polymer blocks, different types of mesoscopic structures are created. For instance, for a DBC PA-*b*-PB, the volume fraction of the block A is defined as:

$$\phi_A = \frac{N_A}{N_A + N_B} \tag{2.14}$$

While, the volume fraction of block B is ϕ_b = 1- ϕ_a.
At $N_a \ll N_b$ (around f_A <0.17), a body-centered cubic morphology with spherical A domains arranged inside a continuous B matrix prefers to form; at 0.17 <f_A <0.3, a hexagonal array with cylindrical A domains arranged in a continuous B matrix is created; at $f_A \approx$

0.5, the length of both blocks are sufficient to be spaced in a lamellar geometry with alternative arranged sheet A and B domains. In particular, a bicontinuous gyroid morphology with gyroidal A domains interpenetrating a B matrix occurs. As the f_A further increases, the similar morphologies are shown inversely. These diverse morphologies are attributed to the compromise between several factors: enthalpic penalty at interfaces between block domains, entropic penalty associated with localized junctions between blocks at interfaces and configurational entropy of chains.

To some extent, the behavior of a DBC system has an analogy to a binary polymer blend, where either a homogeneous phase or microphase separation can be found. However, the most intrinsic difference between them is: there are two individual components in a binary polymer blends, but only one component presents in DBC systems. Therefore, the solid line in the phase diagram of the binary polymer blends (Figure 2.4), which shows the phase boundary between a homogeneous mixture and phase separation, includes no information regarding the internal composition. The transition of an ordered phase separated domains to a disordered homogeneous mixture is defined as order-disorder transition (ODT). [66] This ODT occurs at a value of critical point, $\chi N = 2$, for a symmetric polymer blend ($f_A \approx 0.5$). However, for a DBC system, having the polymer blocks with the same types, N, and f compared with a binary polymer blend system, the critical point, χN, of the ODT increases to 10.5. [69] On the face of it, the DBCs tend to form more stable phase separation compare to the binary polymer blends. The Flory-Huggins parameter of the DBC, χ_{A-b-B}, is greater or equal to the corresponding interaction parameter of the binary polymer blends, χ_{A+B}, ($\chi_{A-b-B} \geq \chi_{A+B}$). The increase of χ originates from the change of the entropic part, because the end-to-end distance of polymer chain in the DBCs is larger than that of the binary polymer blends. In addition, based on thermodynamical theory, the physical status of BC is thermally reversible between the ordered microphase separation and the disordered mixtures as indicated in Figure 2.6. [69]

The resulting phase diagrams of DBC are not quite similar using different theories. Generally, the majority of theories are valid for monodisperse polymer systems.
The unifying weak- and strong-segregation theories of BC have been reviewed by Matsen and Bates. [70] The theories were derived from the standard model with full mean-field theory without any additional approximations. The parameter, χN, functions as a quantity to describe the degree of segregation between polymer blocks. For a symmetric DBC ($f_A = 0.5$), A-segment profiles of the lamellar phase at different χN is shown in Figure 2.7. The segregation behavior is mainly divided into three types of regimes: weak-, intermediate-, and strong-segregation. However, there is no strict standard to categorize the three regimes. They are generally investigated in ambiguous terms. It is observed

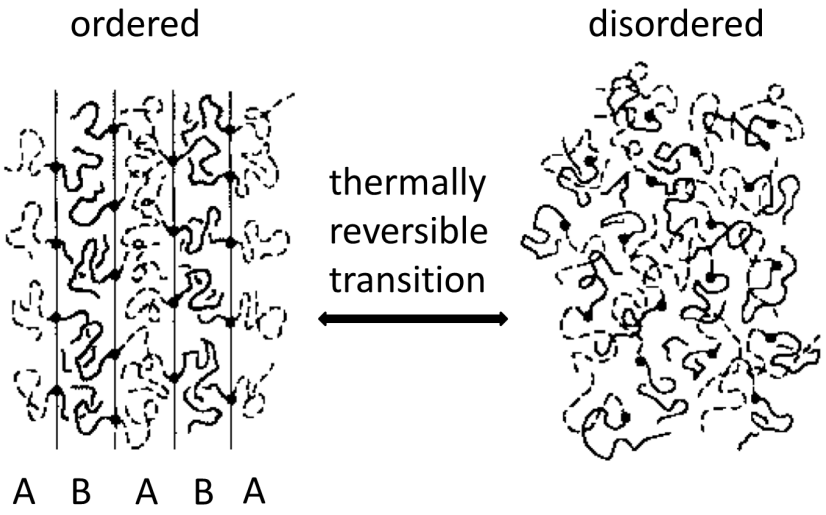

Figure 2.6: Sketch of the thermally reversible transition between ordered and disordered phase for a symmetric DBC ($f_A \approx 0.5$). Image modified from reference [69].

from Figure 2.7, the sharpness of the boundaries of the microphase separated domains depends on the χN.

Based on the mean-field theory, for a symmetric DBC ($f_A = 0.5$):

(1) At $\chi N \ll 10.5$, the interactions between polymer blocks are rather low, and a homogenous DBC mixture is formed. In this case, polymer chains are not stretched and can be expressed by Gaussian distribution with $R_g \sim \mathrm{aN}^{0.5}$. Where R_g is the radius of gyration of the polymer chain, a is a constant, which indicates the statistical segment length.

(2) At $\chi N < 10.5$, a disordered DBC mixture remains yet. However, 15% deviation of the center of mass is shown, which originates from a Gaussian coils with $R_g \sim \mathrm{aN}^{0.72}$.

(3) At $\chi N \approx 10.5$, a weak demixing occurs to the DBC due to the repulsion between the two blocks becomes large enough to result in the microphase separation. This behavior is considered as in the framework of the weak-segregation limit. The sinusoidal profiles with mild slop shown in Figure 2.7 describe the weak-segregation regime. The Landau theory describes that a second-order phase transition of disordered mixture to an ordered lamellar phase tends to happen. [71, 72] Afterwards, Fredrickson et al. developed the proceeding work with the Brazovskii's Hartree method. [73, 74] The investigation indicates the critical value of χN depends on a Ginzburg parameter, $\underline{\mathrm{N}}$,

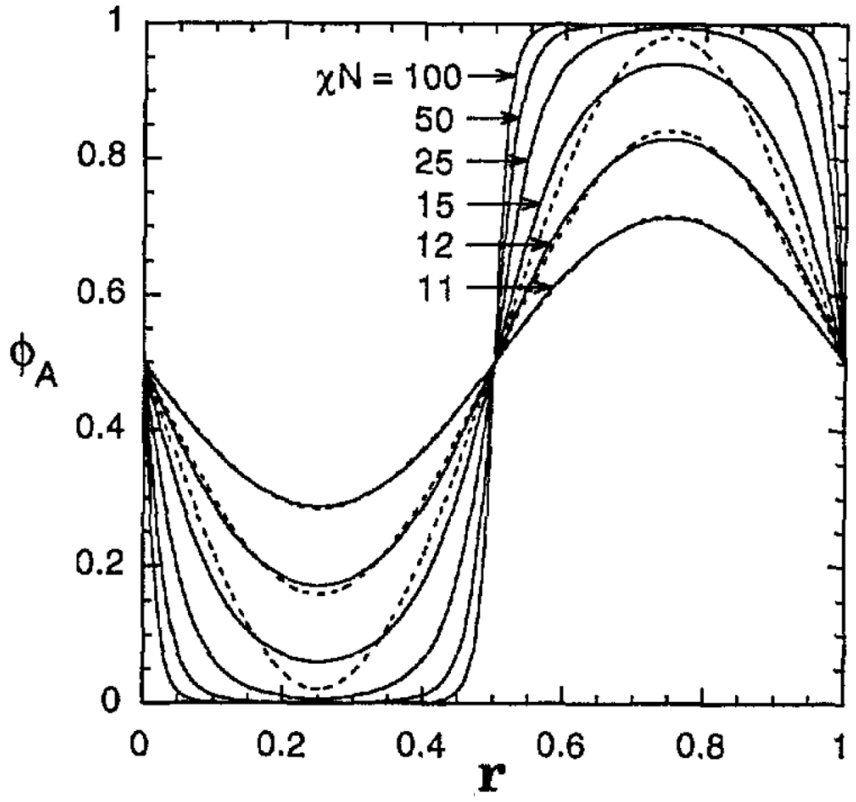

Figure 2.7: For a symmetric DBC ($f_A = 0.5$), A-segment profiles (solid lines) of the lamellar phase at different χN are shown. Dashed lines indicate profiles with first-harmonic approximations at χN of 11, 12, and 15. Image taken from reference [70].

which is well proportional to the molecular mass of DBC (M_w), $\underline{N} = 6^3(R_g^3\rho_c)^2$. ρ_c indicates the number density of DBCs. In addition, instead the critical χN is equal to 10.5, a supplementary definition of the critical χN is given with a weak first-order transition at a relative lower temperature as $(\chi N)_{ODT} = 10.5 + 41\underline{N}^{-1/3}$. [75] The expected periodic distance (D) of the lamellar structure originated from microphase separation is $D = 3.2R_g \propto N^{0.5}$.

(4) At $\chi N > 10.5$, the intermediate segregation regime occurs, which is the crossover from the weak to strong segregation regime.

(5) At $\chi N \gg 10.5$, the middle transition of each block domain is much sharper, which is shown with the rectangular shape of concentration profiles in Figure 2.7. A so-called strong-segregation regime occurs. The blocks A and B segregate sharply, which means they are stretched strongly and the crossover between their internal interfaces is rather narrow due to the increased immiscibility between them. The theoretical predicted width of the interface is defined as $\chi^{-1/2}$, which is provided with the self-consistent

field theory (SCFT). The expected periodic distance (D) of the lamellar structure is obtained with $D = 1.03\chi^{1/6}aN^{2/3}$. [76–78]

As discussed above, the expected periodic distance (D) of the lamellar and the width of the crossover between internal interface of lamellar domains are varied with χN. Based on SCFT and SST, the summarized investigations reported by Matsen and Bates are shown in Figure 2.8 in a logarithmic scale. [70]

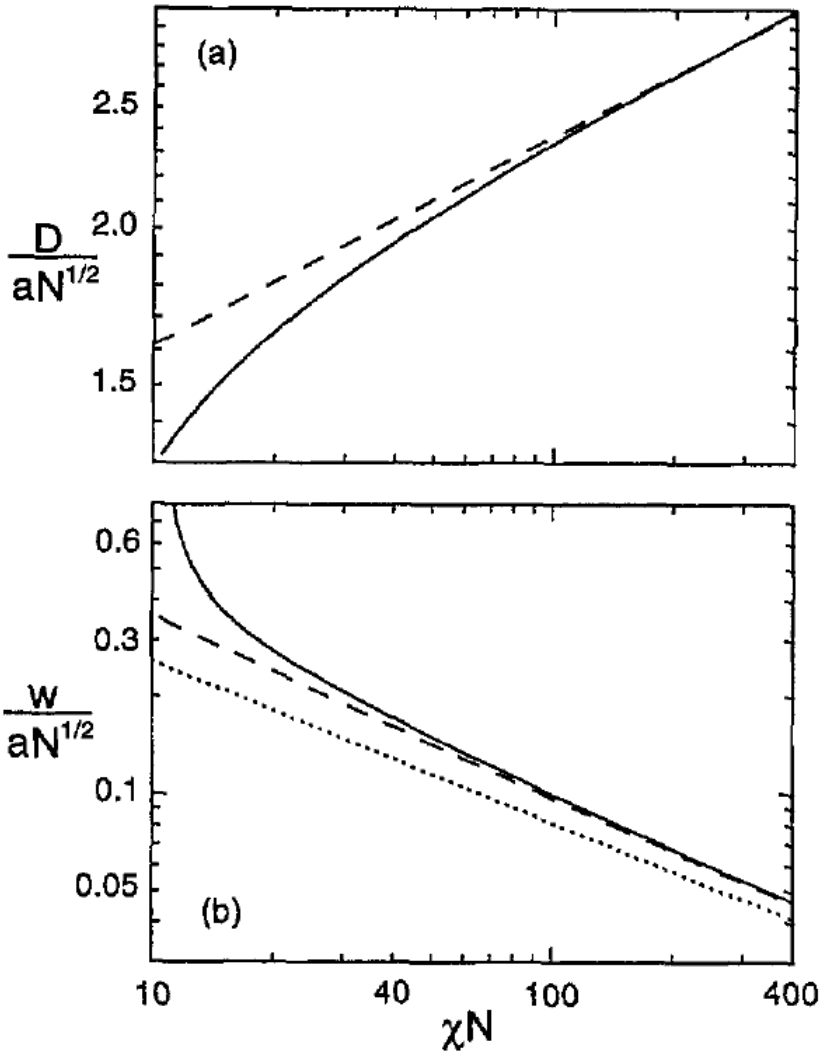

Figure 2.8: For a symmetric DBC ($f_A = 0.5$), (a) periodic distance, D, and (b) the interfacial width of lamellar domains, w, as a function of χN. Solid lines and dashed lines denote the prediction obtained from SCFT and SST, respectively. The dotted line of (b) describes $w = 2a/(6\chi)^{1/2}$. Image taken from reference [70].

In Figure 2.8, the scaling of $N^{1/2}$ is associated with the absence of segregation. [79] The solid lines are calculated from a more precise SCFT, which represent mild exponent

jumps when the χN approaches the weak-segregation limit (WST) and cross the critical point. [79, 80] Taking the fluctuations into account, the segregation initials in the disordered phase, which contributes to the increase of exponent prior to the ODT. [81–83] This theoretical expectation also keeps consistent with experimental observation. [84, 85] For the transition from weak- to intermediate-regimes, an exponent of 4/5 was obtained from experimental measurements. [85, 86] At the strong-segregation limit, the experiment observed D is scaled with an exponent of 2/3, which is consistent with the calculation of Equation 2.15 obtained from SST shown with the dashed line. [77, 87, 88]

$$\frac{D}{aN^{1/2}} = 2(\frac{8}{3\pi^4})^{1/6}(\chi N)^{1/6} \tag{2.15}$$

Meanwhile, at the strong-segregation limit, interfacial width, w, represented with the dotted line shows the independence of N along $w = 2a/(6\chi)^{1/2}$. [70] In order to improve the accuracy of w, Semenov developed an approximation based on SST by including reasonable segregations, which is shown in Equation 2.16. [79, 89]

$$\frac{w}{aN^{1/2}} = \frac{2}{(6\chi N)^{1/2}}[1 + \frac{4}{\pi}(\frac{3}{\pi^2\chi N})^{1/3}] \tag{2.16}$$

Phase diagram of DBC

A large collection of DBC is defined as a polymer melt. Below a certain critical temperature, the DBC melt will show a phase transition; above this temperature, polymer blocks are equally distributed disordered throughout the entire material.

The competition of entropy and enthalpy presents in all thermodynamic systems, which can be rendered as the minimization of the free energy. When temperature is higher than a certain critical value, polymer melt dominated by the entropy presents highly disordered homogeneity. At relative low temperatures, the polymer melt shows ordered structures. In this case, a certain periodic distribution of polymer blocks is formed and several unique geometries have been created. Some common morphologies have been experimentally observed, such as lamellae, hexagonal cylinders, and body centered cubic. As discussed in previous section, the lamellar morphology forms at $f = 0.5$. However, in the case of $f \neq 0.5$, the shorter block tends to end up less stretched than the longer block, which leads to a tendency of forming curved interface. Therefore, instead of lamellar, else morphologies favor to form. Consequently, the different f results in different corresponding equilibrium morphologies. These diverse structures with distinct geometries impart specific physical characteristics to the BCs, which render them a novel class of materials. Each particular geometry potentially exhibits different physical features thus, the possibility to switch

amongst the diverse phases provides materials with tunable characteristics. In order to exhibit the possible phase transition, phases of DBC melt are concisely interpreted with a phase diagram. The most important parameters that influence the phase diagram are χ, N and f.

In this section, several important phase diagrams of DBC melt have been organized based on different theories. It is worth to note, to overcome certain complexity in the case of the DBC in solution status, modest amounts of a neutral solvent to both DBC blocks are added. Thus, contacts of the A-B are diluted. The selected neutral solvent is one kind of solvent that has no preferential to each block.

Phase diagram based on SSL

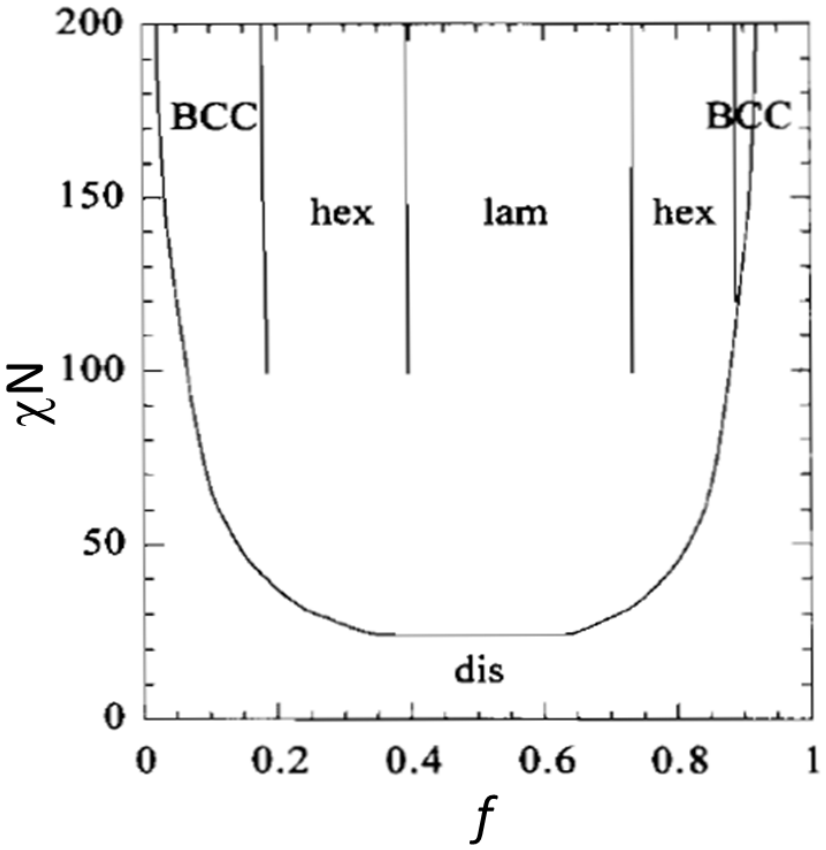

Figure 2.9: A theoretical prediction of the phase diagram for A-B type DBCs based on the strong-segregation limit theory. BCC, hex and lam indicate body-centered-cubic (sphere), hexagonal (cylinder) and lamellar morphologies. Image taken from reference [69, 90].

Figure 2.9 shows the phase diagram postulated based on the strong-segregation limit

theory, which was well-established by pioneering investigations of Meier, [89] Helfand and Wasserman, [91–93] Leary and Williams. [94, 95] Notably, Helfand and Wasserman assumed that the main principal contributions to the free energy originates from: [91–93]

(1) the presence of contact enthalpy in the narrow interfaces between nearly pure A and B domain.

(2) entropy loss combined with stretched chain configurations to guarantee incompressibility.

(3) confinement entropy arises from the localization of the DBC covalent bonding in the interfacial area.

The SSL theory is greatly simplified by introducing the narrow interphase approximation, which assumes that the narrow internal interfaces separate well-developed, nearly pure A and B domains at the situation of sufficiently strong A-B interactions ($\chi \gg 10.5$). The main feature of this phase diagram is:

(1) Phase boundaries only depend on the composition of DBC melt. The exhibited morphology changes with increasing asymmetry.

(2) This theoretical expression is only valid at $10.5 \ll \chi N \ll 100$, and it cannot extend to the weak-segregation regime.

(3) The boundary of the order-disorder transition is inaccurate.

Phase diagram based on WSL

The most far-reaching weak-segregation limit theory were greatly improved by Leibler. [96] Utilizing the Landau mean field approximation, the phase diagram of DBCs in the vicinity of the ODT region was mapped out by preserving only the leading harmonics in a Fourier description of diverse ordered-phase composition patterns. [96] The resulted phase diagram is shown in Figure 2.10.

According to Landau approximation, at $f = 0.5$, a critical point at $(\chi N)_c = 10.495$ is predicted. Only at this critical point, a direct second-order phase transition from a disordered status to a lamellar phase can be occurred for compositionally symmetric DBCs. With the increase of χN, the extent of the lamellar phase expands continuously. The predicted critical point coincides with the spinodal. In addition, the periodic distance of the lamellar, $D = 3.23\ R_g$, is weakly disturbed by inhomogeneous compositional region. Whereas, for DBCs with asymmetric composition ($f \neq 0.5$), a weak first-order phase

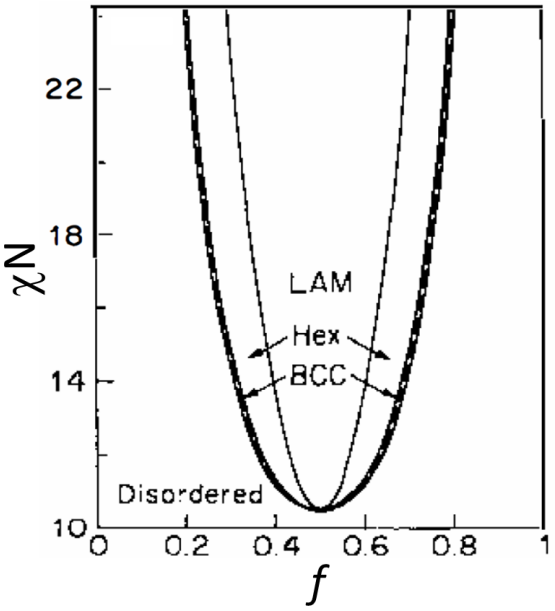

Figure 2.10: A theoretical prediction of the phase diagram for A-B type DBCs based on the mean-field theory in the framework of weak-segregation limit. BCC, Hex and LAM indicate body-centered-cubic (sphere), hexagonal (cylinder) and lamellar morphology. Image taken from reference [69].

transition from a disordered status to a body-centered-cubic (BCC) phase is calculated from the mean-field theory. Compared with the conditions of SSL, mean-field theory provides a first-order transition between solid phases, which can be realized by changing temperature.

Brazovskii et al. reported the critical point presented in last paragraph is restrained by large-amplitude order parameter fluctuations. [97] Based on a self-consistent Hartree method, Brazovskii exhibited a weak first-order phase transition, which is induced via fluctuations, instead of the previous sole critical point. [98] The resembling fluctuation-induced first-order phase transitions have been speculated to be happened in various else physical systems. [98]

In the framework of Brazovskii's Hartree appraoximation, Fredrickson and Helfand developed an analysis of the DBC melt computed by Leibler. [97] They demonstrated that a Ginzburg parameter, $\underline{N}$, dominates the fluctuation corrections. The so-called Ginzburg parameter is defined as $\underline{N} = 6^3(R_g^3\rho_c)^2$, which is proportional to the molar mass of the DBCs, where ρ_c is the number density of DBCs in the melt. [83, 99] In the case of a settled χN with an infinite $\underline{N}$, the result of their investigation matches the asymptotically approached description predicted by Leibler' mean-field theory. However, with a finite $\underline{N}$,

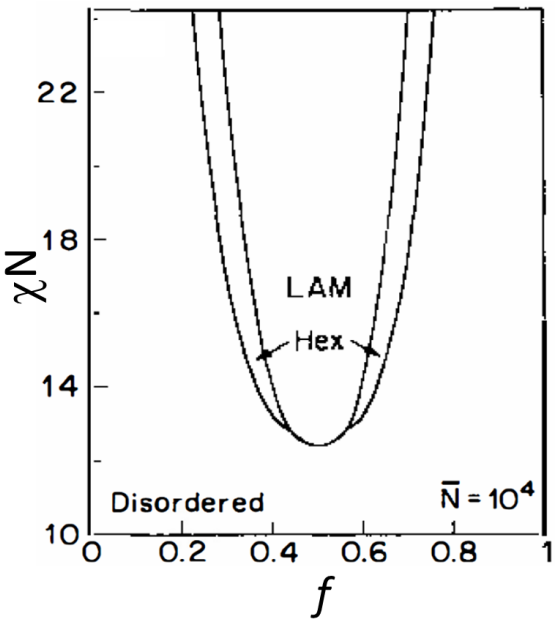

Figure 2.11: A theoretical prediction of the phase diagram for A-B type DBCs based on the fluctuation theory in the framework of weak-segregation limit. Hex and LAM indicate hexagonal (cylinder) and lamellar morphology. Image taken from reference [97, 98].

significant changes of the phase diagram (in Figure 2.11) are shown in both qualitative and quantitative aspects, which are induced by the fluctuation corrections. The disordered melts extend to larger χN values, since the critical point ($(\chi N)_c$= 10.5, in Figure 2.10) of symmetric compositional DBC predicted by mean-field theory is replaced by a weak first-order transition at $(\chi \underline{N})_c = 10.495 + 41.022[6^3(R_g^3\rho_c)^2]^{-1/3}$. Due to $\chi \propto 1/T$, the phase transition occurs at lower temperatures. The $\underline{\mathrm{N}}$ of the typical employed DBC sample is in range of 10^3-10^4. Figure 2.11 is exemplified for $\underline{N} = 10^4$. In this circumstance, the fluctuation corrections are considerable. Additional, for asymmetric compositional DBCs, the changes of phase diagram appear even more substantial. Compared with the phase diagram based on mean-field theory (Figure 2.10), the most distinct differences of the phase diagram calculated with fluctuation theory is that the direct transition from disordered melts into lamella phase in a larger amplitude around $f = 0.5$. Therefore, even at $f \neq 0.5$, both BCC and lamella phase are present at the ODT.

Phase diagram based on self-consistent field theory (SCFT)

Self-consistent field describes a method of simplifying the calculating problem of the interactions in external fields, which are obtained self-consistently with the composition profile. This computational approximation is not restricted to any degree of segregation

and traverses both the weak- and strong-segregation theories. This section has been demonstrated by following the literature reported by Matsen et al. [70]

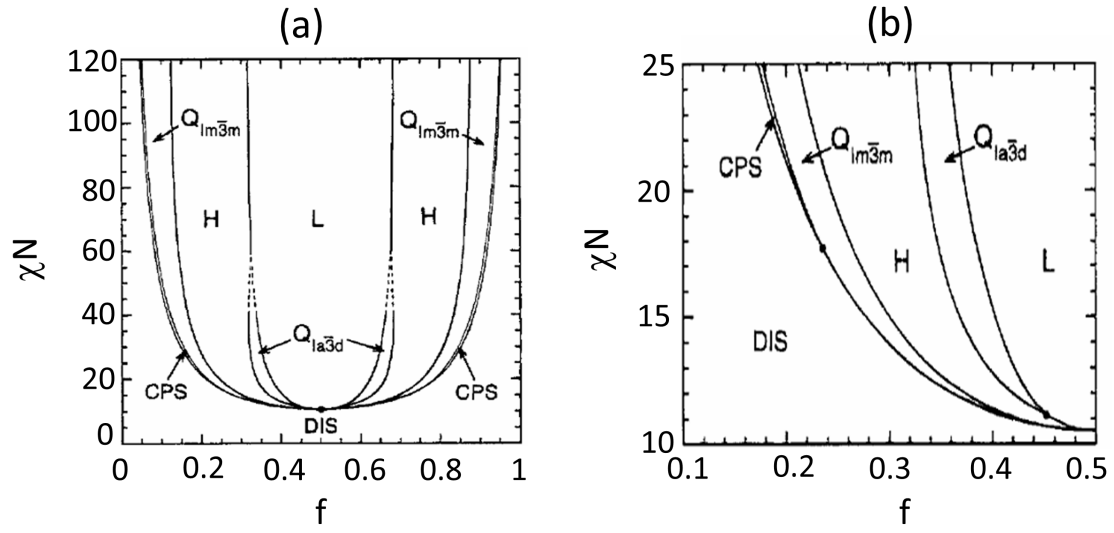

Figure 2.12: (a) Phase diagram for A-B type DBCs based on SCFT. (b) Partial expanded view of the phase diagram in (a). DIS, CPS, Qlm3m, H, Qla3d, and L indicate disordered melt, close-packed sphere, body-centered-cubic (sphere), hexagonal cylinder, bicontinuous la3d cubic, and lamellar, respectively. Dashed lines present the extrapolated phase boundaries. The dot in (a) is the ODT critical point. More critical points amongst the phases of DIS + CPS + Qlm3m and H +Qla3d + L are shown with dots in (b). Image taken from reference [70].

Based on the SCFT, the phase diagram with χN until 120 is shown in Figure 2.12a. In general, with the increase of the χN, the stable regions of the classical body-centered-cubic sphere (Qlm3m), hexagonal cylinder (H), and lamellar (L) grow up. The variation tendencies of the classical phases are similar with the previous prediction obtained from weak-segregation theory.

In the partial expanded view of the phase diagram (Figure 2.12b), in agreement with a theoretical calculation made by Semenov, [100] the narrow amplitude of stable close-packed sphere (CPS) phases along the ODT boundaries extend approaching the strong-segregation regime from the critical points (amongst the phases of DIS + CPS + Qlm3m) at $\chi N = 17.67$ and f or $1–f = 0.234$. With the increase of χN, the CPS phases subsequently extend to approach $f = 0$ or $f = 1$. In principle, for these classical phase transitions of DIS + CPS and CPS + Qlm3m, the prediction of infinite χN limit can be determined with the strong-segregation theory. In this case, excluding the effect of external zones, with the implement of the unit-cell approximation, these limits are calculated to be f or $1–f = 0.117$ and 0.299, respectively. [89, 101, 102] Additional corrections are

suggested by Fredrickson or Likhtman Semenov, who predicted the limit of L + H at f or 1–f = 0.287 and f or 1–f = 0.293. [92,103] However, a contradict correction described by SCFT is that such limit is predicted to be f or 1–f = 0.310 at infinite χN, which also points out an unidentified bias with the strong-segregation theory.
Seen from Figure 2.12b, the bicontinuous la3d cubic (Qla3d) phases start from the critical points (amongst the phases of H +Qla3d + L) at $\chi N = 11.14$ and f or 1–f = 0.452. With the increase of χN, the amplitude ($\triangle f$) of the Qla3d phase firstly expands and afterwards follows by a monotonic shrink. The amplitude reaches its maximum of 0.037 at $\chi N \approx$ 18, but reduces to 0.019 at $\chi N \approx 40$. As the χN increases further, the amplitude becomes narrower and even pinching off. If such behavior is not to occur, it might result in the trends, which have tardily and monotonically developed, to create an unprecedented and unphysical reversal. It is too absolute to assert the pinching off, but it seems most likely that it occurs. Moreover, this assumption is supported by strong-segregation theory as well. [101, 102] Notably, the critical points of the transition for both the Qla3d and CPS phases calculated with SCFT lag behind the pinch off points of them predicted by weak-segregation theory, because the principal scattering vectors regarding SCFT do not form an octahedron. [71] Finally, based on related extrapolations regarding Qla3d phase boundaries, they are ended at $\chi N \approx 60$. Afterwards, the subsequent phase boundaries between H and L phases are predicted up to $\chi N \approx 120$.
In summary, all mentioned theoretical phase diagrams have exhibited a thorough morphological manifestation of abstract mathematical principles with the control of the three main characterized parameters of DBC (χN, N and f). Following the instruction of phase diagrams, the desirable selection of morphologies can be accessible by using versatile DBCs with different block ratios.

Experimental observed phase diagram

In previous sections, several theoretic phase diagrams have been discussed. However, in the circumstance of practical experiments, not all the predictions of the morphologies can be realized. Therefore, it is also important to establish the actual connections between the phase behavior and the related impact parameters (χN, N and f) experimentally. [104] Nevertheless, only a few measured phase diagram can be obtained so far due to the numerous workload of the phase determination process even for only one type of DBCs.

As an example, Figure 2.13 shows a phase diagram based on experimental observed phase behavior of 10 different polystyrene-*block*-polyisoprene (PS-*b*-PI) DBCs with the varied block composition in the range of 0.24 to 0.82. Compared with the theoretical calculated phase diagrams, the main features of the measured phase diagram are:

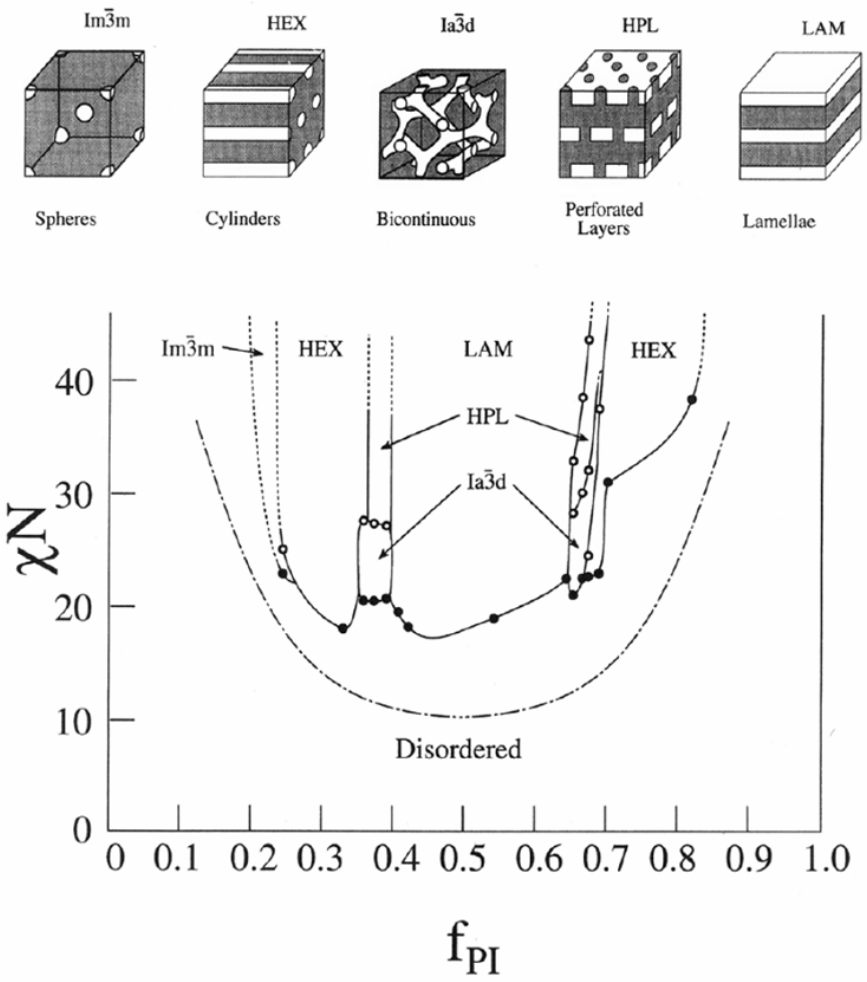

Figure 2.13: A phase diagram of PI-*b*-PS DBCs as a function of f_{PI}. Hollow and solid circles indicate the experimental examined order-order transition (OOT) and order-disorder transition (ODT), respectively. The dash-dot curve represents the ODT predicted with mean field theory. Solid curves are guidelines used to describe the determined phases but might not match those precise phase boundaries. Hex and LAM indicate hexagonal cylinder and lamellar morphology. Disordered, Im3m, HEX, Ia3d, HPL and LAM indicate disordered melt, spheres (body-centered-cubic), cylinders, bicontinuous Ia3d cubic, and lamellae, respectively. The sketches of those diverse morphologies are shown in the top. Image taken from reference [104].

(1) it is asymmetric.

(2) very complex structures could be observed.

(3) ordered phases are moved to higher values of χN, which means the disordered phase is extended to a larger area.

(4) transitions between different phases are possible.

To determine the morphology of diverse DBCs, many characterization methods can be employed, such as atomic force microscopy (AFM), scanning electron microscopy (SEM), transmission electron microscopy (TEM), small-angle X-ray/neutron scattering (SAXS/ SANS), grazing incidence small-angle X-ray/neutron scattering (GISAXS/GISANS), rheology, and so on. Some of them will be discussed in details in the next chapter.

2.1.3 Block copolymer films

So far, the phase behavior of DBCs in bulk has been discussed without involving any surface constrains. However, the most essential and practical applications require the DBCs in a film regime. In this case, the DBCs are confined between at least two interfaces, which has a strong impact on the different orientations of the DBCs film with respect to the interfaces. In the present thesis, the DBC film is installed on a solid substrate and its top surface contacts with the air, which means the DBC film is located between one solid wall and one free surface. In this case, surface impacts spread from each interfaces of DBC/substrate and DBC/air, which can induce ordering at surface. [105, 106] In contrast to the DBC film placed between two hard walls, the periodic distance of the formed periodic morphology located in the free surface film can achieve an equilibrium value. Segalman reported the possible orientations of some classic morphologies with respect to substrates (in Figure 2.14). [107] In particular, perpendicular lamellae (B) and parallel cylinders (C) are highly interesting for applications of nanowires. [108] Perpendicular cylinders (D) are greatly appreciable for devices regarding high-density data storage with their highly ordered patterning of hexagonal arrays, [109, 110] which is one of the most important targeted morphology in this thesis.

Potemkin constructed a phase diagram in the framework of the strong-segregation theory (Figure 2.15) to show the orientation of lamellae installed in thin, free-surface films fabricated with compositional symmetric DBCs. [111] The phase diagram is built in variables and relies on the total number of the film layers (n) and the dimensionless surface tension coefficient of multiple interfaces ($\overline{\gamma}$). In Figure 2.15, region I, at wetting conditions (the interaction of polymers and the solid substrate are attractive), the stable lamellae with the perpendicular orientation are observed. If the interactions of the both polymers with the substrate are comparable, which implies the spreading parameters of the both polymers are similar, such stable perpendicular orientation can remain even in the thick film regime. [111] In addition, if the film has a tendency to be spread on the substrate, the stretching rate of the chains in the lamellae with the perpendicular orientation is larger than that with the parallel orientation, thus in the case of perpendicular orientation, the area of the contact interfaces between polymer A and B is smaller. In brief, the

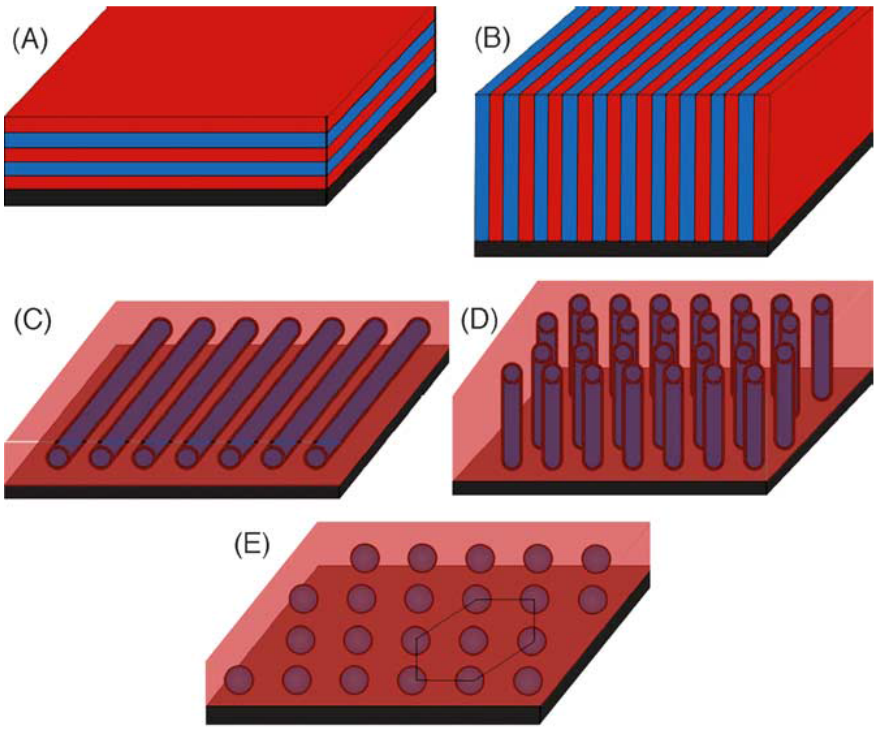

Figure 2.14: 3D sketches of possible orientations of diverse DBC morphologies. The solid substrates are marked in black. (A) and (B) are lamellae aligned parallel and perpendicular to the substrate, respectively. (B) and (C) are cylinders aligned parallel and perpendicular to the substrate. (E) Spheres. Image taken from reference [107].

incompatibility of the polymer A and B determines the stability of the lamellae with perpendicular orientation. At nonwetting conditions, if the polymer phases and substrate are unfavorable, the stable perpendicular lamellae tend to occur with smaller stretching rate of the chains compared to the parallel lamellae. [111] In other words, the resulting orientation depends on the interactions between all interfaces and is the consequence of interfacial energy minimization. This theoretical prediction is an excellent exemplification of the description regarding structural orientations.
As discussed above, the inner and surface morphologies of the DBC films can be induced by: (1) the entropic attribution of the chain conformation at each interfaces and (2) the preferential affinity of the different blocks of DBCs with respect to the different interfaces. However, such surface induced morphologies can only propagate into limit depth of the inner DBC films. Therefore, the thickness of the DBC film also greatly affects the film morphology. [112, 113]

All the DBC films have two interfaces: substrate/DBC and DBC/air. With different ratios of the periodic distance of DBC (D) to the film thickness (l), the arrangements

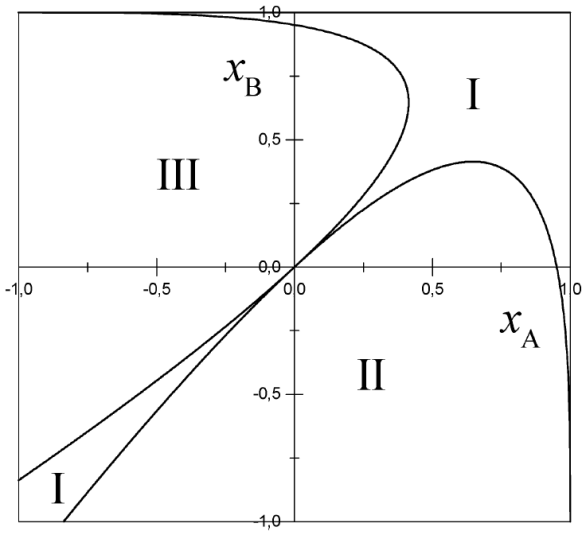

Figure 2.15: Phase diagram of a supported, compositional symmetric DBC lamellar orientation in free surface films in the framework of the strong-segregation theory. The variables χ_A and χ_B are defined as $S_A/[\overline{\gamma}_{AB}(n+1)]$ and $S_B/[\overline{\gamma}_{AB}(n+1)]$, where S_A and S_B represent the spreading parameters of polymers A and B, $\overline{\gamma}_{AB}$ represents the dimensionless surface tension coefficient of interfaces between A and B, and n represents the total number of the internal A and B layers within the film, each with the thickness of $d/2$. I, II and III indicate the regions of stable perpendicular lamellae, symmetric structure of parallel lamellae with boundary A, and symmetric structure of parallel lamellae with boundary B layer, respectively. Image taken from reference [111].

of lamellar morphologies of DBC thin films are approximately presented in four different regimes.

(1) At l > D, in case one block of the DBC has preferential affinity to both interfaces, a parallel symmetric lamellae with this preferable block contacted between the both interfaces is formed (Figure 2.16a), because the maximization of the favorable contact minimizes the total free energy of the system. [112, 114] In order to minimize the entropic penalty that results from the chain stretching and also possibly expand the favorable contact, with the post-treatment of annealing procedure, the film thickness is quantized by $l \approx nD$, where n is an integer. If each block prefers opposite interfaces, a parallel asymmetric lamellae with each block contacted with its preferable interface is formed (Figure 2.16b). When the $l \approx (n+0.5)D$, perfect lamellae is formed. [115–118] However, if the original film thickness does not match these quantized values, which depict the optimal conditions of enthalpy, the film surface grows islands and holes of height of D, depending on the amount of excess material covering the surface (in Figure 2.16c). In Figure 2.17, optical microscopy images of PS-*b*-PMMA DBC

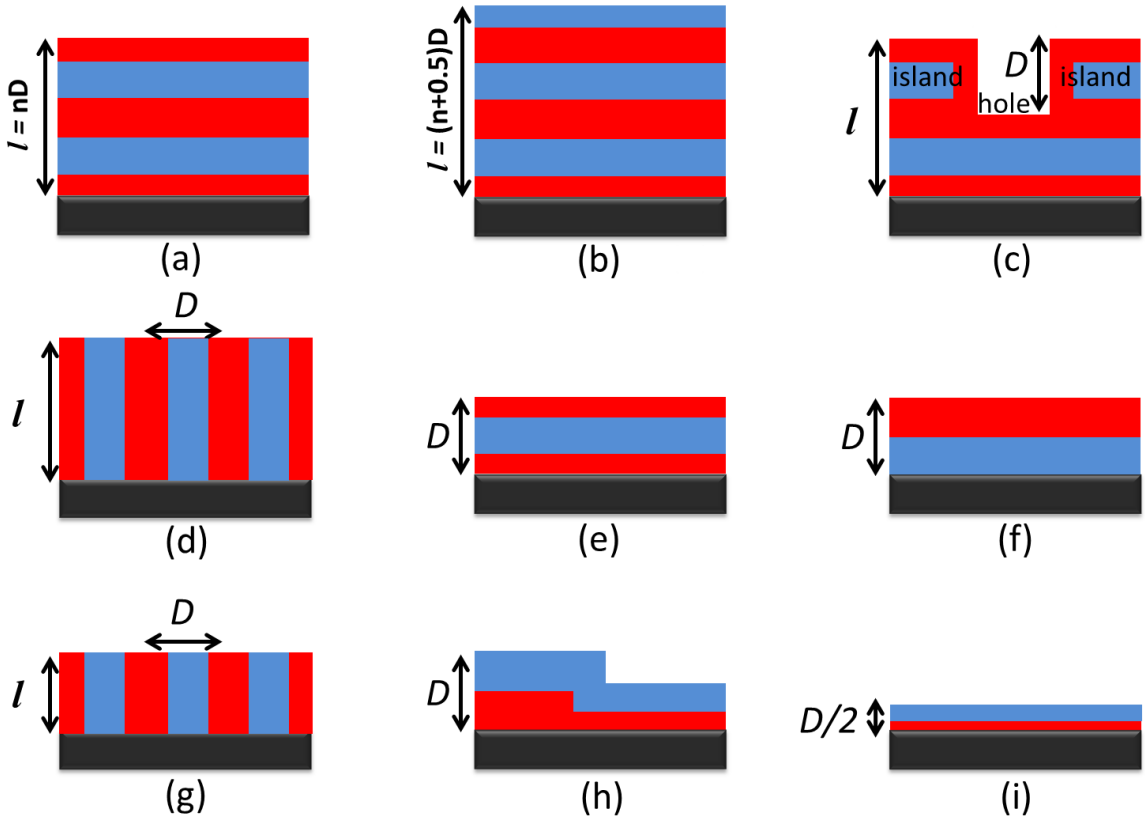

Figure 2.16: Schematic representation of the cross section of a DBC thin film installed between two physical different interfaces of air and a solid substrate. The surface induced lamellar morphologies are occurred based on different regimes regarding the different ratios of the periodic distance of DBC (D) to the film thickness (l): At $l > D$, (a) parallel symmetric lamellar, with one block in both interfaces; (b) parallel asymmetric lamellar, with each block in different interfaces; (c) parallel lamellar with islands and holes, in case film thickness does not match certain quantized values; (d) perpendicular lamellar, blocks of DBC with neutral preferential affinity to the both surfaces; At $l \approx D$, (e) symmetric and (f) asymmetric parallel lamellar, (g) perpendicular lamellar; At $D/2 < l \leq D$, (h) parallel stretched lamellar with two different film thicknesses; At $l < D/2$, and (i) asymmetric parallel lamellar.

films with two different molar mass in gradient film thicknesses show the lamellae with different surfaces as the film thickness increases. Thus, the flat surfaces, the surfaces with large holes and islands, and the trasition phase between them are observed. Moreover, in case both of the blocks have no preferential affinity to any interfaces, the formation of a perpendicular lamellar is possible (Figure 2.16d). [119]

(2) At $l \approx D$, in Figure 2.16e and f, the similar typical flat parallel symmetric and asymmetric lamellae can be formed due to the similar preferential behavior between

the DBC blocks and interfaces discussed previously. In particular, in case both blocks have neutral preferential affinity to the both interfaces, a stable perpendicular lamella is favored (Figure 2.16g). [112, 119]

(3) At $D/2 < l \leq D$, the formation of a film with two different thicknesses of D and $D/2$ is possible. The formation of islands and stretched monolayer is shown in Figure 2.16h, which is also determined by related preferential behavior. [120] With the neutral affinity, perpendicular orientation is much more favored.

(4) At $l < D/2$, depending on the affinity, preferential segregation induces the formation of parallel lamellar (Figure 2.16i). Notably, in such thin film thickness, the roughness of the substrate significantly influences the morphology of DBC film. [121]

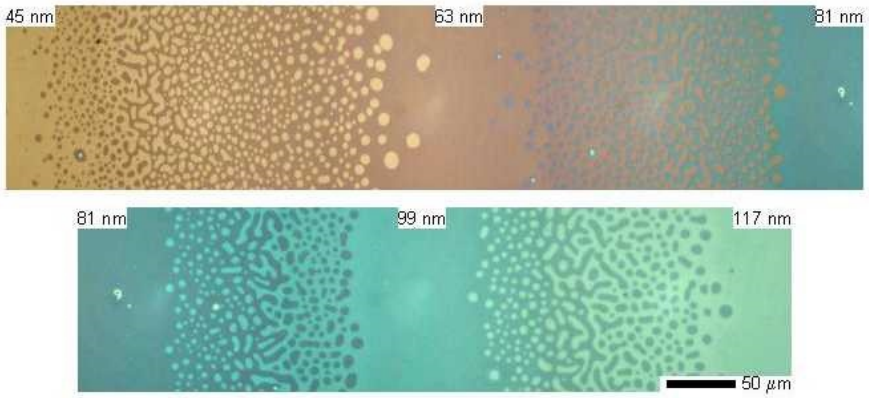

Figure 2.17: Optical microscopy images of PS-*b*-PMMA DBC films with two different molar mass in gradient film thicknesses showing the addition of lamellae to the surface with increasing thickness. Image taken from reference [122].

Compared to the lamellar morphology, the cylinder morphology is in a more complex condition. At the surface of DBC thin films with cylindrical composition, there are various deviations have been observed, such as perforated lamellae, cylinders with necks, a wetting layer and others. [123, 124] However, in principle, the surface induced arrangement of cylindrical morphology obeys with the analogous theories in lamellar, which is mainly determined with the preferential affinity of blocks of DBC to the both interfaces. At $l > D$, parallel orientated cylinder (Figure 2.14c) morphology is dominant. The formation of holes and islands is determined by the wetting properties of DBC blocks to both surfaces. At $l \leq D$, with the condition of neutral preference, stable perpendicular cylinders (Figure 2.14d) are theoretically predicted and experimentally observed. [112, 121, 123] With the decrease of the film thickness, the confinement of the thin film between two physically different interfaces plays a more important role, because the interplay between the periodic

distance of DBC and film thickness becomes more significant. In one result (Chapter 5) of the present thesis, for a PSd-*b*-PBMA DBC film with a film thickness slightly smaller than the periodic distance of the DBC, a special ordered, perforated microphase separated morphology with a PSd enrichment layer at the polymer/substrate interface and perpendicular PSd cylinders in a continuous PBMA matrix at polymer/air interface is thoroughly investigated. [110] This observation perfectly matches the surface induce ordering and the confinement of film thickness regime.
DBC thin films with regular periodic structures in a large length range are used in diverse applications. They require uniform length scales. Thus, fully understanding of the orientation of structures is essential to the desired applications.

2.2 Fundaments of magnetism

Magnetic materials are widely applied in daily life. Their characteristic properties make them an indispensable type of material. [125] The present chapter is written based on a classic text book named *Introduction to Magnetism and Magnetic Materials*, [126] and gives an insight into fundamentals of magnetism, types of magnetic materials, and magnetic nanoparticles.

2.2.1 Basic concepts

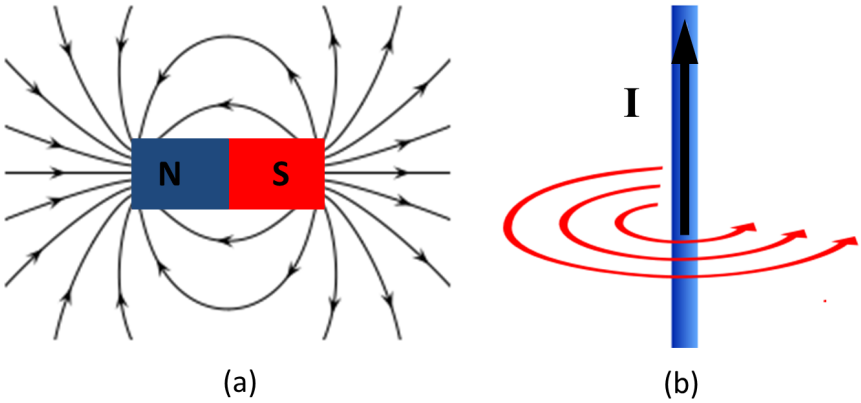

Figure 2.18: Sketches of magnetic fields are produced with (a) a permanent magnet and (b) moving electrical current. N and S are the north pole and south pole of the permanent magnet. I indicates the electrical current. The black and red curves with arrows show the magnetic field lines.

A magnetic field is the perturbation in a space originated by moving charges oriented dipoles. [126] The natural magnetic fields present in permanent magnets (Figure 2.18a) originated from the orbital motion and the spin of the electrons in a material, the behavior of which leads to the formation of magnetic moments. Magnetic fields can also be generated with electrical charges in motion (Figure 2.18b). [126] The first observation of the produced magnetic field throughout the flow of electrical current in a conductor was reported by Oersted et al. [127] The magnetic field is a vectorial field, thus, it contains both a direction and a magnitude at any pointed location. In general, the two different but related terms of magnetic induction (flux density) and magnetic field are employed to evaluate magnetic materials, which are denoted as B and H, respectively. In a vacuum condition, the relationship of them is expressed with:

$$\mathbf{B} = \mu_0 \mathbf{H} \tag{2.17}$$

where μ_0 is called the vacuum permeability and is a physical constant in a classical vacuum. The permeability indicates the degree of magnetization of a material in response to a magnetic field. [126] However, in different medium, the permeability is different. The magnetization of a material is defined with the total magnetic moment per unit volume of the material. Instead of a vacuum atmosphere, in a magnetic material, the relationship of $\mathbf{B}$ and $\mathbf{H}$ is expressed with:

$$\mathbf{B} = \mu_0(\mathbf{H} + \mathbf{M}) \tag{2.18}$$

where $\mathbf{M}$ denotes the magnetization vector field of the material, and the quantify $\mu_0\mathbf{M}$ is called magnetic polarization. We assume, there are n elementary atomic magnetic dipoles in each unit volume and a magnetic moment m in each dipole. In case all the dipoles are oriented parallel, the magnetic moment per unit volume of the material is named saturation magnetization, and it is denoted as M_0.

2.2.2 Magnetic domains

Pierre Weiss reported an assumption that ferromagnetic materials are consisted of magnetic domains, which is the first theory to interpret the hysteresis feature. [128] These magnetic domains are separated by domain walls. On one hand, the magnetostatic energy increases with the volume of the magnetic materials; on the other hand, the domain wall energy increases with the total surface area of domain walls. In order to reach the minimization of net energy in the whole system, a critical domain size is obtained. When the domain size is smaller than the critical value, the formation of the domain is energy unfavorable because of the relative larger domain wall energy. Hence, the magnetic materials

consist of uniformly magnetized domains and each domain acts like a small permanent magnet. The radius of the single critical domain size (r_c) is expressed as: [129]

$$r_c \approx 9\frac{(AK_u)^{1/2}}{\mu_0 \mathbf{M}_s^2} \tag{2.19}$$

where A is the exchange constant, and K_u is the uniaxial anisotropy constant. The typical critical radius of our employed maghemite material is 30 nm. [130]

2.2.3 The classification of typical magnetic materials

Based on the susceptibility of the bulk magnetic materials, the classification of typical magnetic materials are obtained. The susceptibility, χ, is a dimensionless constant, which describes whether an employed material is attracted into or repelled out of an external applied magnetic field. [126] Susceptibility is defined as:

$$\chi = \frac{\mathbf{M}}{\mathbf{H}} \tag{2.20}$$

In our case, vacuum permeability does not properly describe our experimental conditions. In this case, a relative permeability, μ_r, is introduced into the system, which describes the permeability in the experimental medium. The relationships amongst these important characteristics are expressed as:

$$\mathbf{B} = \mu_0(\mathbf{H}+\mathbf{M}) = \frac{\mu}{\mu_r}(\mathbf{H}+\mathbf{M}) = \frac{\mu}{\chi+1}(\mathbf{H}+\mathbf{M}) = \mu\mathbf{H} \tag{2.21}$$

where μ is the magnetic permeability.
In general, the types of magnetic materials are:

(1) $-10^{-6} \leq \chi \leq -10^{-5}$. The materials, which possess small and negative susceptibility, are defined as diamagnetic, such as gold, silver, copper, and beryllium.

(2) $10^{-5} \leq \chi \leq 10^{-3}$. The materials, which have weak magnetization behavior, are called paramagnetic materials, such as platinum, aluminum and manganese.

(3) $\chi \gg 0$. The materials, which possess positive and strong susceptibility, are defined as ferromagnetic, such as cobalt, nickel, iron, certain rare earth metals and their alloys.

The response behavior of a material to an applied magnetic field is the most crucial factor in their related applications. To estimate the magnetic materials, the **M**-**H** curve (magnetization as function of magnetic field curves) is essential. In the following sections, the magnetic features of diamagnetic, paramagnetic, and ferromagnetic materials are introduced.

Diamagnetism

The intrinsic property of magnetism in materials originates from the motion of electrons in atoms. However, in diamagnetic materials, there are only filled electron shells. The net magnetic moment of diamagnetic materials is zero, because the magnetic moments of the electrons, which spin in the different directions inside the full filled shells, counteract each other. Hence, when diamagnetic materials are subjected to an applied magnetic field, the induced magnetization resists the external applied field and presents fairly weak and negative susceptibility (oblique line) as shown in Figure 2.19. Based on the Langevin theory regarding the diamagnetic materials, the susceptibility is defined as:

$$\chi = -\frac{\mu_0 Z e^2 n < r^2 >}{6 m_e} \tag{2.22}$$

where, Z is the number of the electrons in each atom, e is the charge of the electron, n is the number of atoms in each magnetic domain, $< r^2 >$ is the root-mean-square (rms) atomic radius, and m_e is the mass of the electron. The diamagnetic susceptibility is independent of temperature.

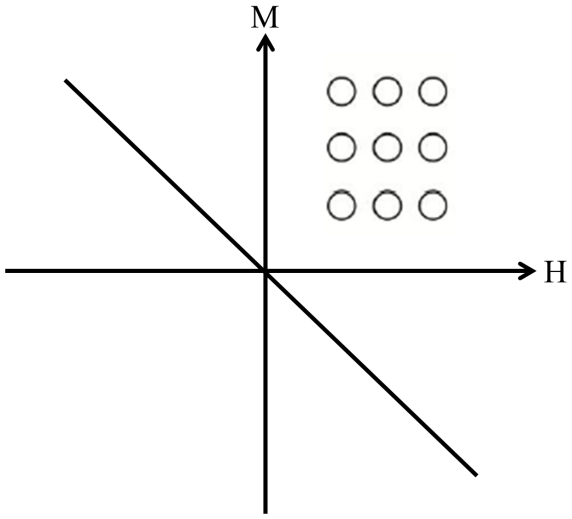

Figure 2.19: The **M-H** curve of diamagnetic materials. The hollow circles indicate the net magnetic moment of zero. Image taken from reference [131].

Ferromagnetism

Ferromagnetic materials possess rather high and positive relative permeability. There are a large number of unfilled electron shells in ferromagnetic materials. The individual magnetic moments generated by such electrons are highly-ordered and well-oriented.

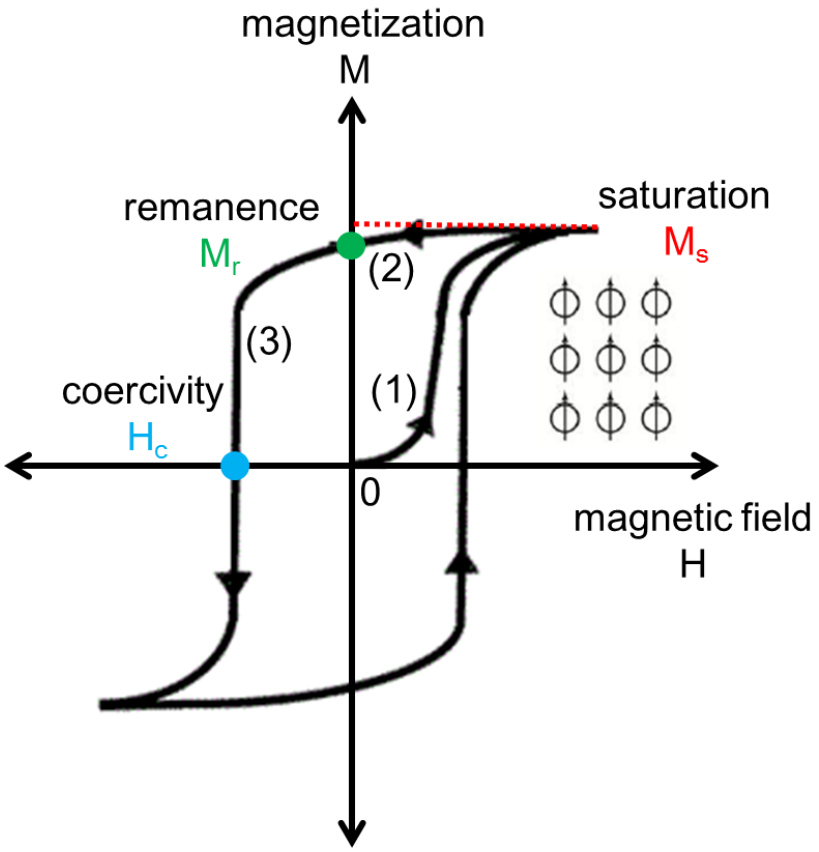

Figure 2.20: The **M**-**H** curve of ferromagnetic materials. The closed curvilinear loop is a typical magnetic hysteresis loop of the ferromagnetic materials. The inset of hollow circles with parallel arrows in the same orientation indicates the well-orientated magnetic moments. M_s, M_r and H_c is saturation magnetization, remanence, and coercivity, respectively.

Therefore, the net magnetic moments of ferromagnetic materials are nonzero. A typical magnetic hysteresis loop of ferromagnetic materials and important ferromagnetic features are depicted in Figure 2.20. The ferromagnetic materials are not magnetized at the initial stage (zero point in Figure 2.20). As the strength of the external applied magnetic field increases, the induced magnetization (**M**) shows a non-linear behavior (process (1) marked in Figure 2.20). When the materials are subjected to a rather high magnetic field, all the magnetic moments will be oriented following the direction of the external magnetic field, and any further increase of the magnetic field strength cannot make the magnetization increase further. Thus, the ferromagnetic material reaches saturation. Saturation magnetization is denoted as M_s (M_s in Figure 2.20). The M_s equals:

$$M_s = nm \tag{2.23}$$

where n is the number of magnetic domains, m is the magnitude of each individual magnetic moment. Afterwards, when external magnetic field decreases, the **M** decreases non-linearly but in a different track as the increasing process, which is called demagnetization (process (2) marked in Figure 2.20). When the external magnetic field has been completely removed (**H**=0), the remaining magnetization of the material is called remanence, M_r (M_r in Figure 2.20). Further, when an applied field equals to the coercivity, H_c, (H_c in Figure 2.20) in a negative direction, the magnetization will be reduced to zero (process (3) marked in Figure 2.20). Both M_r and H_c are important characteristics to describe the magnetic features of materials. In addition, H_c is highly sensitive to domain arrangement and orientation.

Paramagnetism

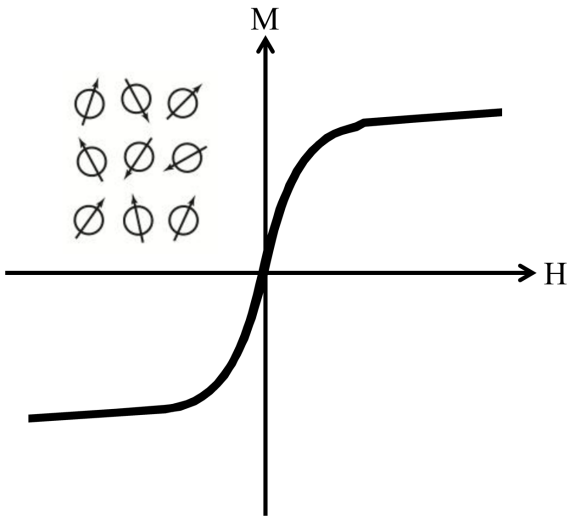

Figure 2.21: The **M**-**H** curve of paramagnetic materials. The inset of hollow circles with arrows in disordered directions indicates the randomly arranged magnetic moments. Image modified from reference [131].

The paramagnetic materials possess a small, positive susceptibility, and fall in between diamagnetic and ferromagentic materials. They have the atoms with unfilled electron shells, which contribute to a nonzero net magnetic moment. However, each atom of paramagnetic materials has an indivdual, randomly arranged magnetic moments (in the inset of Figure 2.21), which results in the zero net magnetic moment. By applying an external magnetic field, all the magnetic moments are reorganized and oriented along the same direction of the external magnetic field. Figure 2.21 presents the typical paramagnetic behavior. It is observed, with the increase of the field strength, more magnetic moments

are oriented thus, **M** linearly increases along the direction of the field. If the field withdraws, the magnetic moments back to the random status, and the net magnetic moment returns to zero again. In this case, both M_r and H_c of the ideal paramagnetic materials are zero. Based on the *Curie law*, [132] the susceptibility of the paramagnetic materials is inversely proportional to the temperature (T) and is expressed as:

$$\chi = \frac{C}{T} \tag{2.24}$$

where C is the Cuire constant. In particular, when ferromagnetic materials are subjected to a sufficiently high temperature, they will turn to paramagnetic materials. The transition temperature is defined as *Curie temperature*. [132] Beyond this critical temperature, due to the large thermal agitation involved, the M_r and H_c drop to zero, and the permeability of ferromagnetic materials sharply reduces. The slope in Figure 2.21 shows the linear increasing behavior of magnetization of the paramagnetic materials. A classic *Langevin function* well describes this relationship among the magnetization, magnetic field and temperature:

$$\frac{\mathbf{M}}{n\mathbf{m}} = coth(\frac{\mu_0 \mathbf{mH}}{k_B T}) - (\frac{k_B T}{\mu_0 \mathbf{mH}}) \tag{2.25}$$

where k_B is the Boltzmann's constant. Usually, $\mu_0 \mathbf{mH}/k_B T \ll 1$, thus, with the Equations 2.25 and 2.24, the Cuire constant, C, can be expressed as:

$$C = \frac{n\mu_0 \mathbf{m}^2}{3k_B} \tag{2.26}$$

2.2.4 Superparamagnetism

Superparamagnetic materials consist of single-domain ferromagnetic particles. [132] These particles are sufficiently small thus, they can flip randomly due to the thermal fluctuation. Therefore, without external magnetic fields, the entire material is not magnetized. Commonly, the magnetization of these single-domain ferromagnetic particles is oriented parallel or anti-parallel to a specific direction, which is defined as the easy axis. Such easy axis is caused by magnetic anisotropy (details in the later Section 2.2.5). The magnetic anisotropy energy (denoted E) of the uni-axial, single-domain particles is defined as:

$$E = KVsin^2\theta \tag{2.27}$$

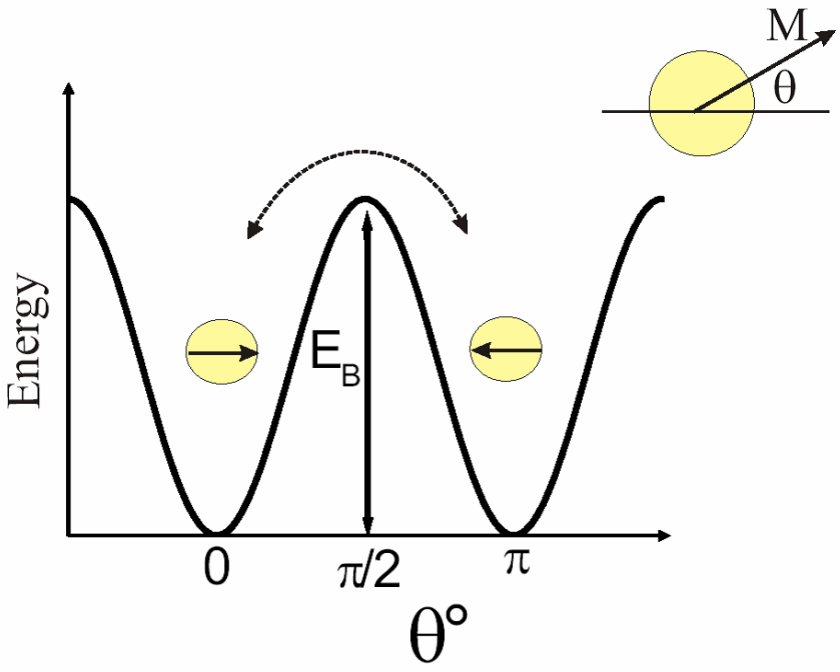

Figure 2.22: Schematic view of the potential energy of a single-domain particle with uni-axial anisotropy as a function of the direction of the magnetization. E_B indicates the energy barrier, which is required for the rotation of the magnetization. θ indicates the angle between the net magnetization and the easy axis. Image taken from reference [132].

where K is the anisotropy constant, V is the volume of particle, and θ is the angle between the magnetization and the easy axis.

In Figure 2.22, two energy minimums of parallel ($\theta = 0$) and antiparallel ($\theta = \pi$) (with respect to the direction of the easy axis) magnetization are separated with an energy barrier ($E_B = KV$). The flip behavior has been explained by Néel: if the single-domain particles are sufficiently small, KV becomes small enough so that the anisotropy energy can be overcome by energy fluctuations. Thus, the spontaneous magnetization reversal of a particle from one easy axis to another can take place, even without applying an external magnetic field. [133]

Based on an assumption of ignoring all interactions between particles, at $k_BT \gg KV$, the system behaves similarly as a paramagnet. The single-domain ferromagnetic particles include more than 10^5 atoms ferromagnetically coupled by exchange forces. [134] Such system is defined as superparamagnetism. At $k_BT \approx KV$, the magnetization fluctuation between two energy minima may occur depending on the time scale of the measurement, which can be described with a frequency f or a characteristic relaxation time $\tau = 1/2\pi f$.

In the framework of an Arrhenius-type activation law, the Néel-Brown expression is developed:

$$\tau = \tau_0 exp(\frac{KV}{k_B T}) \tag{2.28}$$

where $\tau_0 \sim 10^{-10}$s is the inverse attempt frequency. The Equation 2.28 reveals the temperature has a great effect on the dynamics of the magnetization reversal. At relatively high temperatures, magnetic moments fluctuate rather fast, which means the relaxation time is short, because they possess enough thermal energy to overcome the energy barrier. With the decrease of the temperature, the fluctuations decrease. At rather low temperatures, the attainable thermal energy is too low to overcome the energy barrier, hence the fluctuations are strongly suppressed and even are completely blocked eventually. For a selected time scale of a measurement, a characteristic blocking temperature (denoted T_B) is present. Below T_B, the magnetic moments appear blocked; Above T_B, the fluctuation of magnetic moments take place. At T_B, the timescale of both the fluctuation of magnetic moments and the particular measurement are comparable, which is expressed as: [132]

$$\tau_{exp} = \tau(T_B) = \tau_0 exp(\frac{KV}{k_B T_B}) \tag{2.29}$$

$\Rrightarrow$

$$T_B = \frac{KV}{k_B ln(\tau_{exp}/\tau_0)} \tag{2.30}$$

where τ_{exp} is the time scale of the measurement. For the Mössbauer spectroscopy experiment used in this thesis, τ_{exp} is in the range of $10^{-10} \sim 10^{-7}$s. T_B is not an intrinsic property of the magnetic system and is determined with the experimental observation time.
The identification of superparamagnetism contains at least two conditions: [132]

(1) According to thermodynamic theory, with infinite time scales, there is no hysteresis shown in the system regardless of the temperature.

(2) When ignoring the effects resulting from particle interactions, for isotropic materials, the hysteresis loops measured at different temperatures must be superimposed and show temperature dependence in M_r and H_c.

2.2.5 Magnetic anisotropy

The dependence of the internal energy on the orientation of magnetic domains in magnetic materials is called magnetic anisotropy. The magnetic moments of the materials with magnetic anisotropy prefer to lie along the easy axis due to the energetic favor. In particular, the shape anisotropy, which is attributed to the dipolar moments and is calculated under the assumption of a uniform distribution of magnetic poles, [134] is mainly focused in this thesis. The shape anisotropy is absent for the magnetic materials with complete symmetric structures in all directions, because the demagnetizing factor in one direction is fully cancelled with that in the antiparallel direction. The magnetic shape anisotropy is shown in the magnetic materials with asymmetric shape. The magnetization occurs along the shorter axis, since the demagnetizing field of the shorter axis is smaller than that of the longer axis.

2.2.6 Magnetic nanoparticles

The term nanoparticles (denoted NPs) describe one type of particles, the dimension of which is below 100 nm. The most significant advantage of NPs is attributed to the large surface to volume ratio. [135] The so-called magnetic NPs are the NPs that exhibit magnetic properties and behave like magnetic materials of ferromagnetic, paramagnetic and superparamagnetic. Due to their irreplaceable magnetic features, magnetic NPs are wildly used in various applications, such as the contrast agent in magnetic resonance imaging, drug deliverer in targeted therapy, the elements of inductor in magnetic sensors, and especially the single-bit elements in high-density digital storage medium. [21,26,136–138] The metal, metal alloy, and metallic oxides of cobalt (Co), nickel (Ni), and iron (Fe) are most commonly fabricated to be the employed magnetic nanoparticles. With several types of surfactant or selected polymer chains grafted or coated onto the surface of NPs, the monodispersity of NPs can be realized, and the self-agglomeration of NPs can be suppressed as well. [109,110] In case NPs are incorporated into a DBC film with the purpose of fabricating the NPs/DBC hybrid film, the more important function of such surface chemistry is to enhance the compatibility of the NPs to the desired block of the DBC. This process is called direct self-assembly approach, since the enthalpic interaction at the interfaces between NPs and selected domains favors mixing. [41,139] In the present thesis, PS-coated $\gamma - Fe_2O_3$ NPs in two different sizes (6.5 and 10 nm) are employed with the purpose of fabricating NPs/DBC hybrid films for the potential applications in the fields of magnetic medical instruments, magnetic sensors and magnetic recording devices.

2.3 Scattering techniques

The inner structures of the investigated NPs/DBC hybrid films are crucial for fully understanding the film morphologies and their evolution with the incorporation of NPs. X-ray and neutron scattering are advanced, nondestructive techniques to examine the inner morphologies with excellent resolutions down to several nanometers. The basic conceptions of elastic scattering , which assume the wavelength of the scattering wave remains constant throughout the entire scattering event, is described in the following Section 2.3.1. The introduction to the x-ray specular reflectivity and the scattering contrast for neutrons are in Sections 2.3.2 and 2.3.3. The primary used scattering methods in the present thesis of grazing incidence scattering measurement are introduced in Section 2.3.4.

2.3.1 Scattering basics

Based on the definition given by Tolan, the physical mechanism of the scattering event shows that an electromagnetic wave or a particle deflects from an object or in matter. [140] The scattering basics regarding x-rays are described in the present section, however, they apply for neutron scattering as well with the introduction of specific characteristics of neutrons (in Section 2.3.3).
The electric field vector ($\vec{E}(\vec{r})$) for a plane electromagnetic wave is defined as:

$$\vec{E}(\vec{r}) = \vec{E}_0 exp[i\vec{k}_i\vec{r}] \tag{2.31}$$

where $\vec{E}_0$ contains the polarization and the amplitude, $\vec{k}_i$ and $\vec{r}$ represent the wave vector and position. The modulus of the wave vector is given by:

$$k = \left|\vec{k}_i\right| = 2\pi/\lambda \tag{2.32}$$

where λ is the wavelength. The Hemholtz equation explains the process of the propagation of an electromagnetic wave in a medium: [140]

$$\triangle\vec{E}(\vec{r}) + k^2 n^2(\vec{r})\vec{E}(\vec{r}) = 0 \tag{2.33}$$

where $n(\vec{r})$ is the refractive index of the medium. This position dependent refractive index is defined as:

$$n(\vec{r}) = 1 - \delta(\vec{r}) + i\beta(\vec{r}) \tag{2.34}$$

where $\delta(\vec{r})$ and $\beta(\vec{r})$ are the dispersion and the absorption, which can be written as:

$$\delta(\vec{r}) = \frac{\lambda^2}{2\pi} r_e \rho(\vec{r}) \sum_{j=1}^{N} \frac{f_j^0 + f_j^{'}(E)}{Z} \tag{2.35}$$

and

$$\beta(\vec{r}) = \frac{\lambda^2}{2\pi} r_e \rho(\vec{r}) \sum_{j=1}^{N} \frac{f_j''(E)}{Z} = \frac{\lambda}{4\pi} \mu(\vec{r}) \tag{2.36}$$

$\rho(\vec{r})$ is the position dependent electron density. N is the number of the electrons in the unit volume, which indicates that the equations of the dispersion and the absorption are based on the sum of N atoms in unit volume. r_e is the radius of the classical electron, which can be written as: [141]

$$r_e = e^2/(4\pi\epsilon_0 mc^2) \tag{2.37}$$

The forced oscillator strength of the atom j is written as: [140]

$$f_j = f_j^0 + f_j'(E) + f_j''(E) \tag{2.38}$$

with respect to the small scattering vector:

$$\vec{q} = \vec{k_f} - \vec{k_i} \tag{2.39}$$

$\vec{k_i}$ and $\vec{k_f}$ represent the incident and exiting x-ray wavevectors, and f_j^0 is described with the number of the electrons of the atom j. For x-rays, the refractive index $n(\vec{r})$ only slightly deviates from 1, hence the total reflection appears at small angles (usually $< 1°$). In case the refractive index $n(\vec{r})$ is position independent in matter, the dispersion and the absorption are represented with δ and β. The total reflection occurs at

$$\alpha_c \approx \sqrt{2\delta} \tag{2.40}$$

and δ is usually on the order of 10^{-5}, which sets α_c at $< 1°$. In the case of hard x-ray ($\geq$ 8 keV) with the soft matter, the typical absorption β is rather small of about 10^{-6}. Thus, the effect of the absorption on the thin films is nonsignificant.

Figure 2.23 shows the sketch of the reflection geometry of the principle scattering setup. The incident wavevector $\vec{k_i}$ and the sample determine the coordinate system. The scattering plane is in the x-z plane. The exiting wavevector $\vec{k_f}$ can be splitted with the vectors following the directions of the exit angle α_f and the exit angle ψ_f in the out-of plane direction. The penetration depth Λ of the scattering signal can be written as: [142]

$$\Lambda = \frac{\lambda}{\sqrt{2\pi}} (l_i + l_f)^{-1} \tag{2.41}$$

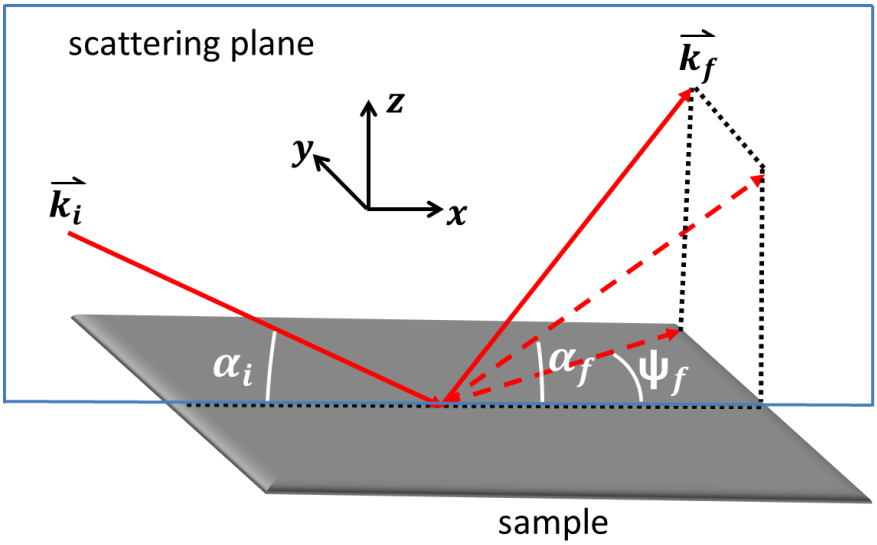

Figure 2.23: Sketch of the reflection geometry of the principle scattering setup. $\vec{k_i}$ and $\vec{k_f}$ are incident and exiting beam. α_i and α_f are incident and exit angle in the scattering plane. ψ_f is the out-of-plane angle in the sample plane.

$$l_{i/f} = \sqrt{(sin^2(\alpha_c) - sin^2(\alpha_{i/f})) + \sqrt{(sin^2(\alpha_{i/f}) - sin^2(\alpha_c))^2 + \frac{\mu\lambda}{2\pi}^2}} \tag{2.42}$$

Commonly, the penetration depth of the x-rays with respect to the softer matter is in μm scale even at shallow angles.

2.3.2 Specular reflectivity

The term of x-ray reflectivity (XRR) denotes the case if the out-of-plane angle (ψ_f) is zero, which records the specular scattering vs. the incident angle α_i, namely, the exit angle α_f equals the incident angle α_i. In the geometry of XRR, the scattering vector $\vec{q}$ is perpendicular to the sample plane, and only the z-component is collected: [140]

$$q_z = \frac{4\pi}{\lambda} sin(\alpha_i) \tag{2.43}$$

When the incident beam impinges on an interface, which is installed between two different materials with different refractive index n, the beam is approximately split into two parts of transmitted and reflected beams. Furthermore, Snell's law describes the angle of the transmitted beam α_t. The Fresnel transmission coefficient t^F and the Fresnel reflection

coefficient r^F are employed to describe the ratios of the amplitudes of the transmitted and reflected beam, respectively. The transmission and reflectivity can be written as: [140]

$$T^F = \left|t^F\right|^2 \tag{2.44}$$

and

$$R^F = \left|r^F\right|^2 \tag{2.45}$$

So far, the discussed scattering behaviors are based on one assumption that the interfaces are perfectly flat and involve no interfacial roughness. Interfacial roughness describes the deviation from a flat interface, which is commonly demonstrated with the root-mean-square (rms) surface roughness σ_{rms}: [143]

$$\sigma_{rms} = \sqrt{\frac{1}{N_{\sigma_{rms}}} \sum_{i=1}^{N_{\sigma_{rms}}} \triangle z_i^2} \tag{2.46}$$

where $N_{\sigma_{rms}}$ is the number of the selected sampling spots following the interface, and $\triangle z_i$ is the distance between the specific sampling spot i and the average interface. Taking into account the interfacial roughness for the analysis, the Fresnel reflection coefficient can be corrected with an exponential function of $N\acute{e}vot - Croce$ factor. [144] However, in case the roughness is beyond the film thickness, this correction cannot be applied any more. [140]

Figure 2.24 is an exemplification of a typical XRR data of measured reflectivity of a PS-*b*-PBMA DBC thin film on a silicon substrate. At $\alpha_i < \alpha_{c(PS-b-PBMA)}$, total reflection occurs; at $\alpha_i = \alpha_{c(PS-b-PBMA)}$ and $\alpha_i = \alpha_{c(Si)}$, the intensity drops sharply, which indicate the minimum for PS-*b*-PBMA and silicon; at $\alpha_i > \alpha_{c(Si)}$, oscillations appear, which are defined as Kiessig-fringes and reveal the information of the film thickness, d: [145]

$$d \approx 2\pi / \triangle q_z \tag{2.47}$$

where $\triangle q_z$ is the distance between two neighboring minima of the Kissing fringes.

2.3.3 Scattering contrast for neutrons

X-rays interact with the electron cloud of atoms, while neutrons are scattered from the nuclei of atoms. In the reflectivity regime, the Q_z component of the neutron wave function $\psi_n(z)$ can be obtained with a 1D Schrödinger equation: [146]

$$[-\frac{\hbar}{2m_n} \triangle + V(z)]\psi_n(z) = E\psi_n(z) \tag{2.48}$$

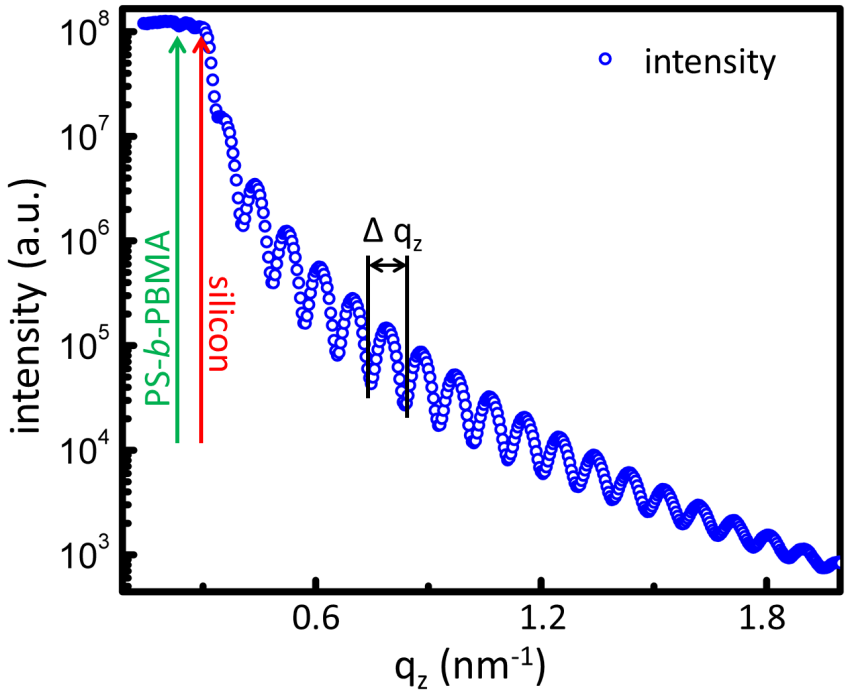

Figure 2.24: Measured XRR reflectivity intensity of the PS-*b*-PBMA thin film on the supported silicon substrate. Green and red arrows point out the critical q_z of the PS-*b*-PBMA and silicon, respectively. $\triangle q_z$ is indicated with the distance between two of the neighboring minima of the Kiessig fringes.

where $\hbar$ is the reduced Planck's constant, m_n is the neutron mass and $V(z)$ is the potential. An analogous expression of so-called Helmholtz equation can be applied to interpret the neutron reflectivity:

$$V(z) = -\frac{\hbar k_n^2 n_n^2(z)}{2m_n} + E \tag{2.49}$$

where k_n is the wavevector of the plane wave solution arisen from the Equation 2.48. For x-rays, n_n indicates the refractive index. However, for neutrons, n_n is the scattering length density (SLD). In accordance with x-rays, the SLD is commonly written as: [147]

$$n_n = 1 - \delta_n + i\beta_n \tag{2.50}$$

The absorbing part β_n in neutron scattering is so small that it can be ignored for most of elements. [147] Since the neutron interacts with the nucleus of the atom, the dispersive part δ_n can be changed by replacing certain original atom with its isotopes without altering its chemical properties. In the present thesis, for some batches of samples, selected hydrogen atoms (H) of the investigated DBC are replaced with the deuterium atoms (D) to enhance the scattering contrast, the process of which is called deuteration.

2.3.4 Grazing incidence small angle scattering

In addition to the specular scattering information, the diffuse scattering information arisen from interfaces can not be obtained with a reflectivity method (in previous Section 2.3.2). Besides the interface roughness, the lateral structures as well contribute to diffuse scattering. Such lateral contribution can be probed with the grazing incidence small angle x-ray/neutron scattering (GISAXS/ GISANS). In the geometry of GISAXS/ GISANS (see Figure 2.23 with $\alpha_i < 1°$), for examining a large sample area with higher statistics, a small grazing incidence angle $\alpha_i < 1°$ is commonly selected. In general, the typically size of the mesoscopic structures is in the range of several nms to 2 μm. [148] The diffuse scattering of these structures is recorded on a 2D detector. Based on the geometry, the scattering vector $\vec{q}$ is defined as: [149]

$$\vec{q} = \frac{2\pi}{\lambda} \begin{pmatrix} cos(\alpha_f)cos(\psi_f) - cos(\alpha_i)cos(\psi_i) \\ cos(\alpha_f)sin(\psi_f) - cos(\alpha_i)sin(\psi_i) \\ sin(\alpha_f) + sin(\alpha_i) \end{pmatrix} \tag{2.51}$$

For small exit angles α_f, the q_x contribution can be ignored due to its rather small value. [150] Based on the commonly used distorted wave Born approximation (DWBA), the diffuse scattering process is treated as a perturbation of an ideal system. [151,152] The calculation regarding the scattering cross section can be realized with first-order perturbation theory. [151] In this case, flat interfaces are considered as the ideal system, while the lateral structures and roughness are treated as perturbations. Thus, the differential cross section is given by

$$\frac{d\sigma}{d\Omega} = \frac{C\pi^2}{\lambda^4}(1-n^2)^2 \left|t_i^F\right|^2 \left|t_f^F\right|^2 F(\vec{q}) \propto F(\vec{q}) \tag{2.52}$$

where C is the area of the illuminated surface, and $F(\vec{q})$ is the diffuse scattering factor. This transmission function has a feature maximum, which brings a characteristic intensity in the diffuse scattering. This maximum occurs at $\alpha_f = \alpha_c$ (α_c is the critical angle of the probed material) and is called Yoneda peak. [153] α_c is determined by the scattering length density ρ of the probed material. [153, 154] The transmission function works only as the overall scaling factor, and the scattering signal is proportional to the diffuse scattering factor $F(\vec{q})$. [155] Bodies with a specific dimension and an interference function on a reflecting substrate are employed to simulate and thus to interpret a specific GISAS scattering pattern within the DWBA. Based on the assumption of the presence of N identical bodies in a random orientation, $F(\vec{q})$ can be expressed as: [156]

$$F(\vec{q}) \propto NS(\vec{q})F(\vec{q}) \tag{2.53}$$

where $S(\vec{q})$ is the interference function (structure factor), which explains the spatial arrangement of the bodies, and $F(\vec{q})$ is the form factor of the bodies. [156] The expression 2.53 is commonly applied for analysis of the lateral structures obtained from GISAS scattering patterns. [150]
In the present thesis, GISAXS/GISANS is the most important characterization method for probing the inner structures of our investigated NPs-DBC hybrid films. For a thorough investigation, 1D cuts of the obtained 2D GISAXS/GISANS data are analyzed based on a constructed modeling composed of cylindrical objects. In the modeling, a 1D paracrystal (1DDL) is considered as the structure factor. Those cylindrical bodies are supposed to be arranged periodically, and the deviation of the position increases with the increasing distance from the origin. Hence, instead of the long-range order, the short-range order is shown. Notably, the arrangement of 1DDL is irrespective of the direction in the system. [157] In addition, the size distribution of the bodies are included using a local monodisperse approximation (LMA). Details regarding the LMA is described elsewhere. [146] Furthermore, the contributions originated from reflections before and after the scattering (in the DWBA regime) have to be considered. Taking into account all contributions, the final form factor is realized. While, the roughness effect within the possible scattering events can be included with the Fresnel reflection coefficients as well. [158]
To fit the line cuts made from 2D GISAXS/GISANS data, the form factor of the modeled cylinders are fitted with a Gaussian distribution, which is given by: [159]

$$f(x) = \frac{1}{\sigma\sqrt{2\pi}} e^{-\frac{(x-x_0)^2}{2\sigma^2}} \tag{2.54}$$

x_0 is the value of the peak center, and σ is the standard deviation. The full width at half maximum (FWHM), which indicates the ordered degree of the assumed structure, is determined with the standard deviation:

$$FWHM = 2\sqrt{2ln2}\sigma \tag{2.55}$$

GISANS with TOF-mode

Time-of-flight (TOF) mode GISANS is realized via a bunch of neutrons with different wavelengths separated by a double-chopper separation system due to the time resolved detection arising from their different velocities, i.e. the neutrons with different wavelengths have different velocities, thus the time is different when they pass the identical distance between two choppers, then with such neutron flight process a wavelength discrimination is achieved (seen in Figure 2.25). [160, 161] With the TOF mode, GISANS measurements applying a bunch of neutrons with different wavelength can be carried out simultaneously, which equals to multiple GISANS measurements with a single wavelength performed with

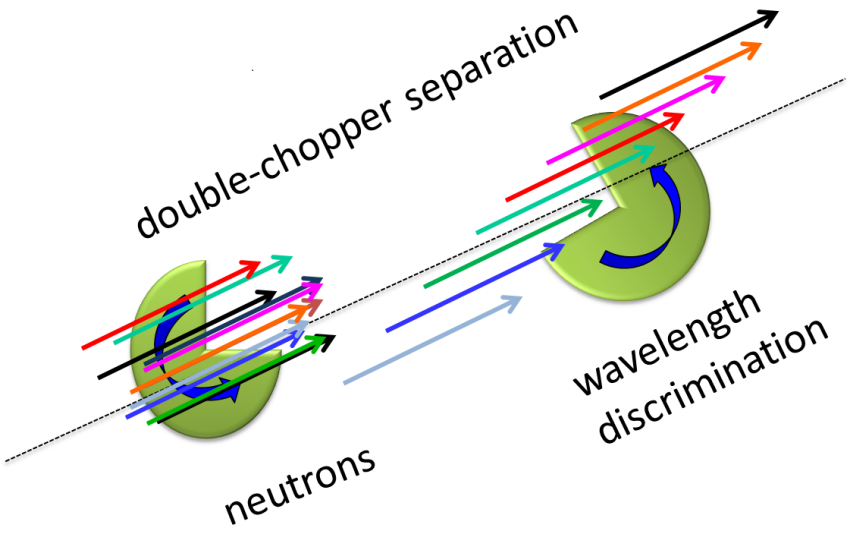

Figure 2.25: Sketch of double-chopper separation system for the neutron wavelength discrimination. The green plates are choppers, which rotate with the directions marked with blue curve arrows. The colorized straight arrows indicate the neutrons with different wavelengths.

several different incident angles. [160] Therefore, compared with regular GISANS, TOF-GISANS has a large advantage in time consumption.
The wavelength of the neutron is determined by the momentum of the neutrons $p(v_n)$ via deBroglie wavelength, which can be written as: [66]

$$\lambda = \frac{h}{p(v_n)} \tag{2.56}$$

where h is the Planck's constant, and $p(v_n)$ is determined by the velocity of the neutron v_n. Accordingly, the neutron with a shorter wavelength has a higher velocity. During the GISANS measurements, the neutrons drop in negative q_z direction due to the gravity effect. Neutrons with longer wavelengths suffer from a more serious gravity effect, because their lower velocities result in longer flight time. In the subsequent analytical process, the gravity effect is corrected and the details of correction are described elsewhere. [66]

Chapter 3

Characterization methods

In the present thesis, four batches of NPs-DBC hybrid films with different purposes and fabricating methods are fully characterized with a variety of techniques. The film structures are investigated with several real-space and reciprocal space techniques. The magnetic properties are probed with a magnetic property measurement system (MPMS) of a superconducting quantum interference device (SQUID). Furthermore, Mössbauer spectroscopy, x-ray reflectivity and small angle x-ray scattering are applied to examine the employed maghemite NPs. All the characterization techniques employed in this thesis are introduced in the present chapter.
In detail, the real-space techniques optical microscopy (Section 3.1.1), scanning electron microscopy (Section 3.1.2) and atomic force microscopy (Section 3.1.3) are applied to probe the surface structures of the hybrid films. To examine the buried nanostructures, the reciprocal space techniques grazing incidence small angle x-ray scattering (Section 3.1.8) and time-of-flight grazing incidence small angle neutron scattering (Section 3.1.9) are used. To investigate the magnetic functionality of the hybrid films, SQUID magnetometer (Section 3.2.1) was performed. Furthermore, to examine the chemical identities and the sizes of NPs, Mössbauer spectroscopy (Section 3.2.2), x-ray reflectivity (Section 3.1.5), and small angle x-ray scattering techniques (Section 3.1.7) are applied.

3.1 Structural characterization

3.1.1 Optical microscopy (OM)

Optical microscopy (OM) allows for the examination of the surface structures of the hybrid films in micrometer scale, which is used for the determination of the length and the width of metallic wires in our investigations, and is also applied as a fast quality check of the

magnification [×]	resolution [μm/pixel]
1.25	6.26
2.5	3.11
10	0.82
50	0.17
100	0.082

Table 3.1: Resolutions for corresponding different magnifications of OM.

prepared films. The used OM is an Axiolab A microscope (Carl Zeiss) equipped with five different magnifications objectives from 1.25× to 100× and combined with a PixeLink USB Capture BE 2.6 charge coupled device (CCD) camera. The size of the obtained OM images is 1280 × 1024 pixels. The corresponding resolutions of each pixel for different magnifications are presented in table 3.1. For measuring the length and the width of the metallic wires, the magnifications of 50× and 100× are used. To process and analyze the images, the software ImageJ 1.46r is applied.

3.1.2 Scanning electron microscopy (SEM)

To probe the surface structure of the hybrid films with a much higher resolution compared with OM, scanning electron microscopy (SEM) is applied. Instead of optical visible light, electrons are used in SEM, which can provide a higher resolution due to the smaller wavelength. There are two possibilities for generating the electrons, supplied by either a hot cathode or a field emission electrode. [162] In the case of using a field emission electrode, the electrons are produced by a strong electrical field that allows them to be emitted from the cathode. Afterwards, the electrons are accelerated by a voltage of several kV and are focused by a set of magnetic and electrostatic lenses. The accelerated electrons hit the film surface and cause the emission of secondary electrons out of the hit material. Subsequently, the secondary electrons are recorded on a detector at small sample-detector-distance. Meanwhile, backscattering of the electrons and cathodoluminescence appear. [162] However, they do not contribute to the generation of the SEM images. The intensity of the emitted secondary electrons is collected for each scanned point and influenced by the nature of the material and the sample-detector-distance. Depending on different examined materials and their topography, a monochrome SEM image with corresponding brightness values can be obtained with a penetration depth within 10 nm. [154] However, the perpendicular changes with respect to the film surface have very limited contribution

to the secondary electron intensity.
In the present thesis, all SEM images are collected from a FESEM Gemini NVision 40^2 (Carl Zeiss) controlled by the software SmartSEM (Carl Zeiss). To get possible high resolutions and avoid oversaturated charging for SEM images, acceleration voltages of 0.4, 2 and 4 kV at working sample-detector-distance of 0.9, 1 and 1.2 mm with an aperture of 10 μm are used. For a stable working environment, the vacuum pressure of the gun and the system are 2×10^{-9} and 2×10^{-6} mbar, respectively. The signal of secondary electrons is recorded on an InLense detector, which is placed around the primary electron beam with a ring-like shape. All SEM images are processed and analyzed by adjusting brightness and contrast, tuning Gauss blur parameters, and making FFT patterns via software ImageJ 1.46r.
Although the embedded metal-oxide NPs are conductive, the probed hybrid films are still considered as a non-conductive material because the ratio of the incorporated NPs is fairly low in the entire hybrid film system. Because of the poor electrical conductivity of the hybrid film, it can easily be charged up in a short time. Hence, the obtained image quickly appears dark, which increases the difficulty of the focusing. By selecting appropriate working parameters, SEM measurements for the non-conductive hybrid films can be realized. In this case, highly conductive substrates are necessary in order to conduct the accumulated electrons away from the films. In the present thesis, silicon is used as a proper conductive substrate. To modify the measuring process, a highly conductive graphite tape is used. A long strip shaped graphite tape is pasted close to the investigated position and is connected to the metallic sample holder to accelerate the transport of the accumulated charges. To check the sample homogeneity, the SEM images are taken at several selected spots, which are located close to the four corners and at the center of each sample.

3.1.3 Atomic force microscopy (AFM)

Since OM and SEM only provide 2D structural image, the height profile of the film surfaces is inaccessible. A 3D map of the film surface can be obtained by atomic force microscopy (AFM) with full quantitative preservation of the height profile.
The primary working principle of AFM is based on the atomic interaction between the AFM tip and the sample surface. The AFM tips are rather small, and the typical radius of them is only a few nanometers. The tips can approach the sample surface very closely. In this case, an extremely small interatomic force is accessible. AFM measurements have three basic modes: tapping, contact, and non-contact mode. In order to minimize surface damage of our investigated soft materials from the AFM measurements, tapping mode is

applied in the present thesis. Figure 3.1 presents a sketch of a simplified AFM setup and its functional principle.

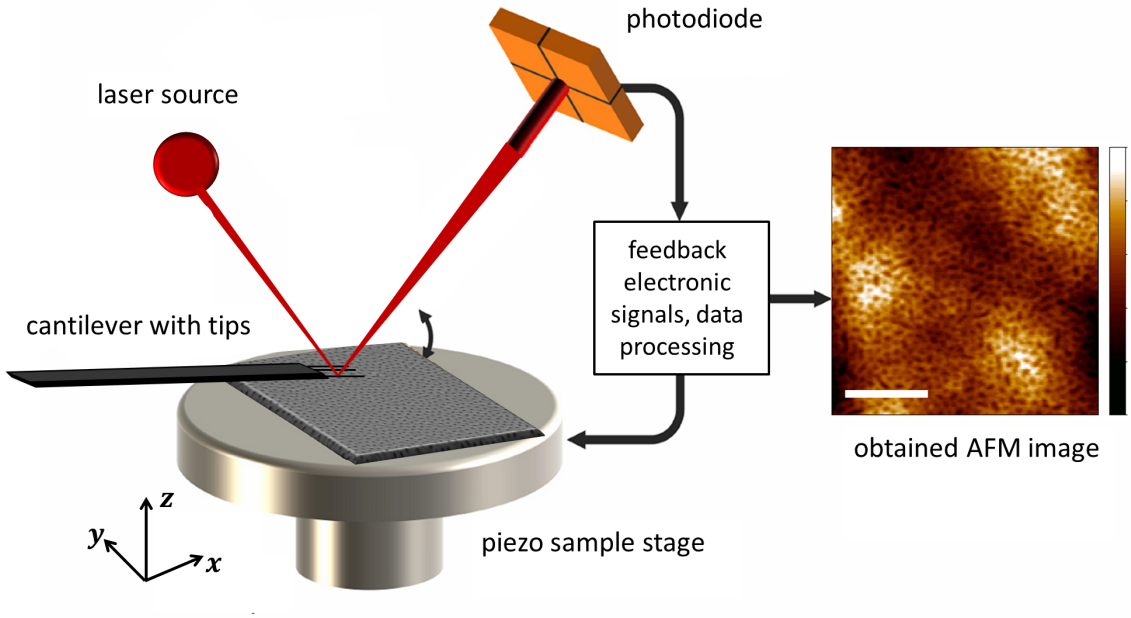

Figure 3.1: Sketch of AFM equipment. The sample is placed horizontally on a 3D mobilizable piezo sample stage. The cantilever is placed above the sample, with 3 tips on its front end communicating with the sample surface. A laser beam is focused on the top of one of the tips. The tip moves along with the film surface. The displacement of the tip is detected via a reflective laser recorded on a photodiode. The readjustment of the sample position and the data processing are realized with a feedback system connected with a computer.

The tips are installed on a cantilever with a well-defined spring constants. In tapping mode, the applied cantilever is excited to its constant resonance frequency ω, and the sample is mounted underneath the tip with a sample-tip distance smaller than 100 nm. The sample holder is controlled by a piezo stage, which enables the sample movement in the xy-plane. During the measurement, the tip touches the sample surface with high frequency. The information of the change in height is passed to the cantilever and induces a change of its amplitude. Meanwhile, the changed amplitude is detected due to a change in the deflected laser signal, which focuses on the topside of the cantilever near the tip region, on a multi-segmented photodiode. The feedback electronics collect the data and adjust the sample to a new position along z-direction. In this way, the initial sample-tip distance is restored. The sample surface is being scanned line by line and the height profile (vertical change of each position) is recorded simultaneously.
All AFM measurements are carried out in ambient conditions. Two different AFM in-

struments are employed in the present thesis. The corresponding functional parameters are presented below:

(1) AFM-1: JSPM-5200 AFM (JOEL). The applied tips, with a curvature radius of less than 15 nm, are mounted onto the one cross-side of the cantilever (ULTRASHARP NSC35/ALBS, MikroMasch) with a spring constant of 7.5 N/m and a resonance frequency of 170 kHz.

(2) AFM-2: Autoprobe CP Research AFM (Veeco Metrology Group). The applied tip, with a curvature radius of 10 nm, is mounted onto the backside of conically shaped cantilever (Ultralever OLNC-B) with a spring constant of 2.1 N/m and a resonance frequency of 75 kHz.

The AFM data collected from both AFM instruments contain 256 × 256 data points. The software WinSPM v2.14 is used to process and analyze the obtained AFM data, e.g., background subtraction, roughness calculation, and line cuts representation of topography images.

3.1.4 Surface profilometry

Film thickness can be measured with a surface profilometer in a simple and fast procedure. In the present thesis, a Dektak XT Surface Profiler (Bruker) is employed to examine the height deviation between the supported silicon substrate and top surface of the film, which is defined as film thickness. To proceed, part of the film is required to be lifted off from the substrate with the help of a sharp plastic knife. Afterwards, the prepared sample is horizontally placed on a sample stage installed underneath a measuring tip. The computer controlled tip descends to the film surface and approaches a selected edge of the substrate and the film. With a slow scan speed of 1 μm/s and a stylus force of 9.8 μN, the tip crosses over the edge, and then the film thickness is obtained after the data processing. For statistics, 3 edges and 5 times measurements of each edge are examined for each sample.

3.1.5 X-ray reflectivity (XRR)

In order to get more information on the vertical dimension of thin film samples, x-ray reflectivity is employed. The regarding theoretical basics have been discussed in the reflectivity part of Chapter 2 (Section 2.3.2).
XRR measurements were performed on a D8-advance (Bruker). The software XRDcommander and XRDwizard are used to control and program the measurement protocols,

respectively. The x-ray radiation is supplied by a copper anode with a wavelength of λ_{Cu} = 0.154 nm. The examined sample should be longer than 2.5 cm to avoid the experimental inaccuracy caused by over-illumination. During the measurement, the sample is placed horizontally on a circular sample stage.
The XRR instrument mainly consists of an x-ray source tube, a sample stage and a signal detector. The change of the incident angle θ is realized by varying the angle 2θ between the detector and the incoming x-ray beam. [163]
In order to block the noise originating from part of the x-ray beam, a knife-edge is placed above the sample with only tiny spacing. The knife-edge confines the illuminated region to obtain a high angular resolution. To well define the x-ray beam, narrow slits with the width of 0.05 and 0.1 mm are installed at the x-ray entrance and before the detector, respectively. In this case, a high resolution and decreased intensity are accessible. A typical XRR curve in the present thesis is measured for an angular range of $0° < 2\theta < 7°$ with an increment size of 0.01°. An absorber is applied to block the high intensity of the total reflected signal. For our probed samples, a counting time of 20 s is selected. Film thickness information is obtained by fitting the reflectivity profiles using the software of Parratt algorithm. [164]

3.1.6 X-ray diffraction (XRD)

The x-ray diffraction (XRD) is necessary for the determination of the chemical identity of the employed NPs. In the present thesis, the previous discussed XRR instrument has been applied for the XRD measurement. Working principles of the XRD are similar to the XRR as well. The most important difference is that no knife-edge is applied in the XRD measurement. Typical XRD data in the present thesis are performed with an angular range of $15° < 2\theta < 70°$ with an incremental size of 0.01°. A counting time of 40 s for each step is selected. Slits with the width of 0.05 are installed both at the x-ray entrance and before the detector.

3.1.7 Small-angle x-ray scattering (SAXS)

To determine the dimension of the NPs, small-angle x-ray scattering (SAXS) is performed on a Ganesha 300XLWSAXS-WAXS system (SAXSLABApS, Copenhagen/Denmark). The x-ray is produced at 50 kV and 0.6 mA, using a Cu anode with a wavelength of 0.154 nm. [108, 110] The sample-to-detector distance is 1.051 m. For avoiding NP aggregation and other possible effects, a highly diluted NP solution is made with the NPs dissolved in the solvent toluene. The NP solution is injected into a glass capillary, which

functions as a sample holder and allows for x-ray transmission. [108,110] The transmission data is recorded on a 2D detector. For a quantitative analysis of the NP dimension, a line cut of the azimuthal integration of the intensity distribution from the 2D SAXS data is required. Such a line cut is fitted using SAXSFit 2.3 software [165] assuming hard sphere particles to get the precise NP size with its distribution.

3.1.8 Grazing incidence small-angle x-ray scattering (GISAXS)

To probe the inner structures underneath the film surface with high statistical relevance, grazing incidence small-angle x-ray scattering (GISAXS) is performed. The corresponding theoretical basics have been described in the Section 2.3.4.

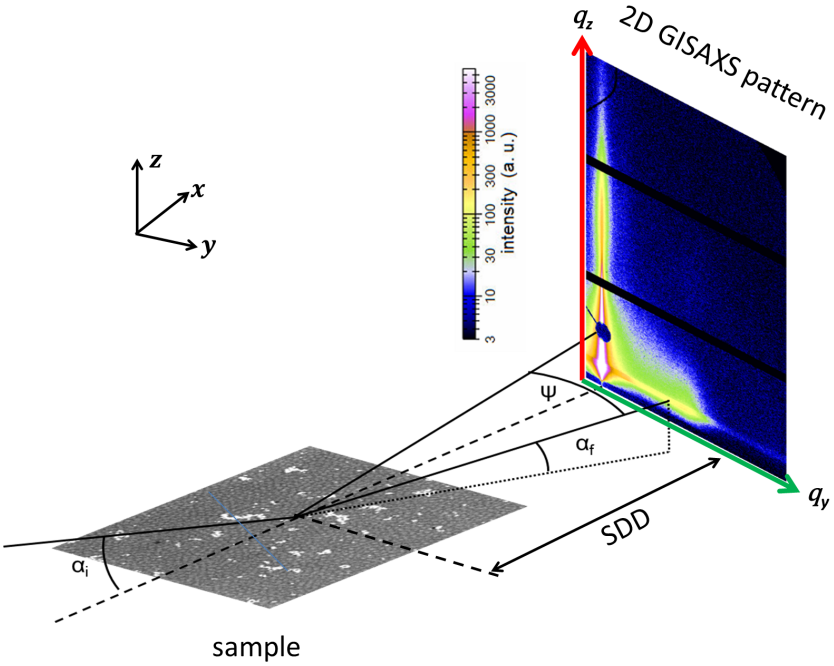

Figure 3.2: A schematic view of the GISAXS geometry. The x-ray impinges on the sample with a shallow incident angle ($\alpha_i < 1°$), and an exit beam with an angle of α_f is recorded on a 2D detector. The sample-detector distance (SDD) can be adjusted based on the structures to be probed. The scattering plane is defined in the xz plane.

The GISAXS measurements are performed at the beamline P03, Micro- and nanofocus x-ray scattering (MiNaXS) of the PETRA III storage ring (DESY, Hamburg, Germany). [166, 167] The details of alignment are explained elsewhere. [168]
A schematic view of the GISAXS geometry is shown in Figure 3.2. The selected x-ray wavelength is $\lambda_{P03} = 0.0957$ nm with the x-ray energy of 13.0 keV. The shallow incident

angle (α_i) is set to 0.35°, which is well above the total reflection angles (critical angles) of all the materials involved in our investigated hybrid film systems. In this case, the entire films can be fully penetrated with the selected x-ray beam. Hence, the provided scattering data contain the information throughout the full depth of the films. The x-ray beam size at P03 is shaped to 20 × 40 μm^2 in vertical × horizontal direction by parabolic beryllium compound refractive lenses (Be CRLs). [169]

The samples are horizontally placed on a 3D movable sample stage. The scattered data are recorded on a 2D detector (Pilatus 300K Dectris Ltd., Switzerland, with 487 × 619 pixels, pixel size 172 × 172 μm^2). To access the desired dimension range, SDD are set to 2.49 and 2.55 m, respectively. To minimize the scatter noise from air, an evacuated flight tube with a flexible length is installed between the sample stage and the detector to cross over the gap. For avoiding oversaturation, two point-like beam stops are installed in front of the detector at the positions of the direct beam and the specular reflection, respectively. For interpreting the intensity in the 2D GISAXS data (seen in Figure 3.2), a color bar from black via purple, blue, green, yellow, orange, and red to white is used.

The software fit2d (developed by Andy Hammersley, ESRF, Grenoble) is applied to analyse the 2d GISAXS data. The different scattering directions provide the structural information relative to the substrate. For a quantitative analysis, based on the geometry of GISAXS, the so-called horizontal cuts (q_y direction, parallel to the substrate, marked with a green arrow in Figure 3.2) and vertical cuts (q_z direction, perpendicular to the substrate, marked with red arrow in Figure 3.2) of the 2D intensity distribution are integrated from the 2d data. The integration averages the intensity over approximately 5 pixels for statistics. Furthermore, for a precise determination of lateral structures, the horizontal cuts (q_y profiles) are fitted with a model assuming a Lorentzian distribution of length scales, the details of which are described elsewhere. [90] The lateral structural size and its distribution are revealed via the fit results.

In particular, due to shape anisotropy, one batch of samples in the present thesis regarding the fabrication of nano- and microwires (in Chapter 7) were measured in two orientations: The x-ray beam was oriented parallel or perpendicular with respect to the wire shaped NP aggregates, which were visualized on top of the hybrid films. Combined with the understanding of the GISAXS geometry, the horizontal cuts, which were probed with the direction of x-ray beam parallel or perpendicular to the wire shape aggregates, show the lateral structures perpendicular or parallel to the NP wires, respectively.

3.1.9 Time of fight grazing incidence small-angle neutron scattering (TOF-GISANS)

As an alternative to x-rays, neutrons also can be applied for scattering under grazing incidence. A different contrast can be obtained with neutron scattering, and thus more structural information can be accessed. In the present thesis, nanostructures and composition for two batches of hybrid films are investigated with GISANS in the time-of-flight mode, which is called TOF-GISANS. The related theoretical basics have been discussed in Section 2.3.4.

TOF-GISANS measurements were carried out at the REFSANS instrument of the Helmhol tz Zentrum Geesthacht at the Heinz Maier-Leibnitz Zentrum, Garching, Germany. [170–173] A sketch of the TOF-GISANS experiment set-up is shown in Figure 3.3. The basic geometry of GISANS is similar to that of GISAXS (in Figure 3.2). The main difference in GISANS is that an extra transmission signal can be detected, because the silicon substrate is transparent to the neutron source.

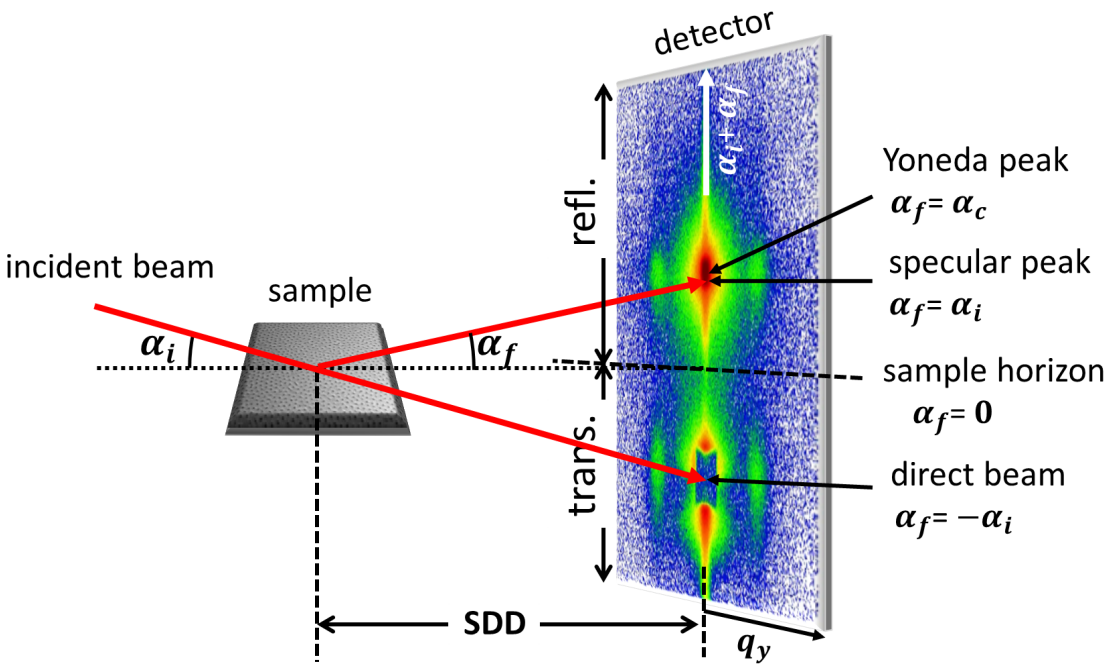

Figure 3.3: Sketch of the geometry applied in the TOF-GISANS measurements. The incident and exit angle are indicated with α_i and α_f. The horizon (dashed line) separates the reflected and transmitted signal. Image taken from reference [110].

During the TOF-GISANS measurements, the neutron beam impinges on the sample with a fixed incident angle of 0.50°. The critical wavelength for total external reflection

is at λ_c= 0.97 nm for our investigated DBC films. Instead of a monochromatic neutron beam, a continuous neutron spectrum with a varied wavelength range from 0.23 nm to 1.22 nm is applied. For wavelength discrimination, the incident neutron beam is split by a high-speed rotated double-chopper system. [172] The basic principle of the TOF mode has been described in Section 2.3.4. For data processing, the neutron spectra are on purpose sliced into several wavelength channels with a resolution of 10% for each channel. [174] Neutrons with short wavelengths can fully penetrate the investigated hybrid films, while neutrons with a wavelength longer than 1.02 nm are only scattered at a finite depth of less than 60 nm at the selected incident angle. [110] The penetration depth strongly depends on the scattering length density, ρ, of the investigated material. Therefore, depth profiles of the film structure can be obtained from the TOF-GISANS data with corresponding neutrons in different wavelengths.

The sample is horizontally placed on a movable sample stage. The scattering signal is detected on a 2D ^3He detector (consists of 340 × 340 pixels, pixel size 1.38 × 1.38 μm^2) with a SDD of 10.52 m. [171] To obtain sufficient statistics, the counting time is set to 24 hours. For protecting the detector from large intense damage, a beam stop is installed at a fixed position in front of the detector to block the direct beam. All measurements are performed at ambient conditions with no solvent present. The software LAMP (v6.2) developed by ILL, Grenoble is used to process the 2D GISANS data. A color bar, from black via purple, blue, green, yellow, orange, and red to white, represents the intensity. Similar to data analysis procedures of GISAXS, structural information in different orientations is obtained from horizontal (q_y direction, parallel to the substrate) and vertical cuts ($\alpha_i + \alpha_f$ direction, perpendicular to the substrate) of the 2D GISANS data. The horizontal cuts (q_y profiles) were fitted with a model assuming a Lorentzian distribution of length scales. The information of the critical angles corresponding to different components in the hybrid film systems is obtained from the vertical cuts, which are fitted with a linear function of the neutron wavelength with the slope proportional to their scattering length density (seen in Equation 2.50).

3.2 Characterization methods of magnetic property

3.2.1 SQUID magnetometry

Direct current (DC) magnetization measurements as a function of temperature are performed with a superconducting quantum interference device (SQUID) magnetometer (MPMS XL-7, Quantum Design, San Diego, CA, USA). A schematic view of the SQUID setup is represented in Figure 3.4. The probed sample is cut into 0.6 × 0.6 cm^2 and

is inserted inside a plastic straw, which functions as a sample holder without magnetic disturbance. The sample is placed in the center of a superconducting solenoid. The sample chamber is sealed and is fully filled with liquid helium. For our investigated magnetic material (maghemite, γ-Fe_2O_3), to reach its saturation magnetization, the sample is measured with an applied external magnetic field varied from -700 to 700 mT. During the measurement, the sample is surrounded by a superconducting pick-up coil with four windings, which collect the magnetic signal from the sample. For transferring the magnetic flux from the sample to an rf-SQUID device placed in the liquid helium bath, a SQUID sensor is connected to the coil and functions as a converter of magnetic flux-to-voltage. The voltage is amplified and is shown by the electronics of a magnetometer. The sample is oscillated in vertical direction with amplitude of 3 cm. Such oscillation results in the change of the magnetic flux in the pick-up coil, which causes a change of the output voltage of the SQUID device. Moreover, the measuring result of magnetic moment is proportional to the output voltage as well. The investigated hybrid films are in nano scale, which results in rather small magnetic responses. Therefore, the employed measuring device requires extremely high sensitivity, which can be obtained by locking the frequency of the readout to the frequency of the movement (RSO). [175] More details regarding the setup and the conversional principles of the SQUID device are described elsewhere. [175]

The measurements were performed at different temperatures of 2, 3, 4, 5, 10, 20, 50, 100, and 200 K. For examining the magnetic shape anisotropy, one batch of samples regarding the fabrication of nano- and microwires (in Chapter 7) was measured in two orientations: The magnetic NP wires on the sample were oriented either parallel or perpendicular to the direction of the external magnetic field. In the data analysis, a strong diamagnetic contribution originating from the silicon substrate was subtracted. Important magnetic characterizations of the investigated hybrid films, including magnetization saturation, remanence and coercivity, are extracted from the measured magnetic moments.

3.2.2 Mössbauer spectroscopy

Mössbauer spectroscopy provides precise information regarding the local magnetic and electronic environment of Mössbauer nuclei in the probed materials. In contrast to SQUID, no external magnetic field is required during the Mössbauer measurement. Without the disturbance of the external magnetic field, the sensitivity of the device is strongly enhanced. Hence, observation of rather weak magnetic interactions is possible. [177]
The basics of Mössbauer effect is the observation of fine structure in the transition be-

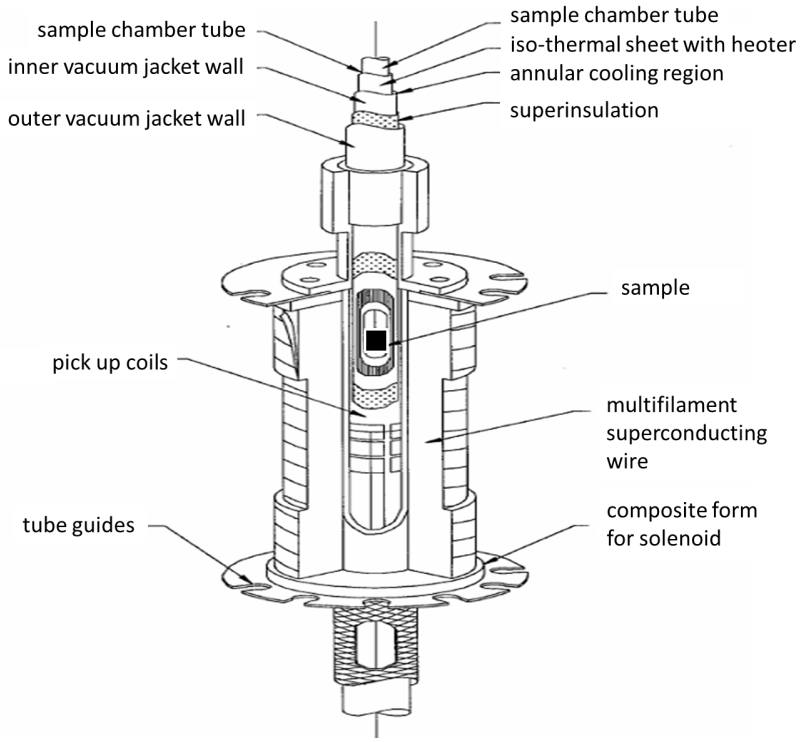

Figure 3.4: A schematic view of a simplified SQUID setup. Image taken from reference [176].

tween different nuclear energy levels through nuclear resonance absorption or fluorescence radiation. [134] In the measurement, a source of ^{57}Co nuclei supply excited ^{57}Fe nuclei, which decay into ground state with a γ-ray emission. [134] In case the γ-ray energy equals the energy gap in the probed material, a nuclear transition occurs in absorption. [134] The source shifts with a certain velocity and the γ-ray frequency can be fine regulated due to the Doppler effect, which is rather remarkable due to the high frequency of the γ photon. Therefore, all the splitting of the ground state of the source or absorber nucleus, which could produce the magnetic or other interactions, can be examined. [134] Details of the splitting regime can be found elsewhere. [134]

In the present thesis, Mössbauer spectra were measured in transmission geometry with a standard electromechanical spectrometer using a sinusoidal velocity waveform and a source of ^{57}Co in rhodium. [178] The measurement was performed at 4.2 K in a liquid He bath cryostat, with the source and the absorber at the same temperature. The original data were folded for reducing the geometry discrepancy. The processed data were fitted with two sets of sextet Lorentzian distribution function lines. [178]

The measured spectrum was fitted using the software Mos90 with two Lorentzian distributions, which indicate two different Fe^{3+} lattice constructions of octahedral and tetrahedral individually.

Chapter 4

Sample preparation

The employed materials and the film fabrication involved in the present thesis are described in this chapter. The particular details for the different topics are presented at the beginning of the corresponding chapters. All investigated materials are shown in Section 4.1, following by the substrate cleaning procedures in Section 4.2. Section 4.3 presents the coating methods of the hybrid films. The post-treatment of thermal annealing is described in Section 4.4.

4.1 Materials

The involved materials can be mainly divided into two groups: DBCs act as structural templates, and magnetic NPs as functional fillers.

4.1.1 Diblock copolymer

With the purpose of fabricating desired nano-structures with different types, three DBCs are selected: polystyrene-*block*-polymethyl methacrylate (PS-*b*-PMMA), polystyrene-d8-*block*-polyn-butyl methacrylate (PSd-*b*-PBMA), and polystyrene$_{e61}$-*block*-polyN-isopropyl acrylamide$_{e115}$, (PS-*b*-PNIPAM). Details of the investigated DBCs are listed in the table 4.1. The chemical structures of the DBCs are shown in Figure 4.1.

All these DBCs are so-called coil-coil like copolymers, which indicates that both blocks of the DBCs are coil-like polymers. Based on the Flory-Huggins segment-segment interaction parameter (χ) and the degree of polymerization (N), the investigated DBCs of PS-*b*-PMMA and PSd-*b*-PBMA lie in the intermediate segregation regime. According to the theoretical phase diagram of DBCs discussed in the previous Section 2.1.2, the sphere, cylinder, and lamella are expected for the bulk DBCs of PS-*b*-PMMA (f_{PS} =

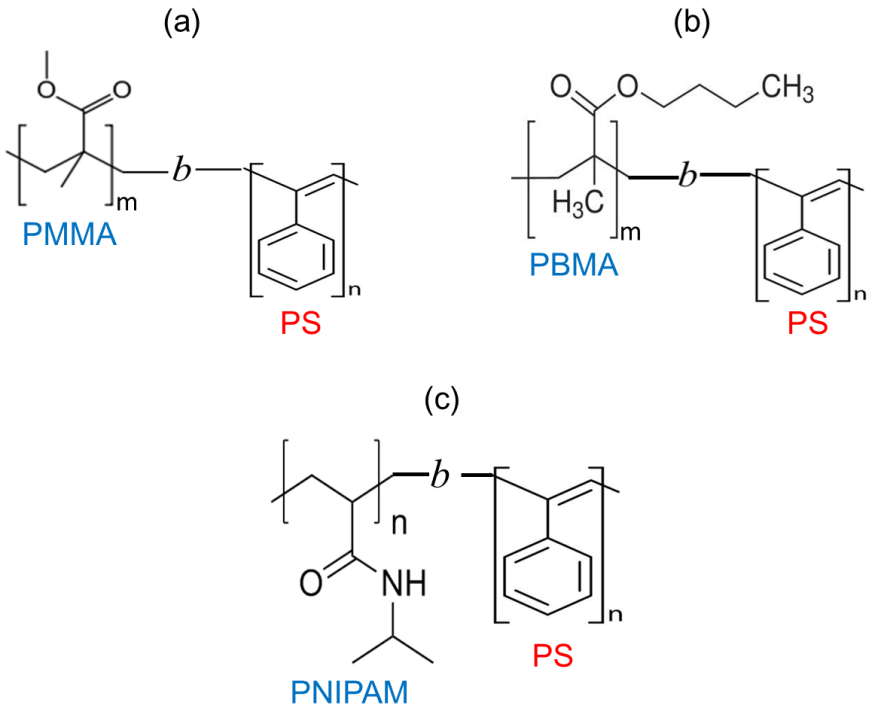

Figure 4.1: The chemical structures of the investigated DBCs.

0.15), PSd-*b*-PBMA ($f_{PS} = 0.53$), and PS-*b*-PNIPAM ($f_{PS} = 0.32$), respectively. PS-*b*-PMMA and PSd-*b*-PBMA are commercially synthesized. Moreover, PS-*b*-PNIPAM was synthesized via consecutive RAFT polymerizations of styrene and NIPAM using *n*-S-butyl-S′-benzyltrithiocarbonate as chain transfer agent in the group of A. Laschewsky in Potsdam. [182, 183] Details of the synthesis protocols and polymer characterizations for such type of DBC are described elsewhere. [184, 185] With the purpose of improving the scattering contrast in the TOF-GISANS experimental, the structure of the DBC PS-*b*-PBMA is modified with deuterated polystyrene (d8-PS) to PSd-*b*-PBMA.

4.1.2 Nanoparticle

Maghemite (γ-Fe_2O_3) NPs acted as the functional filler also can modify the morphology of hybrid films to some extent. The NPs are properly functionalized with surface coated PS chains, thus they exhibit an enthalpic driving force for the selective deposition of the NPs inside one domain of the microphase separated structure during the self-assembly process of the NPs-DBC mixture. [44, 45] Furthermore, such surface coating can prohibit NPs self-aggregation in the polymer phase as well. [46] The length scales of the selected NPs are on the same order magnitude as characteristic periodic distance of the employed

polymer	M_n [kg/mol]	PI	polymer block	M_n [kg/mol]	T_g [°C]
PS-*b*-PMMA	218.0	1.18	PS	32.7	107 [179]
			PMMA	185.3	105 [180]
PSd-*b*-PBMA	158.0	1.07	PSd	83.7	95
			PBMA	74.3	20
PS-*b*-PNIPAM	21.0	1.14	PS	6.7	107
			PNIPAM	14.3	152 [181]

Table 4.1: Properties of the structure-directing DBCs: number average molecular mass M_n, polydispersity index PI, and glass transition temperatures T_g of the different blocks of the DBCs are given.

DBCs. Therefore, the NPs can be well arranged in the DBC templates and the interaction between them benefits the desired morphologies. The maghemite NPs coated with PS chains were synthesized using α-lithium polystyrenesulfonate (LPSS, purchased from Polymer Standards Service Mainz, Germany). [186] The NPs were synthesized in toluene solution with a density of 1.09 g/cm^3 by the addition of an aqueous mixture of $FeCl_2$ and $FeCl_3$. The weight ratio of NPs in toluene solution was 2 wt%. [187] In our investigations, the employed NPs have the mean diameters of 6.5 and 10 nm, with the width of log-normal size distribution of 0.2. The specific chemical identity and the size of the NPs are examined using Mössbauer, XRD, and SAXS measurements, which are provided in the corresponding chapters.

4.2 Substrates

The n-type Si 100 wafers with a diameter of 10 cm and a thickness of 525 μm purchased from Si-Mat are selected as the solid substrates. The entire silicon wafers were cut into pieces with the sizes of 25 $\times$ 25 mm^2 or 70 $\times$ 70 mm^2 according to the different requirements of the investigation techniques applied to samples. The silicon wafer was firstly scratched on the back side with a diamond cutter, following the careful break on the scratching. To well proceed the scattering techniques, it is important to avoid the bending of the substrate. Due to the undefined surface properties of silicon substrates as received, cleaning procedures are mandatory to obtain a well-defined silicon surface. Due to the difference of the investigated hybrid film systems, different substrate cleaning

ingredient	volume [mL]	purity	company
H_2SO_4	200	95.0%	Carl Roth
H_2O_2	70	30.0%	Carl Roth
H_2O	130	99.9%	-

Table 4.2: The composition of the acid cleaning recipe used for silicon substrate cleaning.

methods are required for the DBC films preparations. In the present thesis, acid cleaning and basic cleaning are mainly used.

4.2.1 Acid cleaning

For the hybrid film systems based on the PS-*b*-PMMA and PSd-*b*-PBMA DBC templates, a well-defined hydrophobic surface is required. Therefore, an acid cleaning method based on sulfuric acid is applied, the specific composition of which is presented in Table 4.2.

Both sides of precut silicon substrates were rinsed with deionized (DI) water to remove any possible dust particles. Afterwards, the substrates were vertically installed in a Teflon sample holder and were immersed into a fresh prepared acid bath at 80 °C for 15 min. Thereafter, they were taken out and stored in the DI water, and each piece was vigorously rinsed with deionized DI water (around 350 mL). Subsequently, the substrate was drying with oil-free Nitrogen (N_2) gas and placed in petri dishes. Normally, the acid cleaned substrates are required to be used on the same day. [188]

4.2.2 Basic cleaning

Because the PS-*b*-PNIPAM DBC is composed of a hydrophobic PS block and a hydrophilic PNIPAM block, a basic cleaning method is required to establish a hydrophilic silicon oxide layer of 1 nm at the Si surface. The detailed composition of the basic bath is presented in Table 4.3.

The pre-cleaning procedures are the same as the acid cleaning. Afterwards, the Si substrates were immersed in dichloromethane (purity 99.5%) at 46 °C for 30 min, followed by strong rinsing with DI water. In order to remove any possible organic traces, substrates were immersed in the basic bath at 76 °C for 2 h. Then, substrates were stored shortly in DI water. Before spin-coating, all possible traces from the basic bath were removed by copious rinsing with DI water, followed by thorough N_2 blow drying. [109]

ingredient	volume [mL]	purity	company
NH_3	30	30.0%	Carl Roth
H_2O_2	30	30.0%	Carl Roth
H_2O	350	99.9%	-

Table 4.3: The composition of the basic bath used for silicon substrate cleaning.

4.3 Film preparation method

Because the employed DBCs and NPs are organic solution soluble, hybrid films can be easily fabricated out of well-mixed solutions with techniques such as spin coating, dip coating, solution casting, doctor blading, and printing etc. In the present thesis, solution casting and spin coating are applied, which are described in details in following Section 4.3.2 and 4.3.3.

4.3.1 Solution preparation

The most important precondition is that all the involved materials have to be well dissolved in the selected solvent. Besides the employed substrate cleaning procedures, an appropriate solvent is essential for obtaining homogeneous films. Therefore, different types of DBCs require different kinds of solvents. For the investigated systems based on the DBCs of PS-*b*-PMMA or PSd-*b*-PBMA, toluene was used; for the DBC of PS-*b*-PNIPAM, 1,4-dioxane was selected.
All materials were used as received without any purity. The materials were placed in a pre-cleaned welted glass container and were weighed with a precise electronic auto-balance. The calculated amount of solvent was added into the glass container with a precise pipette. To avoid the evaporation, the container was closed with a cap and was sealed with a tape. Afterwards, to ensure the thorough dissolution of all the involved materials, the container was placed on a shaker, which keeps shaking for 24 hours.
To probe the effects of the NP incorporation on the morphology and magnetic properties of the hybrid film system, the mixed solutions contain maghemite NPs and DBCs with varied weight ratios. Different hybrid film systems were targeted for different types of applications, which require different film thicknesses accordingly. In this case, different fabrication methods are selected. The details of the concentration of DBCs and NPs in the solution are described in the beginning of each chapter separately.

4.3.2 Spin coating method

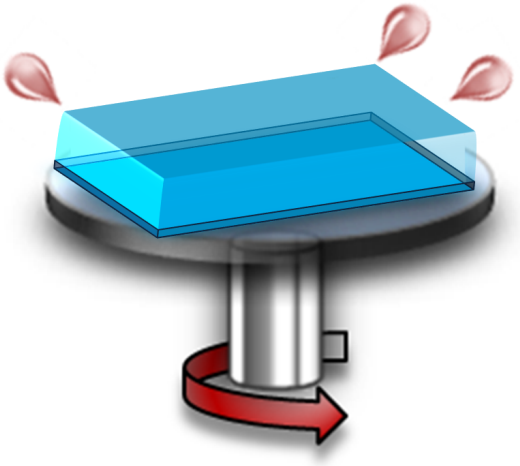

Figure 4.2: Schematic representation of the working principle of the spin coating. Black and blue cuboids indicate the silicon substrate and the established film, respectively.

In the present thesis, three batches of hybrid films were fabricated with a simply, fast, and highly reproducible spin coating method, which was performed with a spin-coater Delta 6 RC TT (Süss MicroTec Lithography GmbH). The schematic representation of the working principle of the spin coating is shown in Figure 4.2. Firstly, a pre-cleaned silicon substrate was placed horizontally on a rotator of the spin coater and was sucked on the backside via small holes in the rotator connected with a vacuum pump. Afterwards, the prepared, well-mixed solution was dispersed and was fully covered on the surface of the substrate. Immediately, the rotator started with pre-set parameters. Finally, a homogenous film with well-defined film thickness was obtained.

In general, such spin coating procedure can be explained with a three-step regime: [189]

(1) The majority of solution is thrown away from the substrate due to the strong centrifugal force.

(2) Convection is dominating.

(3) The solvent diffuses through the film surface.

The resulting film thickness can be predicted with an equation: [190, 191]

$$d = A\omega^{-1/2}c_0M^{1/4} \tag{4.1}$$

Where A is an experimental parameter depending on the employed spin coater and the actual environmental situations, ω is the speed of rotation, c_0 is the concentration of the solution, and M is the molar mass of the employed polymer. From the results of pre-test experiments, the parameters of spin coating procedures were fixed at acceleration time 9 s, spin-coating time 30 s, and spinning speed 2000 rpm, at room temperature 22 °C and relative humidity 40%. With these fixed parameters, the film thickness can be simply tuned by varying the concentration of the polymer in the solution. The concentration dependence can be described in three regimes: [191]

(1) At rather low polymer concentrations, not sufficient polymer material is present and no continuous and homogeneous film can be formed.

(2) At mediate polymer concentrations, a linear relation between film thickness and polymer concentration (described in Equation 4.1) is established under the assumption of the absence of the solution viscosity.

(3) At relative high polymer concentrations, due to the viscosity is too large to ignore, the linear behavior remains but with steeper slope.

Therefore, the viscosity has a direct effect on the film thickness in principle.

4.3.3 Solution casting method

The hybrid films based on PS-*b*-PMMA were fabricated with solution casting method, which proceeded with an applied external magnetic field. The schematic representation of the special designed solution casting set-up is shown in Figure 4.3. The desired external magnetic field was realized with two plate-shape permanent magnets (Ferrit Y35, 4100G, Magnets4you GmbH), which were separated with two plastic spacers. The entire set-up was installed inside a plastic box on a leveled bottom plate. Magnetic fields with different strengths can be achieved via simply adjusting the distance between the magnets. In our investigation, the varied magnetic field of 149, 329, 657 and 1112 G were used. In Figure 4.3, a glass sample holder, the height of which equals to the half-height of the applied magnets, was placed in the middle between the magnets. The pre-cleaned substrate was horizontally placed on the sample holder. In this case, the external magnetic field was parallel to the sample surface. For each sample, the same amount (350 μL) of solution was casted and was fully covered on the whole substrate surface. Afterwards, the box was closed with a lid to create a stable atmosphere, which can isolate the external disturbance and keep the solvent evaporation in a slow and defined condition. To ensure the film being completely solid, the solution casting procedure lasted for 24 h. The edges of the

established film were thicker than the centric part of film. To avoid unnecessary errors in the subsequent measurements, all the thicker edges were completely removed. In contrast

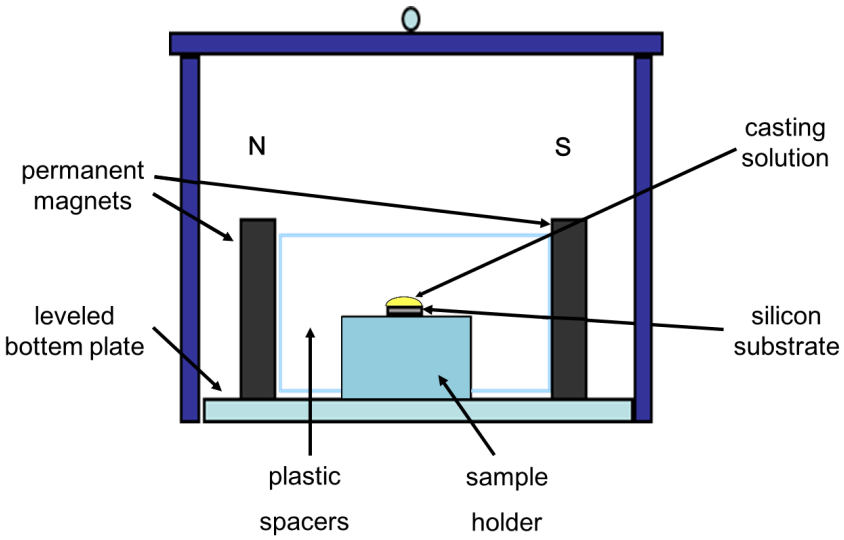

Figure 4.3: Schematic representation of the solution casting set-up. All the components are indicated as the legends for clarity.

to previous mentioned spin-coating method, solution casting has many advantages. The most significant advantage for our investigation is the relative slow speed of the solvent evaporation, which provides enough time for the hybrid film to reach equilibrium of the microphase separation. Additional, it also offers sufficient time to allow the NPs for responding to the external magnetic field. The hybrid film with a thickness in a μm-scale can be easily produced via solution casting. Moreover, the DBC concentration dependent solution viscosity is an essential factor, which can influence the mobility of the NPs as well. High viscosities can hinder the mobility to some extent due to the high friction with the surrounding matrix. Consequently, a relative low DBC concentration of the solution (10 mg/mL) is selected.

4.4 Thermal annealing

The hybrid films fabricated with spin coating are in a non-equilibrium condition due to the fast established process, which freezes the polymer structure in rather short time. Such semi-finished morphology may not be ideal for desired applications. Therefore, certain post-treatment, such as annealing process, is required for allowing the film to reach equilibrium. The annealing process can increase the mobility of the polymer chains, so that the rearrangements of structures can be realized. For our investigated coil-coil

like DBCs, the structures originated from microphase separation are developed with the annealing process. Particularly, a so-called thermal annealing was applied in the present thesis. Thermal annealing describes an event, the film is heated up with a well-defined procedure to a selected temperature for certain time, following as well a well-defined cooling down process. The heating temperature is most important factor. On one hand, it requires to be higher than the glass transition temperature of the DBC, so that the chains of the DBC have the possibility to move and rearrange; on the other hand, it must be lower than the order-disorder transition temperature of the DBC, to avoid establishment of a disordered structure. The resulting film morphology is affected by the rates of heating up and cooling down, and the annealing duration.

Thermal annealing was applied on the hybrid films based on DBC of PS-*b*-PBMA. The whole batch of as-prepared hybrid films were placed in an airtight oven fully filled with inert N_2. The function of the N_2 is to avoid the possible oxidation and degradation. Furthermore, such thermal annealing also helps the residual solvent completely getting removed from the hybrid film. The specific parameters of the thermal annealing process are presented in the beginning of the corresponding chapters.

Chapter 5

Perforated lamella via self-assembly PSd-*b*-PBMA and maghemite NPs

Parts of this chapter have been published in the article "Self-assembly of diblock copolymer–maghemite nanoparticle hybrid thin films", *ACS Appl. Mater. Interfaces*, **2014**, *6*, 18152-18162.

In the current chapter, the work is presented aiming at making the nano-structure of polystyrene-d8-*block*-poly(n-butyl methacrylate) (PSd-*b*-PBMA) DBC films in relation to the embedded maghemite NPs for the special morphology of a perforated lamella with an enrichment layer containing NPs at the film/substrate interface. Commonly, preparation of highly ordered nanostructures requires complex processes, or elaborate treatments of substrates. [32–34] In current study, a simple, economical, highly replicable process is used for the film fabrication. Morphological modifications of the nanostructured hybrid films are realized with incorporation of the maghemite NPs. The lateral nanostructures at the surface of the hybrid films are constant, which is irrespective of the NP loading. Such significant feature makes them interesting for applications as it does not change the periodicity of the magnetic nanostructure.

The chemical identity and the size of the current used NPs are characterized with Mössbauer and SAXS measurements. Both, real-space techniques AFM (AFM-1, described in Chapter 3.1.3) and SEM and reciprocal-space techniques XRR and TOF-GISANS, are employed to probe the entire film structure. Particularly, with the TOF-GISANS, film structures in various depths are accessible simultaneously (related theory has been presented in Section 2.3.4). Further, additional structural information such as possible polymer enrichment at either polymer-air or polymer-substrate interfaces as well as the DBC/NPs morphological correlation can be probed. [160,192] The incident beam impinges the hybrid films with a fixed shallow angle of 0.48°. In this case, for the investigated PSd-*b*-PBMA film, the critical wavelength (λ_c) for total external reflection is 0.97 nm. Instead

of a monochromatic neutron beam, a continuous neutron spectrum with a wavelength range from 0.23 nm to 1.22 nm was used. Consequently, depth profiles of the film structure are obtained from the TOF-GISANS data with different neutron wavelengths (in Section 2.3.4). Finally, the related magnetic behaviors of the hybrid films are examined with a SQUID device.

The hybrid films are fabricated with the spin coating method. Afterwards, a post treatment of thermal annealing in an inert N_2 environment at 160 °C for 5 hours is applied. The deuterated PS block is selected to enhance the neutron contrast for the TOF-GISANS experiment. The scattering length densities of the involved materials are PSd of 5.99 $\times$ 10^{-4} nm^{-2}, PBMA of 5.54 $\times$ 10^{-5} nm^{-2}, PSd-*b*-PBMA of 3.44 $\times$ 10^{-4} nm^{-2}, and γ-Fe_2O_3 of 7.18 $\times$ 10^{-4} nm^{-2}, which possess significant differences. The important Flory-Huggins segment-segment interaction parameter (χ) of PS and PBMA is 0.015 at room temperature. [113] Based on the mean-field theory (in Chapter 2.1.2), the probed DBC with $\chi N \approx 44$ lies in the intermediate segregation regime. [75] The sample size of 7 $\times$ 7 cm^2 is selected. The spin coating parameters and the DBC concentration are selected to create a film thickness nearly equaling to the periodic domain distance of the employed DBC. Via several pre-tests, the DBC concentration of 12.4 mg/mL is turned out to be necessary for achieving the desired film thickness. Varied NP concentrations with respect to DBC solutions (0, 0.1, 0.5, 1, 3, 7, and 15 wt%) are prepared using toluene as solvent. All the preparation procedures are carried out at room temperature.

5.1 NP characterization

5.1.1 Characterization of NP size

Figure 5.1a presents a 2D SAXS data of the employed NPs in highly diluted toluene solvent. The direct beam position is shielded with a round-shaped beamstop for preventing the detector from high intensity damage. For a quantitative analysis, the azimuthally averaged 2D SAXS data together with its fit are shown in Figure 5.1b. At low q range (first 2 data points), the beamstop shields the detector against the x-ray beam. Assuming a hard sphere model, the fit result reveals the size of γ-Fe_2O_3 NPs, 6.5 $\pm$ 0.9 nm with a log-normal size distribution (width 20%).

5.1.2 Chemical identity of NPs

Figure 5.2 shows the Mössbauer spectrum carried out at 4.2 K for the NPs. A magnetic sextet is observed, which presents the standard characterizations of maghemite material

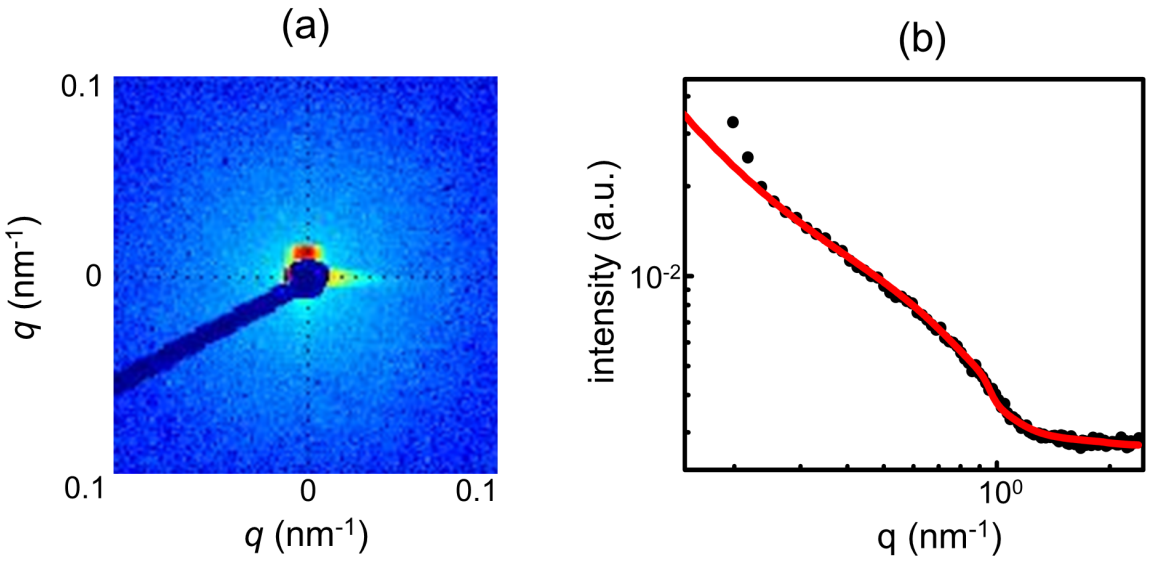

Figure 5.1: (a) 2D SAXS data of γ-Fe_2O_3 NPs in highly diluted toluene solvent. (b) Azimuthally averaged 2D SAXS data (black spheres) with its fit (red solid line). Image modified from reference [110].

and thereby allows for a distinct identification of the type of iron oxide NP. The measured spectrum (black hollow circles) was fitted with two Lorentzian distribution lines (green dashed line and blue dotted line), which stand for two different Fe^{3+} lattice constructions of octahedral (green dashed line) and tetrahedral (blue dotted line) individually.

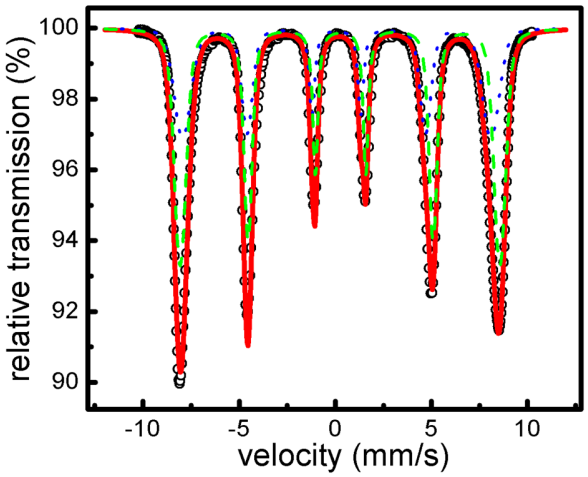

Figure 5.2: Mössbauer spectrum of NPs performed at 4.2 K (black hollow circles) together with its fit (red solid line). Image taken from reference [110].

5.2 Determination of film thickness

In literature, many studies focused on the effect of the film thickness on the morphology orientation of the BC films. [113, 193–195] Since the precise determination of the film thickness is crucial for the present studied hybrid films, XRR measurements are employed. Figure 5.3a shows the values of the film thicknesses obtained from the fit of the corresponding XRR data vs. the NP concentration.

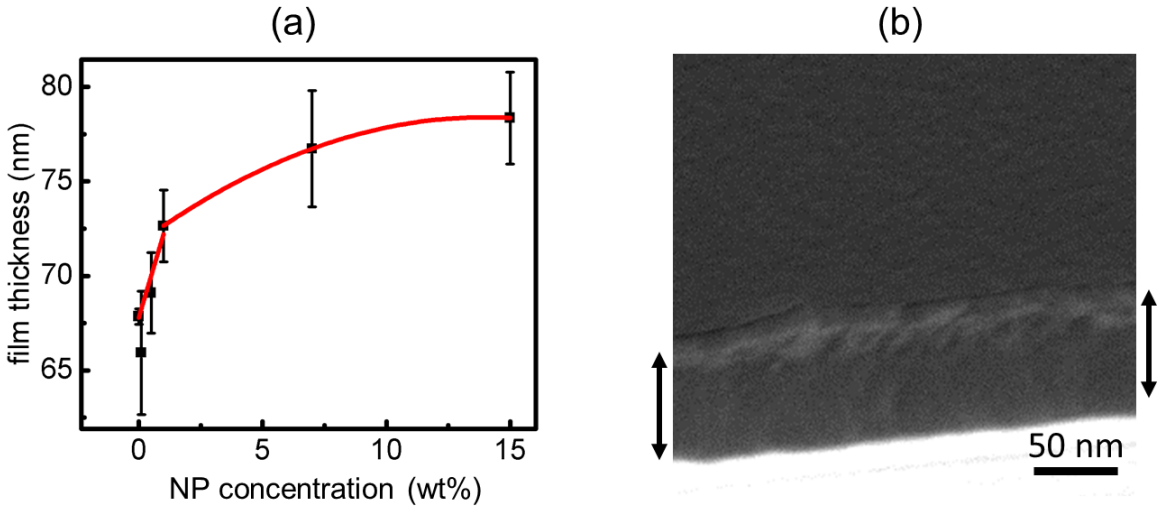

Figure 5.3: (a) Thicknesses of the hybrid films vs. NP concentration (the solid line serves as a guide to the eye). (b) A cross-section SEM image of the NP-free DBC film. The film thickness is pointed out with black double headed arrows.

As the NP concentration increases, the thickness of the thin hybrid film increases from 65.9 ± 3.3 nm to 78.4 ± 2.4 nm monotonically. During the film preparation procedures, all parameters were controlled identically, and the effect of the addition of the NPs on the viscosity of the solution using for spin coating was fairly limited. Therefore, the embedded NPs in the hybrid films are the main contributing factor for the increase behavior of the film thickness. Since the values of the Flory Huggins interaction parameter χ and the degree of polymerization N of the investigated DBC are 0.015 and 2912, the χN is 43.68, which indicates the DBC lies in the intermediate-segregation (in Section 2.1.2). Therefore, the theoretically expected periodic domain spacing, d, in the bulk can be obtained with [77]

$$d \sim a N^{\frac{2}{3}} \chi^{\frac{1}{6}} \tag{5.1}$$

where a of 0.67 nm is the characteristic segment length, yielding a d of 68 nm. Due to the symmetric block fraction of the DBC, a lamellar morphology is expected (in Section 2.1.2). The theoretically expected d of 68 nm is slightly smaller than the obtained film thickness. Based on the previous studies regarding DBC thin films, two main possible film morphologies arise: [113, 115, 196, 197]

(1) In the case of film thickness $\leq d$, a perpendicular (with respect to the film surface) lamellar morphology is favored, because it maximizes the conformational entropy of the polymer chains by allowing the equilibrium periodic domain to be expressed laterally. [113, 196, 197]

(2) In the case of film thickness $> d$, a parallel lamellar morphology is more possible to form because of the surface boundary conditions (in Section 2.1.3, Figure 2.16). [113, 115]

In general, the free energy minimization of the system mainly contributes to the morphological orientation. [113] As the NP concentration increases, the film thickness shows a non-linearly increase (Figure 5.3). With NP concentrations ≤ 1 wt%, the film thickness increases with a sharp slope. However, in the case of NP concentrations ≥ 7 wt%, the increase of the film thickness is less pronounced. Such non-linear NP concentration dependent behavior of the film thickness implies that the NPs are initially embedded into the film at a small NP volume, which expand the DBC domains and cause a film swelling. However, at high NP concentrations, the majority of excessive NPs cannot be incorporated into the hybrid film any longer. Consequently, the NPs form isolated random arrangements of large aggregates on the top surface. [110]
Furthermore, the thickness of the NP-free DBC film is measured with a cross-section SEM image (Figure 5.3b). Black double headed arrows indicate the film thickness, which is the distance between the silicon substrate and the film top surface.

5.3 Surface structure

SEM measurements are used to probe the nanoscale surface structures of the hybrid films. SEM images at different NP concentrations are exhibited in grey scale in Figure 5.4. The dark regions correspond to the PS domains, and the lighter grey regions indicate the PBMA domains. [198] In particular, certain rather bright objects are observed, which are small NP aggregates.
In Figure 5.4a, for the NP-free DBC film, instead of a lamellar morphology, a cylindrical-like structures are observed (dark areas) with an imperfect lateral ordering. In Figure

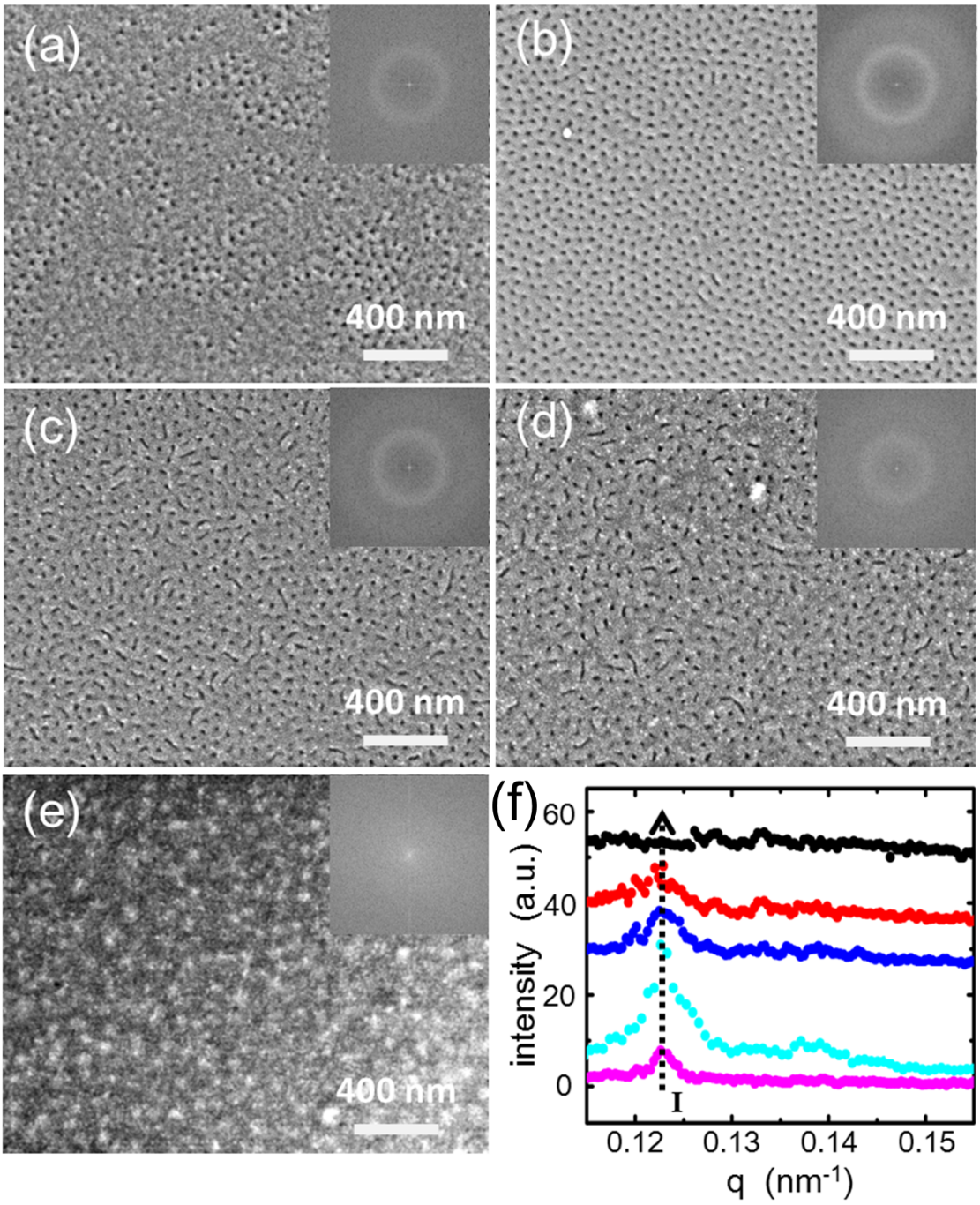

Figure 5.4: SEM images of the hybrid films with varied NP concentrations: (a) 0, (b) 0.5, (c) 7, (d) 15, and (e) 25 wt%. Upright insets are the FFT patterns. (f) Power spectral density (PSD) functions extracted from azimuthally integration of the FFT patterns at different NP concentrations (from bottom to top): 0, 0.5, 7, 15, and 25 wt%. The PSD profiles are shifted against y axis for clarity. A black arrow I indicates the constant q value of the lateral structure of the film surface.

5.4b, highly ordered, well-oriented arrays of cylinders with a long-range lateral order are established with the incorporation of a small amount of NPs (0.5 wt%). Because the surface of the NPs is modified with the PS coating, the compatibility of the NPs to the PSd block is enhanced significantly. In consequence, the enthalpic interaction at the interfaces between NPs and PSd domains favors mixing. [139] Commonly, the Flory-Huggins interaction parameter, χ, is in the range of 0.01-0.1. [199] Three χ-parameters raise from the probed hybrid film system: $\chi_{PSd-PBMA}$, $\chi_{PSd-NPs}$ and $\chi_{PBMA-NPs}$, which indicate the chemical incompatibility between PSd and PBMA, PSd and NPs, and PBMA and NPs, respectively. Notably, the χ between PS and deuterium-substituted PS (PSd) is 1.8 $\times$ 10^{-4}. [200] Because the PS-coating fully covers the surface of the NPs, the $\chi_{PSd-NPs}$ can be considered as χ_{PSd-PS}, which implies the NPs are compatible with PSd. Furthermore, $\chi_{PBMA-NPs}$ can be presumed to be rather close with the value of the $\chi_{PSd-PBMA}$ (0.015), ignoring the changes in the entropic contribution. Since the ratio of $\chi_{PBMA-NPs}$ to $\chi_{PSd-NPs}$ approximates 85, the PS-coated NPs have a much higher affinity for the PSd domains. [201]

Differing from the pure DBC template, with the incorporation of a small amount of NPs (0.5 wt%), Figure 5.4b exhibits a highly ordered, densely packed cylindrical morphology, which indicates that the structural ordering of the hybrid film is improved significantly with the NPs loading. The similar behaviors of a better structural order and switchable orientation of a lamellar structure from a parallel to a perpendicular are as well found in previous investigations in the case of adding a low concentration of NPs into a DBC. [202] In literature, the Russell group reported that the incorporation of selectively embedded CdSe NPs into a PS-*b*-P2VP DBC caused the perpendicular orientation, due to the compensation of the surface energies difference between PS and P2VP domains. [41] In the current study, the obtained highly ordered cylindrical arrays at low NP concentration is ascribed to the increased diffusion of the NPs within the PSd domains during the thermal annealing procedure, leading to an enhanced distribution of the NP doped PS domains.

In the case of NP concentration $>$ 0.5 wt%, the previous long-range systematic order has been disturbed, and a deformed cylindrical morphology is found (Figure 5.4c,d). Plenty of NPs entangled with the PS chains restrict their ability to diffuse and localize. Consequently, the PS domains have less chance to optimally organize. The FFT patterns of the corresponding SEM images are shown in the upright insets of Figure 5.4. In general, the isotropic ring-like FFT patterns imply that the probed surface structures are isotropically dispersed all over the films. The radii and the width of the FFT circular rings represent the center-to-center domain distances and their distributions. In Figure 5.4b (0.5 wt%), the ring of FFT becomes more prominent and even a second order ring raises. As the NP concentration further increases, the intensity of the ring decays and its width broadens.

Generally, in the case of NP concentrations $\leq$ 0.5 wt%, the NPs are perfectly arranged inside the favorable PSd domains and swell the domains. When NP concentrations $>$ 0.5 wt%, the PSd cylinders begin to develop anisotropically, which enlarges the interfacial curvature. With the purpose to adapt more possible NPs inside, the PSd domains persist stretching and deforming. Consequently, the previous well orientated perpendicular cylindrical morphology arisen at low NP concentrations is inclined to form parallel-like cylinders at high NP concentrations. Similar transition phenomena have been found for the NPs-DBC hybrid systems with a large amount of NPs loading in literature. [203–205] In Figure 5.4e, with rather high NP concentration (25 wt%), excessive NPs cannot be contained inside the PSd domains any longer. Therefore, the entropy penalty dominates and the NPs tend to form aggregates, which results in an ill-defined morphology. Monte Carlo simulations predict the analogous behavior, revealing NP aggregation in the case of a large amount of NPs incorporated in a DBC system. [206]
The PSD functions obtained from corresponding FFT are represented in Figure 5.4f. The most pronounced feature is the peak I (marked with an arrow) remained at the constant q value irrespective of the NP concentration. It reveals the most prominent lateral structure of the film surface, representing the microphase separated inter domain distance. With a quantitative analysis, a NP concentration independent lateral spacing of 58 $\pm$ 2 nm is extracted from the PSD profiles. As the NP concentration increases, the peak I becomes more intense and narrower firstly, indicating the formation of the highly periodic, well-ordered structures. In the case of NP concentration beyond a critical value, the peak I begins to decay and broaden but with the q value remaining, which implies that the NP aggregates only influence the systematic order of the nanostructure but do not affect the domain spacing.

The film surface in large scale is also probed with SEM (Figure 5.5). In general, more NP aggregates appear as the NP concentration increases. However, even at rather high NP concentration (25 wt%, Figure 5.5f), no large NP aggregates are observed. It reveals that the DBC has a great capacity for accommodating NPs. Such behavior distinctly differs from our previous investigation [109]: the NP aggregates form network structures with a percolation path and fully cover the film surface. [109] Particularly, Figure 5.5b presents a perfect upright cylindrical morphology, which is quite attractive to versatile applications.

Compared with SEM, AFM provides the 3D surface profile with a different contrast. Figure 5.6 represents the AFM topographical images for the hybrid films at different NP concentrations. The exhibited nano-morphology of the AFM follows the same behavior as the observation from the SEM images. In general, bright and dark regions indicate the PBMA and PSd domains, respectively. In the case of NP concentration $\leq$ 0.5 wt%

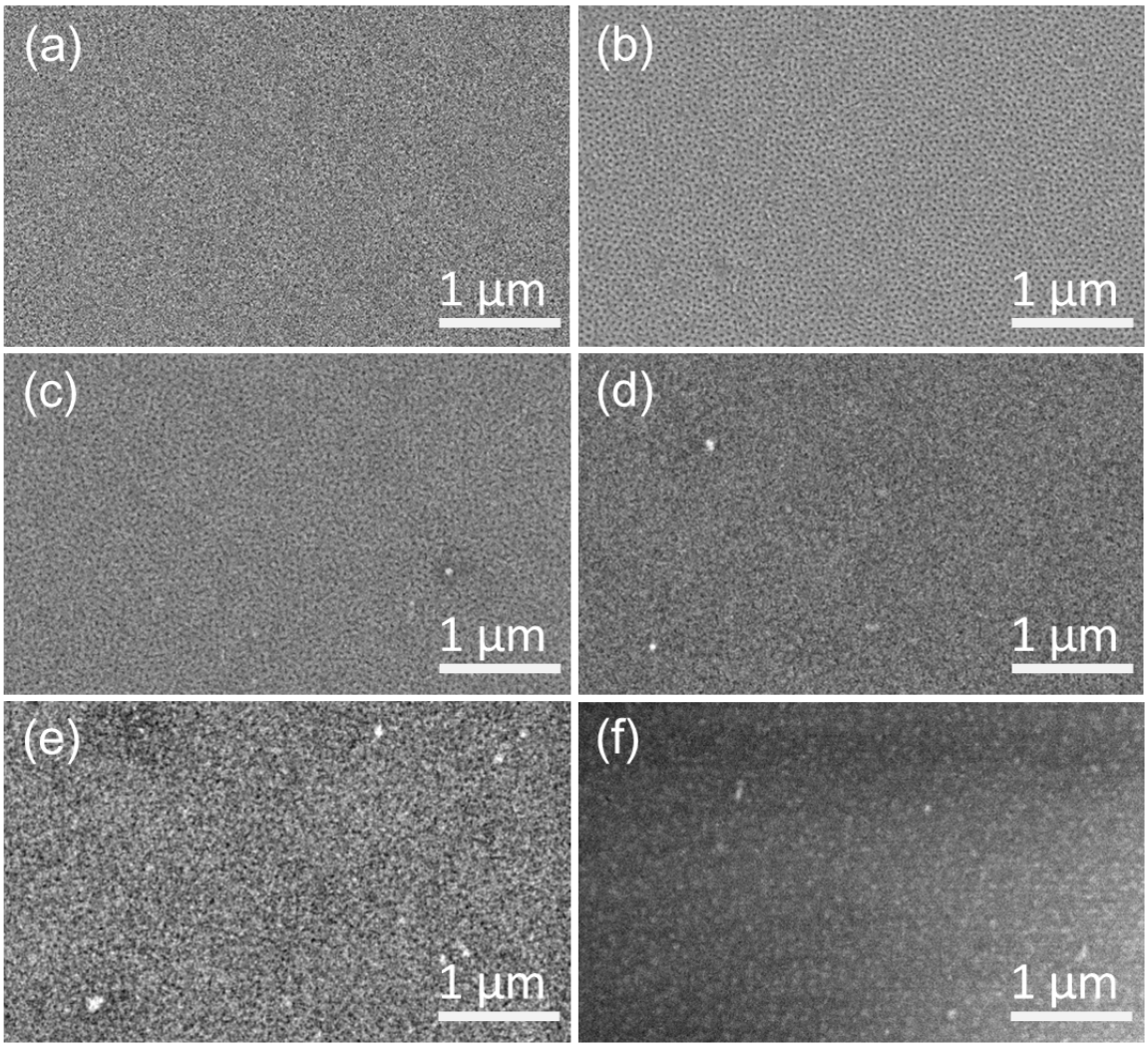

Figure 5.5: Large scale SEM images of the hybrid films with varied NP concentrations: (a) 0, (b) 0.5, (c) 3, (d) 7, (e) 15, and (f) 25 wt%.

(Figure 5.6a, c and e), the order of the cylinders increase as the concentration increases; However, when NP concentration increases further ($1 \leq$ conc. ≤ 15, Figure 5.6g, i, k, and m), the order of the system decays due to a great amount of NPs loading; At highest NP concentration (25 wt%, Figure 5.6o), large irregular sized NP aggregates with a broad distribution prefer to scatter randomly on the film surface, rather than well install in the PSd domains provided via the DBC template. The excessive NP aggregates cannot be adapted by the PSd domains. Consequently, the structural guide function of the DBC is lost, which leads to ill-defined structures.

To probe the film surface in a larger area, Figure 5.7 represents an improved visualization of the developed NP aggregates, which provides the statistical evidence and

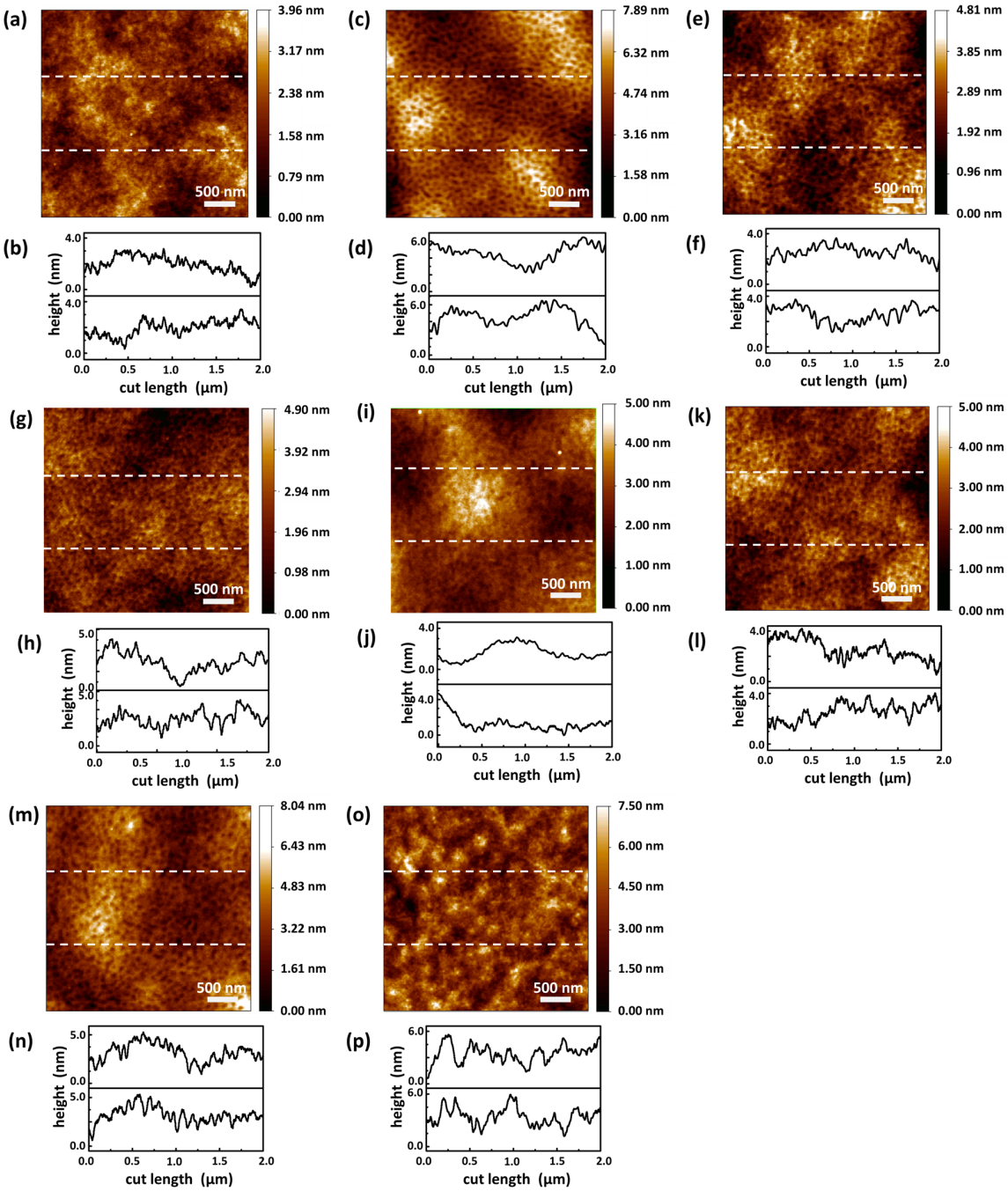

Figure 5.6: AFM images of the hybrid films and corresponding representative line cuts (from 2 positions marked by white dashed lines) at different NP concentrations: (a) (b) 0, (c) (d) 0.2, (e) (f) 0.5, (g) (h) 1, (i) (j) 3, and (k) (l) 7, (m) (n) 15, and (o) (p) 25 wt%.

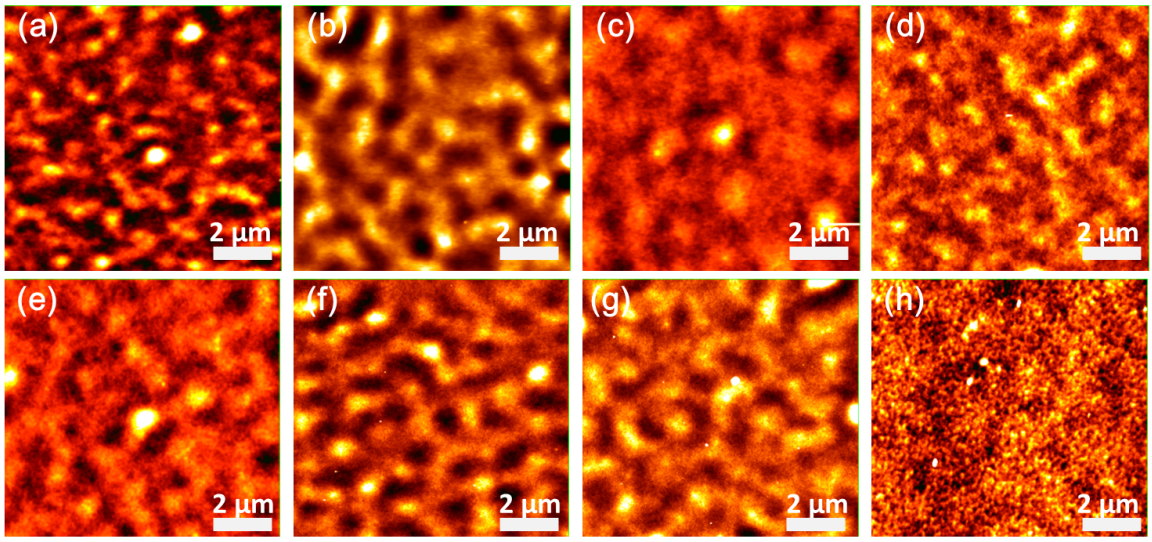

Figure 5.7: AFM images of the hybrid films in a larger scan size for different NP concentrations: (a) 0, (b) 0.2, (c) 0.5, (d) 1, (e) 3, (f) 7, (g) 15, and (h) 25 wt%.

confirms the uniformity of the film. For all NP concentrations, besides the periodic nanomorphology originated from the microphase separation (PSd cylindrical domains), certain larger wave-like structures in the μm scale are found.
Moreover, root-mean-square (rms) surface roughness can be obtained from AFM data as well. The corresponding quantitative height profiles vs. line cut length are shown in the Figure 5.6. For the pure DBC film, the surface rms roughness is 1.11 nm in the examined local scale shown in the Figure 5.6a. As the NP concentration increases from 0.2 to 25 wt%, the roughness monotonically increases from 1.13 nm to 3.48 nm. Although the roughness mensuration is significantly influenced with the large NP aggregates, the rms roughness still remains smaller than 4 nm, revealing a relatively homogeneous surface of all prepared films.

5.4 Inner structures

In the previous sections, the real space techniques, such as AFM and SEM have examined the top surface of the hybrid films. However, the inner morphologies buried beneath the film surface and especially the structural information from the polymer-substrate interface are inaccessible for such real space techniques. To adequately investigate the morphological evolution of the entire films, the TOF-GISANS technique is employed. Based on the theory and working principle of the TOF-GISANS, which have been discussed in the previous Sections 2.3.4 and 3.1.9, it can provide not only the structure characterization

from the film surface, but also the inner film morphology in terms of lateral structures and size distributions with depth-dependence. [160, 207] Furthermore, the obtained morphological information possesses a high statistical relevance because a large sample volume is illuminated during the measurements.

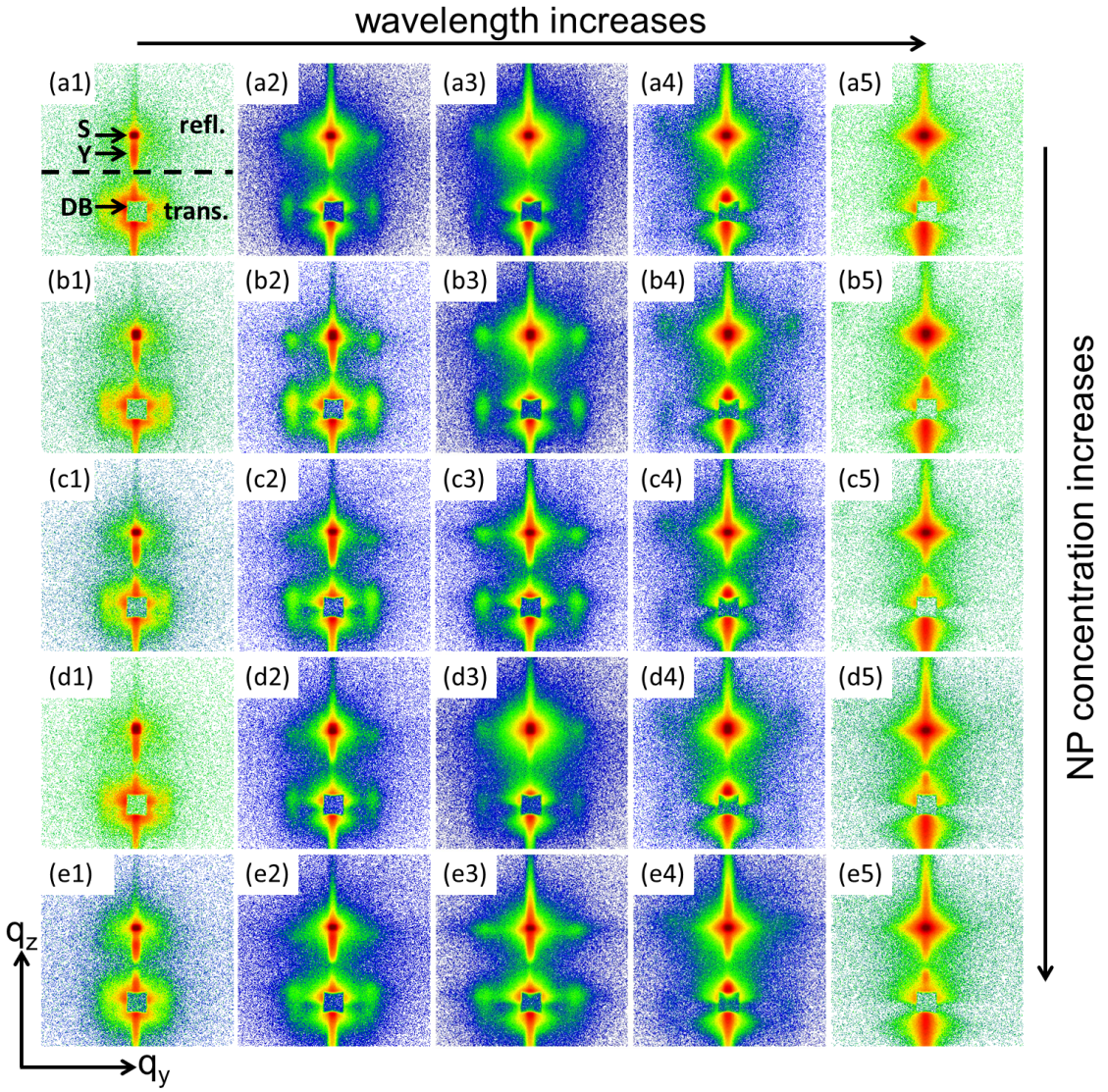

Figure 5.8: 2D GISANS data of hybrid films at different NP concentrations: (a1-a5) 0, (b1-b5) 0.5, (c1-c5) 1, (d1-d5) 7, (e1-e5) 15 wt%. The mean wavelengths of 1-5 (from left to right) are 0.325, 0.475, 0.575, 0.775, and 1.025 nm, respectively. The Yoneda peak (marked with Y) shifts with the wavelength. The specular peak (marked with S) locates at a constant position. The intense direct beam signal (marked with DB) is blocked with a square beamstop. The transmission (marked with trans.) and reflection (marked with refl.) intensities are separated with the sample horizon (marked with dashed line).

2D GISANS data of hybrid films with different NP concentrations ((a) 0, (b) 0.5, (c) 1, (d) 7 and (e) 15 wt%) are shown in Figure 5.8. The 5 series of 2D GISANS data selected from available neutron wavelengths are exhibited. The wavelength increases from left to right: 0.325, 0.475, 0.575, 0.775, and 1.025 nm. For all presented GISANS data, the minimum intensity (marked with dashed line in Figure 5.8a) shows the sample horizon. The scattering signal below the horizon is the transmission intensity, which is dominated by the intense direct beam and partially blocked with a square-shaped beamstop for preventing the detector from damage. Above the horizon, the reflection intensity is shown. [155, 208, 209] In this upper part, the most prominent intensity is the specular peak, where the incident angle equals to the exit angle ($\alpha_i = \alpha_f$). In principle, the specular peak is always located in a constant position. However, at high neutron wavelengths, a slight drop (within 2 pixels) in vertical position is observed for the specular peak, which is caused by the gravity effect acting on the neutron beam. [210, 211] In the further analysis procedures, certain corrections have been done for compensating gravity. In Figure 5.8a, a less pronounced Yoneda peak, slightly beneath the specular peak, is found. As the neutron wavelength increases, Yoneda peak shifts towards higher positions along the ($\alpha_i + \alpha_f$) direction. The Yoneda peak position strongly relies on the material chemical composition and mass density (Section 2.3.4), [212] which locates at the critical angle (α_c) of the investigated materials:

$$\alpha_c = \lambda(\frac{\rho}{\pi})^{\frac{1}{2}} \tag{5.2}$$

where ρ is the neutron scattering length density of the probed materials (Section 2.3.4). [160] Based on the wavelength dependent critical angle, the sensitivity of the neutron beam can be divided into two groups:

(1) At longer wavelengths ($\alpha_c \geq \alpha_i$), only a few neutrons can penetrate the hybrid film. The surface sensitivity with a specific penetration depth is obtained.

(2) At shorter wavelengths ($\alpha_c < \alpha_i$), the neutrons can systematically penetrate the entire film, which leads to the bulk sensitive measurements.

Therefore, by employing neutron beam with different wavelengths in the TOF-GISANS measurement, the depth structural profiles from surface to bulk sensitive are realized. In addition, for all measured neutron wavelengths, no intensity modulation is found along the q_z direction of the 2D GISANS patterns, which indicates that no well-defined parallel (with respect to the film surface) periodic structure are present. In the q_y direction of the 2D GISANS patterns, two side peaks located at the same height along the both sides of the Yoneda peak are found, which indicate the highly-ordered, well perpendicular

(with respect to the film surface) orientated lateral structure arisen from the microphase separation of the DBC (Figure 5.8). For the hybrid films at all the NP concentrations, the intensity of the side peaks reach their maximum at the wavelength of 0.474 nm, which are shown in the third column of the Figure 5.8 (Figure 5.8a3-e3). As the NP concentration increases (from top to bottom), the 2D GISANS data change distinctly. With the incorporation of a small amount of NPs, (0.5 wt%, Figure 5.8b3), the side peaks become more significant and the entire scattered signals are more intense, revealing an enhancement of the structural order and an improvement of the contrast between the two phases, the PSd domains embedded with NPs and the NP-free PBMA domains, respectively. However, as the NP concentration increases further (conc. $\geq$ 1 wt%, Figure 5.8c3 – e3), the intensity of the side peaks decay and broaden again, which reveals the presence of less ordered structures.

5.4.1 Vertical structure

For a further quantitative analysis, vertical line cuts made at $q_y = 0$ from the corresponding 2D GISANS data for the hybrid films with varied NP concentrations are shown in Figure 5.9. Structure information perpendicular to the film surface is provided with the vertical cut. The sample horizon at minimum intensity is indicated with a vertical dotted line (marked as H, $\alpha_i + \alpha_f = 0.48°$), which separates transmission signal (left, $\alpha_i + \alpha_f < 0.48°$) and reflection signal (right, $\alpha_i + \alpha_f > 0.48°$). The transmission scattering through the neutron transparent silicon substrate contributes to the transmitted signal. At a scattering angle $\alpha_i + \alpha_f = 0°$, the direct beam (marked as DB) is blocked with a beamstop. The trend of observed Yoneda peak (Y) is guided with a titled dashed line. The specular peak (marked as S) locates at $2\alpha_i = 0.96°$.

In literature, the ideal scattering length densities of all components involved in the hybrid film system are: $\rho_{\gamma-Fe_2O_3} = 7.18 \times 10^{-4}$ nm^{-2}, $\rho_{PSd} = 5.99 \times 10^{-4}$ nm^{-2}, $\rho_{Si} = 2.07 \times 10^{-4}$ nm^{-2} and $\rho_{PBMA} = 5.54 \times 10^{-5}$ nm^{-2}. [110] Based on the Equation 5.2, the theoretically predicted wavelength dependent critical angles are plotted in the Figure 5.10a. The experimentally observed Yoneda peak positions (from Figure 5.9) are filled out with the squares in the plots for all investigated NP concentrations in Figure 5.10b-f. For the pure DBC film (Figure 5.10b), at short wavelengths, the Yoneda peak positions match the theoretically predicted critical angle of the PSd component. However, at longer wavelengths, no Yoneda peak can be observed because it has been overlapped with the much stronger specular intensity. The observation of the Yoneda peak positions agreeing with the critical angle of the PSd component reveals the presence of a PSd enrichment layer at the polymer/substrate interface. Looking back on the SEM images (Figure 5.4),

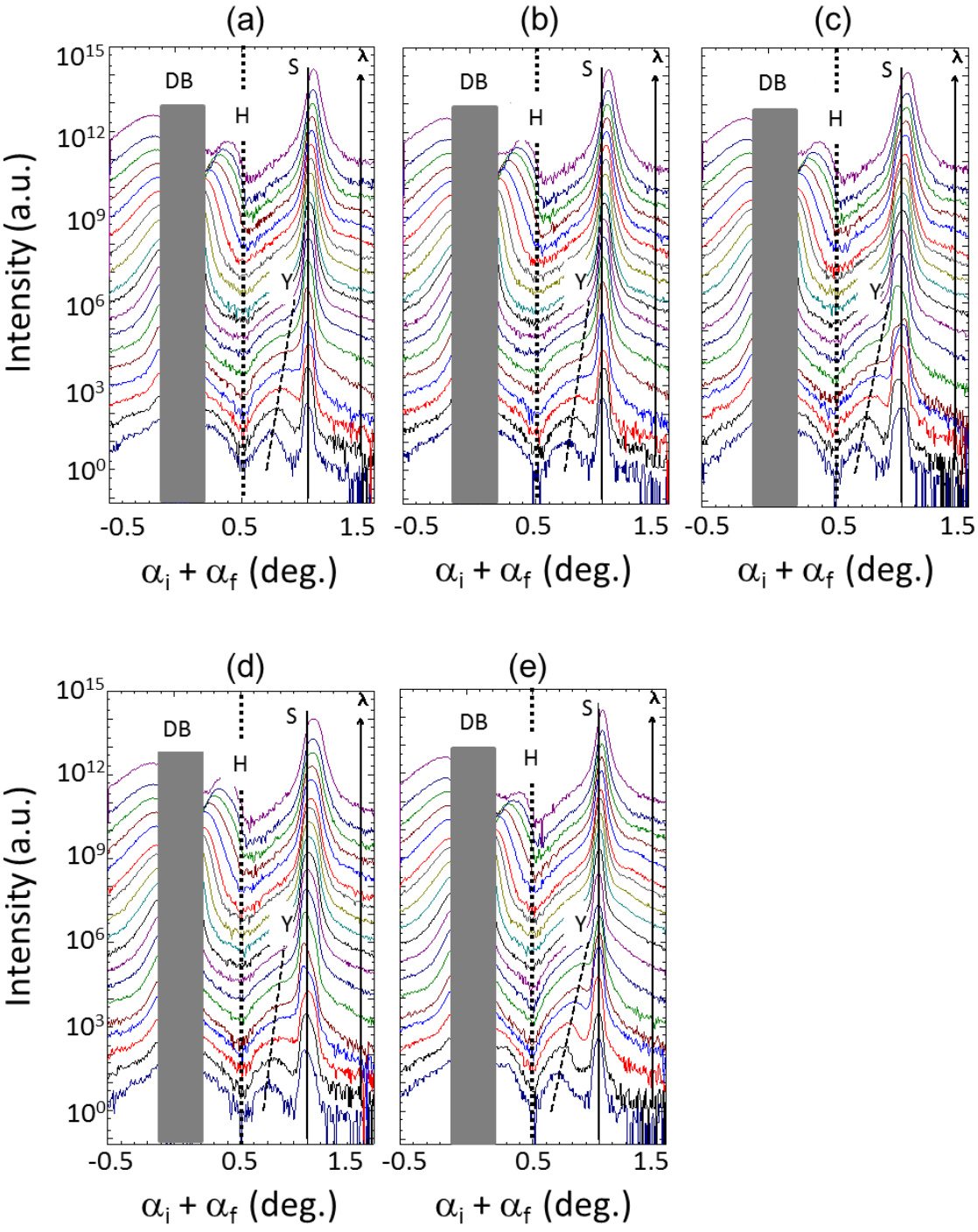

Figure 5.9: Vertical line cuts (at $q_y = 0$) made from the 2D GISANS data as function of the detector angle ($\alpha_i + \alpha_f$) for the hybrid films with varied NP concentrations: (a) 0, (b) 0.5, (c) 1, (d) 7, and (e) 15 wt%. The trend of Yoneda peak (Y) is guided with a dashed line. The positions of sample horizon and specular peak are marked with H and S. For clarity, all cuts are shifted against y axis from bottom to top, with the neutron wavelength increases as follows: 0.225, 0.275, 0.325, 0.375, 0.425, 0.475, 0.525, 0.575, 0.625, 0.675, 0.725, 0.775, 0.825, 0.875, 0. 925, 0.975, 1.025, and 1.075 nm.

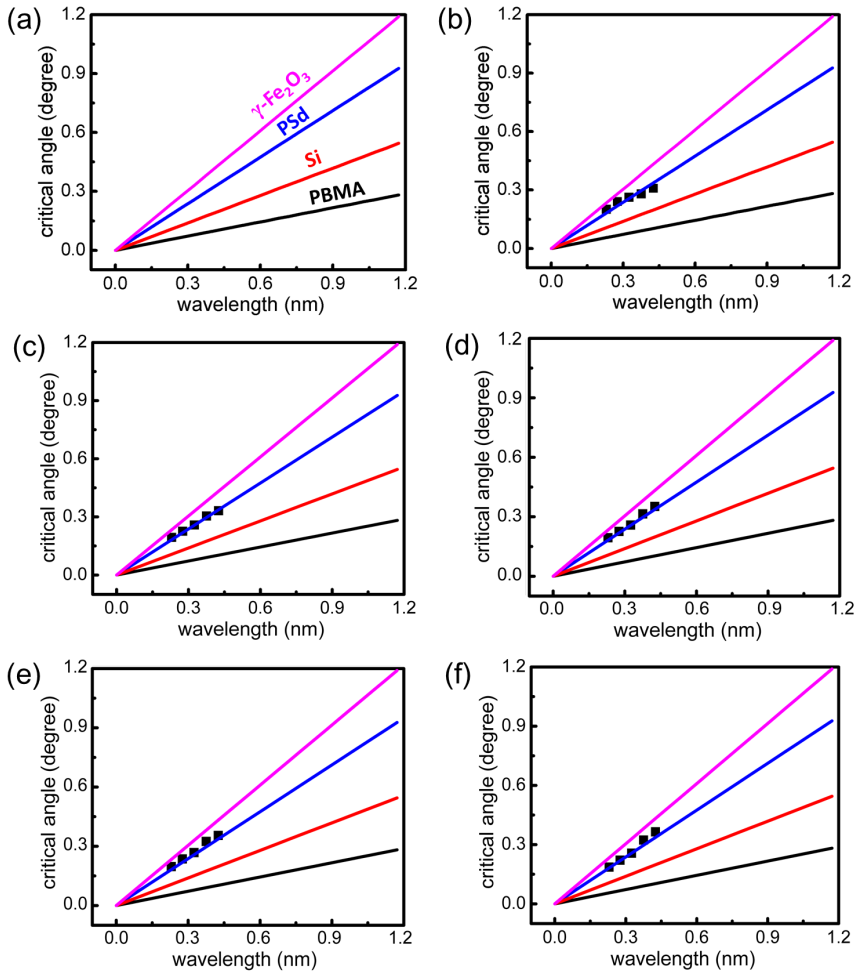

Figure 5.10: (a) Theoretically predicted positions of critical angles (solid lines) of the involved components (γ-Fe_2O_3, PSd, Si, and PBMA) vs. wavelength for hybrid films with NP concentrations: (b) 0, (c) 0.5, (d) 1, (e) 7, and (f) 15 wt%. The solid squares are the experimentally observed Yoneda peak positions extracted from the corresponding vertical cuts.

a surface morphology, PSd cylinders dispersed in a majority PBMA matrix, is observed, even though the PSd possesses the relative larger volume fraction (f_{PSd}) of 0.53 in the DBC. Therefore, from the related GISANS measurements, it can be concluded that a PSd enrichment layer must exist at the polymer/substrate interface. Such enrichment layer induces a morphological transition to a perforated lamella. [110] Figure 5.10c-f present the experimentally extracted critical angle positions of the hybrid films with NP concentration of 0.5 to 15 wt%. In general, they show the similar behavior as the NP-free DBC film (Figure 5.10b), which indicate that the presence of a PSd enrichment layer at the polymer-substrate interface is not influenced by the NP incorporation. Furthermore, with a great amount of NPs loading (7 and 15 wt%, Figure 5.10e and f), the Yoneda peak positions

are inclined to a higher value towards the theoretical positions of the critical angle for the γ-Fe_2O_3 (pink solid line), because the neutron scattering length density of the hybrid film becomes larger due to the embedded NPs.

5.4.2 Lateral structure

Figure 5.11 presents the full set of 18 channels horizontal line cuts made from the 2D GISANS patterns of the hybrid films at different NP concentrations of 0, 0.5, 1, 7, and 15 wt%. Lateral structure information is provided by the horizontal line cuts. All the horizontal cuts (points) are shown together with their fits (solid line), which are fitted with a model assuming prominent lateral distances with a Lorentzian distribution. Each horizontal cut contains a different q_y range because of the varied wavelengths used in the TOF-GISANS measurements. In general, for all the NP concentrations, a smooth decay of the scattered signal at smaller q_y values is shown. Moreover, only broad intensity peaks are found at small wavelengths (four q_y profiles from bottom, $\alpha_c \ll \alpha_f$). It reveals the presence of an ill-defined lateral structure at the film/substrate interface. Furthermore, a main feature of the pronounced peak I, located at large q_y values, is found. However, the prominent peak is on longer visible at longer wavelengths, because the corresponding q_y range is inaccessible.

Further, the most prominent intensity maximum of the horizontal line cuts is analyzed for investigating the effect of the NP concentration on the film morphology. Figure 5.12a presents the data (squares) and their fits from a selected neutron wavelength of 0.425 nm for different NP concentrations. It is observed that, the peak position stays as a constant irrespective of the NP amount. Such behavior reveals that the NP concentration is independent from the inter-domain distance which is originally created with the microphase separation of the DBC. The value of the inter-domain distance obtained from the fit is 59 ± 1 nm. In addition, the significance of the peak reveals the systematic order of the probed nano-structures. Therefore, the Full width half maximum (FWHM) as well extracted from the fit is shown in Figure 5.12b. Both, the value and the deviation of the FWHM revealed from the fits demonstrate the inner lateral structure of the hybrid films. It is observed that, the FWHM shifts towards a small value and its deviation becomes much narrower with a small amount of NPs loading (0.5 wt%). However, as the NP concentration increases, FWHM increases monotonically and the deviation broadens again to a very broad width at last. Briefly, selectively deposited NPs with proper amount can improve the long range order of the nano-morphology. However, the inter-domain distance stays constant with a systematic loss of order upon further addition of NPs. [110]

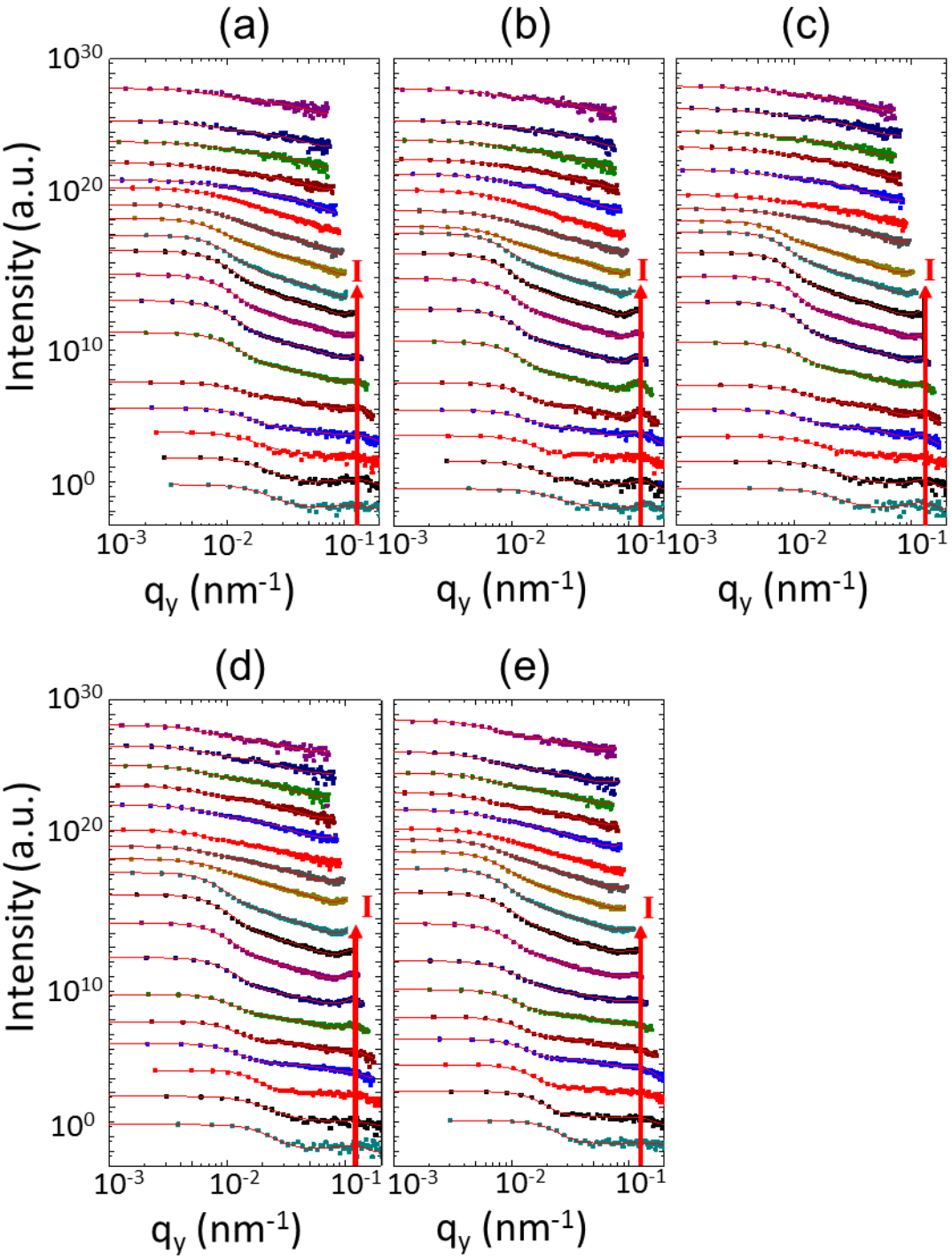

Figure 5.11: Horizontal line cuts of the hybrid films for varied NP concentrations: (a) 0, (b) 0.5, (c) 1, (d) 7, and (e) 15 wt%. The red solid lines are the fits to the data. The arrow (marked with I) is a guide to the eye, showing the determined peak position. For clarity, all cuts are shifted against y axis from bottom to top, with the neutron wavelength increases as follows: 0.225, 0.275, 0.325, 0.375, 0.425, 0.475, 0.525, 0.575, 0.625, 0.675, 0.725, 0.775, 0.825, 0.875, 0.925, 0.975, 1.025, and 1.075 nm.

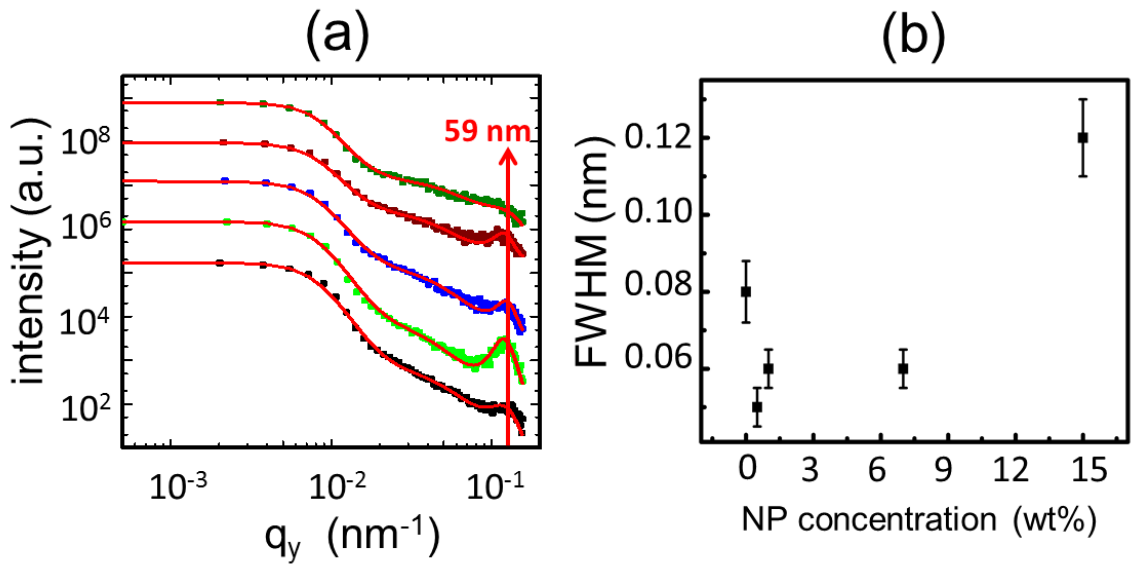

Figure 5.12: (a) Horizontal line cuts (squares) of the 2D TOF-GISANS patterns obtained from a selected wavelength of 0.475 nm together with their fits (red solid lines) of the hybrid films at different NP concentrations: 0, 0.5, 1, 7, and 15 wt%, from bottom to top. (b) Full width half maximum extracted from the fits of the horizontal line cuts vs. NP concentration.

The determination of the TOF-GISANS complements the inspections obtained from the real space techniques SEM and AFM.

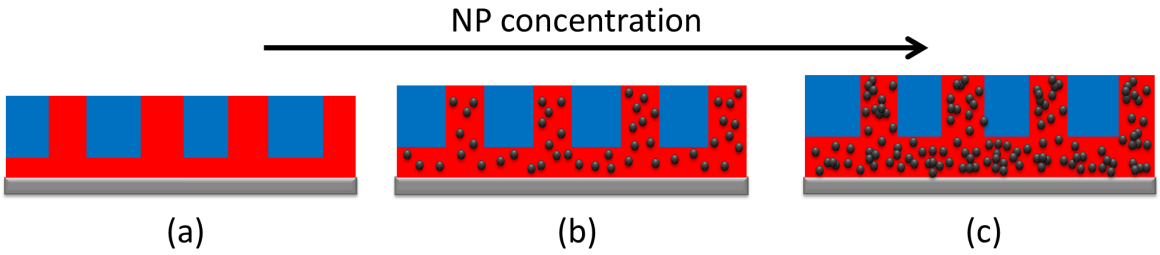

Figure 5.13: Sketch of the cross-section of (a) pure DBC film, NPs-DBC hybrid films at (b) low and (c) high NP concentrations. The PSd domain, the PBMA domain, the NPs and the silicon substrate are indicated in red, in blue, in black, and in grey, respectively. Image modified from reference [110].

Figure 5.13 presents the nano-morphological evolution of the hybrid films at different NP concentrations. In Figure 5.13a, a morphology of moderately ordered, perforated lamella, with a PSd enrichment layer located at the polymer-substrate interface is shown for the pure DBC template. Such special morphology mainly attributes to two factors:

(1) In literature, PBMA and PSd are inclined to segregate to the polymer-air and polymer-substrate interface, respectively, for a lower surface energy. [213]

(2) In case the DBC film thickness approximates to the periodic domain distance of the DBC, a surface-perpendicular morphology is favored to form. [205]

Based on a mean-field theory mentioned in the previous Section 2.1.3. Block copolymer films, the orientation of lamella in DBC films has been discussed. [214] Moreover, the similar phase transition throughout the different depth of the DBC film has been reported by the Zimmermann group. [214] They observed a lamella orientational transition across the BC film from a parallel oriented lamella at a selective boundary to a perpendicular oriented lamella at a neutral boundary due to lower free energy. [214] In Figure 5.13b, upon incorporation of a small amount of NPs, a highly ordered structure is found. It ascribes to that the selectively incorporated NPs are well dispersed within the PSd domains, which improves the systematic enthalpy contribution. Furthermore, because of the increase of the NPs embedded inside the bottom PSd enrichment layer, the expansion of the film thickness appears. In Figure 5.13c, with a large amount of NPs loading, the previous highly ordered cylindrical morphology is deformed. Even more, the long range ordered structures are perturbed by arisen small NP aggregates. As well, the film thickness expands prominently, since plenty of NPs are embedded inside the bottom PSd enrichment layer.

5.5 Magnetic properties

To investigate the magnetic behaviors of the hybrid films, a Quantum Design magnetic property measurement system (MPMS) of SQUID magnetometry is used. Figure 5.14a shows the temperature dependent hysteresis loops for a selected hybrid film with NP concentration of 15 wt%. In a previous investigation regarding the hybrid film systems with randomly distributed DBC matrix with γ-Fe_2O_3 NP, [215] the observed saturation magnetization and slope of the hysteresis loops are independent from the temperature. However, the temperature dependent maximum magnetization (magnetic moment per unit volume) is shown in Figure 5.14b, which is attributed to the special film morphology (perforated lamella with an enrichment layer containing NP). At a temperature of 2 K, the M_s reaches its highest value of 8.9×10^{-9} Am^2. In addition, the ratio of M/M_s is inversely proportional to the temperature, which is in agreement with Equation 5.3 [216]

$$\frac{M}{M_s} = \frac{\mu B}{3k_B T} \tag{5.3}$$

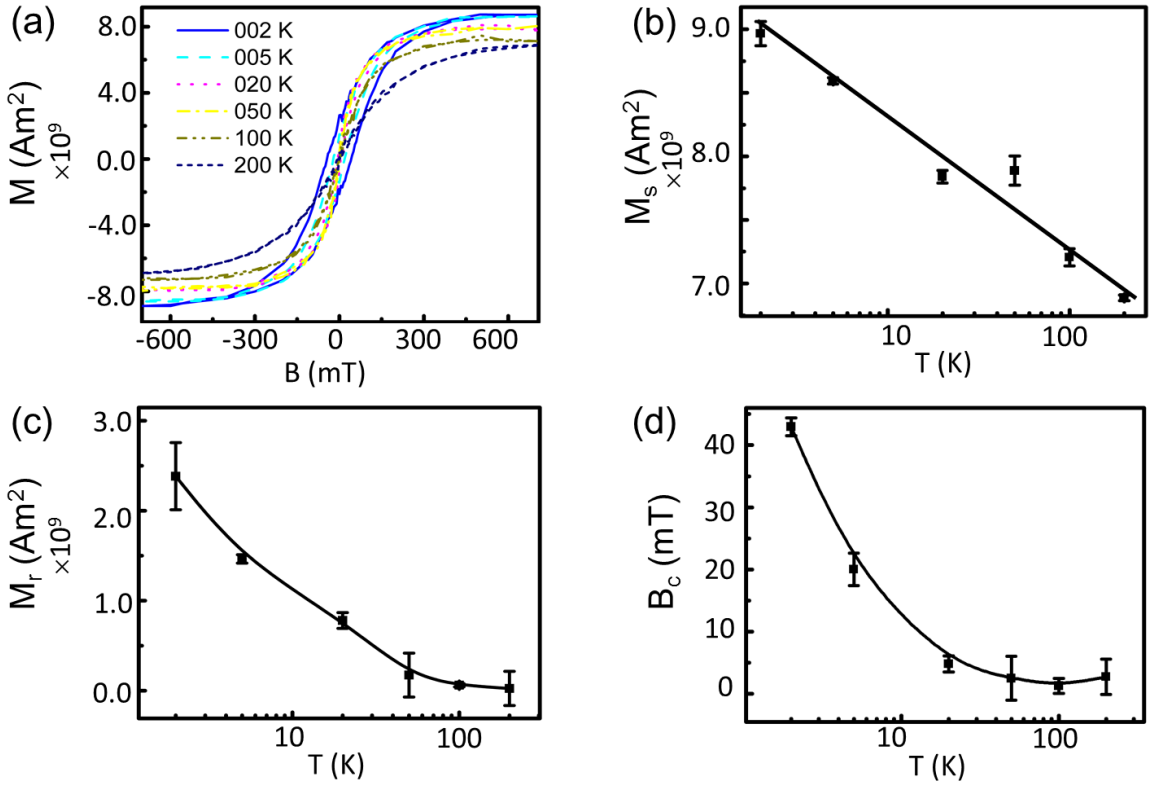

Figure 5.14: (a) Magnetic moments measured as a function of the external magnetic field, (b) the saturation magnetization, (c) the remanence and (d) the coercivity at different temperatures for a hybrid film with 15 wt% NP concentration (the black solid lines are guide to eyes).

where μ is the magnetic moment, B is the magnetic field, and k_B is the Boltzmann's constant. In Figure 5.14c, a temperature dependent remanence obtained from the measured magnetic moments (Figure 5.14a) is found. As the temperature increases, the remanence decays sharply, which differs from a milder decreasing behavior reported in another DBC films with embedded iron oxide NPs. [215] Meanwhile, the observed coercivity (Figure 5.14d) as well reduces strongly with the increase of the temperature. Such descendent behavior is ascribed to the thermal agitation. Based on the Néel-Brown expression (in Section 2.2.4, Equation 2.28), [133] the hysteresis can only be observed below a certain characteristic temperature, which is the finger print of a superparamagnetic behavior. [134]

Figure 5.15a present the magnetic moments measured at 2 K for hybrid films at different NP concentrations. In Figure 5.15b, the M_r and M_s, extracted from the corresponding magnetic moments, are dependent on the NP concentration. As the NP concentration increases, M_r and M_s exhibit the similar monotonically increasing behavior within experimental error. However, the calculated relative remanence, M_r/M_s, remains as a constant

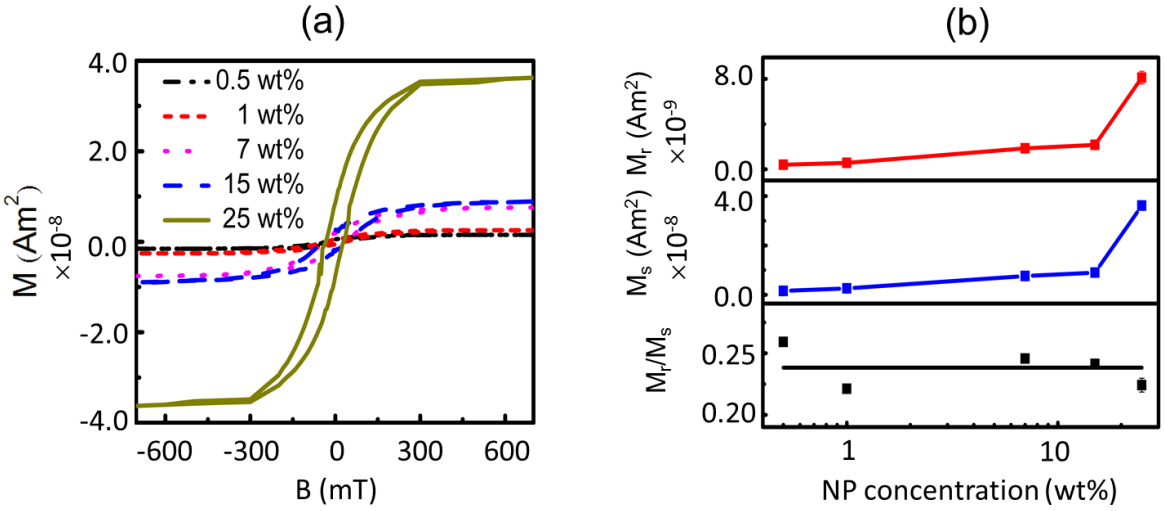

Figure 5.15: (a) Measured magnetic moments vs. external magnetic field at temperature of 2 K for different NP concentrations of 0.5, 1, 7, 15, and 25 wt%. (b) Extracted remanence, M_r, saturation magnetization, M_s, and relative remanence, M_r/M_s, vs. NP concentration. Image modified from reference [110].

regardless NP concentration. Considering all the observations from the magnetic properties, the current investigated hybrid film system follows a superparamagnetic behavior, [217] which can be well explained in details with a modified Stoner-Wohlfarth-Néel model developed by Schulz in our group. [133, 160, 218] Differs from a randomly oriented DBC matrix embedded with NPs, for the perforated lamella with an enrichment layer containing NP, the developed thermodynamics of the superspins is not modified by either an elastic torsion mechanism or a statistical distribution of the anisotropy constants, which has been found in previous investigations. [133, 160, 218]

5.6 Summary

In the present chapter, superparamagnetic hybrid films consisting of functional surface modified NPs and structure guiding PSd-*b*-PBMA DBC matrix are systematically studied with XRR, SEM, AFM, TOF-GISANS, and SQUID. A special morphology of a perforated lamella with an enrichment layer containing NP at the film/substrate interface is established, which is realized via properly selecting a film thickness approximating the periodic inter-domain distance of the chosen DBC. Upon incorporation of a small amount of NPs, a highly-ordered alignment of the NPs in the DBC template is achieved via a self-assembly microphase separation driven process combined with the selectively embedded PS-coated

NPs. Notably, irrespective of the NP concentration, the lateral structures, inter-domain distance, always remain constant, which is quite interesting for the applications, as it does not change the periodicity of the magnetic nanostructure. [110] Meanwhile, the systematic order and perpendicular orientation of nanostructures have been improved with the incorporation of a small amount of NPs due to the modification of the system enthalpy. However, the previous established long-range ordered structures have been perturbed due to the presence of the relatively larger NP aggregates at high NP concentrations. Moreover, plenty of NPs are embedded inside the bottom PSd enrichment layer. Hence, the entire film thickness expands significantly. The fabricated hybrid films are superparamagnetic, which renders them interesting for potential applications in fields as diverse as medical devices, magnetic sensors, and magnetic memory devices.

Chapter 6

Parallel lamellar with incorporated maghemite NPs

Parts of this chapter will be published in the article "Lamellar diblock copolymer films with embedded maghemite nanoparticles", *Adv. Mater. Interfaces*, **2016**.

In previous Chapter 5, a special morphology of a perforated lamella with an enrichment layer containing NPs was established with the PSd-*b*-PBMA DBC and the selectively incorporated γ-Fe_2O_3 NPs. In the present investigation, the identical DBC and NPs were employed as in Chapter 5. However, the establishment of, with respect to the film surface, a differently parallel orientated lamellar morphology is intended.

The crucial film thickness is determined with surface profilometry. The surface structures are measured with real-space techniques, such as AFM (AFM-1, described in Chapter 3.1.3) and SEM. Furthermore, the measurement in reciprocal space in the form of TOF-GISANS are employed to characterize the morphology of the bulk hybrid films at both film/air and film/substrate interfaces simultaneously, using the multi-wavelength neutron beam in the TOF mode with a properly selected incident angle. [155] The powerful and depth-resolving method of TOF-GISANS is applied for the structural identification of the highly ordered parallel lamella morphology with minor perpendicular defects. Finally, magnetic properties of the hybrid films with the relation to the film morphology are probed with an advanced quantum design MPMS based on SQUID.

This batch of NPs-DBC hybrid films is prepared by spin-coating in combination with thermal annealing at 160 °C for 72 hours in N_2 atmosphere. The purchased whole Silicon substrates were cut into 70 × 70 mm^2 pieces. In order to redefine the surface oxide layer and removing any possible organic traces, an acid cleaning procedure was applied (details in Section 4.2.1). Toluene was chosen as the solvent, since it is a good solvent for both DBC blocks. Solutions with different weight ratio of NPs vs. DBC (0, 0.1, 0.5, 1, 3, 7, and 15 wt%) were prepared. All films were fabricated under identical conditions of room

temperature (25 °C) in an ambient environment. In preliminary experiments, solutions with various DBC concentrations were used for preparing DBC films with different thicknesses. According to the results, a proper DBC concentration of 36 mg/mL was selected for a desired film thickness of 230 nm, which was used for the present investigation.

6.1 Film thickness

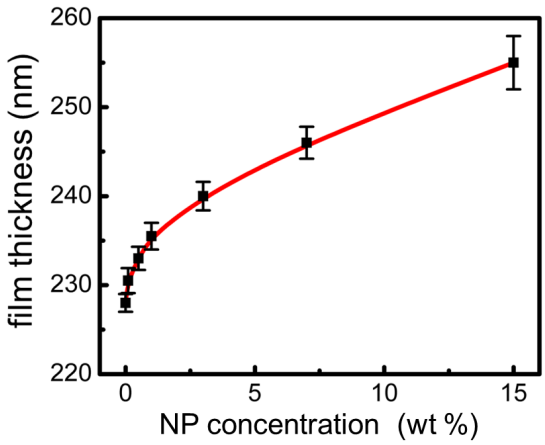

Figure 6.1: Thickness of the hybrid films, t , vs. incorporated NP concentration (the solid line is a guide to the eye)

In previous Chapter 5, the influence of the film thickness on the orientation of DBC morphologies has been discussed in case the DBC film is restricted to two physically different interfaces. [113, 193–195] If the film thickness is much larger or similar to the characteristic periodic distance of the employed DBC, the orientation of parallel or perpendicular (with respect to the film surface) morphology tends to form respectively, which is attributed to the polymeric conformational entropy. [115, 172, 196, 197, 202] Therefore, the precise determination of the film thickness is essential for controlling the structure orientation and thus the potential applications. In the present investigation, the thicknesses of the hybrid films at different incorporated NP concentrations were probed with surface profilometry and shown in Figure 6.1. Firstly, a desired film thickness of 228.1 nm for the NP-free DBC template was obtained. Afterwards, as the NP concentration increases from 0.1 to 15 wt%, the film thickness expands from 231.1 ± 1.2 nm to 255.2 ± 3.1 nm. Since the viscosity of the mixture solutions with varied NP weight ratios is fairly similar, the expanding behavior of the film thickness is mainly ascribed to the different volume of the incorporated NPs. Based on the theoretical DBC phase diagram (in Section 2.1.2), the currently employed PSd-*b*-PBMA DBC with a f_{PS} of 0.53 inclines to form a lamella morphology. Further, a theoretical periodic inter-domain distance of 68 nm is expected according to the Semenov method (Section 2.1.2), [77] which describes this characteristic periodic distance as determined from a balance between the interfacial energy and the

stretching energy originating from the DBC blocks. [77,110] Notably, the film thicknesses are almost 2.5 times larger than the theoretical periodic distance, therefore, a parallel lamella morphology is presumed. In particular, the film thickness increases with a non-linear trend, leveling off in the case of high NP concentrations, which is in close relation to the progressive increase of the experimentally examined periodic distance in parallel orientation (the details will be discussed later in Section 6.4.1).

6.2 Characterization of surface morphology

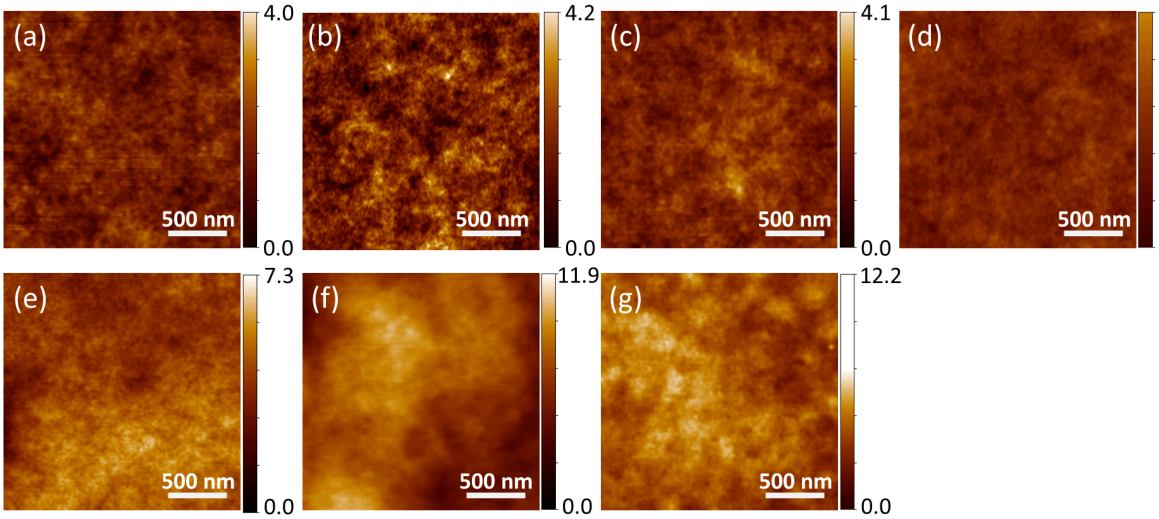

Figure 6.2: AFM topographical images of hybrid films at different NP concentrations: (a) 0, (b) 0.1, (c) 0.5, (d) 1, (e) 3, (f) 7, and (g) 15 wt%.

Tapping mode AFM is employed to examine the surface structure of the NPs-DBC hybrid films. Figure 6.2 shows the AFM topographical images of the film top surface, where no feature of perpendicular (with respect to the sample surface) lamellar morphology is present. Taking the film thickness regime ($t \gg D$) and the featureless surface into account, a periodic parallel lamellar structure is most likely to exist. Moreover, AFM data provide the surface route-mean-square (rms) roughness as well. As the NP concentration increases from 0 to 3 wt%, the rms roughness increases from 0.29 to 0.81 nm monotonically. In case the incorporated NP concentration reaches 7 and even 15 wt%, the rms value significantly rises to 1.65 and 2.15 nm, respectively (Figure 6.2f and g), which is mainly attributed to the NP aggregates formed on the film surface. The Monte Carlo simulation well explicates the agglomeration of the NPs on the similar systems, which

suggests a strong tendency towards aggregate formation at high NP concentration in the NPs-DBC hybrid systems. [206]

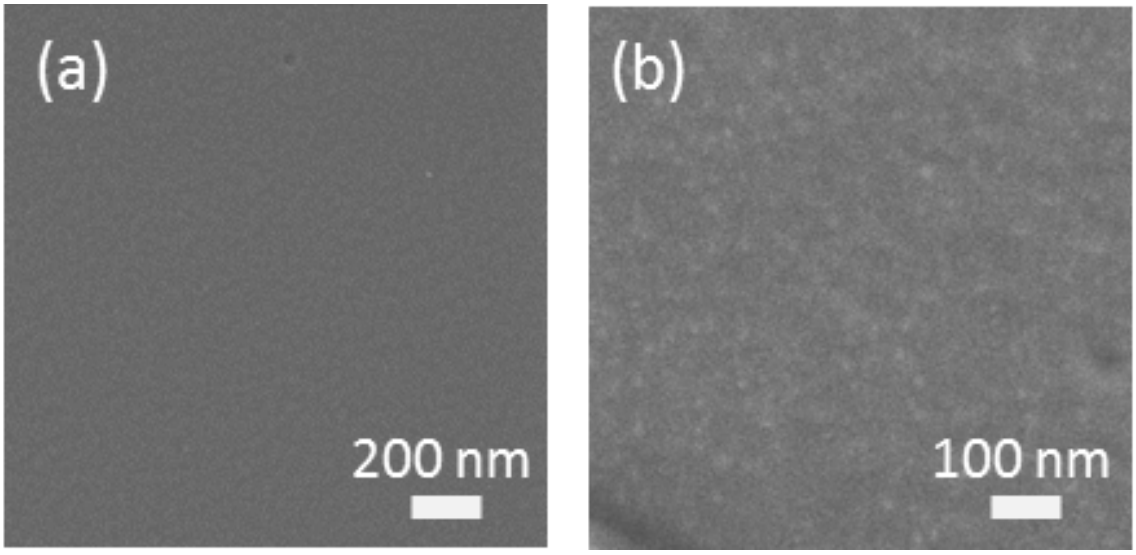

Figure 6.3: SEM images of selected NPs-DBC hybrid films at different NP concentrations: (a) 0 and (b) 15 wt%.

The surface feature of the pure DBC film and the hybrid film with NP concentrations of 15 wt% measured with SEM is shown in Figure 6.3. The surface morphology in a different contrast with a deeper penetrate depth of 10 nm are obtained. Similarly to the corresponding AFM measurements, featureless surfaces are also found here for NP-free DBC film (Figure 6.3a). In Figure 6.3b, several bright grey dots are observed, which supports the previously assumed presence of NP aggregates formed on the surface of the hybrid film with high NP concentration of 15 wt%.

6.3 Inner morphology of NP-Free DBC film

GISANS is applied for probing the buried structures of hybrid films, which gives exceptional structural statistics over a large illuminated film region. The DBC characteristic periodic inter-domain distance and the structural sizes down to the nano-scale could be obtained with this non-destructive measurement. Furthermore, the morphological information from substrate/film interface to the film/air interface is simultaneously examined by employing the TOF mode.

The 2D GISANS data of all the investigated hybrid films are collected for 20 different neutron beam wavelengths. Figure 6.4 presents the full frame of the 2D GISANS data for

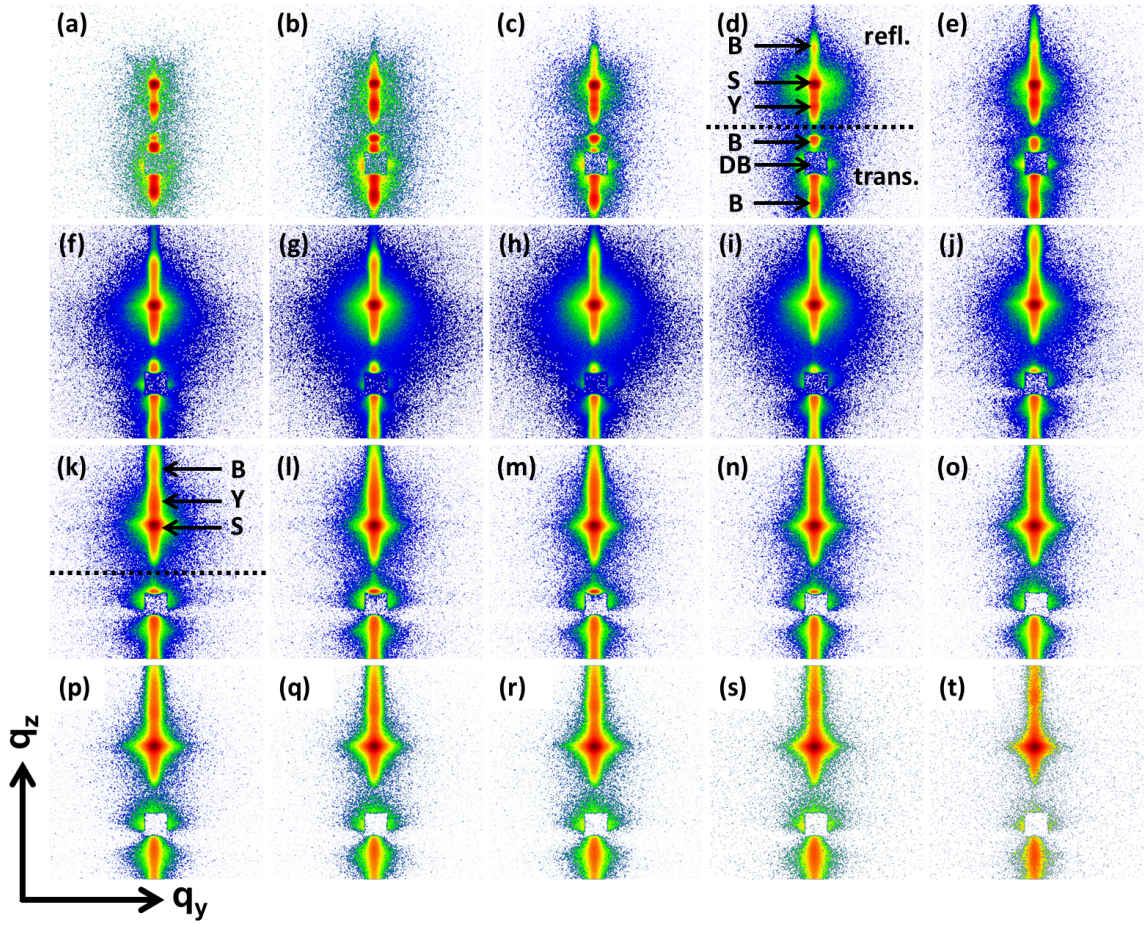

Figure 6.4: 2D GISANS data of the pure DBC film. The corresponding mean wavelengths (a-t) are as following: 0.225, 0.275, 0.325, 0.375, 0.425, 0.475, 0.525, 0.575, 0.625, 0.675, 0.725, 0.775, 0.875, 0.925, 0.975, 1.025, 1.075, 1.125, 1.175 and 1.225nm. All the intensities are shown in a same logarithmic scale for clarity. The Yoneda peak (Y), different order Bragg peaks (B), specular peak (S) and direct beamstop (DB) are pointed out. The reflection (refl.) and transmission (trans.) intensities are separated by the sample horizon (dashed line).

the pure DBC film measured at different wavelengths. Each 2D GISANS pattern has a different corresponding fixed (q_y, q_z) range. [160] In consideration of the geometry of the experimental set-up and the Maxwell type distribution of the neutron beam intensity, a maximum of primary neutron beam intensity appears at the mean wavelength of 0.525 nm (Figure 6.4g), leading to a maximum scattering intensity at the detector.

In general, several characteristic structural features are found in the full frame of the 2D GISANS data. The intensity minima indicate the sample horizon (marked with dashed line, in Figure 6.4d). The upper part of the sample horizon is the reflected intensity (marked as refl.), which contains the specular peak (marked as S), Yoneda peaks (marked

as Y), and different order Bragg peaks (marked as B). However, only the most pronounced specular peak (S) locates nearly in a constant place, where the exit angle (α_f) equals to the incident angle (α_i). [155] Taking the Figure 6.4d as an example, between the specular peak and the sample horizon, a less significant peak is observed, which is the so-called Yoneda peak (Y), where $\alpha_f = \alpha_c$ (material characteristic critical angle) for total external reflection. Based on Equation 5.2, the position of α_c depends on the material neutron scattering length density (ρ) and neutron wavelength (λ). [160] Therefore, as the wavelength increases, the position of the Yoneda peak shifts towards a higher q_z value. Such tendency has been found in the Figure 6.4. In the case of $\alpha_i > \alpha_c$ (short wavelengths, Figure 6.4a-f), the Yoneda peak is well below the specular peak. At intermediate wavelengths (Figure 6.4g, h), the Yoneda peaks overlap with the intense specular peak. After that, the Yoneda peak arises beyond the specular peak and moves further to higher exit angles (Figure 6.4h-l). In addition, some other characteristic weak peaks arise, which are assigned as Bragg peaks (marked as B, in Figure 6.4d). They originate from a partial phase coherence of neutron waves diffusely scattered from different interfaces and induces high intensity in a narrow sheet in reciprocal space. [184] In the current investigation, Bragg peak stems from the refraction and reflection at all the interfaces of parallel lamellar morphology.

Since the silicon substrate is considered transparent to the neutron beam, the transmitted signal can be obtained, which is dominated by the direct beam and locates below the sample horizon. In this part, some significant Bragg peaks are found as well. They indicate the existence of ordered periodic parallel structures along the q_z direction. In general, as the wavelength increases, different ordered Bragg peaks arise at different q_z values. Commonly, the simple approximation $2\pi/D$, where D indicates the periodic distance of structures, can be used to describe the positions of typical Bragg peaks. [207] However, it does not match the detected evolution of the Bragg peaks obtained from the GISANS measurements (Figure 6.4) because of the complexity arising from grazing incidence geometry (Section 2.3.4 and 3.1.9). To better characterize the wavelength-dependent Bragg peaks, Busch et al. have developed a proper approximation involving reflection/refraction effects: [192, 219]

$$\alpha_f = \pm \left(\alpha_{c,p}^2(\lambda) + \{ m\lambda/D \pm \left[\alpha_i^2 - \alpha_{c,p}^2(\lambda) \right]^{1/2} \}^2 \right)^{1/2} \tag{6.1}$$

where m is the order of the Bragg peak. For a further analysis, line cuts at two orientations are carried out:

(1) Vertical line cuts are made at a constant q_y of 0 (marked with a red arrow, in Figure 6.5a). They represent the structure perpendicular to the film surface.

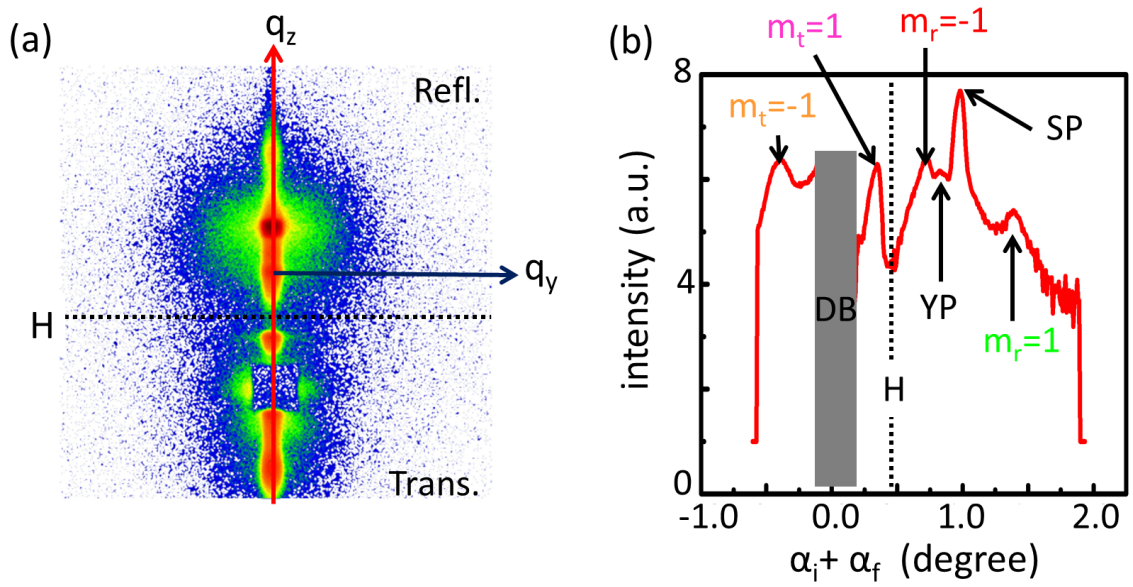

Figure 6.5: (a) An explicative 2D GISANS pattern measured at a mean wavelength of 0.375 nm for pure DBC film. (b) Vertical line cut of (a) is shown with the different orders of Bragg peaks highlighted (m), Yoneda peak (YP), specular peak (SP), beamstop (BS) and horizon (H). The horizon is shown with the dashed line and separates the transmitted and reflected intensities. The direct beam is blocked with a rectangular beamstop.

(2) Horizontal line cuts are made at varied q_z value (marked with a dark blue arrow, in Figure 6.5a). It contains the Yoneda peak region of the employed DBC and changes with the measured neutron wavelength. The information of the horizontal line cuts show the structure parallel to the film surface.

An exemplary 2D GISANS pattern measured at a mean wavelength of 0.375 nm for pure DBC film is presented in Figure 6.5. To explain the complexity of characterizations arisen from a vertical line cut, an example with full illustrations is shown in the Figure 6.5b. H (with the dotted line), at the angle of $\alpha_i + \alpha_f = 0.48°$ (angle recording in the detector), indicates the sample horizon. However, the actual angle of $\alpha_i + \alpha_f$ for the horizon is 0. Based on the GISANS geometry discussed in Section 3.1.9, during the measurement, the sample is titled by the incident angle of 0.48°. It results in the difference of the value of the $\alpha_i + \alpha_f$ recorded in the detector and has been corrected in further analysis. The direct beam is blocked by a beamstop (BS). The most significant intensity is attributed to the specular peak (SP). Bragg peaks in transmission and reflection parts are indexed in terms of m_t and m_r, and the order is numbered with $\pm$ 1, $\pm$ 2. YP indicates the Yoneda peak located between the Bragg peak of m_r -1 and the specular peak.

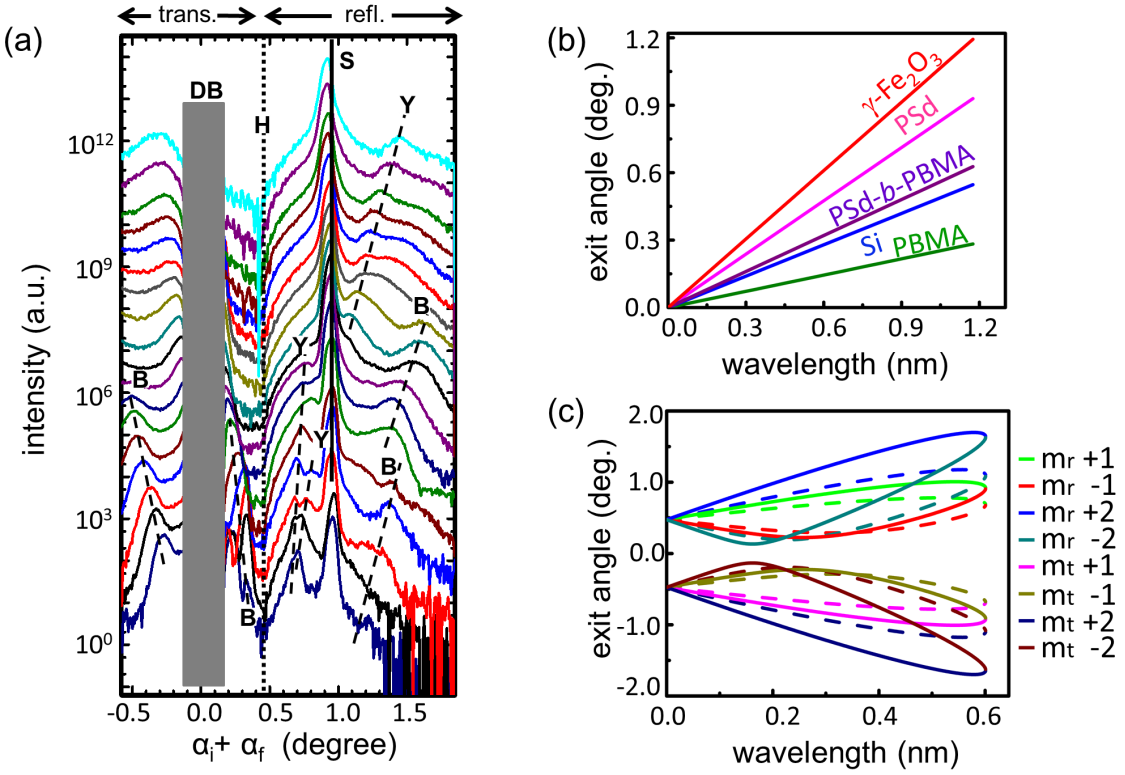

Figure 6.6: (a) Vertical line cuts made from 2D GISANS data at all measured channels for the pure DBC film vs. angle ($\alpha_i + \alpha_f$) recorded on the detector. The trend of Yoneda peaks (Y) and Bragg peaks (B) is guided with dashed lines. For clarity, all cuts are shifted against y axis as the neutron wavelength increases from bottom to top: 0.225, 0.275, 0.325, 0.375, 0.425, 0.475, 0.525, 0.575, 0.625, 0.675, 0.725, 0.775, 0.825, 0.875, 0.925, 0.975, 1.025, and 1.075 nm. (b) The positions of theoretic predicted critical angle vs. the wavelength for the components of the hybrid film: γ-Fe_2O_3 (red line), PSd (pink line), PSd-*b*-PBMA (purple line), Si (blue line), and PBMA (green line). (c) The positions of theoretically predicted Bragg peaks vs. the wavelength at the exit angle α_f are indicated with two exemplary periodic lamellar distances of 44 nm (solid lines) and 64 nm (dashed lines). The orders of Bragg peaks in both transmission (m_t) and reflection (m_r) parts are presented with different colors in the illustrations.

For selected sample of the pure DBC film, vertical line cuts made from 2D GISANS data at all measured channels are shown in Figure 6.6 a. They are plotted vs. the angle of $\alpha_i + \alpha_f$ (recorded on the detector). In general, two distinct Yoneda peaks are observed. As the wavelength increases, both of them increase linearly. However, at high wavelengths, the Yoneda peak appearing at smaller exit angles is overlaid by the more intense specular peak; the higher exit angle Yoneda peak passes through the specular peak region and then increases to an even higher angle. Moreover, different slopes for the Bragg peaks are

clearly observed. The specific information of the structure requires further analysis. Based on a critical wavelength (λ_c), at which the Yoneda peak exceeds the specular peak, the whole set of employed wavelengths can be divided into two groups:

(1) $\lambda \leq \lambda_c$, neutron beam penetrates the entire film. Hence, bulk sensitive structural information can be obtained.

(2) $\lambda > \lambda_c$, neutron beam can only pass through part of the film. Therefore, the structural profiles in different depths are accessible.

Particularly, the wavelength dependent penetration depth of neutron beam are defined with the equation of scattering depth of the neutrons: [155]

$$D = \frac{\lambda}{\sqrt{2}\pi(l_i + l_f)} \tag{6.2}$$

$$l_{i,f} = \left[\left(\alpha_c^2 - \alpha_{i,f}^2\right) + \sqrt{\left(\alpha_{i,f}^2 - \alpha_c^2\right)^2 + 4\beta^2}\right]^{1/2} \tag{6.3}$$

where D is the penetration depth from the beam impinged surface, which is the film/air interface in the present investigation, β is the absorption. Since the probed film thickness is large enough for allowing an unperturbed structure, both bulk and surface sensitive structural information can be obtained. On the basis of Equations 6.2 and 6.3, the theoretically expected penetration depth of the neutron beam for all film components are plotted in Figure 6.7.

Furthermore, on the basis of Equation 5.2, theoretically expected wavelength dependent Yoneda peak positions are presented with the corresponding scattering length densities (SLD): $\rho_{\gamma-Fe_2O_3}$ of 7.18×10^{-4} nm^{-2}, ρ_{PSd} of 5.99×10^{-4} nm^{-2}, $\rho_{PSd-b-PBMA}$of 3.44×10^{-4} nm^{-2}, ρ_{Si} of 2.07×10^{-4} nm^{-2}, and ρ_{PBMA} of 5.54×10^{-5} nm^{-2} (in Figure 6.6b). The experimentally observed Yoneda peak positions provides a simple approach for an analytical determination of the included chemical components since the Yoneda position will depend on the chemical composition of the film components. [192] Moreover, the partially deuterated DBC block significantly enhances the scattering contrast, which benefits the determination of chemical components as well.
On the basis of Equation 6.1, which includes the refraction effects, the wing-shape wavelength dependence of the theoretically expected Bragg peak positions at m^{th} order are shown in Figure 6.6c. In principle, m can be $\pm$ 1, $\pm$ 2, $\pm$ 3.... However, using the q range of the currently examined GISANS measurements, only orders of $\pm$ 1 and $\pm$ 2 have been found. In addition, the theoretically predicted Bragg peak curves at two exemplary characteristic periodic spacing, D, of 44 and 64 nm with orders of $\pm$ 1 and $\pm$ 2 are shown.

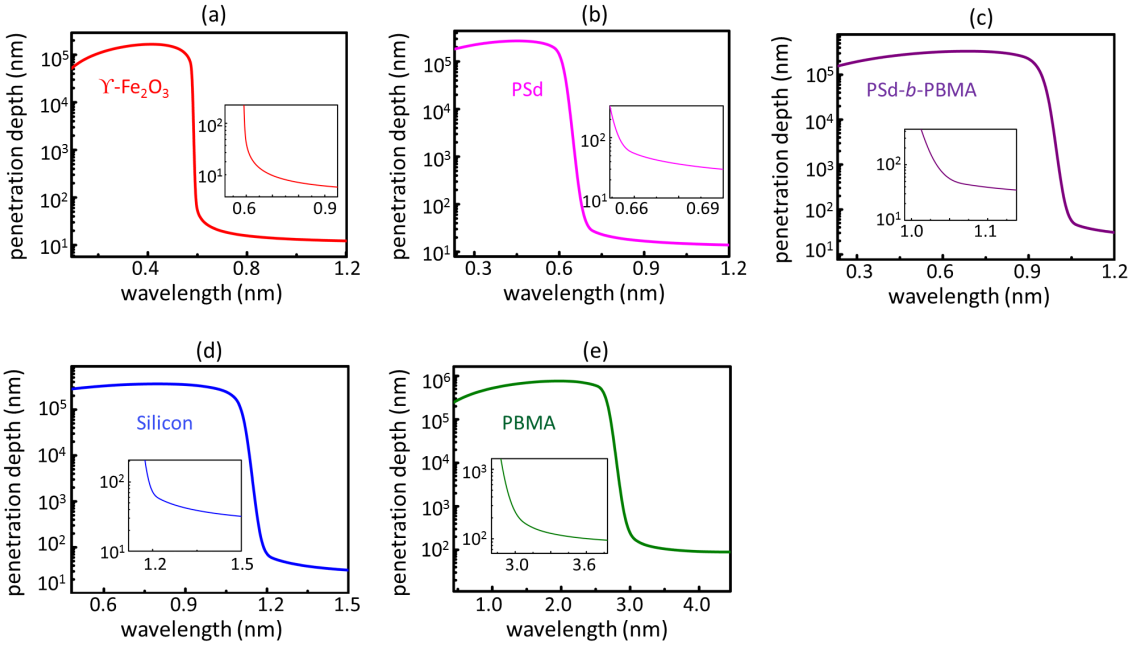

Figure 6.7: Penetration depth vs. neutron wavelength for all components in the hybrid film system: (a) γ-Fe_2O_3, (b) PSd, (c) PSd-*b*-PBMA, (d) Silicon, and (e) PBMA.

6.4 Effect of NP concentration on the inner structures

To probe the effect of NP concentration on the inner structures, the hybrid films with the incorporation of different NP concentrations have been examined with TOF-GISANS at all wavelength channels. In Figure 6.8, the 2D GISANS data measured at mean wavelength of 0.375, 0.475 and 0.775 nm are exemplarily shown for the hybrid film with NP concentrations of 0 to 15 wt%. At low NP concentrations, the 2D GISANS data appear almost the same. However, significant changes are observed with increasing NP concentrations. First of all, the overall scattering intensities have been improved strongly with the incorporation of NPs. In the q_z direction, several phenomena are observed. Firstly, for both transmission and reflection signals, the different orders Bragg peaks remain pronounced with the NP concentration up to 1 wt% (in Figure 6.8a-c), but they become weaker and broader as the NP concentration further increases. Even more, the Bragg peaks in the reflection part are hard to distinguish at high NP concentration of 15 wt% (in Figure 6.8f). The change in the Bragg peaks reveals the initially highly ordered, parallel periodic structure established with the incorporation of a small amount of NPs is perturbed due to the high amount of embedded NPs. Secondly, the Yoneda peak (Y)

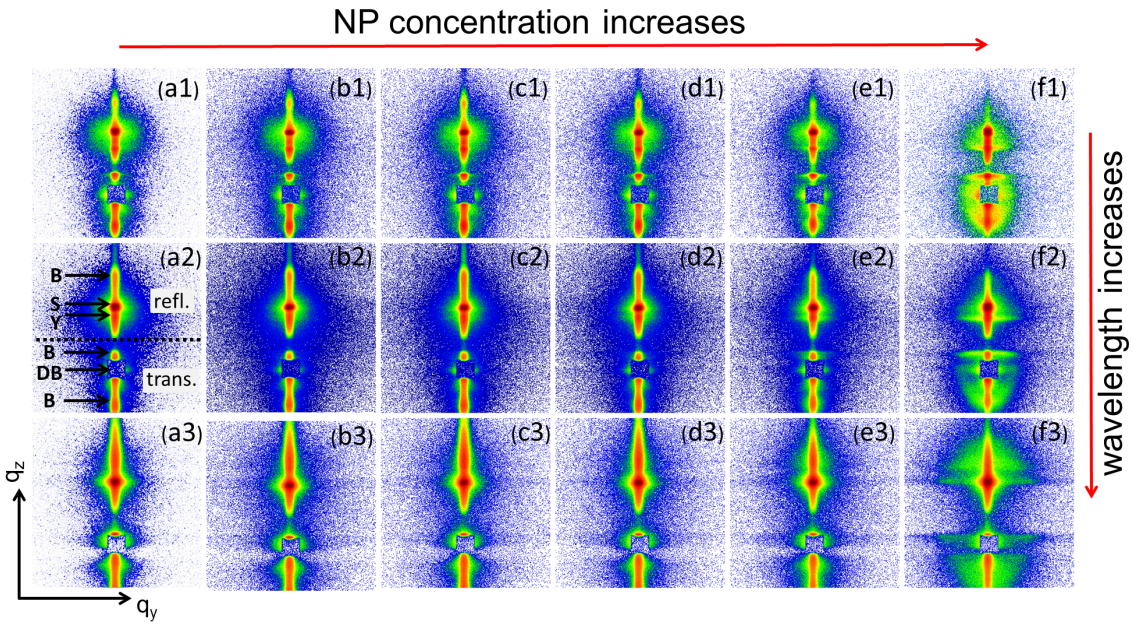

Figure 6.8: 2D GISANS data with mean wavelengths of 0.375, 0.475 and 0.775 nm (from top row 1 to bottom row 3) for hybrid films with different NP concentrations: (a) 0, (b) 0.1, (c) 1, (d) 3, (e) 7, and (f) 15 wt%.

moves to slightly higher angles with the increase of the NP concentration. Particularly, such increase is prominently observed for the hybrid film with the highest NP concentration of 15 wt% (Figure 6.8f1-f3). It is ascribed to the increase of the total scattering length density (ρ) with the maghemite NPs loading, since $\rho_{\gamma-Fe_2O_3}$ (7.18×10^{-4} nm^{-2}) $> \rho_{PSd-b-PBMA}$ (3.44×10^{-4} nm^{-2}). Thus, it can be inferred that the composition of the chemical component for the bulk hybrid film and the surface of the hybrid film is different. A higher exit angle of the Yoneda peak at a longer wavelength indicates the presence of a larger ratio of NPs at the film surface.

The other prominent changes are found in the q_y direction. The intensity of the Yoneda peak region becomes more prominent in case the NP concentrations is larger than 3 wt%, which is attributed to the higher electron density contrast of NPs and DBC than that of PSd and PBMA. In the transmission part, a distorted ring-shaped intensity is observed at NP concentration of 15 wt% (Figure 6.8f), which indicates the presence of an imperfect orientation of grain-like structure in the hybrid film. [220, 221] In the present hybrid film system, such feature mainly results from the dispersed NP aggregates, which perturbs the previous highly ordered, parallel lamella structures.

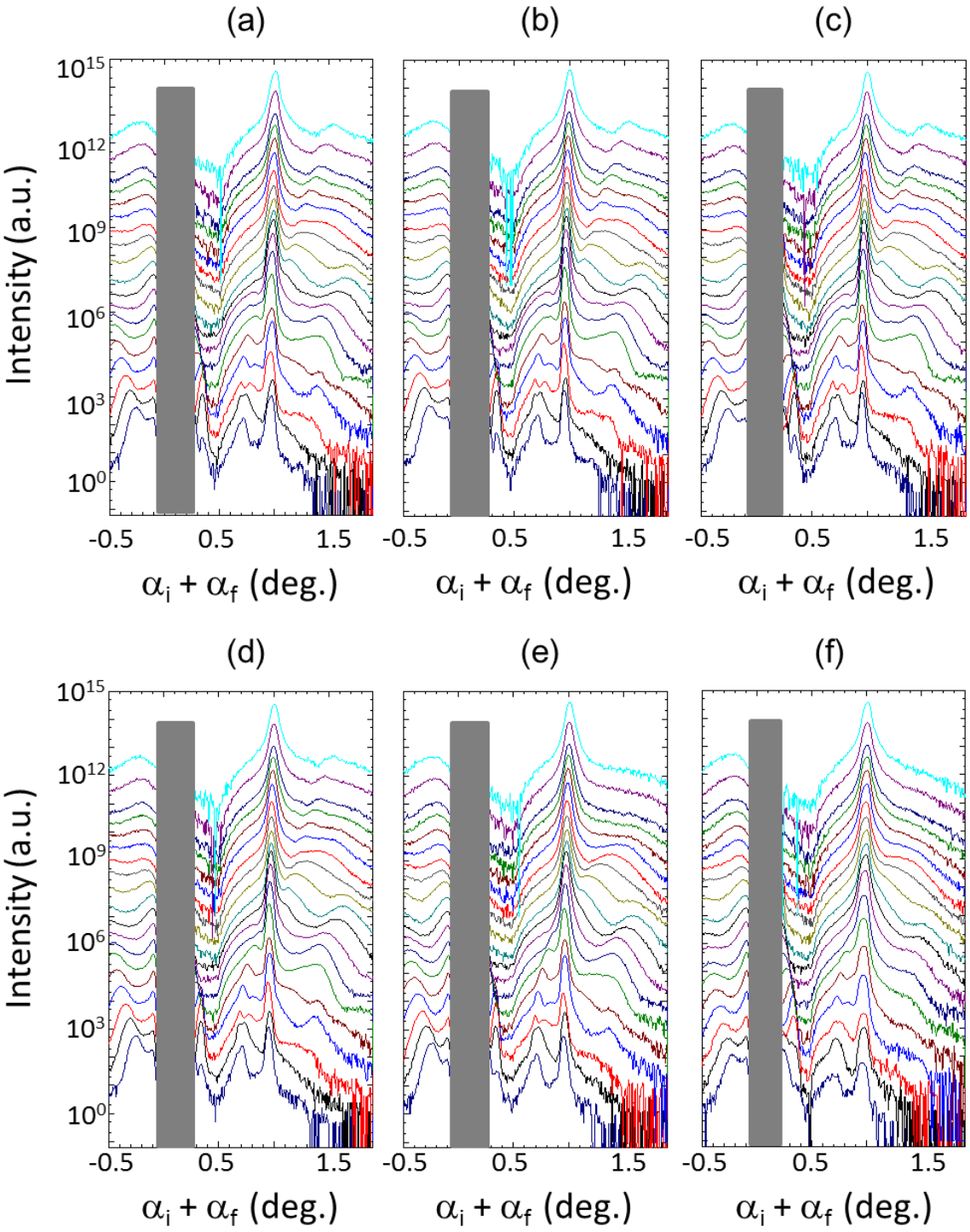

Figure 6.9: Vertical line cuts (at $q_y = 0$) made from 2D GISANS data at all measured channels vs. angle ($\alpha_i + \alpha_f$) recorded on the detector for the hybrid films with varied NP concentrations: (a) 0.1, (b) 0.5, (c) 1, (d) 3, (e) 7, and (f) 15 wt%. For clarity, all cuts are shifted against y axis as the neutron wavelength increases from bottom to top: 0.225, 0.275, 0.325, 0.375, 0.425, 0.475, 0.525, 0.575, 0.625, 0.675, 0.725, 0.775, 0.825, 0.875, 0.925, 0.975, 1.025, and 1.075 nm.

6.4.1 Parallel lamella structure

Vertical line cuts made at $q_y = 0$ from the corresponding 2D GISANS data for the hybrid films with varied NP concentrations are shown in Figure 6.9. The major features have been discussed in details in previous Section 6.3 Figure 6.6.

To quantify the effect of the NP concentration on the inner structure, a specific analysis is used. For all probed hybrid films, vertical line cuts are made for all wavelength channels. Furthermore, the positions of characteristic reflection (Yoneda/Bragg) peaks from the vertical line cuts have been extracted and determined for corresponding NP concentrations. Figure 6.10 and 6.11 present the positions of both the Yoneda and Bragg peaks (marked with open circles), respectively.

In Figure 6.10, the difference of the Yoneda peak positions provides a simple approach for an analytical determination of the contained chemical components due to their contribution of the scattering signal with a Yoneda peak. [153] The experimentally observed Yoneda peaks vs. wavelength provide a non-ambiguous assignment to distinguish chemical components. In Figure 6.10a, from top to bottom, three data series of Yoneda peaks are found, which follow the theoretical critical angle of PSd, PSd-*b*-PBMA and Si, respectively. Such phenomenon reveals that the Yoneda peaks are characteristics for the components of PSd, PSd-*b*-PBMA and Si. At low and intermediate wavelengths, the experimentally extracted Yoneda peaks are nearly independent of the NP concentration. It reveals that the effect of NP concentration on the total mean SLD of the probed hybrid films is weak. The most significant characteristic is observed at longer wavelengths, where the Yoneda peaks transcend the specular peak, and structural information of the surface is obtained. For the pure DBC film (Figure 6.10a), in case $\lambda \geq 0.625$ nm, the Yoneda peaks follow the PSd line, which reveals the presence of a PSd layer at the film/air interface. As the NP concentration increases (Figure 6.10b-d), in case $\lambda > \lambda_c$ (above the horizontal line), The Yoneda peak slightly moves towards higher angles. Furthermore, if NP concentration reaches 7 wt% (Figure 6.10e), the Yoneda peaks approach the γ-Fe_2O_3 line, especially when $\lambda \geq 0.825$ nm, the penetration depth of which is only 20 nm. As NP concentration increases to 15 wt%, the surface roughness becomes relatively high due to the presence of the large NP aggregates (proven in AFM data of Figure 6.2f and SEM data of Figure 6.3b), which significantly weakens the scattering signal. Therefore, fewer Yoneda peaks can be precisely distinguished (Figure 6.10f). In case $\lambda \geq 0.825$ nm, the Yoneda peaks appear only slightly lower than the γ-Fe_2O_3 line. Such behavior is mainly ascribed to the selectively embedded NPs into the PSd domains, since a PSd layer at the film/air interface is revealed.

In case $\lambda \leq \lambda_c$, the effect of NP concentration on the bulk film structure is fairly limited, because the ratio of the amount of incorporated NPs to the entire hybrid film is relatively

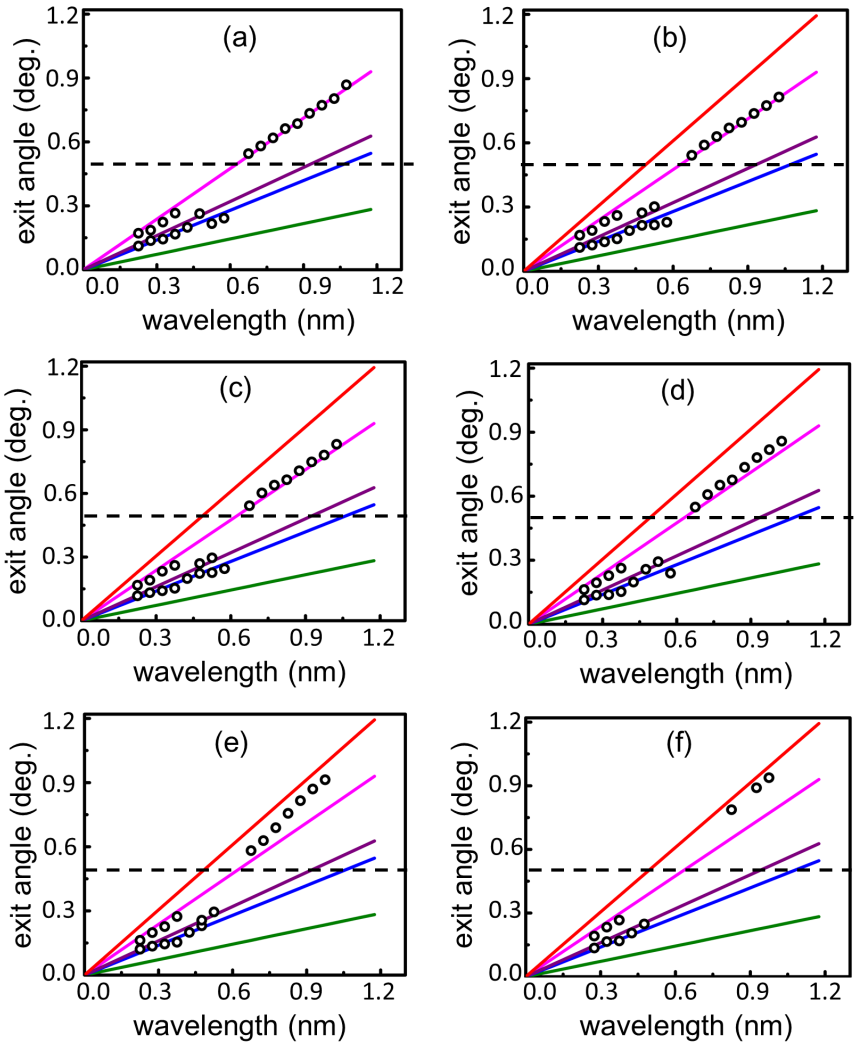

Figure 6.10: Hybrid films with different NP concentrations: (a) 0, (b) 0.5, (c) 1, (c) 3, (c) 7, and (f) 15 wt%. Theoretical critical angles vs. wavelength are shown for including chemical components of $\gamma - Fe_2O_3$ (red line), PSd (pink line), PSd-*b*-PBMA (purple line), Si (blue line) and PBMA (green line). The extracted positions of Yoneda peak from corresponding vertical line cuts vs. wavelengths are plotted with open circles. The specular peak positions ($\alpha_i = \alpha_f$) are pointed out with the horizontal dashed line. The intersection between the colored solid lines (theoretical critical angle) and the horizontal dashed line (specular peak) determines the characteristic critical wavelength λ_c for each component.

small; However, in case $\lambda > \lambda_c$, the surface sensitive structure information is shown, and a PSd layer with a relatively larger volume of NPs at the film/air interface is obtained. Consequently, the behavior of the Yoneda peaks with the increase of NP concentration confirms the chemical selectivity of PS-coated NP in the PSd layers. [201]

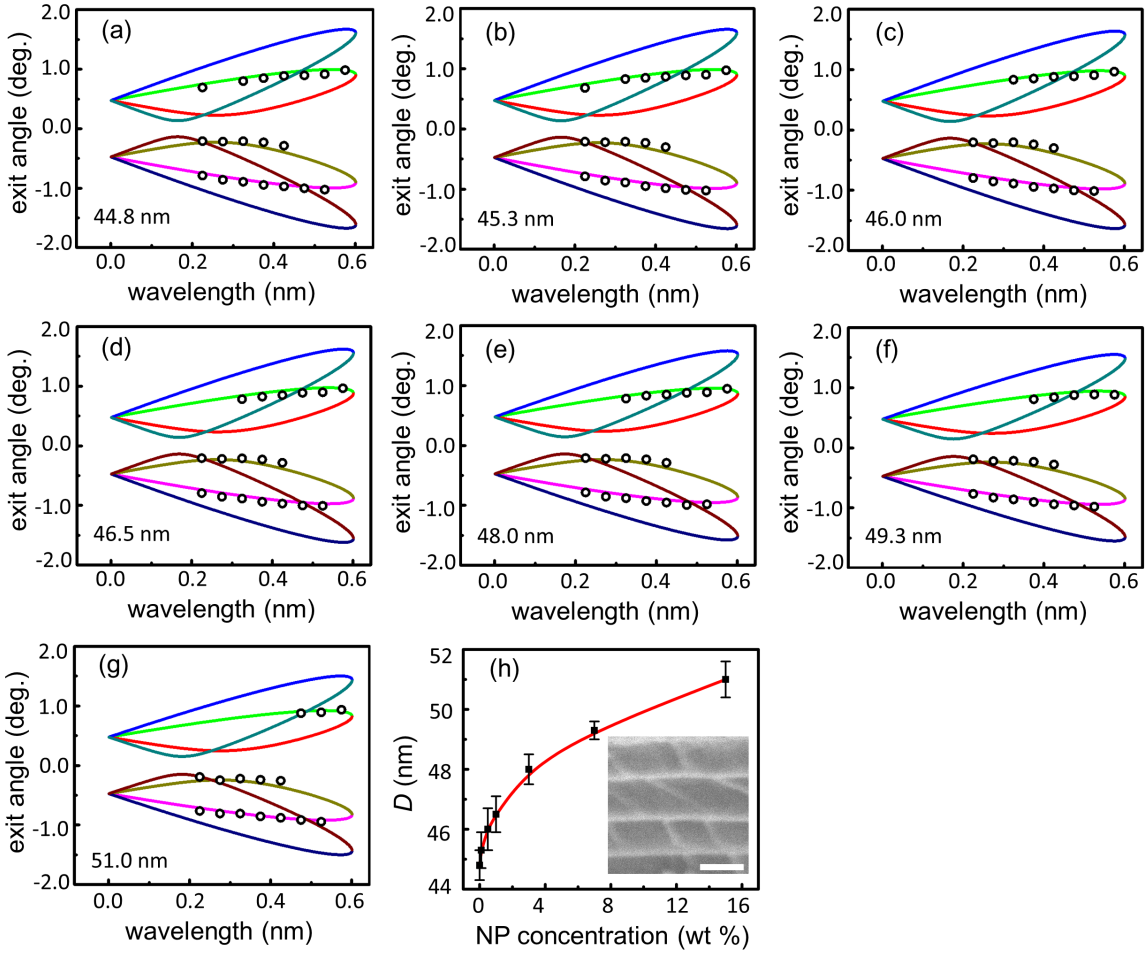

Figure 6.11: Hybrid films with different NP concentrations: (a) 0, (b) 0.1, (c) 0.5, (d) 1, (e) 3, (f) 7, and (g) 15 wt%. Bragg peak positions obtained on the basis of Equation 6.1 by employing different inter-domain distance, D; (a) 44.8, (b) 45.3, (c) 46.0, (d) 46.5, (e) 48.0, (f) 49.3 and (g) 51.0 nm are plotted with solid lines. The reflected and transmitted Bragg peak positions for the orders $m_r\pm$ 2 (blue, cyan), $m_r\pm$ 1 (green, red) $m_t\pm$ 2 (dark-blue, wine), $m_t\pm$ 1 (pink, dark-yellow) are shown. The black open circles indicate the extracted Bragg peak positions from vertical line cuts at corresponding wavelengths. (h) The inter-domain distance, D, obtained from the fits of Bragg peaks as function of NP concentration (the red line is a guide to the eye). The selected cross sectional SEM image of the hybrid film at NP concentration of 1 wt% is shown in the bottom right of (h). The white scale bar is 50 nm.

For hybrid films with different NP concentrations, the Bragg peak positions extracted from the corresponding vertical cuts are shown together with their best fits (Figure 6.11), which are plotted on the basis of Equation 6.1 with different inter-domain distance. Since the Bragg peaks originate from highly periodic, parallel oriented lamella structures, the fits of them reveal the inter-domain distance of the parallel lamellae. In Figure 6.11f, as

the NP concentration increases from 0 to 15 wt%, the inter-domain distance, D, of each NPs/PSd-PBMA layer increases from 44.8 ± 0.5 to 51.0 ± 0.6 nm accordingly, which originates from the selective incorporation of NPs within the PSd domains. In particular, such expansion behavior is more pronounced with a small amount of NPs incorporated. However, at higher NP concentrations, it follows a mildly increased slope. The result well matches the expansion trendy of the probed film thickness (Figure 6.1), which reveals that the increase of film thickness is truly attributed to the accumulated change of multiple alternating parallel layers, consisting of PSd and PBMA, instead of any randomly located enrichment layer of large NP aggregates. A cross sectional SEM image of hybrid film with NP concentration of 1 wt% is shown in the inset of Figure 6.11h. The most prominent parallel white lines are installed in an equidistant array with the mean distance of 46 nm, which is in perfect agreement with the corresponding Bragg peak fit. The result indicates that the orderly aligned NPs follow the arrangement of the parallel located PSd domains. In addition, some perpendicular short white lines are found as well, which may indicate the presence of a few random perpendicular structures within the hybrid films.

6.4.2 Lateral morphology

To further quantify the lateral structure, horizontal line cuts made from all wavelength channels for all investigated hybrid films are plotted from bottom to top with the increase of the wavelength in Figure 6.12. All horizontal line cuts are fitted on the basis of a model assuming a Lorentzian distribution of length scales for the corresponding structure factor, with a resolution function modeled with a Lorentzian function. [110] The fit results are presented with red lines together with the data. In Figure 6.12, at different wavelengths, horizontal line cuts with different q_y ranges are obtained. For small q_y, the first plateau is the resolution limit of the applied measurement for all given wavelengths. It indicates that the structures, which are larger than 1000 nm, cannot be determined. At short wavelengths, the scattering signal broadens with increasing NP concentration, which is ascribed to the increase of the interface roughness resulting from the incorporation of NPs. For all the probed hybrid films, at short and intermediate wavelengths, a shoulder-like maximum with a rather broadly distribution is observed at large q_y values. It arises from the ill-defined lateral structure with a size of 250 ± 50 nm, which could be the mesoscale domain distance between neighboring lateral PSd domains. Such random perpendicular structures have been found from the cross sectional SEM images in the Figure 6.11f. At long wavelengths, a smooth decay is present at the large q_y values. It reveals that no perpendicular structures exist at the film surface, which perfectly matches the observations from AFM data (Figure 6.2).

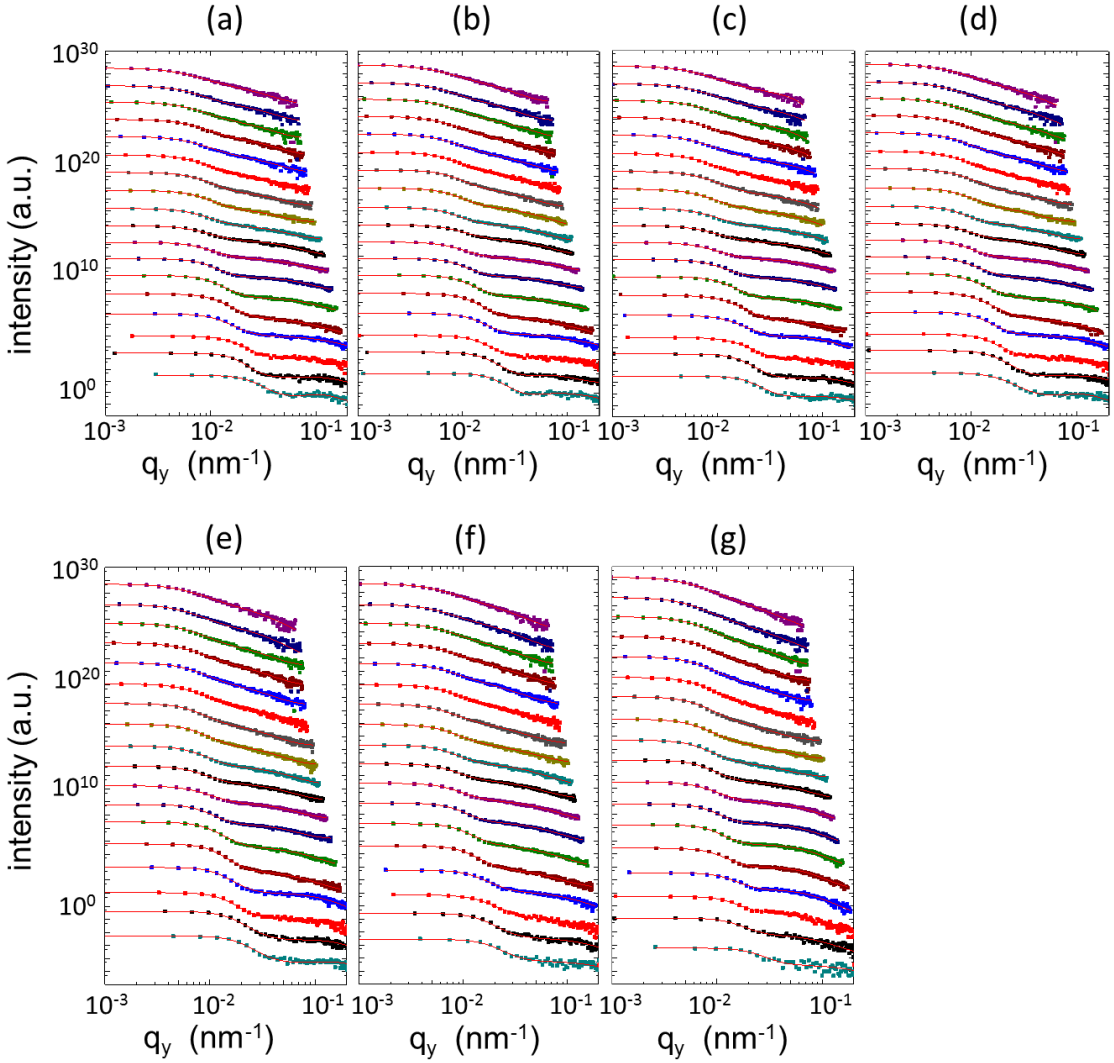

Figure 6.12: Horizontal line cuts of the hybrid film with NP concentration of (a) 0, (b) 0.1, (c) 0.5, (d) 1, (e) 3, (f) 7, and (g) 15 wt%. For clarity, all cuts are shifted against y axis. The corresponding mean wavelength increases from bottom to top: 0.225, 0.275, 0.325, 0.375, 0.425, 0.475, 0.525, 0.575, 0.625, 0.675, 0.725, 0.775, 0.825, 0.875, 0.925, 0.975, 1.025, and 1.075 nm.

For carefully figuring out the effect of the NP concentration on the lateral structures, horizontal line cuts for all probed hybrid films at a selected mean wavelength of 0.475 nm are shown in Figure 6.13. As the NP concentration increases from 0 to 15 wt% (from bottom to top), a broad scattering maximum, at the q_y value of 0.025 nm^{-1}, reveals a broadly distributed perpendicular PSd domains (250 nm) slightly expands within 8 nm. The small increase is ascribed to selectively incorporated NPs inside their favorable PSd domains and only very few perpendicular PSd domains are embedded in the PBMA

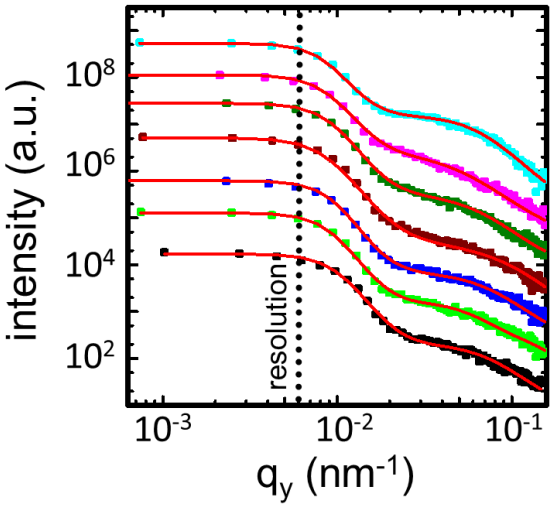

Figure 6.13: At a selected mean wavelength of 0.475 nm, horizontal line cuts at different NP concentrations of 0, 0.1, 0.5, 1, 3, 7, and 15 wt% from bottom to top. The red lines are fits to the data (color solid squares). The dotted line presents the resolution limit.

lamella layers. In addition, with a large amount of NPs loading (15 wt%, top line cut in Figure 6.13), the shoulder-like maximum becomes much more prominent due to the strongly enhanced scattering intensity. The largely improved contrast originates from the embedded maghemite NPs.

6.5 Inner structural evolution

To conclude the inner structural evolution of the hybrid films with the incorporation of different volume NPs, partial cross-sectional sketches are shown in Figure 6.14. In Figure 6.14a, the pure DBC film provides a template with a morphology of highly periodic, well parallel oriented alternating PSd and PBMA lamella with very few perpendicular PSd domains, which originates from a self-assembly microphase separation process. On the basis of surface boundary conditions, for the DBCs with symmetric composition, in case the film thickness is much larger than the periodic inter domain distance of DBC, parallel lamella are favored. [113] The structural information obtained from both real space techniques (AFM and SEM) and reciprocal technique (TOF-GISANS) suggests a parallel lamella morphology with the PSd layer located at the film/air and film/substrate interfaces. In addition, very few perpendicular PSd domains inserted into the PBMA domains are present. At intermediate NP concentrations, NPs are selectively incorporated and well dispersed in their favored PSd domains, therefore, the array of NPs aligned in the middle of the PSd domains are established (Figure 6.14b). At high NP concentrations, non-linear expansion behaviors of the periodic inter-domain distance and the film thickness arise from the fluctuating parallel PSd lamella layers, which is attributed to large NP aggregates (Figure 6.14c). In addition, the interface roughness also increases prominently

as the NP concentration increases. Based on the results, this structural evolution can be mainly ascribed to the free energy minimization of the system. [113]

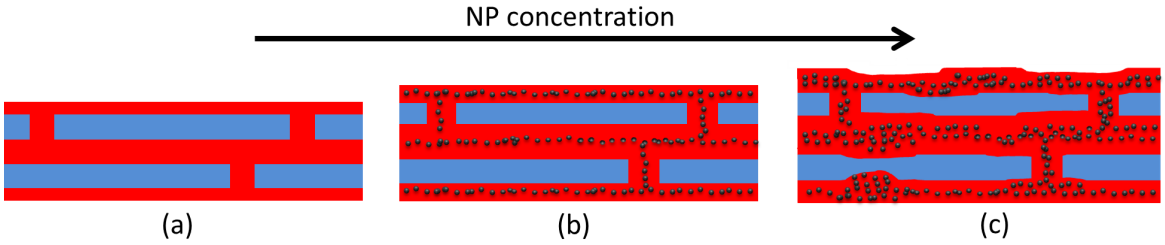

Figure 6.14: Sketch of the inner structures of (a) pure DBC film, hybrid films with (b) intermediate and (c) high NP concentrations. The PBMA domain, the PSd domain, and NPs are marked in blue, red, and black, respectively.

6.6 Magnetic behavior

Magnetic behavior of the investigated hybrid films has been probed with a Quantum Design MPMS, SQUID magnetometry with the external magnetic fields in the range of -500 to 500 mT.

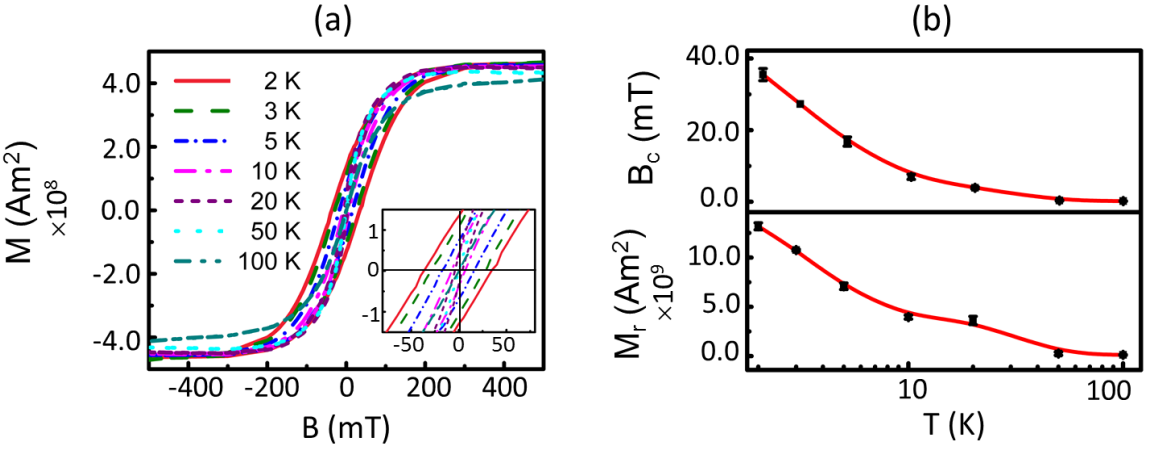

Figure 6.15: (a) Magnetization moments (M) vs. magnetic fields (B) measured at different temperatures for a selected hybrid film with NP concentration of 15 wt%. The bottom right inset of (a) is the partially magnified magnetization moments around zero fields. (b) Coercivity, B_c, and remanence, M_r, extracted from (a) vs. temperature (the red lines are guides to the eye).

Magnetization moments for all probed hybrid films at different temperatures have been measured. One data series of exemplary temperature-dependent hysteresis loops for a selected hybrid film with 15 wt% NP concentration are plotted in Figure 6.15. In general, the superimposed hysteresis loops become narrower as the temperature increases, and even close at a relatively high temperature of 100 K. Such typical superparamagnetic behavior is observed in the hybrid system of Chapter 5 as well. The exception of the hysteresis loop measured at 100 K is ascribed to a large thermal fluctuation, which results in a non-alignment of the NPs on the basis of Curie's law (in Section 2.2.3). [216] Excluding the 100 K, the saturation magnetization (M_s) obtained at different temperatures reach the same value. It differs from the observation in Chapter 5, consisting of the identical components of DBC and NPs but with a different film thickness and a different morphology of perforated perpendicular lamella structures, which presents a temperature dependent maximum magnetization. [110] Hence, the difference of the morphological orientation (parallel or perpendicular) may induce the different magnetic behavior of the hybrid films. To further quantify the essential magnetic features, the remanence (M_r) and coercivity (B_c) have been extracted from Figure 6.15a correspondingly and are presented in Figure 6.15b. Both the B_c and M_r present a similarly mild decay as the temperature increases. It can be well explained with the Néel-Brown theory (in Section 2.2.4, Equation 2.28) which introduces the characteristic blocking temperature of the superparamagnetic NPs in the measurement limits. [133, 222]

To probe the effect of NP concentration on the magnetic properties, hybrid films with varied NP concentrations are examined. The obtained hysteresis loops measured at 2 K are present in Figure 6.16a. The M_r and M_s, extracted from the corresponding magnetic moments, and the calculated M_r/M_s are plotted as a function of NP concentration at 2 and 20 K (Figure 6.16b). As the NP concentration increases, both the M_r and M_s increase with a similar linear slope. Therefore, M_r/M_s is independent of NP concentration. However, for the hybrid films investigated in Chapter 5, which exhibit a morphology of perforated perpendicular lamella, M_r and M_s show a significant increase at high NP concentration. [110] To further determine the difference of the magnetic property exhibited in these two different hybrid film systems, the volume effect of the NPs must be excluded. Therefore, the initial extracted M_s and M_r are normalized by the volume of the contained NPs in these two hybrid films. The result reveals that, the M_s and M_r in the present films are roughly 1.7 and 2.1 times as big as those of the thin hybrid films reported in Chapter 5, respectively. The difference is only ascribed to the better regular oriented, more uniformly arranged NPs in the present investigation. Furthermore, no magnetic shape anisotropy is present from the measurements with two orthogonal orientated external field applied within the film plane, which could be important for potential applications.

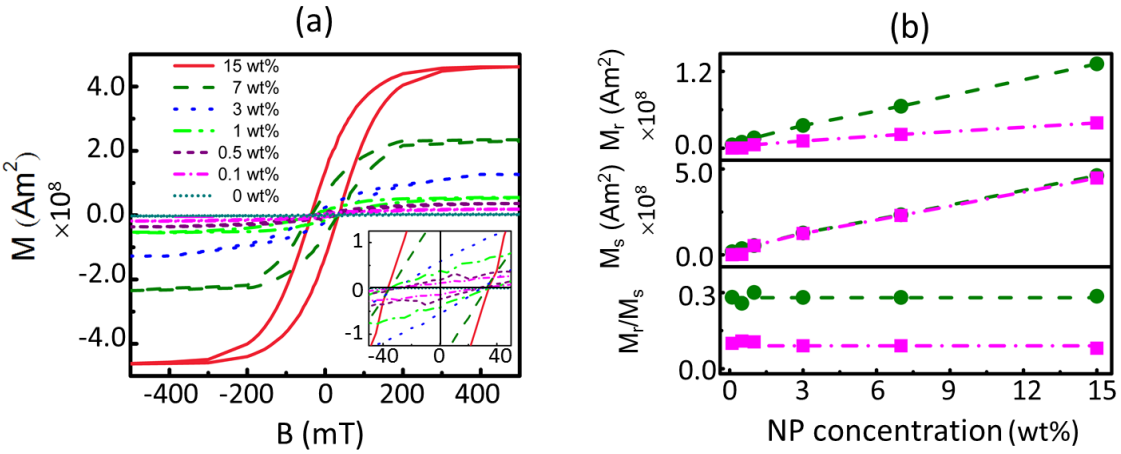

Figure 6.16: (a) Measured magnetization (M) as function of external applied magnetic field (B) for hybrid films with varied NP concentrations measured at 2 K. The partial magnified hysteresis loops around the zero fields is shown in the bottom right inset of (a). (b) Remanence, M_r, and saturation magnetization, M_s, extracted from the corresponding hysteresis loops and calculated relative remanence, M_r/M_s, as function of NP concentration are shown at temperature of 2 K (green) and 20 K (pink), respectively. The dashed lines are guides to the eye.

6.7 Summary

The effect of the NP concentration on the film morphologies and their corresponding magnetic properties of the maghemite NPs/PSd-*b*-PBMA DBC hybrid films have been fully characterized with profilometry, AFM, SEM, TOF-GISANS and SQUID. A morphology of highly periodic, well parallel orientated lamella with very few perpendicular defects is found. At low NP concentrations, NPs are well distributed inside the PSd domains via a simple wet-chemical method. The selectively embedded NPs result in an approximately linear expansion of the inter-domain distance, which further induces the similar increasing behavior of the film thickness. Nevertheless, at high NP concentrations, excessive NPs form multiple parallel layers with very few perpendicular defects, which leads to an overall non-linear expansion of the inter-domain distance. Further, the previous long-range ordered morphology has been perturbed with formed large NP aggregates, which appear with high NP loading. Moreover, they also induce a significant increase of the roughness by introducing interfaces. In the present investigation, the hybrid films with multiple parallel layers of ordered magnetic NP arrays are established via an economic, simple and highly reproducible film preparation method. The functional magnetic NP arrays endue the hybrid films with superparamagnetic features, which are promising for a large number of applications in the fields of medical instruments and magnetic sensors.

Chapter 7

Magnetic field guided structures of maghemite NPs in PS-*b*-PMMA

Parts of this chapter have been published in the article "Nano- and microstructures of magnetic field-guided maghemite nanoparticles in diblock copolymer films", *ACS Appl. Mater. Interfaces*, **2014**, *6*, 5244-5254.

In previous investigations, several hybrid nanocomposite systems based on different types of PS-coated iron oxide NPs and DBCs already have been studied. [90, 110, 215, 223, 224] The main target of the present work is to fabricate superparamagnetic films with shape anisotropy from a low temperature, wet-chemical deposition method, which is realized by hybrid films of metal-oxide nanowires and a DBC with dispersed NPs. A simple process has been applied to establish the sub-μm-sized metal-oxide wires and to fine-tune the possible parameters controlling the length and width of the wires in/on the DBC matrix. Commonly, the conditions of high voltage, [32] high energy costs, [33] and high temperature [34] are required for the fabrication of the relevant magnetic nano- or micromagnetic wires. A novel method has been studied to manufacture arrays of magnetic metal-oxide wires at room temperature and atmospheric pressure in fairly low energy cost, with the help of the DBC matrix and external applied magnetic field, which was used for controlling the aggregation of magnetic NPs into a defined dimension.

Recently, most of studies are regarding the self-assembly of NPs embedded inside a BC template, which are strongly limited to the systems of the employed BCs. [223,224] In the present work, the structure guided template provided by the DBC is combined with the application of external magnetic fields. Both the DBC and the external fields function as the guide of the NPs to form novel structures. In literature, one-dimensional superparamagnetic NP-chains have been reported. [225–228] Keng et al. reported 260 nm Pt-Co_3O_4 heterostructures nanowires with polymer-coated ferromagnetic cobalt NPs. [229] Benkoski et al. investigated on chain-like NP assemblies of a mixture of 250 nm super-

paramagnetic magnetite colloids and 24 nm ferromagnetic cobalt NPs. [230] However, the reports regarding the novel properties arisen from the magnetic field guided magnetic particles material in case the particles sizes are above μm scale. [231, 232] It is well known that, when the magnetic NPs size is below a single critical magnetic domain size, the NPs have no response to an external magnetic field. Hence, the application of fairly small NPs is highly challenged. To solve it, NPs coated with polystyrene (PS) chains are selected. On one hand, the coated PS chains help the NPs selectively incorporate into one domain of the microphase separation structure of the DBC matrix and inhibit the formation of macroscopic NP aggregates; On the other hand, with the increase of the NP concentration, the possibility of the NPs to form aggregates increases and thus, NP aggregates above the critical domain size are formed. Afterwards, under-controlled small NP aggregates respond to the external magnetic field and build stripe-like metal oxide wires following the external magnetic lines spontaneously.

In the present chapter, the hybrid films consisting of DBC polystyrene-*b*-polymethyl methacrylate (PS-*b*-PMMA, f_{PS} of 0.15) and PS-coated Maghemite NPs (γ-Fe_2O_3) are fabricated with solution casting method in combination with the application of varied external magnetic fields. The used sample size is 2.5 $\times$ 2.5 cm^2. Based on the volume fraction of the employed DBC (f_{PS} of 0.15), a sphere morphology in bulk is likely to form (seen from the theoretic phase diagram in previous Section 2.1.2). The DBC concentration of the NP-DBC solutions is fixed at 10 mg/mL. The weight ratio of the NPs with respect to the DBC is varied: 50, 25, 15, 8, 3, 1, 0.5, 0.1, 0.05, 0.01 and 0 wt%.

The chemical identity and the size of the present investigated NPs are examined with Mössbauer, XRD and SAXS measurements. SAXS is as well employed to characterize the morphology of the bulk DBC. Surface structures of the hybrid films are probed with OM, AFM and SEM. The AFM measurements are carried out with the AFM-2 (described in Section 3.1.3). The SEM measurements are performed with an accelerating voltage of 0.4 kV and a working distance of 1 mm. Inner structure are probed with GISAXS, with the specific sample-detector distances (SDD) of 2.49 m. Each sample are measured in two orientations with the X-ray, which are aligned parallel or perpendicular to the wire shaped NP aggregates visualized on top of the hybrid films. Furthermore, the magnetic measurements with a SQUID magnetometer are carried out in the same two orientations mentioned previously.

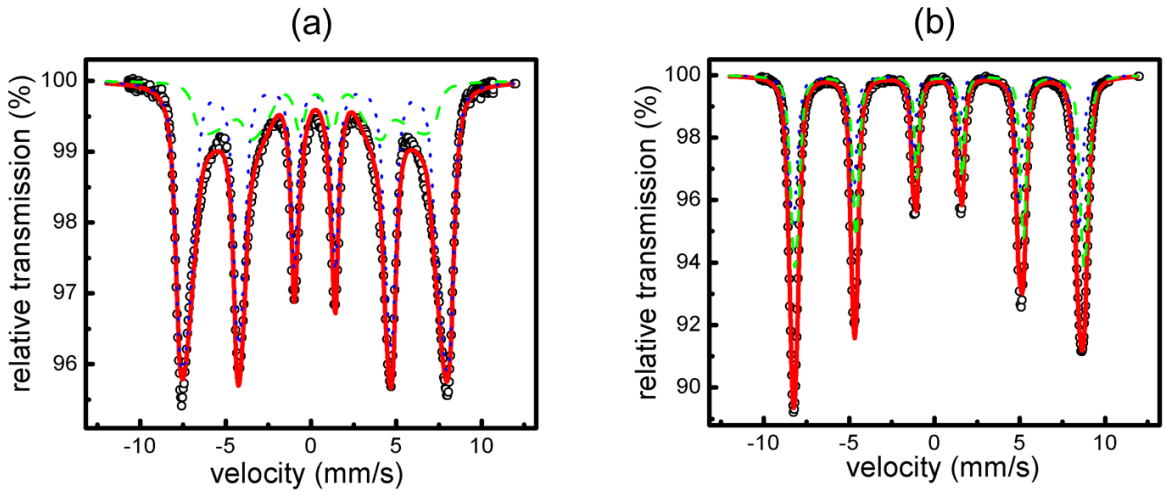

Figure 7.1: Mössbauer spectra of maghemite NPs performed at (a) 295 K and (b) 4.2 K (black circles) together with the fit (green dashed line, blue dotted line, and red solid line). Image modified from reference [108].

7.1 NP characterization

7.1.1 Chemical identity of NPs

A magnetic sextet, which is the standard characterization of maghemite material and is used for a distinct identification of the type of iron oxide, is shown in the probed Mössbauer spectra (Figure 7.1). The data (black circles) at 298 K (room temperature) and 4 K are fitted by the software Mos90 with two Gauss distribution functions and two Lorentzian distributions, respectively. The two fit curves (red solid line) explicate two different Fe^{3+} lattice constructions of octahedral (green dashed line) and tetrahedral (blue dotted line) individually. Because of the relaxation effects arisen from the small NPs, the line is broadening at room temperature (Figure 7.1a). At 4 K, the NPs cannot overcome the energy barrier due to the fairly small thermal movement, hence a narrow line width is shown.

The XRD data of the maghemite NPs with indexed Bragg peaks are shown in the Figure 7.2. The positions of the displayed Bragg peaks are in accordance to the values of the maghemite material provided in literature. [233, 234] The result confirms the observation from Mössbauer measurements.

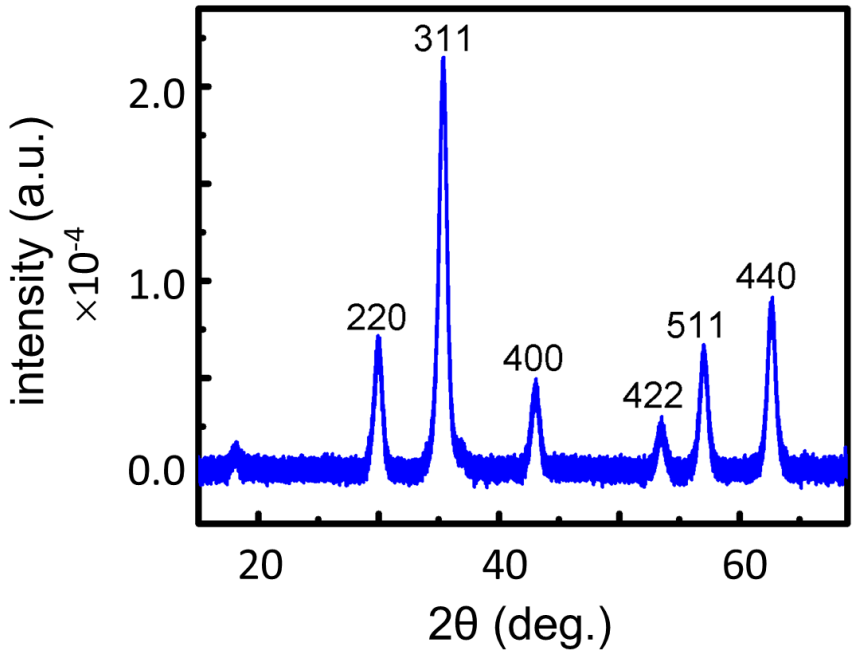

Figure 7.2: XRD data of maghemite NPs with the labeling of the corresponding Bragg peaks. Image taken from reference [108].

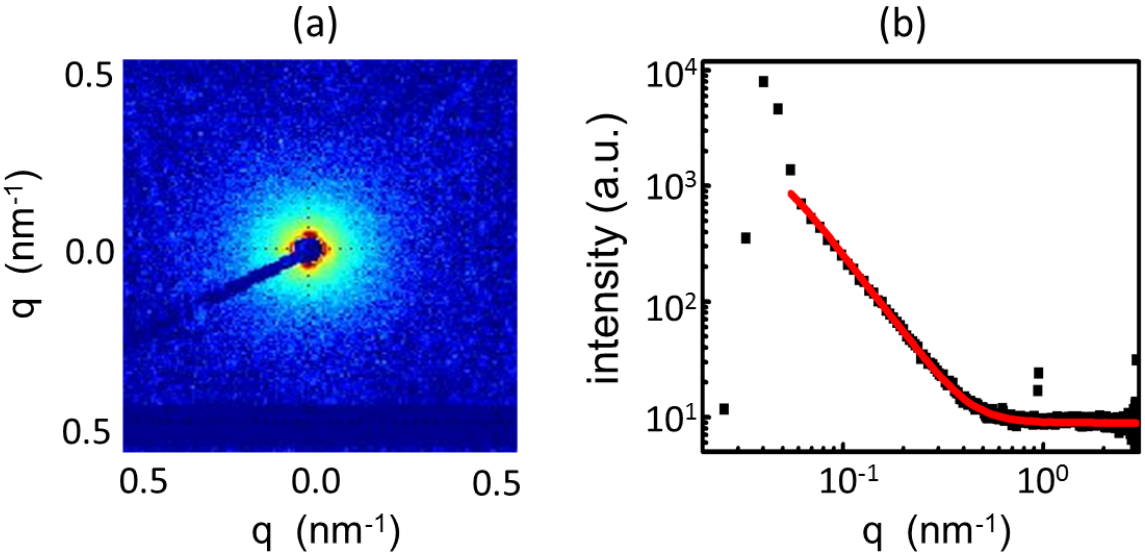

Figure 7.3: (a) 2D SAXS data of maghemite NPs in diluted toluene solvent. (b) Azimuthally averaged 2D SAXS data (black squares) with its fit (red solid line). Image taken from reference [108].

7.1.2 Characterization of the NP Size

An isotropic 2D SAXS data of the NPs in diluted toluene solvent is shown in Figure 7.3a. A round-shaped beamstop is applied to shield the intensive direct beam intensity. For a quantitative analysis, the azimuthally averaged 2D SAXS data is made and is plotted with corresponding fit as function of the scattering vector q in Figure 7.3b. At low q values (first 5 data points) the beamstop shields the detector against the x-ray beam. Assuming the hard sphere particles model, the fit result exhibits that the size of maghemite NPs is 10 ± 1 nm (width 0.2).

7.2 Characterization of bulk DBC

To probe the microphase separation structure of the bulk PS-*b*-PMMA DBC, SAXS measurement is performed. For a quantitative analysis, the azimuthally averaged SAXS data are integrated and plotted together with their fit in Figure 7.4. A prominent first order Bragg peak and weak higher order Bragg peaks are shown, which originate from the micro-phase separation structure. Assuming a body centered cubic (BCC) of spheres model, a periodic characteristic distance, 78 nm, of neighboring spheres is obtained.

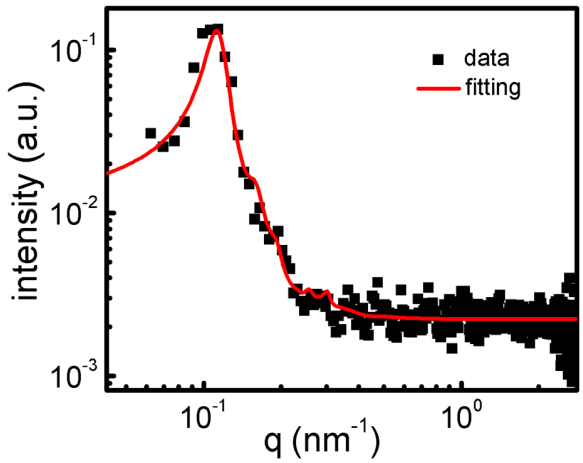

Figure 7.4: Azimuthally averaged 2D SAXS data (black scatters) together with its fit (red solid line) of the bulk PS-*b*-PMMA DBC. Image taken from reference [108].

7.3 Surface characterization

The thickness of the hybrid films is 1.5 μm. OM is employed to probe the micro-structures on the film surface. Firstly, in Figure 7.5, the comparison of the hybrid films fabricated with or without the application of an external magnetic field is observed. In Figure 7.5a, with the presence of the external magnetic field, sub-μm and μm sized wire shaped NP aggregates have been found on the film surface. However, in Figure 7.5b, without the

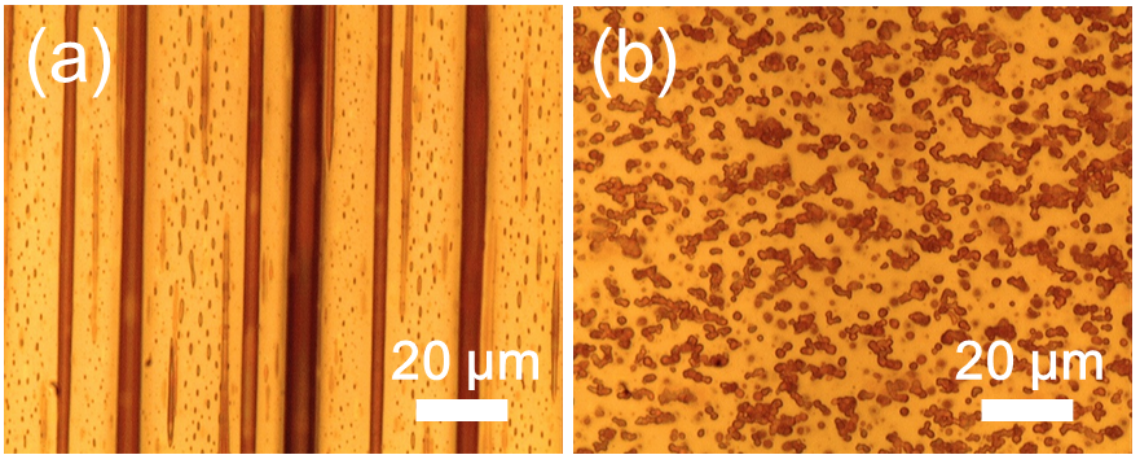

Figure 7.5: OM images of the hybrid films with a NP concentration of 8 wt% at a magnetic field of 149 G (a) and without external magnetic field (b). Image taken from reference [108].

external magnetic field, only a random powder like orientation of the NP aggregates is shown. Therefore, the function of the external magnetic field for the formation of the wire shaped stripes of NPs is confirmed with these observations.

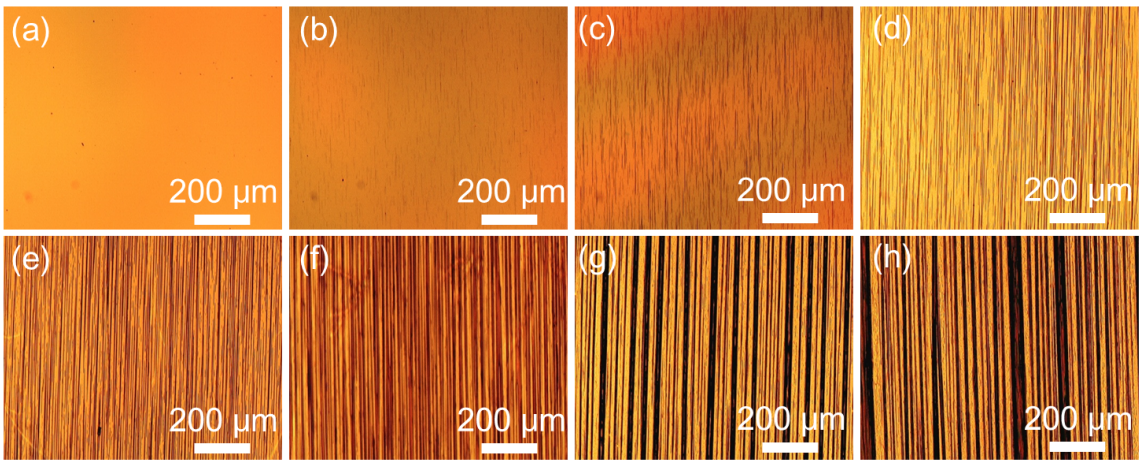

Figure 7.6: Large scale OM images of the hybrid films prepared at an external magnetic field of 149 G with different NP concentrations of (a) 0.01, (b) 0.05, (c) 0.1, (d) 0.5, (e) 1, (f) 3, (g) 8, and (h) 15 wt%.

Large scale surface structures of the hybrid films with varied NP concentrations are present in Figure 7.6. In Figure 7.6a, almost no large scale metal oxide NP wires are found for the hybrid film with an extremely low NP concentration of 0.01%. In Figure 7.6b-f, along the direction of the external magnetic field, well orientated NP wires are observed.

In general, the length, the width, and the distributed density per unit surface area of the NP wires increase significantly as the NP concentration increases. An enhancement of the overall system order is found with higher NP concentrations.

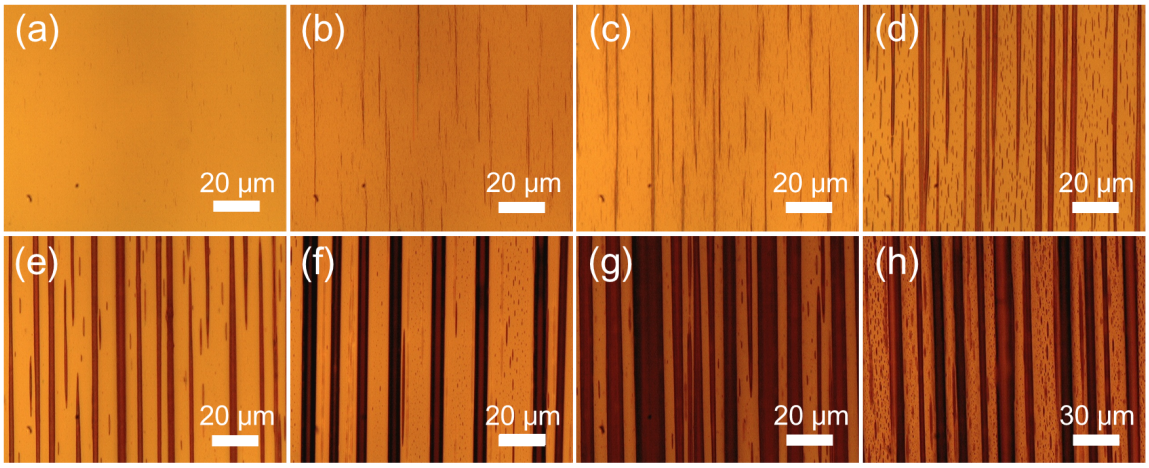

Figure 7.7: OM images of the hybrid films fabricated at an external magnetic field of 149 G with varied NP concentrations: (a) 0.01, (b) 0.05, (c) 0.1, (d) 0.5, (e) 1, (f) 3, (g) 8, and (h) 15 wt%.

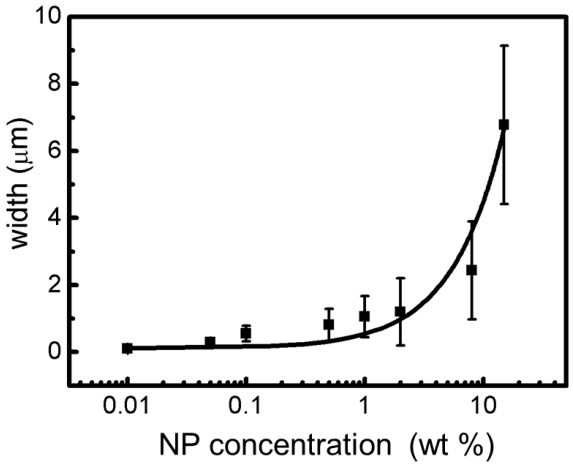

Figure 7.8: Extracted averaged width of the NP-wires from Figure 7.7 as function of the NP concentration (the solid black line serves as a guide to the eye).

To further analyze the width of the NP wires, a full set of OM images of the hybrid films with a much larger magnification are shown in Figure 7.7. The extracted width from the corresponding OM image is monotonically increasing with the NP concentration (Figure 7.8). The distribution of the width also increases accordingly. In case NP concentrations $\ll$ 8 wt%, the width of the NP wires is in the range of 0.1 to 2.5 m with the magnetic field of 149 G. However, when NP concentration is larger than 8 wt%, the width increases much prominently.

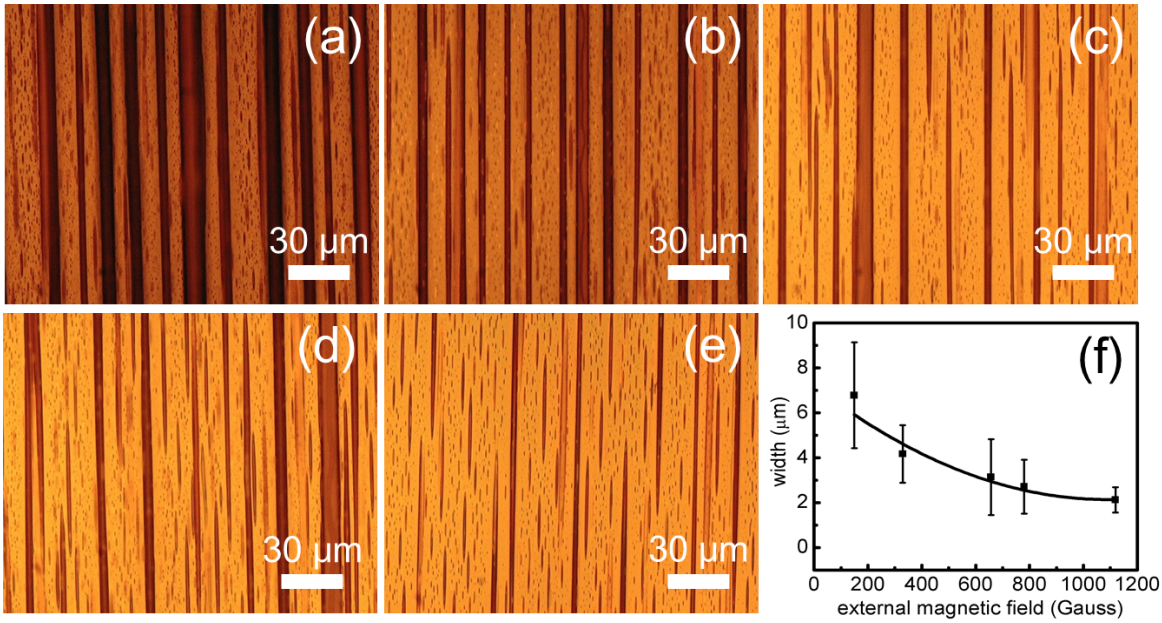

Figure 7.9: OM images of the hybrid films with a NP concentration of 15 wt% at different external magnetic fields: (a) 149, (b) 329, (c) 657, (d) 795 G, and (e) 1119 G. (f) The averaged widths of the NP wires as function of the external magnetic field (the solid line serves as a guide to the eye).

Figure 7.9 shows the effect of the magnetic field on the width of the NP wires. It is observed, as the magnetic field strength increases, the uniformity of the width and the length of the NP wires decays, and the width of the NP wires decreases (Figure 7.9f). This behavior results from the force F, which is applied from the external magnetic field H on the magnetic NPs: $F = mH$. Such applied magnetic forces improve the mobility of the magnetic NPs in the drying solution and lead them to the macroscopic sample edges.

Figure 7.10a, c and e reveal a better homogeneity of the structures formed by the external magnetic field at the film center with varied length scales. In contrast, Figure 7.10b, d and f show that the NP wires located close to the film edges differ from the center of the film because of the edge effects. Such edge effects have to be expected within at least a distance on the order of the capillary length (several mms). Consequently, instead the NPs disperse uniformly inside or on top of the film, large aggregations form at film edges. In general, the observations of OM indicate that well-aligned, highly-oriented metal oxide wires can be fabricated at low magnetic field strengths (such as 149 G) rather than at higher magnetic fields.

AFM with a tapping mode is used for probing the surface morphology of the hybrid film in nm-scale. Particularly, instead of the topography image, the microphase separa-

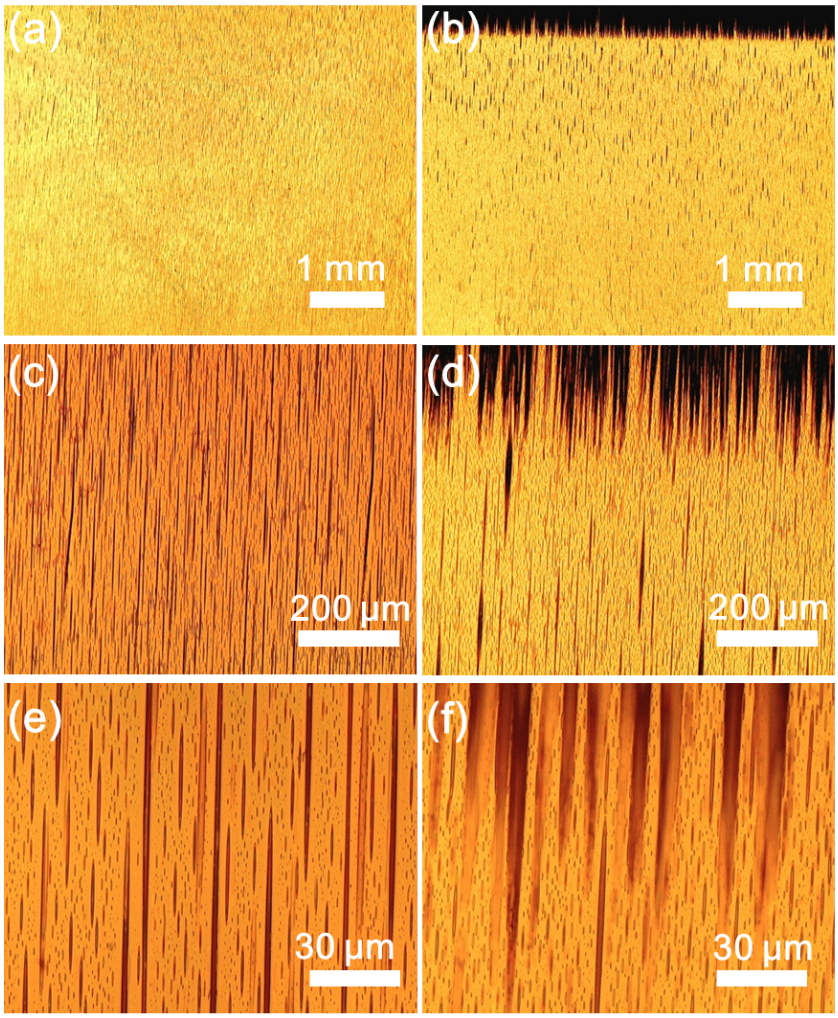

Figure 7.10: OM images at different magnifications for the hybrid films at a magnetic field of 149 G with NP concentration of 15 wt%. (a), (c) and (e) are measured at the sample center; (b), (d) and (f) are measured at the sample edge.

tion nanostructure of the DBC is better shown with the phase image, in case different materials (here: polymer and metal oxide) are involved. Therefore, Figure 7.11 presents phase images of a selected hybrid film with NP concentration of 3 wt% at the magnetic field of 149 G. The large dark areas and bright parts indicate the DBC matrix and the NP wire, respectively. In general, Figure 7.11 shows the well orientated, prominent stripe-like metal oxide wires, small ellipse-like metal aggregates, scattered NPs in PS domains of the DBC, and close packed NPs in NP aggregates. In Figure 7.11a-c, the wire-shaped NP aggregate consisted of individual maghemite NPs are densely packed. Furthermore, the DBC morphology is limitedly modified with the formation of the wire-shaped NP aggregates. Certain smaller NP aggregates formed dots of different sizes are well distributed

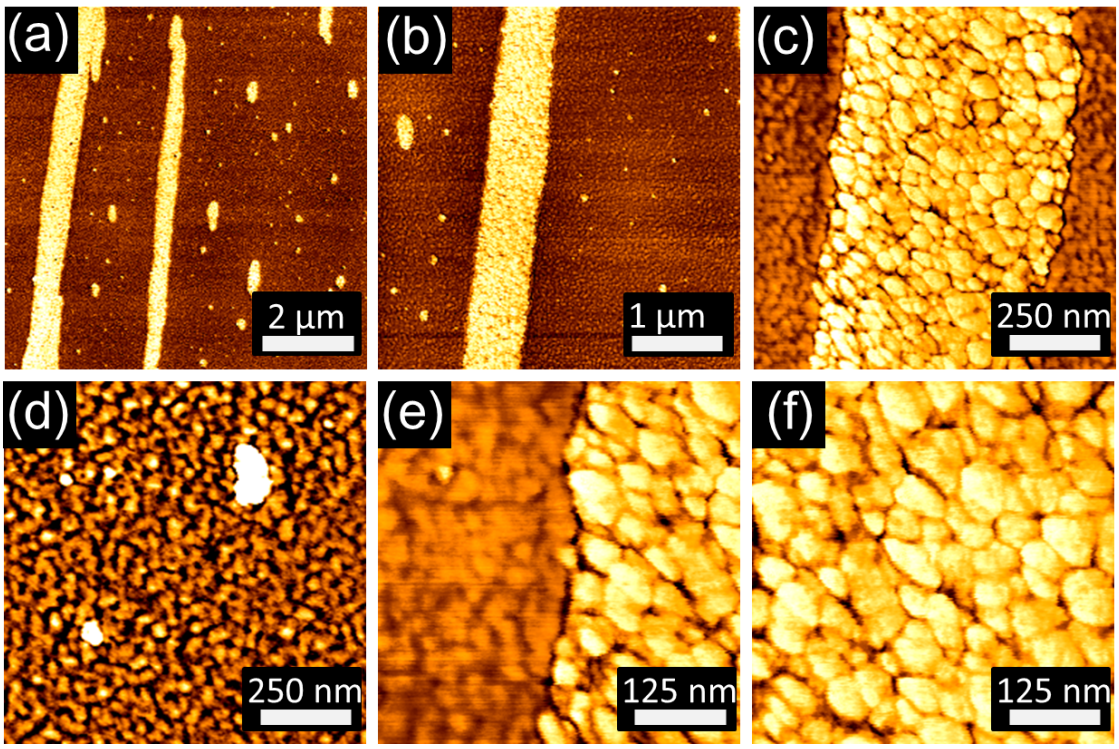

Figure 7.11: For a selected hybrid film with NP concentration of 3 wt% fabricated at an external magnetic field of 149 G, AFM phase images with different emphasis and magnifications: (a), (b) well orientated wire-shaped NP aggregates, (c) wire-shaped NP aggregate consists of differently sized NPs, (d) scattered NPs are selectively embedded in the microphase separated DBC film, (e) interface of the DBC and the NP aggregate, and (f) close packed NPs in the NP aggregate.

in the DBC matrix. Since the NP aggregates are in different sizes, it can be inferred, the NP wire is an aggregate consisted of NP aggregates with different shapes and sizes. The nanostructured DBC film originated from microphase separation is well presented in Figure 7.11d. It also shows that the individual NPs are selectively incorporated within the PS nano-domains. In case large quantities of NPs are embedded inside the PS domains, the domains start to swell, and then ill-defined structures of large NP aggregates are formed. If the aggregates grow above a certain critical size, they will respond to the external magnetic field and lead to the formation of NP wires with high shape anisotropy. The interface of the NP aggregate and the DBC are clearly observed in Figure 7.11e. Near the interface, several incorporated NPs within the PS domains show a tendency of merging into the NP aggregate.

Moreover, the route-mean-square (rms) roughness is as well obtained from the corresponding topography AFM data. For the hybrid film with NP concentration of 3 wt%, the rms roughness is smaller than 5 nm in NP wire free region. As the volume of the incorporated

NP increases, the rms roughness of the hybrid films increases. However, even for the NP concentration up to 15 wt%, the rms roughness still remains small and below 10 nm in NP wire free region. The height of NP wire is around 7 nm as revealed from the AFM topographical images. This indicates that the NP wires are not only supported on the film surface but also partially embedded underneath the film surface.

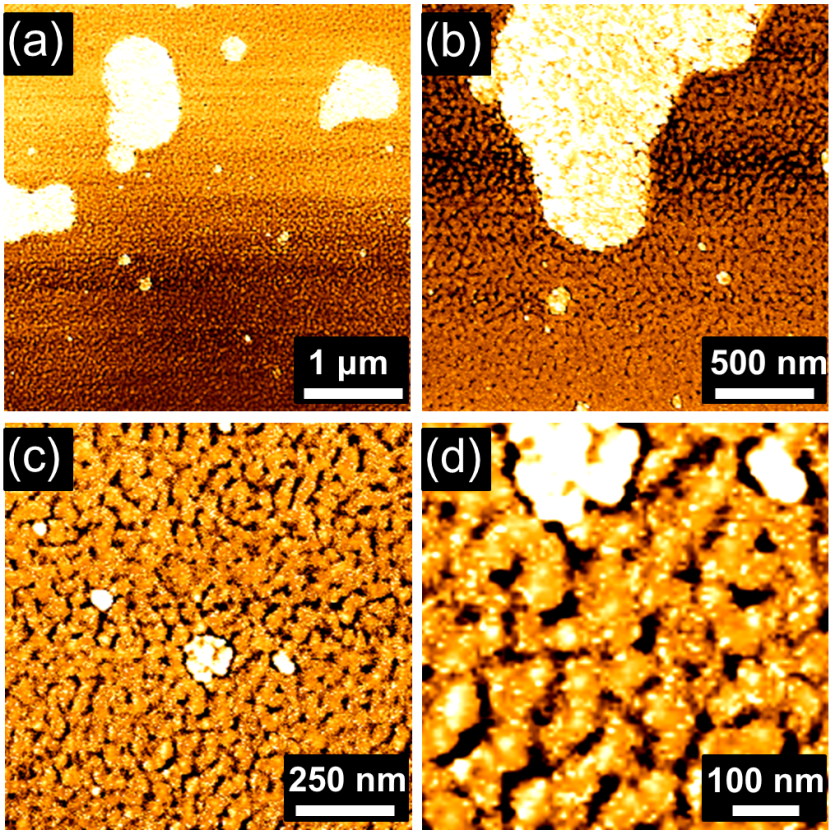

Figure 7.12: AFM phase images with different magnifications for a selected hybrid film with NP concentration of 3 wt% fabricated without external magnetic field.

Figure 7.12 shows AFM phase images of a hybrid film with NP concentration of 3 wt% prepared without external magnetic field applied. In general, no shape anisotropy is observed in Figure 7.12, the function of the external magnetic field is confirmed. In Figure 7.12a and b, irregular shaped NP aggregates with multiple sizes randomly distributed in the hybrid film. In Figure 7.12c, in case the size of the NP aggregates is comparable to the microphase separated structures of the DBC, they follow the morphology of the PS domains and grow to a larger size gradually. In Figure 7.12d, the individual NPs well selectively embedded inside the PS domains are found.

To confirm the AFM observations of the film surface, SEM measurement is performed on a larger investigated area with a different contrast as compared with AFM. In Figure

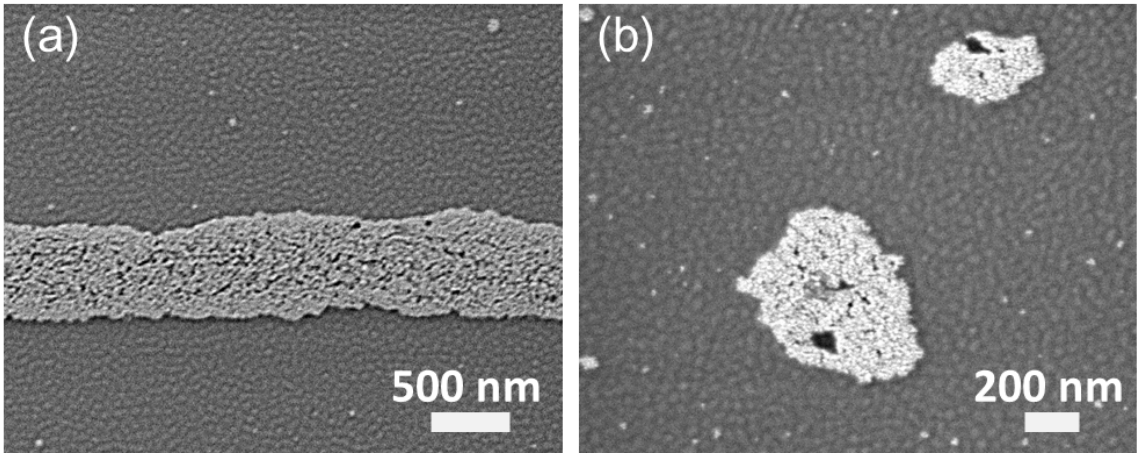

Figure 7.13: SEM images of hybrid films with NP concentration of 0.5 wt% fabricated (a) at a magnetic field of 149 G, and (b) without external magnetic field.

7.13, the brightest objects, the second brighter domains and the dark phases are NPs, spherical PS blocks and the majority block PMMA. In the NP-free DBC region, a highly ordered spherical morphology arisen from microphase separation is found. In case the size of NP aggregates is smaller than the PS domains, they are well embedded inside the PS spheres and surrounded with PMMA via wet-chemical self-assembly process as explained in previous Section 2.2.6. The NP aggregates with different sizes reveal their different growth stages. In Figure 7.13a, very prominent NP wire, consisting of a large number of densely packed NPs, is observed. However, in Figure 7.13b, only a random irregular shaped NP aggregates are shown. In general, the observations from SEM are consistent with the AFM.

7.4 Formation of the NP wires

The critical magnetic domain size is essential for all applied magnetic NPs. The related important theory has been discussed in previous Section 2.2.6. Below this critical magnetic domain size, the formation of a magnetic single domain NP is energetically unfavorable. [134] Above this critical size, the NPs can act as a single magnetic domain. [129] For our employed maghemite material, the critical radius is 30 nm, [130] which is 6 times greater than the size of the current employed NPs. At the temperature (25 °C) of sample preparation process, the energy fluctuation originates from thermal energy (k_BT, in Section 2.2.4) can exceed the effective anisotropy energy barrier ($\triangle E_B = KV$, in Section 2.2.4). Hence, the employed NPs in initial status present superparamagnetic behavior and will not respond to the external magnetic field.

Based on the previous discussed magnetic theories in combination with the observation of the film surface, a three-stage process for the employed maghemite NPs to form large NP wires is assumed:

(1) Initially, the size of NPs is below the critical domain size. The driving force arisen from microphase separation of the DBC is greater than the interaction between NPs, thus NPs are well swollen inside the PS domains.

(2) With the increase of the NP concentration, the possibility of the NPs to form NP aggregates increases. Afterwards, NP aggregates grow up and the size of that exceeds the critical domain size. The ordered DBC domains are gradually disrupted with the large NP aggregates.

(3) The NP aggregates and large-sized NPs from the tail of the NP distribution respond to the external magnetic field and form stripe-like NP wires following the external magnetic lines spontaneously.

In general, the localization of NPs insides the different DBC domains or at the interfaces of the two blocks causes a competition of entropy and enthalpy. Normally, any localization of the NPs harms the ordering of the DBC template, since the incorporated NPs change the interaction parameter of the system and increase the energetically unfavorable entropy penalty. However, installing the NPs with PS coating in the PS domains is enthalpically favorable compared with the contact to the other PMMA domains. Such PS coating optimizes the interaction parameter between NPs and DBC, thus the ordering of the DBC matrix even gets an enhancement. [229] In this case, the favorable enthalpic interaction is the primary guiding force, which leads the localization of PS-coated NPs in the PS domain.
As the NP concentration increases, NPs constantly swell inside the PS domain. Meanwhile, the PS chains continue to stretch for accommodating more NPs. As the NP concentration increases further, the entropy penalty is dominating, thus NPs tend to form aggregates. It results in the highly ordered PS domains to lose its orientation as well to form ill-defined structures. Additional, the super-exchange interaction between maghemite NPs are isolated by the insulating DBC matrix. Such super-exchange interaction can occur via intermediate atoms or ions depending on the structure and the nature of the matrix as well as the bonding at the particle-matrix interface. [235] Because of the composition of these forces, NPs accumulate into aggregates with the sizes greater than the critical magnetic domain size. In other words, the shape anisotropy behavior sets in. The magnitude of the maghemite NP moment is proportional to its volume. [132] Large NP aggregates can be considered as multiple magnetic units and contain a large quantity

of magnetic moments. In case asymmetric NP aggregates form, the hard or easy magnetization axis is created. Magnetic moments have a tendency to align along the longest axis, which defines the direction of shape anisotropy (in previous Section 2.2.5). [236] The shape anisotropy is a dipolar contribution and is calculated by assuming that magnetic poles are distributed uniformly on the surfaces. [132] If NP aggregates are magnetized by an external magnetic field, the dipole-dipole interaction between NPs and the strength of interaction increases with the NP concentration. Normally, magnetized NPs align in head-to-tail patterns. The movement of NP magnetic moment provides a primary driving force to build large NP wires. Within a defined area, as the concentration increases, the mean distances between NPs decrease. Based on Equation: [216]

$$E = \left(\frac{\mu_0}{4\pi r^2}\right)[\vec{m_1} \cdot \vec{m_1} - \frac{3}{r^2}(\vec{m_1} \cdot \vec{r})(\vec{m_2} \cdot \vec{r})] \tag{7.1}$$

where $\vec{r}$ is the distance vector. The dipole-dipole interaction is inversely proportionally to the $\vec{r}$. Thus, as the NP concentration increases, the driving force increases because of a reduced NPs inter-distance. However, besides the driving force, several opposing forces exist. Firstly, friction occurs at the interfaces between NPs and DBC, and it is as well depending on the NP concentration. The competition between dipolar-dipolar attractive force and friction is much more complex. At higher NP concentrations, the NP aggregates grow up to larger sizes. Because the attractive force is proportional to the volume of the NP aggregates, it dominates the system. Based on the volume of the spherical particles $V = \frac{4}{3}\pi R^3$, the attractive force increases with the third power of the aggregate radius. While, the friction is a resistance force against the mobility of the aggregates, and it depends on the surface area of the aggregates ($A = 4\pi R^2$), which increases with the square power of the aggregate radius. Briefly, increasing NP concentration significantly contributes to the size growth of the NP aggregates. Hence, both the dipolar-dipolar attractive force and the friction increase. However, the driving force arisen from the dipolar-dipolar attractive force increases at a much faster rate than the friction resistance. Moreover, the NP wires are highly aligned due to a side-by-side dipolar mutual repulsion as the magnetic moments align in the same orientation.
To conclude, the NP concentration is an essential factor for tuning the size of the NP wires. The arrangement of the maghemite NPs is obtained via a compromise of the driving force of head-to-tail dipolar interaction, resistance of interphase friction, and side-by-side dipolar interaction. The size, the width, and the spacing to the neighbors of the NP wires can be tuned by manipulating the forces.

7.5 Inner structures

In addition to the film surface, the inner nanostructures located beneath the surface are probed with GISAXS in a high statistical relevance. Details of the GISAXS technique are described in previous Section 2.3.4. [161] Due to the shape anisotropy of the investigated hybrid films, all films are examined in two orientations of the NP wires with respect to the x-ray beam: oriented parallel or perpendicular. To focus on the nano-morphology, the resolution limit in the GISAXS measurement is selected in a way that the large NP wires are not resolved. Therefore, the morphological information obtained with GISAXS is only regarding the film structures in nano-scale, e.g., the microphase separation structure of the DBC and the NPs.

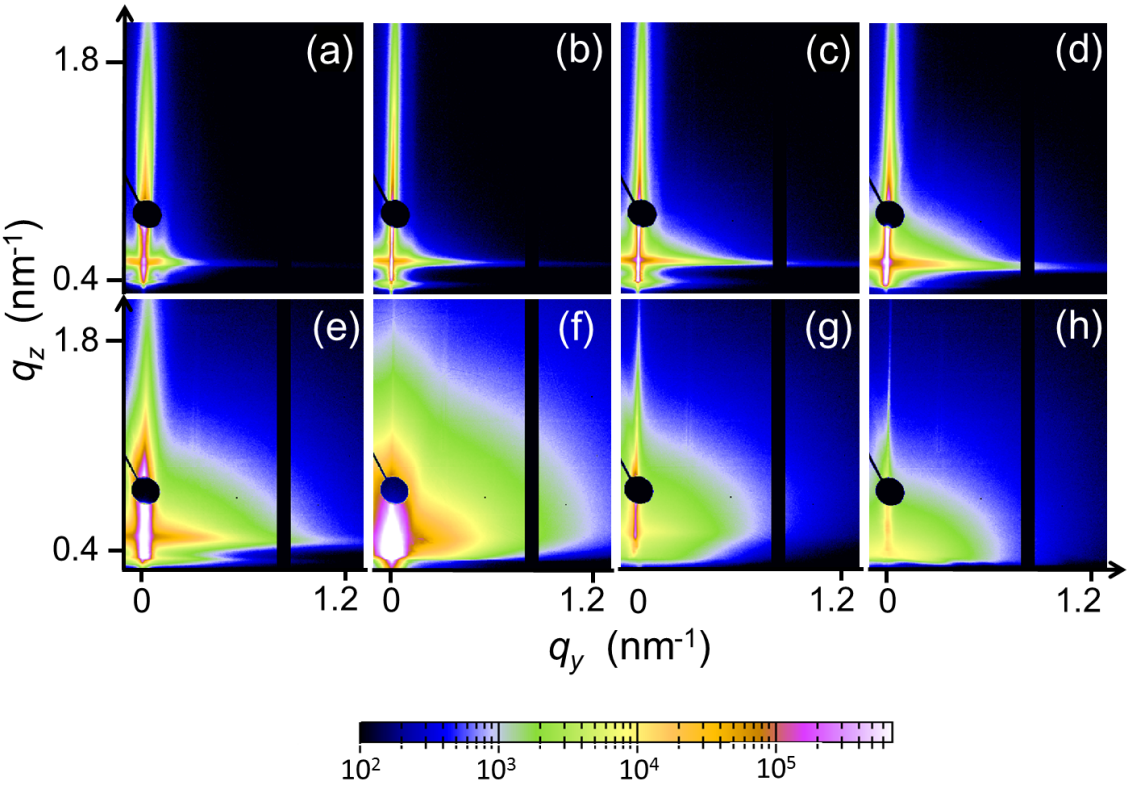

Figure 7.14: With the x-ray beam oriented parallel to the observed NP wires on the film surface, 2D GISAXS pattern of the hybrid films at varied NP concentrations: (a) 0, (b) 0.01, (c) 0.05, (d) 0.1, (e) 0.5, (f) 3, (g) 8, and (h) 15 wt%. All intensities are shown using the same intensity scale bar as indicated.

Figure 7.14 shows the 2D GISAXS pattern of hybrid films at different NP concentrations for the parallel orientation of the x-ray beam with respect to the surface observed NP wires. For all performed GISAXS measurements, the specular intensities are well sep-

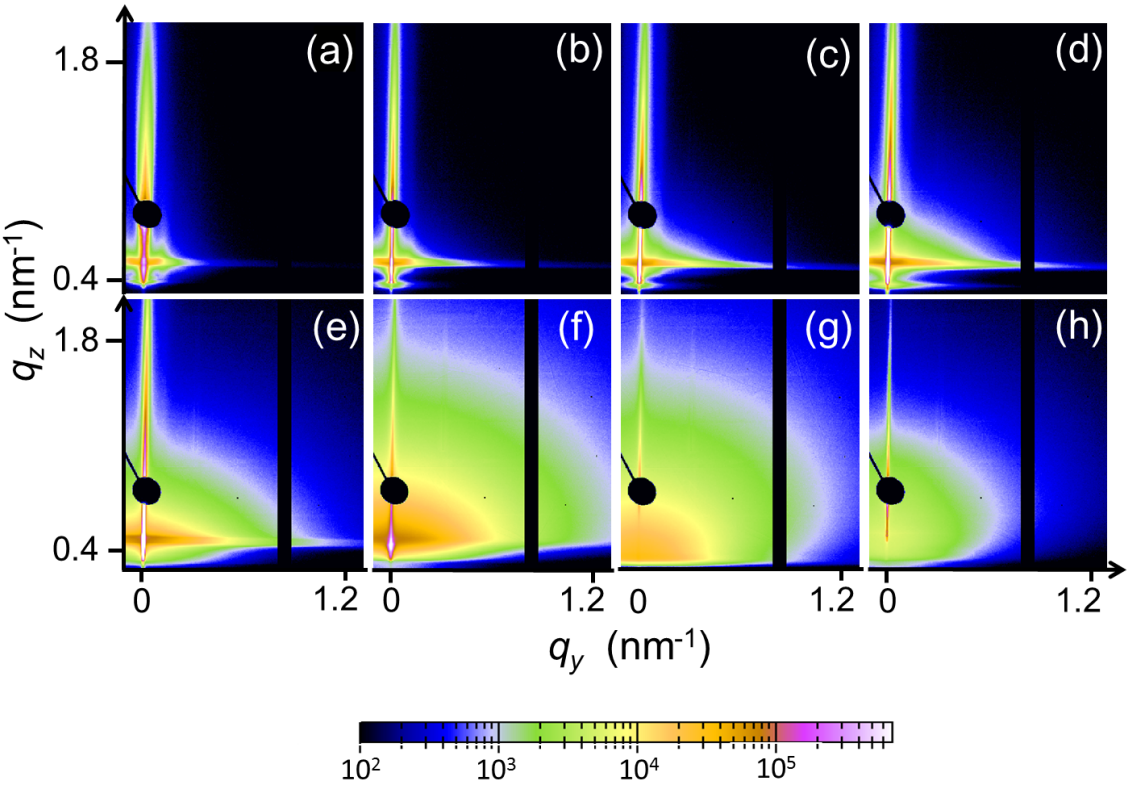

Figure 7.15: With the x-ray beam oriented perpendicular to the observed NP wires on the film surface, 2D GISAXS pattern of the hybrid films at varied NP concentrations: (a) 0, (b) 0.01, (c) 0.05, (d) 0.1, (e) 0.5, (f) 3, (g) 8, and (h) 15 wt%. All intensities are shown using the same intensity scale bar as indicated.

arated from the Yoneda peak (material characteristic position, details in Section 2.3.4) and blocked with a round-shaped beam stop for preventing the detector from the high intensity specular reflection. The structural information perpendicular to the film surface is gained following the vertical direction (along the q_z direction). No intensity modulation is found in the q_z direction, which indicates the absence of the correlated roughness. [237] As the NPs incorporate, the 2D GISAXS patterns change prominently. The observed side maxima of the pure DBC film (0 wt%, Figure 7.14a) correspond to the well ordered spherical domains of the DBC. As the NP concentration increases, the maxima decay. They vanish upon the incorporation of a small NP concentration (0.05 wt%, Figure 7.14c). However, the intensity in the Yoneda region is more prominent due to the electron density contrast between γ-Fe_2O_3 and PS/PMMA. The general frame of the 2D GISAXS patterns remains similar at low NP concentrations (Figure 7.14b-d). For higher NP concentrations, the Yoneda peak broadens and the comprehensive scattered intensity

is improved (Figure 7.14e and f). At NP concentration ≥ 8 wt% (Figure 7.14g and h), the characteristic scattering signal of the DBC is lost, because the surface roughness increases significantly as the NP concentration increasing.

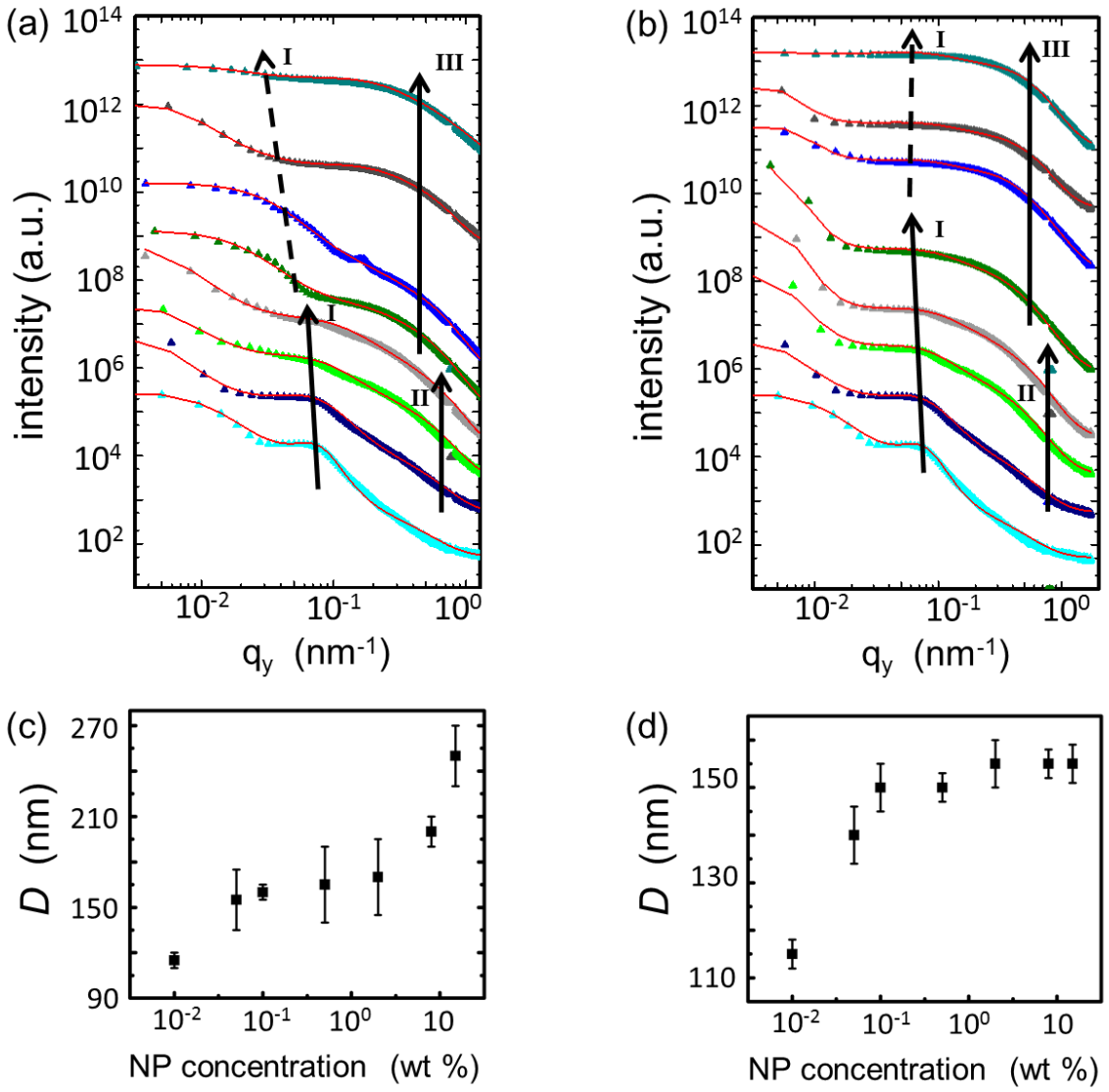

Figure 7.16: Horizontal line cuts (color symbols) made from the 2D GISAXS patterns of the hybrid films at different NP concentrations (0, 0.01, 0.05, 0.1, 0.5, 3, 8, and 15 wt% from bottom to top) in case the x-ray beam is oriented (a) parallel or (b) perpendicular to the surface observed NP wires, which reveals the inner structure perpendicular or parallel to the surface observed NP wires, respectively. For clarity, the cuts are shifted against y axis and shown together with the fits (red solid lines). Inter-domain distance (D) of the (c) perpendicular and (d) parallel structures plotted as function of NP concentration. Image modified from reference [108].

For a quantitative analysis, horizontal line cuts made from the 2D GISAXS pattern

are plotted for the parallel orientation (probing the inner structure perpendicular to the surface observed NP wires) together with fits (in Figure 7.16a). Three main characterizations are found (marked with I and II / III). Peak I locates at small q_y values. It is clearly observed at very low NP concentrations, but it becomes less prominent in case the NP concentrations of the films are greater than 0.1 wt%. The periodic distance between two neighboring DBC domains originated from microphase separation is revealed via the position of the peak I. This structure factor is modeled with a Lorentzian distribution function. The corresponding inter-domain distance, D, obtained from peak I, increases from 92 ± 2 nm to 165 ± 5 nm with the NP concentrations increases from 0 to 0.5 wt% (Figure 7.16c). The increase is arisen from the selective swelling of the PS domains resulted from the incorporation of the NPs. Further, as the NP concentration increases above 0.5 wt%, the intensity of the peak I gets less pronounced, which reveals the formation of an ill-defined structure of the hybrid film. Briefly, due to the overload of the PS domains with NPs, the relatively long range order structure is disturbed. The latter peak progressively shifts to smaller q_y values as the NP content increases (dashed arrow, in Figure 7.16a), which indicates that large NP aggregates form at high NP concentrations. Broad shoulder-like peaks (peak II or III) appear at larger q_y values, which are originated from the form factor. In Figure 7.16a, at the NP concentration below 0.5 wt%, peak II is perfectly modeled with a form factor contribution assuming isolated NPs with the diameter of 10 ± 1 nm. The fit result reveals the NPs are well dispersed in the PS domains at rather low NP concentrations. However, at high NP concentrations, NP incorporation is not selective any more. Hence, isolated NPs are no longer dispersed in the DBC matrix. When the NP concentration is greater than 1 wt%, the scattering pattern is dominated with the form factor of small NP aggregates, which is observed as peak III positioned at q_y values corresponding to 23 ± 1 nm and this position remains the same nevertheless the NP concentration increases (Figure 7.16a). Consequently, these small NP aggregates are found for all DBC films with high NP content.

The 2D GISAXS patterns with the x-ray beam is oriented perpendicular to the surface observed NP wires (probing the inner structure parallel to the metal oxide wires) are represented in Figure 7.15. Compared with the 2D GISAXS patterns obtained in parallel orientation, the scattering characterizations are similar at low NP concentrations (Figure 7.15a-d). While, a significant difference is found at higher NP concentrations (Figure 7.15e-f): the intensity of the Yoneda peak is prominently decayed, which results from the presence of many NP wires on the film surface for films with a high NP content and these surface structures weaken the x-ray beam when penetrating the film.

Corresponding line cuts and their fits are presented in Figure 7.16b. Similarly, several characteristic structural features are found. The position of peak I increases with NP

concentration at small NP content, which presents the same tendency as the parallel orientation (in Figure 7.16a). For high NP concentrations, peak I remains at a constant position (dashed line, in Figure 7.16b). The corresponding inter-domain distance D obtained from the fit reveals an increase from 92 ± 2 nm to 155 ± 10 nm, followed by a tendency without further increase (Figure 7.16d). Additional, the presence of isolated NPs (peak II) and small NP aggregates (peak III) is consistent for both orientations. The comparison of the results from the GISAXS measurement with different orientations indicates: at low NP concentrations, the NPs are well distributed in the PS domains, which results in the increase of the domain distances. Such increasing behaviors are similar for both, parallel and perpendicular orientation. However, at high NP concentrations, the large sized NP aggregates form, which are bigger than the critical size of the single magnetic domain so that they can respond to the external applied magnetic field. Since the NPs are entangled within the PS chains, in case the NPs move, they will drag the PS domains and result in a morphological change. Such behavior strongly disturbs the microphase separation structure and pulls the PS domain structure from a spherical into an elliptical shape, with the long axis oriented parallel to the direction of the magnetic field lines. Briefly, the nano-scale shape anisotropy throughout the entire hybrid films with the influence of the external magnetic field are clearly shown by the GISAXS data. The results reveal that, in addition to the formation of μm-sized NP wires found in OM, the magnetic field has a strong effect on the nanostructure of the hybrid films as well.

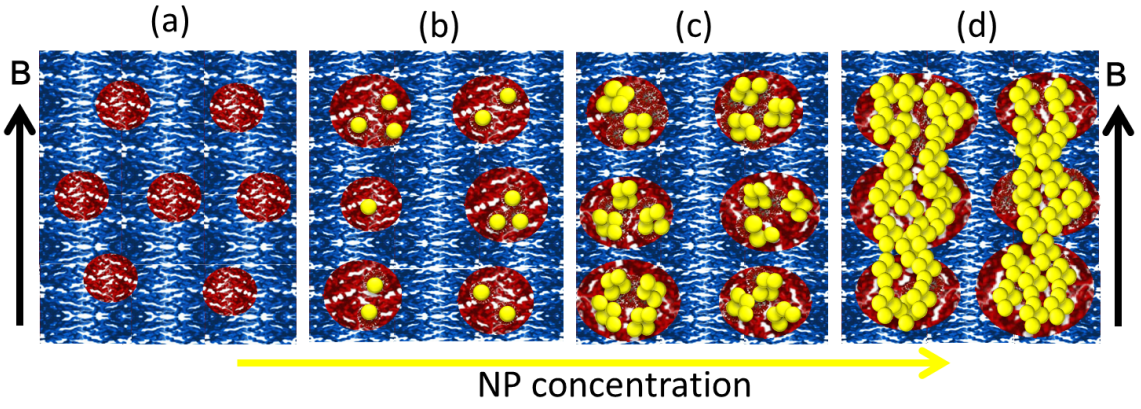

Figure 7.17: Schematic representation of the pure DBC film (a), and the hybrid films at low (b), intermediate (c), and high NP concentrations (d). The PMMA matrix is indicated in blue, the PS block in red, and the maghemite NPs in yellow. The black arrows show the direction of the applied external magnetic field. Image modified from reference [108].

To clearly demonstrate the morphological evolution of the investigated hybrid films in nano-scale, a schematic representation with different NP concentrations are shown in

Figure 7.17. A highly periodic ordered, spherical morphology is presented for the NP-free DBC film. At low NP concentrations, the initial structure remains ordered, and the NPs are well distributed in the PS domains, which results in a swelling of the inter-domain distance; At intermediate NP concentrations, certain small NP aggregates form, which still can be accommodated inside the PS domains; At high NP concentrations, the previous ordered structure is disturbed, and the anisotropic morphology appears. In case NP concentrations are greater than 0.5 wt%, the DBC structure is deformed and large wire-shaped NP aggregates are formed, which is not presented in this schematic representation due to the structures are in μm scale.

7.6 Magnetic properties

Magnetic properties of the probed NPs-DBC hybrid films are examined with a Quantum Design MPMS SQUID magnetometer with the applied magnetic field orientated parallel or perpendicular to the NP wires.

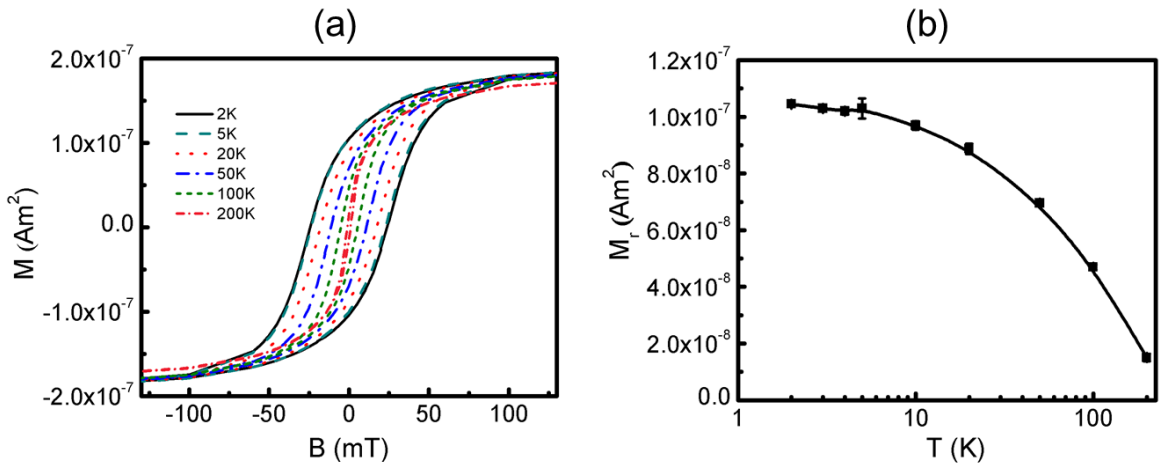

Figure 7.18: (a) Measured magnetic moments vs. external magnetic field with parallel orientation at different temperatures for a selected hybrid film with NP concentration of 0.1 wt%. (b) Extracted remanence vs. measured temperature from (a). Image modified from reference [108]

Figure 7.18a shows the magnetic moment measured at different temperatures with the parallel orientation for the selected hybrid film with a NP concentration of 0.1 wt%. A temperature independent saturation magnetization is found. As the temperature increases, the coercivity becomes much smaller due to the thermal agitation (theory has been discussed in Section 2.2.4). In case temperatures are lower than a characteristic temperature, the magnetic hysteresis occurs. This is the typical super-paramagnetic behav-

ior and the characteristic temperature can be identified with the blocking temperature of super-paramagnetic NPs provided with Néel-Brown expression (in Section 2.2.4, Equation 2.28) [133, 222] Furthermore, the magnetization loops superimpose and present a temperature dependence. In Figure 7.18b, the temperature dependent remanence extracted from the measured magnetic moment curves of the Figure 7.18a is shown. Within experimental errors, the remanence remains constant with small fluctuations at low temperatures, but it decays pronouncedly at higher temperatures.

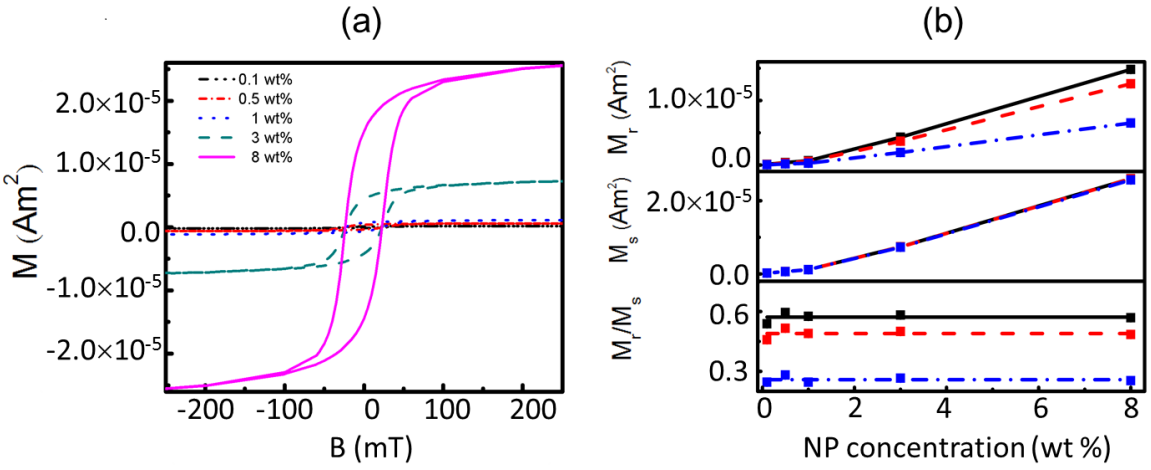

Figure 7.19: (a). Measured magnetic moments vs. external magnetic field at 2K with NP concentrations of 0.1, 0.5, 1, 3, and 8 wt%. (b). Extracted remanence M_r, saturation magnetization M_s and relative remanence M_r/M_s vs. NP concentration at 2 K (black solid line), 20 K (red dashed line), and 100 K (blue dashed-dotted line). Image modified from reference [108].

At 2 K, measured magnetization loops for all investigated NP concentrations vs. the magnetic field applied parallel to the surface observed NP wires is shown in Figure 7.19a. For a further analysis, the remanence M_r, saturation magnetization M_s and relative remanence M_r/M_s are extracted from the corresponding magnetization loops and plotted as function of NP concentration (Figure 7.19b). Within experimental error both, M_r and M_s, increase linearly as NP concentration increases. However, the M_r/M_s stays constant irrespective of the NP concentration. Considering all the observed results, the hybrid film system fulfills the requirements of the super-paramagnetic material, [217] which confirms the NPs have not lost the magnetic characters of nano-size particles. Such behavior can be explained well in the Stoner-Wohlfarth-Néel model. [133, 222]

For the hybrid film with NP concentration of 8 wt%, additional magnetization loops measured at 2 and 20 K with the external magnetic field both, parallel or perpendicular to the surface observed NP wires are shown in Figure 7.20. The observations indicate that

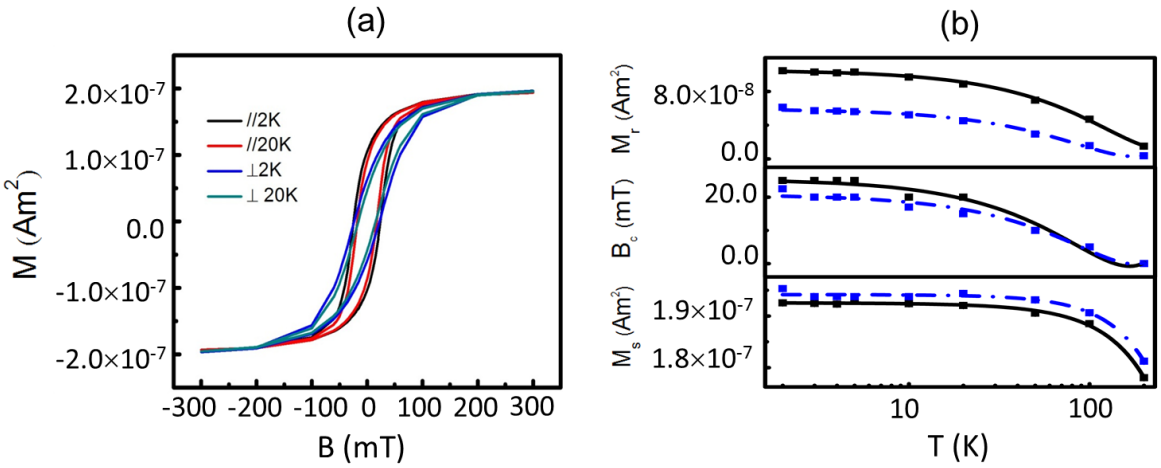

Figure 7.20: For a hybrid film with NP concentration of 8 wt%, (a) magnetic moments measured at 2 and 20 K for the orientation of the surface observed NP wires parallel or perpendicular to the external magnetic field (marked with the legends). (b) Temperature dependent M_r, B_c, and M_s extracted from the corresponding magnetic moments of (a) at 2K with the parallel (black solid line) and perpendicular (blue dash dot line) orientations.

the film is easier to magnetize along the NP wires direction than follow the perpendicular direction. In Figure 7.20b, within experimental error, M_r, B_c, and M_s have strong, weak and no orientation dependence, respectively. The results reveal that the directions parallel and perpendicular to the NP wires are the easy and hard magnetization axis, respectively. The long range magnetic order mainly depends on mutually aligning the dipolar field of the NPs, which results in the magnetization to follow the polar direction along the easy direction, and quantum mechanical super-exchange has been invoked. [238, 239] Comparing with the magnetically isotropic property of the NPs-DBC nanocomposites investigated in our previous investigation, [215] where the NPs are highly dispersed in the DBC film, the current unique magnetic anisotropy is obviously observed for the fabricated films under an external magnetic field due to the formation of magnetic NP wires.

7.7 Summary

In the present chapter, super-paramagnetic hybrid films with shape anisotropy are fabricated from a low-temperature, wet-chemical deposition method. The hybrid films consisted of selective deposited PS-coated maghemite NPs in PS-*b*-PMMA DBC matrix with highly oriented wire shaped NP aggregates are studied with OM, AFM, SEM and GISAXS. The results indicate that, the highly orientated NP wires with different widths,

lengths and neighboring spacing are realized by tuning the NP concentration and the strength of the applied external magnetic field during the film fabrication process. DBC films provide periodic ordered nano-structures with the microphase separation and function as a template material to guide the self-assembly incorporation of the NPs. At low NP concentrations, the NPs with PS-coating are selectively embedded into the PS domains. At high NP concentrations, NP aggregates form, and the sizes of which reach the single magnetic domain critical size. Afterwards, NP aggregates are magnetized and dragged by head-to-tail dipolar-dipolar attractive interaction to align and form long stripe-shaped NP wires following the direction of the external magnetic field. Furthermore, due to the movement of the NPs entangled with the DBC, the morphology of the hybrid film deforms from symmetry to asymmetry. Consequently, the structure of the hybrid films is highly anisotropic, both on the μm and nm scales. The results obtained from both, real space and reciprocal space techniques are consistent. The magnetic properties investigated with SQUID magnetometer indicate that the hybrid film presents the super-paramagnetic behavior and strong shape anisotropy. The possible simple tuning of the maghemite NP wire widths, lengths and spacing by manipulating both, the NPs concentration and the applied external magnetic field, could make this hybrid film system highly desirable for several important applications in high-density magnetic storage devices and magnetic sensors.

Chapter 8

Arrangement of NPs in PS-*b*-PNIPAM DBC film

Parts of this chapter have been published in the article "Arrangement of maghemite nanoparticles via wet chemical self-assembly in PS-*b*-PNIPAM diblock copolymer films", *ACS Appl. Mater. Interfaces*, **2015**, *7*, 13080-13091.

Previous studies are based on the PS-*b*-PMMA and PSd-*b*-PBMA DBCs, which consist of two hydrophobic blocks. In the present study, this approach is extended to a different type of DBC. The asymmetric DBC polystyrene$_{61}$-*block*-polyN-isopropyl acrylamide$_{115}$ (PS-*b*-PNIPAM), consisting of a hydrophobic PS block and a hydrophilic PNIPAM block, is selected. PNIPAM is one of the most investigated thermo-responsive polymer. [240–242] However, almost all the investigations regarding PNIPAM focus on wet swollen films, water induced swelling, thermos-responsive behavior. Only very few investigations relate to dry film regimes. [184,185,243] To our best knowledge, so far no investigation has focused on the arrangement of magnetic NPs inside a PNIPAM host DBC film. The main target of the present investigation is to explore the morphological evolution of NPs-DBC hybrid films, which is fabricated with structure-guided PS-*b*-PNIPAM DBC template upon incorporation of PS-coated NPs with different concentrations. In literature, an unique perpendicularly arranged magnetic nano-dots array is attractive for future storage devices since its potential storage may reach over hundred times more than the routine hard drives. [244–247] As discussed in previous Chapter 7, the employed magnetic NPs must be larger than a critical single domain size to overcome the superparamagnetic limit (fluctuation of magnetization due to thermal agitation, in Section 2.2.4) for the applications of data storage. The nano-dots are considered as a large quantity of small magnets, which have the ability to switch polarity to represent binary digit. [244–247] Hence, the nano-dots-based storage system has the possibility of providing much higher storage density. Generally, switchable high density magnetic storage devices and thermo-responsive

magnetic sensors are potential applications.

All hybrid films were fabricated in identical conditions with spin-coating. No further pre- or post-treatment process was applied. The film size is 2.5 × 2.5 cm^2. Due to the hydrophilic PNIPAM block, a basic bath cleaning was applied for the employed silicon substrates. Based on the theoretical phase diagram (in Section 2.1.2), a cylindrical morphology is expected for bulk PS-*b*-PNIPAM, since the f_{PS} is 0.32. [28] The homogeneity and uniformity of the films are crucial for applications. They are strongly influenced by the solution viscosity, which mainly depends on the DBC concentration. Normally, high viscosity results in high friction, which leads to the inhomogeneity of the hybrid films because the mobility of NPs is restricted. According to the preliminary experiments, a DBC concentration of 45 mg/mL was selected, since it makes macroscopically homogeneous hybrid films. The employed PS coated γ-Fe_2O_3 NPs are identical to the NPs used in the previous Chapter 5.The weight ratios of γ-Fe_2O_3 NPs with respect to the DBC PS-*b*-PNIPAM are: 0, 0.1, 0.5, 1, 3, 7, and 15 wt%.

Film thicknesses are measured with a surface profilometry. The systematic morphological evolution of the film surface is probed with SEM at an accelerating voltage of 2 kV and a working distance of 1.2 mm. The film topography such as rms roughness is examined with AFM-1 (described in Chapter 3.1.3). Inner film structures are investigated with GISAXS. The applied synchrotron radiation wavelength (λ) and photon energy are 0.0957 nm and 13 keV, respectively. The sample-detector distance is 2.55 m. At last, the application relevant magnetic properties are performed with a MPMS SQUID as function of NP concentration and temperature.

8.1 The determination of hybrid film thickness

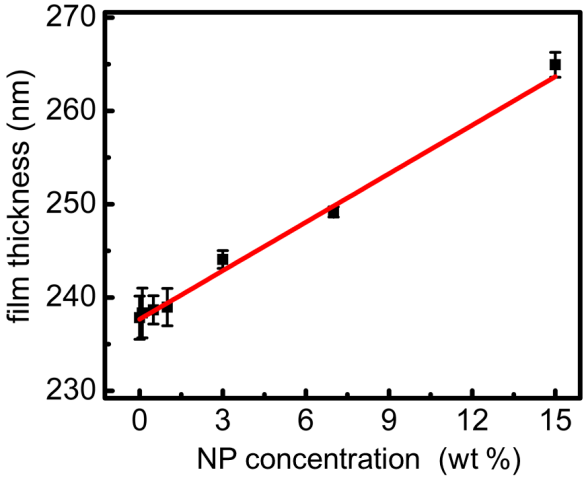

Figure 8.1: Thicknesses of the hybrid films probed as function of NP concentrations (the red solid line is a linear fit). Image taken from reference [109].

In Figure 8.1, as the NP concentration increases from 0 to 15 wt%, the film thickness linearly increases from 238.0 ± 2.0 nm to 264.9 ± 1.3 nm accordingly. Because all the hybrid films were fabricated under the identical circumstances, the influence of the incorporated NPs on the viscosity of the solutions is fairly weak. Therefore, the effect of the viscosity on the film thickness can be excluded. Furthermore, the temperature and relative humidity were well controlled as a constant during the thickness examinations. Hence, the volume of the incorporated NPs is the only reason for the film thickness expansion. Since the films are confined between two different interfaces, different orientations of the microphase separation structure may arise from the change in film thickness based on the film thickness regime discussed in Section 2.1.3. [123, 198, 248, 249]

8.2 Surface characterization

The morphological transition of the full set of the film surface is thoroughly probed with SEM. The grey-scale SEM images are presented in Figure 8.2. The dark areas, bright areas, and the brightest randomly dispersed objects corresponds to the PNIPAM domains, PS domains, and NP aggregates, respectively. On the basis of the self-consistent field theory (in Section 2.1.2), [28] a cylindrical morphology is expected for the employed PS-*b*-PNIPAM with a f_{PS} of 0.34. In Figure 8.2a, labyrinth-like, parallel cylinders (with respect to the film surface) with only small dispersed areas having perpendicular cylinders are found for the NP-free DBC film. In case film thicknesses are larger than the characteristic periodic distance of DBC, the parallel-oriented structures are favored (in Section 2.1.3). [172, 202] In Figure 8.2b, upon incorporation of an extremely low amount of NPs into the DBC matrix, a long-range, lateral ordered of perpendicularly oriented cylinders are shown. To our best knowledge, such perfect perpendicular orientation is mostly found in case sophisticated, special treated substrates are applied, or thin films are confined with the thickness smaller than the DBC periodic distance. [196, 197]
The morphological transition from a parallel to a perpendicular orientation is mainly ascribed to the tuned interfacial energy via incorporated NPs, which originates from a competition between the entropic and enthalpic terms in the hybrid film system with the purpose of minimizing the free energy density. [196] The surface modification of the maghemite NPs with the PS coating energetically promotes the selective deposition of the NPs into the PS domains, [108, 139, 201] since the PS coating is chemically identical to the PS block. Thus, the NPs disfavor entering the chemically incompatible PNIPAM domains, or disperse randomly in the DBC matrix. [205] As a consequence, both the order and the homogeneity of the hybrid film orientation are improved significantly. Certain analogous investigations that presented an enhancement of the long-range order and a

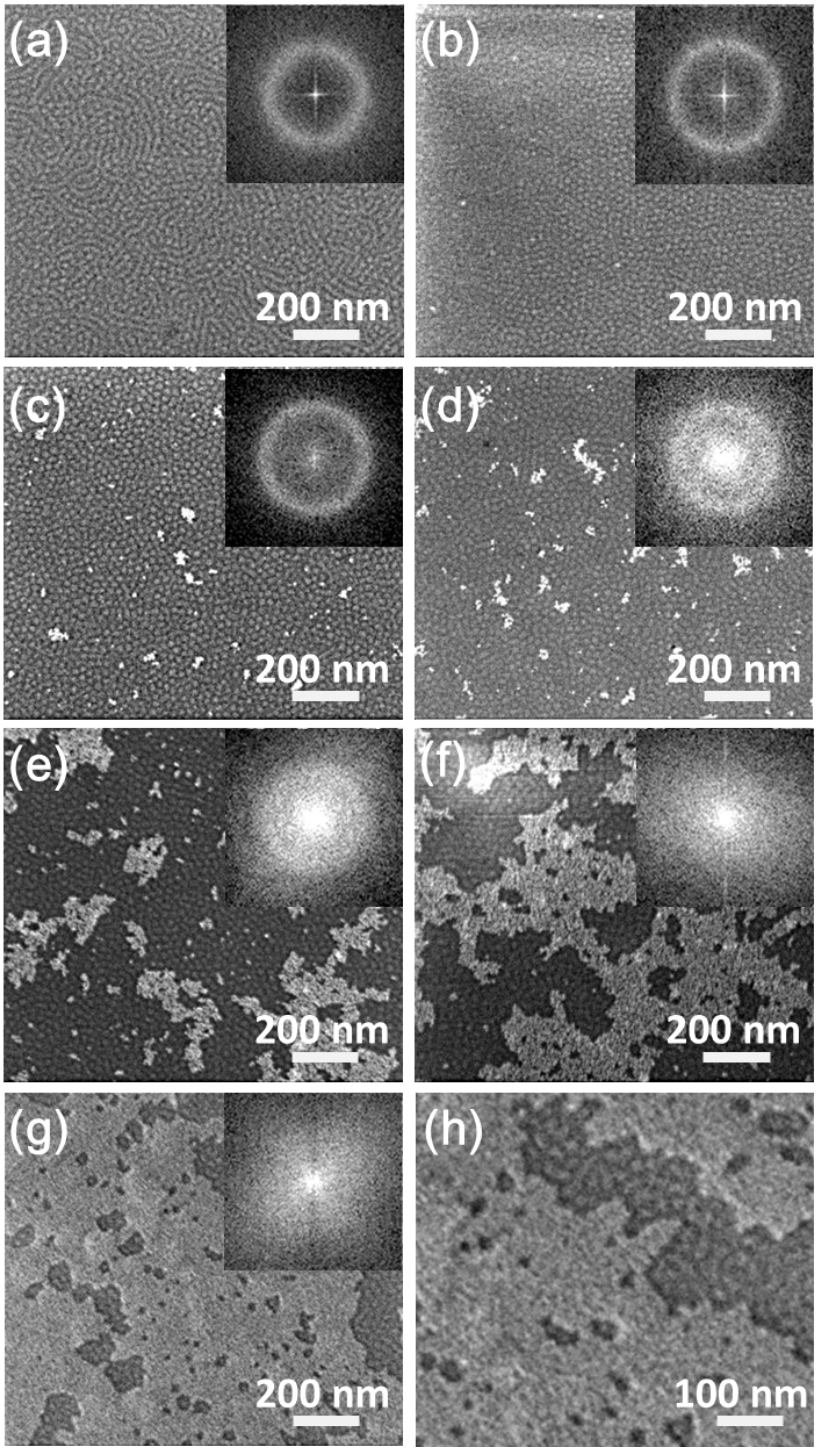

Figure 8.2: SEM images of the hybrid films at different NP concentrations: (a) 0, (b) 0.1, (c) 0.5, (d) 1, (e) 3, (f) 7, (g) and (h) 15 wt%. To clearly present the nanostructure transition in large NP-aggregates free region, the image in (g) is magnified for 2 times with a half scan size in (h). The corresponding FFT patterns are presented in the insets.

switch of the domain orientations with the incorporation of NPs in DBC films have been reported previously. [41, 110, 202]
In Figure 8.2c, at higher NPs concentration of 0.5 wt%, the degree of structure orientation is further enhanced. The contrast of the SEM image is enhanced by a higher amount of NPs incorporation as well. Consequently, the selectivity of the NPs incorporated into specific DBC domains is a crucial factor of the fabrication of highly ordered, well perpendicular-oriented cylindrical morphology.
In the case of NP concentration > 0.5 wt%, the long range ordered morphology is perturbed. In Figure 8.2d-g, as the NP concentration increases further, the NP aggregates start to form and the size of them increases accordingly. Due to the increase of the entropy cost, the accommodation of the PS domains with NPs is limited. In case this limit is overstepped, the excess NPs will be squeezed out of the PS domains and accumulate at the film top surface. The entropic penalty dominates the hybrid film system at high NP concentrations. The behavior of the NPs aggregation is in agreement with Monte Carlo simulations at high NP concentrations within a host DBC matrix. [22, 206] Further, more NPs gradually accumulate surrounding the initial small NP aggregates, which force the NP-aggregates to develop in a larger size. In the case of the NP concentration ≥ 7 wt%, the aggregates form network structures with a percolation path and cover large areas of the film surface. A tendency of a morphological transition from perpendicular back to parallel orientation is observed at the NPs-aggregates free areas with NP concentrations of 3 and 7wt% i(in Figure 8.2e-f). The transition appears even more significantly at the highest NP concentration of 15 wt% (Figure 8.2g). To clearly present the nanostructure transition in a larger NP-aggregates free region, Figure 8.2g is further magnified for 2 times with a half scan size and shown in Figure 8.2h. Although the excessive NPs come to the film surface, part of them still contribute to a further swelling of the PS domains, which expands the PS domains anisotropically and results in a change of the morphology. The insets in Figure 8.2 are the 2D fast Fourier transformation (FFT) patterns of the corresponding SEM images, which are made for a quantitative analysis of the surface order. The observed rings from the FFT reveal that the probed structures are isotropically distributed with a fixed center-to-center distance. As the NP concentration increases (≤ 0.5 wt%, Figure 8.2a-c), the isotropic rings become narrower and more prominent. However, in case NP concentration ≥ 1 wt%, the rings broaden again until fade away because of a large quantity of randomly dispersed NP-aggregate networks.

Figure 8.3 shows the power spectral density (PSD) functions obtained from azimuthal integration of the corresponding 2D FFT patterns. An interesting prominent change of the q value marked with peak I reveals the periodic inter-domain distance on the DBC film surface. From bottom to top, the peak I moves towards a higher q value with in-

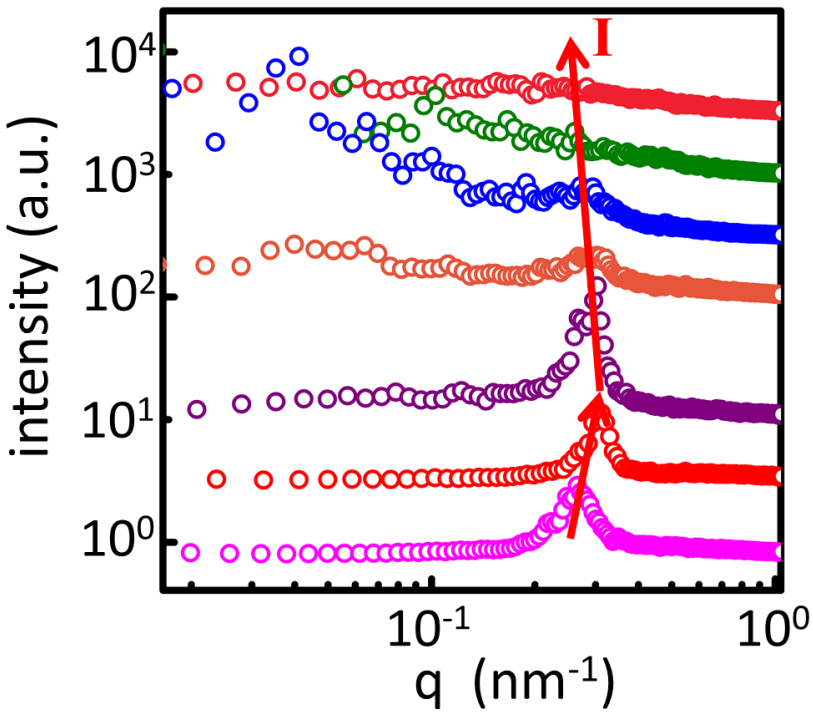

Figure 8.3: Power spectral density (PSD) functions obtained from azimuthal integration of the corresponding 2D FFT patterns at different NP concentrations: 0, 0.1, 0.5, 1, 3, 7, and 15 wt%, from bottom to top. For clarity, the PSD curves are shifted against y axis. The q value of the lateral structure arisen from the microphase separation of DBC is presented with Peak I. Image taken from reference [109].

corporation of an extremely small amount of NPs (0.1 wt%). However, instead of arising from a decrease of lateral periodic distances, the shift originates from the geometrical transition of the microphase separated structure, which differs for calculation of parallel cylinders ($d = 2\pi/q$) and perpendicular cylinders ($d = 4\pi/\sqrt{3}q$, for hexagonal lattice) from reciprocal space to real space. [250,251] The obtained domain distances, D, are 23.7 $\pm$ 0.1 nm (NP-free DBC film, $D = 2\pi/q$) and 23.8 $\pm$ 0.1 nm (NPs-DBC hybrid films, $D = 4\pi/\sqrt{3}q$), respectively. Afterwards, as the NP concentration increases from 0.1 to 3 wt%, the q value of the peak I decreases, which reveals an expansion of the domain distances from 23.8 to 26.2 nm. Moreover, upon the incorporation of the NPs, the width of the peak I becomes narrower firstly and broadens later. It indicates an initial enhancement in order, following by decay later. At high NP concentrations ($\geq$ 7 wt%), the peak I is difficult to observe and the position of that is ill-defined.

To examine the film surface in a larger region, Figure 8.4 presents an improved visual-

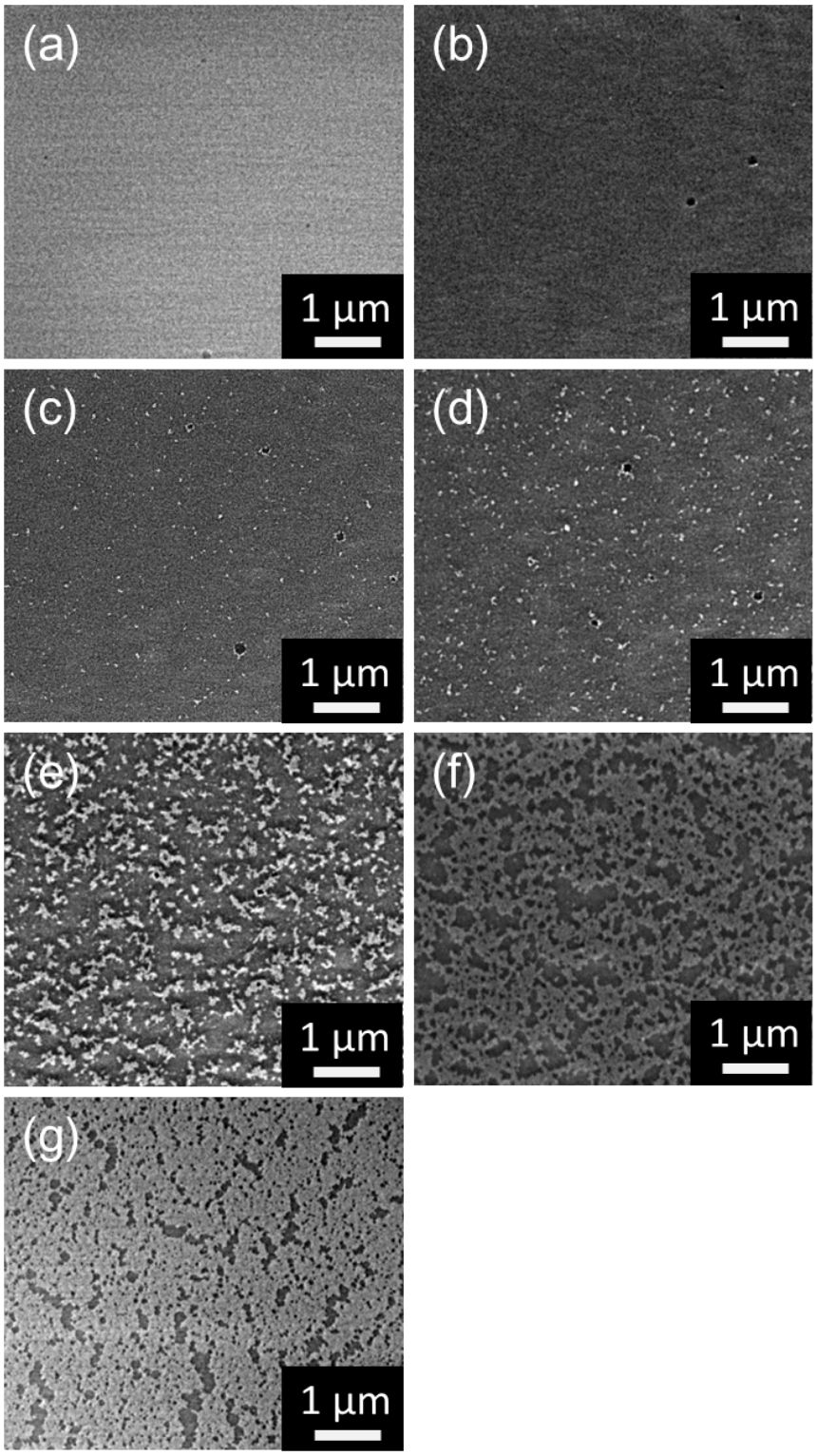

Figure 8.4: SEM images of the hybrid films in a larger scan size for varied NP concentrations: (a) 0, (b) 0.1, (c) 0.5, (d) 1, (e) 3, (f) 7, and (h) 15 wt%.

ization of the developed NP-aggregate network, which provides the statistical evidence for the formation of the NP-aggregate enrichment layer. As the NP concentration increases, the homogeneously distributed small NP-aggregates grow up and form large sized NP-aggregates gradually (Figure 8.4c-f). Eventually, a relative uniform NP-aggregates enrichment layer is established and almost fully covers the top surface (Figure 8.4g).

Since only 2D structure information of the hybrid film surface can be obtained with SEM images, AFM are employed for providing the 3D topography information. In addition, the detected contrast of AFM differs from that of SEM. AFM images are presented in Figure 8.5 for selected films: (a) NP-free DBC film and (b) hybrid film with NP concentration of 15 wt%.

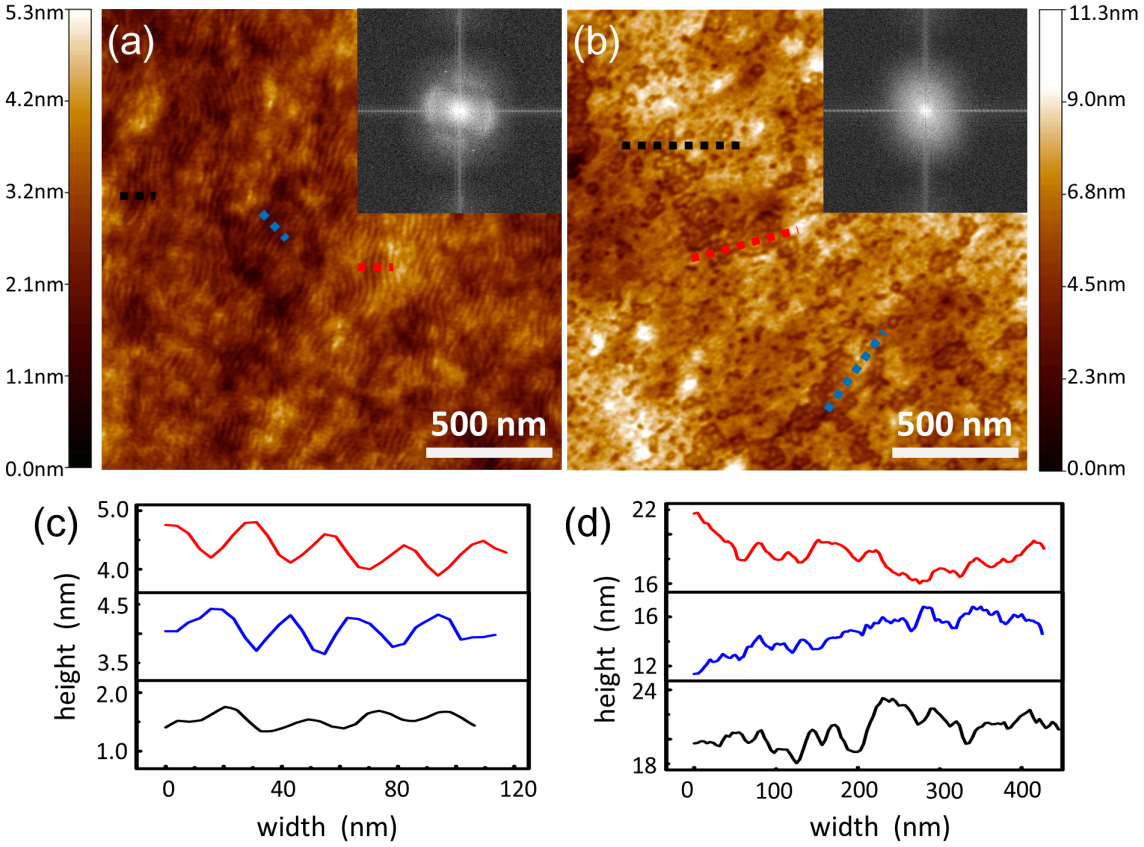

Figure 8.5: AFM topography images of (a) NP-free DBC film and (b) NPs-DBC hybrid film at NP concentration of 15 wt%. (c) and (d) are representative line cuts made from the AFM images at 3 different spots noted with correspondingly colored, dotted lines. The insets are 2D FFT patterns made from corresponding AFM images.

Curved stripe-shaped parallel cylinders, originating from the self-assembly microphase separation of the DBC, are found in Figure 8.5a. A totally different topography is pre-

sented in Figure 8.5b for the hybrid film with NP concentration of 15 wt%. The majority surface of the hybrid film is overlaid with NP-aggregates. In addition, a worm-like cylindrical morphology is presented in NP-aggregates free areas. Figure 8.5c and d show the height (peak-to-valley amplitude) profiles exhibited with representative line cuts, which are obtained from 3 randomly selected spots marked with the corresponding colored dashed line in Figure 8.5a and b. The local height modulations of the NP-free DBC film are well controlled under an amplitude of 1 nm (Figure 8.5c), whereas the mean height differences on a larger scale are on the order of 5 nm. For the hybrid film with NP concentration of 15 wt% (Figure 8.5d), the mean height differences increase to 11.3 nm, with the local height differences remaining small. The increase in mean height differences is attributed to the incorporated NPs. The result reveals that, in addition to the clearly observed NP-aggregates on the film surface, partially NP-aggregates incorporate inside the hybrid film. Moreover, AFM images also provide the information regarding root-mean-square (rms) roughness. On the local scale, the rms roughness of the NP-free DBC and the hybrid film (15 wt%) is 0.6 and 2 nm, respectively.

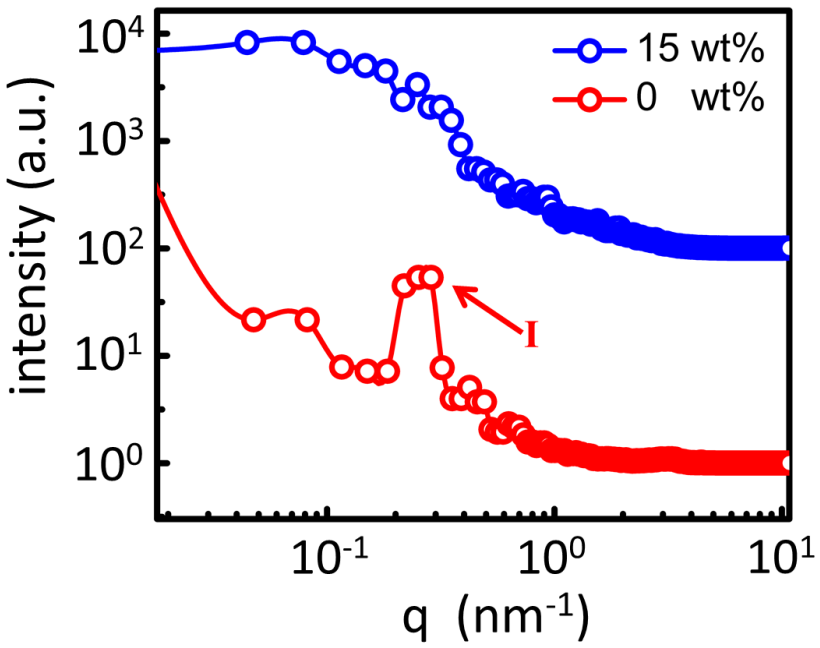

Figure 8.6: The PSD functions made from azimuthal integration of the corresponding 2D FFT patterns indicated with the colored legends. (Hollow circles and solid lines are the data and the guides to the eye). The q value marked with Peak I indicates the lateral structure originated from microphase separation of the DBC. For clarity, the PSD profiles are shifted against y axis. Image modified from reference [109].

To build a quantitative comparison of the PSD functions from SEM and AFM, the PSD function of the AFM images is shown in Figure 8.6. It is consistent with the corresponding PSD of the SEM. The q value marked with peak I, indicating the lateral structure originated from microphase separation of the DBC, is comparable with the corresponding q value obtained from the SEM image (in Figure 8.3).

8.3 Inner film morphology

The inner film morphology was examined with GISAXS, which provides an excellent statistical relevance over a macroscopic illuminated area down to nano-size with respect to the structure sizes, size distributions and spatial correlations. [161]
2D GISAXS data of the hybrid films with different NP concentrations are presented in Figure 8.7. During the measurements, the most intense specular intensity is shielded with a beam stop for protecting the detector. For a better characterization, the position of the specular intensity is well above the material characteristic Yoneda peak via selecting a proper incident angle in the measurements. Hence, the characteristic features of the Yoneda peak and the intensity modulations can be simply discriminated on the 2D detector. Generally, the most prominent changes of the 2D GISAXS data arise with incorporation of different amount of NPs.

8.3.1 Lateral morphology

The morphology information regarding lateral structures is presented in the 2D GISAXS pattern (in Figure 8.7). Firstly, for the DBC template (0 wt%, Figure 8.7a), a prominent side peak is found. It originates from the well-ordered cylindrical morphology because of the difference arisen in the electron density contrast between PS and PNIPAM blocks. With an extremely low amount of NPs incorporated ($\leq$ 1 wt%, Figure 8.7b and c), the signal of the side peak and Yoneda region becomes more significantly, due to the enhanced order and modified electron density contrast arising from the NPs embedded inside the PS block. At high NP concentrations, the side peak decays and even disappears, since the intensive scattering from a large quantity of NPs dominates the scattering signal. Moreover, at NP concentration of 3 wt% (Figure 8.7d), a second side peak arises and becomes more prominent as NP concentration increases. The size of the NPs is revealed with the second side peak, since it results from the structure factor of the closely packed NPs in the NP-aggregates.

For a quantitative analysis, horizontal line cuts of the 2D GISAXS data are made at the Yoneda region of DBC, $q_z = 0.51$ nm^{-1} (Figure 8.8a). Three main characteristic

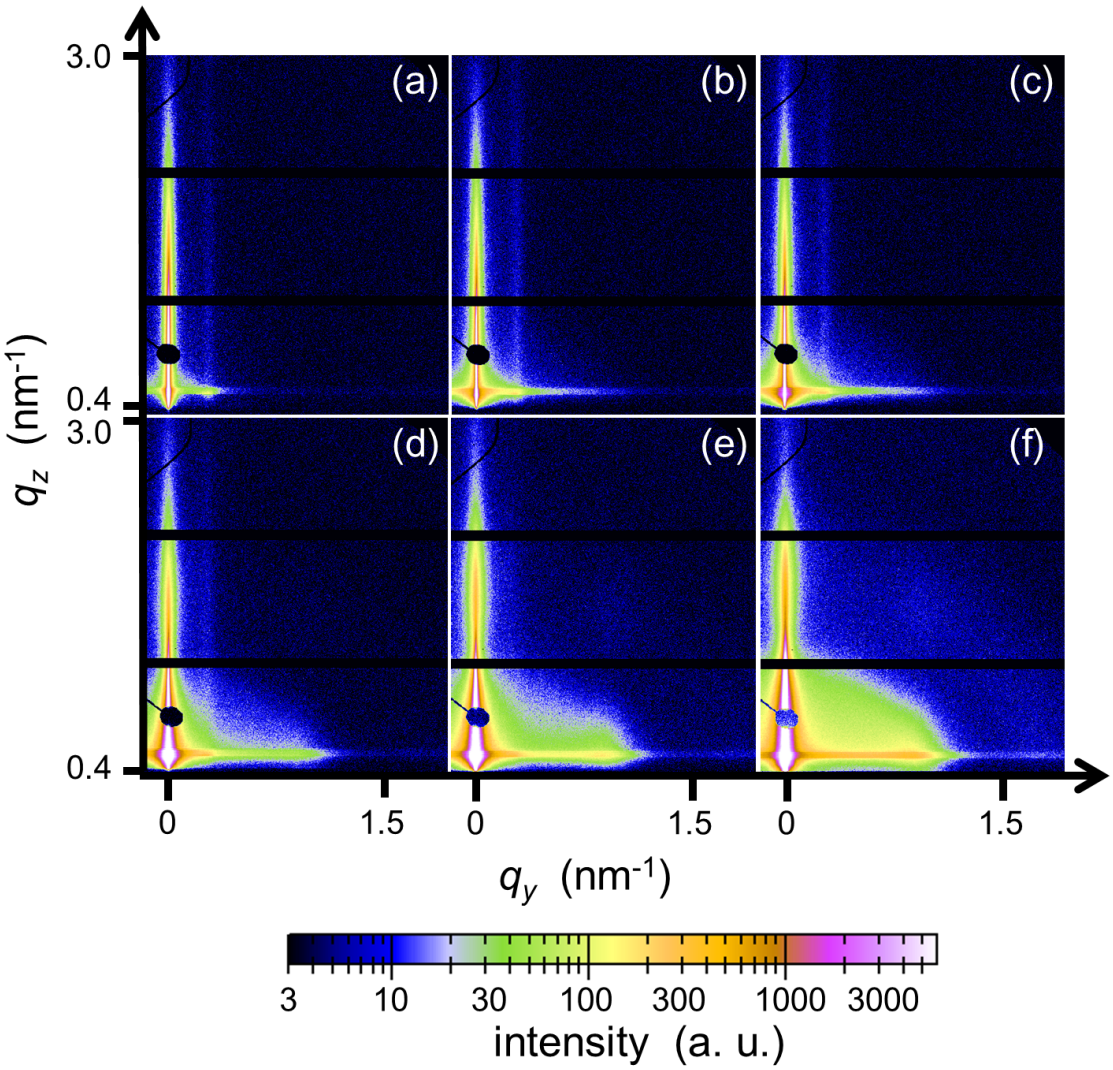

Figure 8.7: 2D GISAXS data of the hybrid films with different NP concentrations: (a) 0, (b) 0.5, (c) 1, (d) 3, (e) 7, and (f) 15 wt%. All the data are exhibited with the same intensity color bar in logarithmic scale. The two horizontal black gaps are the insensitive detector areas between modules. Image modified from reference [109].

features of the contribution of NPs, periodic distance of the DBC, and characteristic inter NP-aggregates distance are indicated as peak I, peak II, and peak III, respectively. Peak I locates at a high value of $q_y = 0.86$ nm^{-1}, and only appears at the NPs-DBC hybrid films. At small NP concentration (≤ 1 wt%), peak I is attributed to the form factor contribution of the NPs and presents a broad shoulder-like shape. At high NP concentration (≥ 3 wt%), the peak I is mainly ascribed to a structure factor of closely packed NPs. Thus, it becomes narrower and appears more pronounced. Notably, the q_y

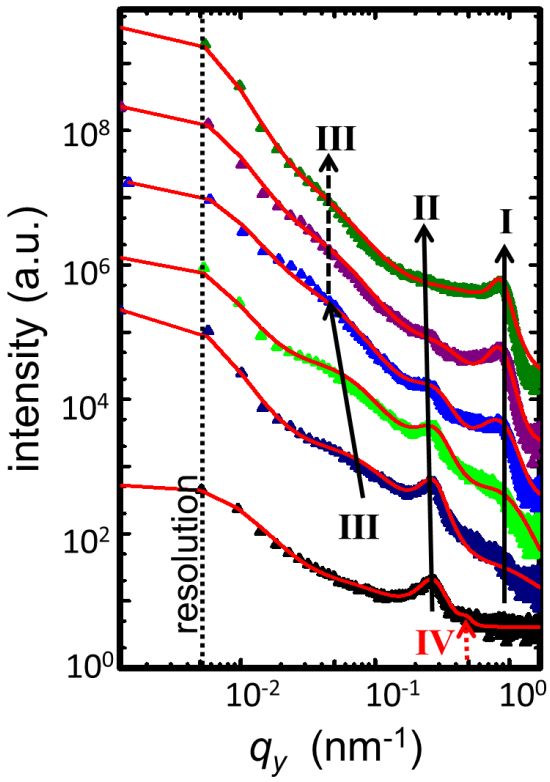

Figure 8.8: Horizontal line cuts (q_y) made from the 2D GISAXS data of the hybrid films with different NP concentrations: 0, 0.5, 1, 3, 7, and 15 wt%, from bottom to top. For clarity, all the data (colored symbols) together with the fits (red solid line) are shifted against y axis. Three main characteristic features of the contribution of NPs, periodic distance of DBC, and characteristic inter NP-aggregates distance are indicated as peak I, peak II, and peak III, respectively. The red dotted arrow points out the second-order peak II. Image modified from reference [109].

value of the peak I is irrespective of the NP concentration. A diameter of spherical NPs, 6.5 ± 0.5 nm, is obtained from the fit to the data. It matches the NP size determined with SAXS measurement in Section 5.1.1. Peak II locates at a smaller q_y value. It corresponds to the most prominent side peak of the 2D GISAXS patterns (in Figure 8.7), which indicates the highly periodic domain distance of the well-ordered PS cylinders in the hybrid films. The peak II appears most prominently at a low NP concentration of 0.5 wt% and gets less significant as the NP concentration increases, nearly disappearing at NP concentration of 15 wt%. In the fit, this structure factor is modeled with a Lorentzian distribution, and the resolution is as well modeled with a Lorentzian-shaped resolution function. For the pure DBC film, a weak second-order peak (marked with red dotted arrow IV), which is ascribed to the well-ordered nanostructures, is shown in Figure 8.8. The

in-plane lengths of the peak II and peak IV are 23.7 nm and 13.1 nm, respectively. The ratio of the q_y value between peak II and peak IV is $0.553 \approx 1 : \sqrt{3}$, which confirms the theoretic expectation of a cylindrical geometry. Hence, the morphology of highly ordered, hexagonally packed, cylindrical PS domains dispersed in a PNIPAM matrix is throughout the entire pure DBC film. As NP concentration increases, peak II shifts towards smaller q_y values (in Figure 8.8). It indicates an increase in the lateral distance between PS cylinders. Figure 8.9c show the corresponding periodic distance, DII, increasing from 23.7 ± 0.2 nm to 30.0 ± 0.6 nm. The expansion of DII is attributed to the selectively swelling of the PS cylinders with the embedded NPs. Notably, the second order of the peak II is absent at NP concentration of 0.5 wt%, which should be existed at a higher structural order. The absence is ascribed to the additional strong scattering from the form factor of the NPs. As the NP concentration increases further, peak II becomes less prominent and broadens, which indicates the over-saturation of the PS domains with NPs. Consequently, the previous long-range ordered structures are perturbed. Figure 8.9d shows the variation tendency of the peak width (full width half maximum, FWHM), which reveals the systematic order of the represented nano-structure. At NP concentration of 0.5 wt%, the FWHM of peak II becomes narrower, which implies an enhancement of the structural order. However, it increases with the increasing NP concentration, indicating the decay of the structural order.

At even smaller q_y values close to the resolution, a broad shoulder-like feature (marked with peak III) presents, which reveals center-to-center distance of the NP-aggregates. As the size of the NP-aggregates increases, the inter distance of NP-aggregates increases accordingly. In Figure 8.8a, peak III appears at NP concentration of 0.5 wt%, and shifts towards smaller q_y values as NP concentration increases until 3 wt %. The inter distance of the NP-aggregates, $DIII$, obtained from the corresponding fit presents a linear increase from 180 ± 10 nm to 380 ± 25 nm with a large distribution (in Figure 8.9e). It reveals the randomly distributed large NP-aggregates. However, in case NP concentration is greater than 7 wt%, the peak III (in Figure 8.8, marked with dashed arrow) weakens sharply with very broad distribution, which originates from large inter-aggregates distance distributions and the presence of ill-defined large sized NP-aggregates. These Observations are consistent with surface characterization provided with SEM and AFM, where large sized interconnected NP-aggregates are found (in Figure 8.2f and g).

8.3.2 Vertical structures

In Figure 8.7d-f (NP concentration ≥ 3 wt%), an intensity modulation along the q_z direction is found. The intensity modulation derives from a partial phase coherence of the x-ray waves diffusely scattered from different interfaces, which gives rise to an increase

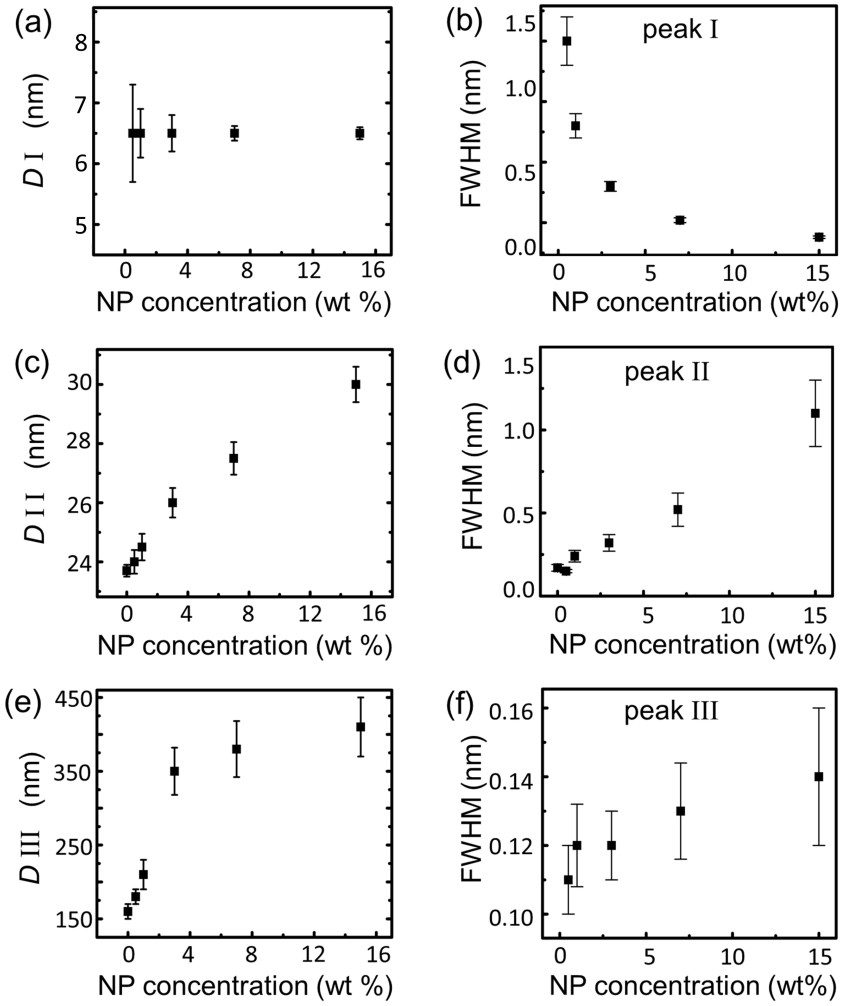

Figure 8.9: The lateral structural information extracted from the fit: (a) the diameter of the NPs (marked with DI, corresponds to peak I), (c) the microphase separated periodic domain distance (marked with DII, corresponds to peak II) and (e) inter NP-aggregates distance (marked with $DIII$, corresponds to peak III) vs. NP concentration. (b), (d) and (f) present the full width at half maxima (FWHM) of peak I, peak II and peak III in Figure 8.8 vs. NP concentration.

in intensity in a sheet in reciprocal space. [184] Differing from SEM and AFM, the most probable source of the partial phase coherence of diffusely scattered wave is the correlated roughness of the large NP-aggregates enrichment layers on top of the hybrid films. [109] Namely, the correlated roughness originates from a locally long-range correlated layer thickness between two adjacent interfaces of the hybrid film/NP-aggregates layer and NP-aggregates layer/air. As a consequence, the intensity modulation along the q_z direction

reveals that the NP-aggregate enrichment layer has a rather uniform thickness with only small variances. [252]

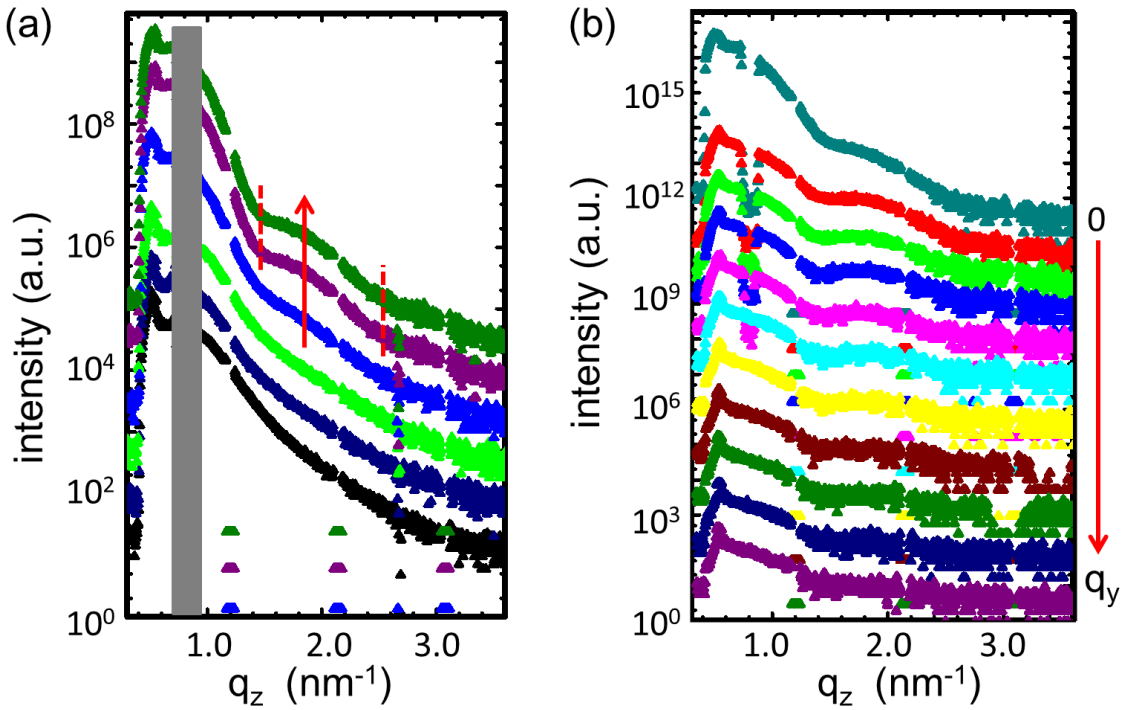

Figure 8.10: (a) Vertical line cuts (q_z) of the 2D GISAXS data made from $q_y = 0$ for films with different NP concentrations: 0, 0.5, 1, 3, 7, and 15 wt% from bottom to top. Dashed lines and arrow in (a) point out the characteristic intensity modulation. (b) Vertical line cuts (q_z) of a hybrid film with a NP concentration of 15 wt% made from a range of equidistant q_y values (q_y from 0 to 0.177 nm^{-1}, from top to bottom as shown with the arrow, the increment $\triangle q_y$ = 1.77 $\times$ 10^{-2} nm^{-1}). For clarity, all profiles are shifted against y axis. Image modified from reference [109].

For further quantitative analysis, vertical line cuts of the 2D GISAXS data made from $q_y = 0$ for films with different NP concentrations of 0, 0.5, 1, 3, 7, and 15 wt% are shown in Figure 8.10a. Using a simplified Equation 8.1, the thickness of the correlated enrichment NP-aggregates layer, d, can be obtained.

$$d = 2\pi / \triangle q_z \tag{8.1}$$

where d is the distance between adjacent minimal intensity (corresponds to the spacing between the dashed lines in Figure 8.10a. With $\triangle q_z = 1.13$ nm^{-1}, $d = 5.56$ nm, the thickness of the NP-aggregates enrichment layer perfectly matches the results from the height

profiles of the AFM measurements (in Figure 8.10d). Analogous roughness correlations have been investigated in many similar systems, which consists of either a single layer or complex multilayer films. [253, 254] In order to investigate the in-plane correlations, vertical line cuts at a range of equidistant q_y values from 0 to 0.177 nm^{-1} are made. In Figure 8.10b, the off-center vertical line cuts are shown for a selected hybrid film with NP concentration of 15 wt%. The applied increment, $\triangle q_y$, is 1.77×10^{-2} nm^{-1} following an indicating arrow. From top to bottom, as the q_y value increases, the intensity of the resonant diffuse scattering along the q_z direction decreases, which reveals the absence of the vertical structural correlation at certain q_y values. Assuming the roughness spectrum of the interface between hybrid film and NP-aggregates layer as a reference, a characteristic decay length of the roughness correlation can be determined, yielding a critical cut-off in-plane length scale (R_c). [255] In the case of R $< R_c$, an individual roughness spectrum is realized irrespective of the underlying hybrid film/NP-aggregates interface. [243] However, with R $>$ R_c, the structure of the hybrid film/NP-aggregates interface can be replicated by the NP-aggregates enrichment layer. The corresponding off-centered vertical line cuts define the value of R_c is 35.5 nm, which is slightly larger than the corresponding lateral periodic distance of 30.0 nm (presented in previous Section 8.3.1).
In a word, the thin NP-aggregates enrichment layer has a mean thickness of 5.6 nm and replicates the topography of the underlying hybrid film surface in case the in-plane structural sizes is larger than 35.5 nm. Most likely, partial NPs are buried inside the hybrid film, since the thickness of the NP-aggregates enrichment layer is smaller than the mean NP diameter.

8.4 Entire film morphology

Figure 8.11 presents the entire hybrid film morphology resolved with both, real-space and reciprocal space techniques. Figure 8.11a shows the DBC template, consisting of cylindrical PS domains homogeneously distributed in a PNIPAM continuous matrix. The highly ordered structures are established via a self-assembly microphase separation procedures and function as a guiding material for the incorporation of the NPs. The majority of PS cylinders favor a parallel orientation (with respect to the film surface), which is mainly attributed to two regimes:

(1) Interfacial preference, originating from a lower surface energy, makes the PS domains have an affinity to air compared with the PNIPAM domain.

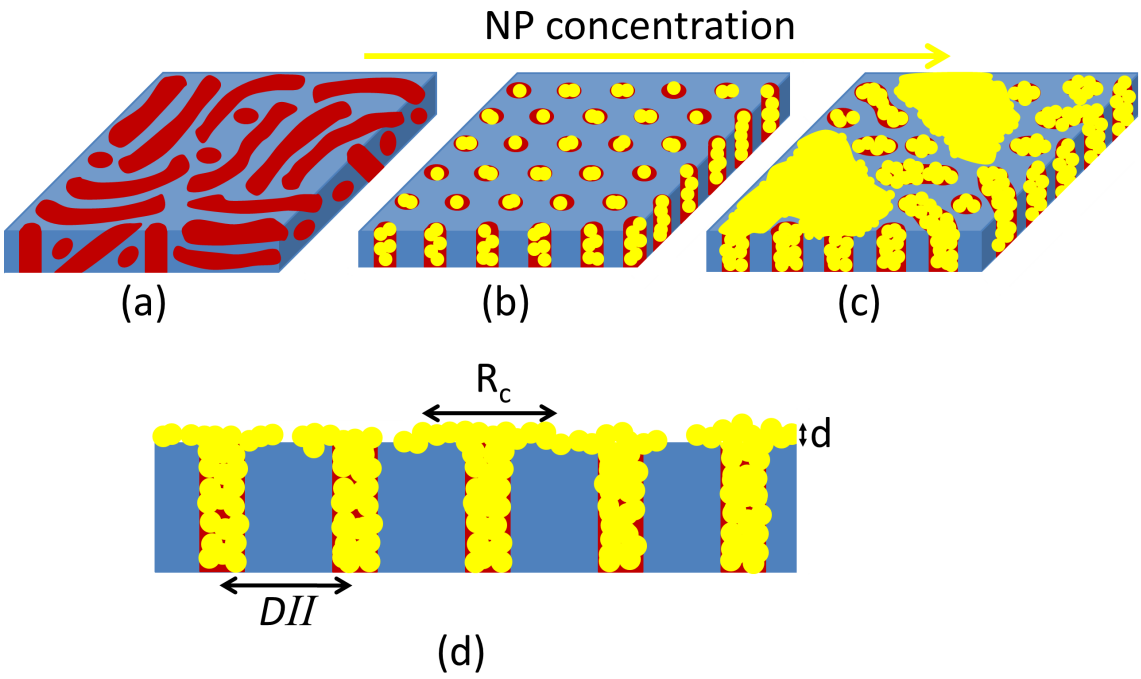

Figure 8.11: Schematic representation of the morphology for (a) pure DBC film, and hybrid films at (b) low, and (c) high NP concentrations. (d) Cross sectional illustration of the NP-aggregates enrichment layer for the hybrid film with large NP content. The PS domain is indicated in red, the PNIPAM domains in blue, and maghemite NPs in yellow. R_c, d, and DII represent the critical cut-off in-plane length scale, thickness of NP-aggregates enrichment layer, and periodic distance of DBC, respectively. Image modified from reference [109].

(2) In case the film thickness is far beyond the DBC periodic distance, the parallel orientation is prone to form due to the surface boundary condition. [113,115] The thickness of the current DBC film is 237 nm, which far exceeds the DBC periodic distance of 23.7 nm.

With a small amount of NPs incorporated into the hybrid film (Figure 8.11b), the NPs are selectively dispersed inside the PS cylinders due to the preferential interaction between the PS-coated NPs and the PS domains. Consequently, the incorporation of the NPs enhances the initial interfacial energy of the film/air and modifies the related Flory-Huggins interaction parameter. Thus, a transition in the orientation of the cylindrical NP/PS domains from parallel to perpendicular is realized. To accommodate NPs, the neighboring PS domain distance expands. Notably, at extremely low NP concentrations, a best ordered morphology can be reached due to the enhanced enthalpic contribution. Figure 8.11c shows the large sized NP-aggregates on the surface of the hybrid film with

high NP concentrations. The previous long-range ordered structures are disturbed to some extent. Although the ordered PS cylinders still stretch much heavier and deform to accommodate NPs as much as possible, the excessive NPs are squeezed out of the PS cylinders and installed on the film surface. Eventually, NP-aggregates grow up and form an enrichment layer. The mean thickness of the NP-aggregate enrichment layer is slightly smaller than the diameter of the NPs, which implies that part of the NPs is buried inside the film (Figure 8.11d). The roughness features of the interface between hybrid film/NP-aggregates are duplicated by the NP-aggregates layer in the case of in-plane structure size R $> R_c$. In addition, the determined inter domain distance of DBC (DII) is slightly smaller the R_c.

8.5 Magnetic properties

The magnetization measurements with the external magnetic fields from -500 to 500 mT are used for examining the magnetic properties of the hybrid films.

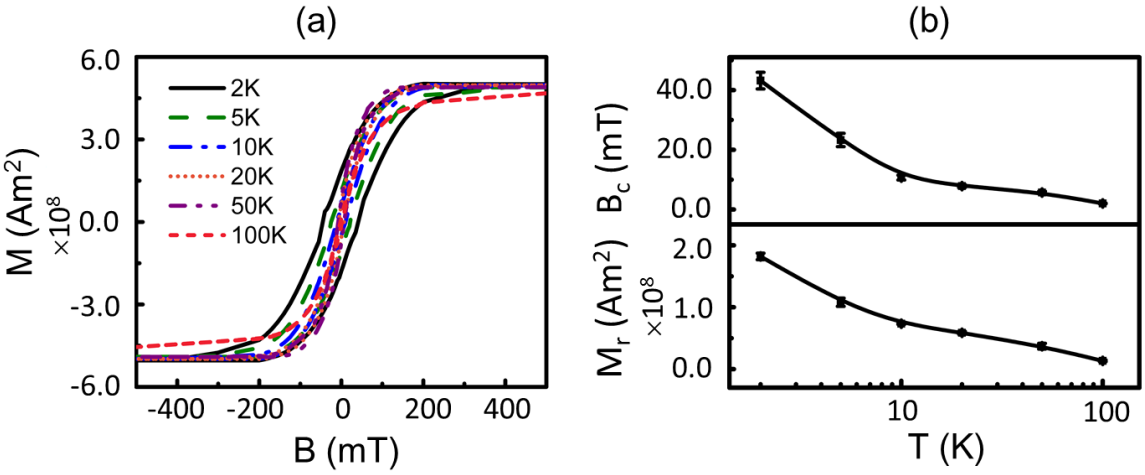

Figure 8.12: Hybrid film with NPs concentration of 15 wt%: (a) magnetic moments vs. external magnetic fields at different temperatures (indicated with the legends); (b) B_c and M_r obtained from the corresponding magnetic moments. The solid lines in (b) are guides to the eye. Image modified from reference [109].

In Figure 8.12, the magnetic moments, measuring for a selected hybrid film with a NPs concentration of 15 wt%, show a temperature-dependent behavior. As the temperature increases, the width of the hysteresis loop decreases. Notably, the current applied external magnetic fields are too small to saturate magnetization at a relatively higher temperature of 100 K, which is consistent with the Curie's law (in Section 2.2.3). [216]

The observed hysteresis loops superimpose and become narrower even approaching zero with the increase of the temperature, which is the fingerprint of a superparamagnetic material. Figure 8.12b presents the extracted B_c, which is defined as the half hysteresis. As the temperature increases, B_c decays significantly, and vanishes eventually in case the temperature exceeds the T_B of the current employed superparamagnetic NPs. The T_B is defined with the integrated Néel-Brown formula (in Section 2.2.4, Equation 2.28) [133,222]. Furthermore, a sharp decay behavior is found for the M_r in Figure 8.12b. However, it differs from a previous investigation, where a more moderate decay is observed for the hybrid film system with a randomly oriented DBC combined with widely distributed maghemite NPs. [215] In general, the temperature-dependent decay behavior of the M_r and B_c is ascribed to thermal fluctuations.

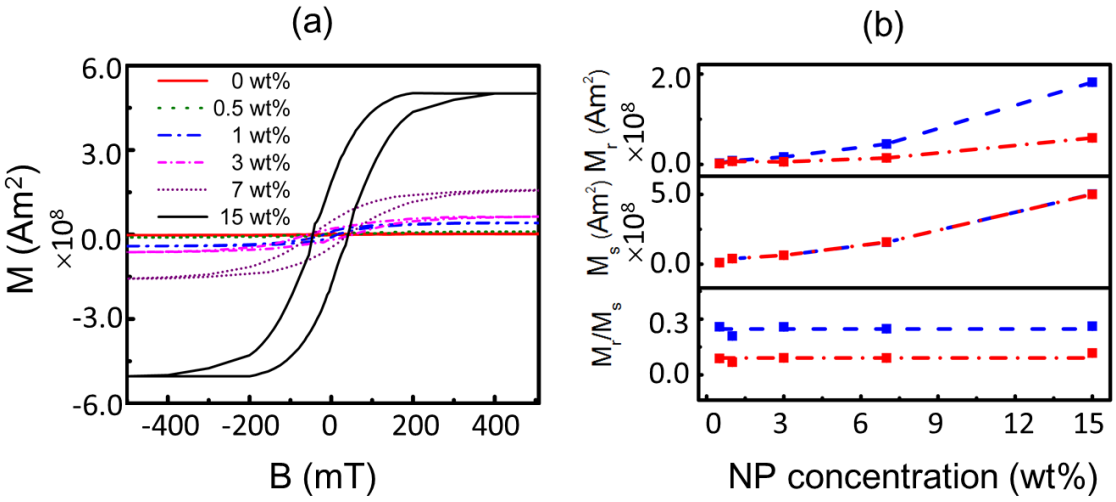

Figure 8.13: (a) Magnetic moments vs. external magnetic fields at 2 K for hybrid films with different NP concentrations (indicated with the legends). (b) M_r, M_s, and M_r/M_s obtained from the corresponding magnetic moments at 2 K (blue dashed line) and 20 K (red dashed dotted line). Image modified from reference [109].

In Figure 8.13a, the NP concentration dependent magnetic properties obtained at 2 K is presented. For a further analysis, M_r, M_s, and M_r/M_s are extracted accordingly and shown in Figure 8.13b. For a better comparison, the results obtained from 20 K are also contained. Irrespective of the temperature, M_r and M_s present the similar tendency, increasing linearly with the increase of the NP concentration. The M_r/M_s is independent of the NP concentration. In addition, no magnetically anisotropy behavior has been found from the extra magnetic moment measurements performed with applied magnetic fields rotated by 90° in the film plane. Thus, an isotropic NP distribution is confirmed, and the presence of the NP-aggregates does not influence the magnetic behavior in terms of

magnetic isotropy. This feature is beneficial for the applications requiring no magnetic anisotropy.
Taking all the observations from the magnetic properties into account, the current probed hybrid films present the typical superparamagnetic behavior and keep consistent with a modified Stoner-Wohlfarth-Néel model, [217, 218] which is based on the developed thermodynamics of super-spins modified with an elastic torsion mechanism. Certain characterizations are interestingly different from previous investigated NPs-DBC hybrid film systems based on other types of DBC templates. [108, 215] Consequently, the exhibited magnetic properties is in close relation to the film morphology.

8.6 Summary

The thoroughly NP concentration dependent morphology of the NPs-DBC hybrid films, comprising of γ-Fe_2O_3 NPs and PS-*b*-PNIPAM DBC, has been investigated with surface profilometry, SEM, AFM, and GISAXS. The morphology has been related to the magnetic behavior. The control of the NPs is achieved via the preferential incorporation of the surface modified NPs inside the PS domains, and guided by the self-assembly microphase separation structures of the DBC template. With the incorporation of the NPs, an unusual orientation transition of the cylindrical structure from parallel to perpendicular is established. At low NP concentrations, the PS domains are stretched for accommodating the NPs, which results in the expansion of the periodic distance of DBC. The selectively incorporated, well dispersed NPs modify the enthalpic contribution, thus the order and the orientation of the nanostructures are enhanced. Such highly ordered, well perpendicularly oriented cylindrical morphology is prepared with a self-assembly, wet chemical approach, using a simple and highly reproducible spin coating method without any pre- or post-treatments. The incorporation of a large amount of NPs intensively disturbs the previous long-range ordered structures, which also leads to the formation of large NP-aggregates. As the NP concentration increases further, a network of NP-aggregates representing an enrichment layer appears on the film surface. The superparamagnetic properties of the hybrid films with all investigated NP concentrations are confirmed. Consequently, the excessive NPs on the surface layer have no negative effect on the magnetic behavior.
Different ordered morphologies of the hybrid films with varied structural emphasis could be realized via selecting proper weight ratios of NPs vs. DBC and fabricated in a simple and low cost approach for versatile potential applications. The DBC with hydrophilic PNIPAM block may be especially useful in the fields of thermo-responsive magnetic sensors.

Chapter 9

Conclusion and outlook

Nanostructured hybrid films composed of maghemite NPs and DBCs have been investigated. Spatial arrangements of the maghemite NPs within the nanostructured DBC films were controlled by the balance of interfacial free energy, Van der Waals forces, enthalpic interactions and the magnetic dipolar interactions of the NPs. It is comprehensively observed that the morphologies of the NPs-DBC hybrid films depend on the preparation conditions as well as on other external parameters, e.g. externally applied magnetic fields. The structural characterizations include several real and reciprocal space techniques. For instance, microscopic imaging (AFM and SEM) and scattering techniques (SAXS and GISAXS) have been employed to provide overall structural details of the hybrid films. The non-destructive TOF-GISANS technique has also been employed in the current thesis to investigate inner film morphologies at different film depths. The reciprocal space techniques (GISAXS and TOF-GISANS) provide much better statistical relevant structural data compared with the real space techniques. Moreover, the magnetic properties of the hybrid films were probed using SQUID magnetometer. Magnetic hysteresis loops were observed and analyzed, showing the possibilities towards applications in magnetic sensors or devices. The comparison of the magnetic properties with the morphology is crucial for gaining better understanding of the structure-property relationship.

Selective inclusion of magnetic NPs in one polymer domain (PS) of DBCs is achieved using PS-coated NPs. Localizing the PS-coated NPs within PS domains is enthalpically favored. This is the most important driving force that guides NPs within one or other domain in the nanostructured hybrid films. Furthermore, an improved microphase separation process was observed for hybrid films at low NP concentrations. Thus, versatile morphologies were established with properly selected DBCs, NP size, NP concentration and preparation conditions. For certain high NP concentrations, the inclusion of NPs was found to deteriorate the initially established ordered morphologies of the hybrid films.

For high NP concentrations, the entropy penalty of the polymer chain to incorporate the NPs is dramatically increased, which is an energetically unfavorable process.

The first hybrid film system investigated in the current thesis is consisting of PSd-*b*-PBMA and PS-coated maghemite NPs. The effect of film thickness and NP concentration on the morphological evolution as well as the magnetic properties of the hybrid films was studied. These hybrid films were fabricated via spin coating followed by a thermal annealing step to establish microphase-separation nanostructured hybrid films. For different morphologies (perforated perpendicular, and parallel lamella), magnetic properties significantly differ. Therefore, the precise determination of the morphology is crucial to achieve complete comprehension of the magnetic behavior of the hybrid films. The powerful TOF-GISANS technique was employed for probing depth profiles of the ordered structures of the NPs-DBC system.
For one set of samples, where the film thickness approximately equals the periodic inter-domain distance D of the DBC, a moderately ordered, perforated lamellar morphology, with a PSd enrichment layer at the film/substrate interface was obtained. Furthermore, with a small amount of embedded NPs (0.5 wt%), the microphase separation was enhanced and a highly ordered perforated lamella morphology with an enrichment of PS containing NPs at the film/substrate surface interface was observed. Interestingly, under a certain NP concentration threshold, the exhibited inter-domain distance D of the films remains almost constant irrespective of NP concentration, since the DBC develops a deformed structure for accommodating NPs at relatively high concentrations. Such unique structure is attractive for applications requiring constant periodicity of a magnetic nanostructure.
The other set of samples was prepared where the thickness of the hybrid film is about 2.5 times larger than periodic inter-domain distance D of the DBC. A morphology of highly ordered, well parallel oriented, alternating PSd and PBMA lamellae was achieved. With the incorporation of NPs at intermediate concentrations, uniform dispersion of the NPs in swelling PSd domains was obtained. Moreover, arrays of NPs were established within the PSd domains, forming alternating layers of NPs rich PSd and NPs-free PBMA. The different established morphologies, originating from the microphase separation of the identical DBC, are ascribed to both the surface boundary conditions and the film thickness. As a consequence, differences of the magnetic properties, arising from different structural arrangements, were observed. For the thin and the thick hybrid films, temperature-dependent and temperature-independent maximum magnetization was observed, respectively. After excluding the NP volume effect, the magnetization saturation (M_s) and remanence (M_r) of the thick films were approximately 1.7 and 2.1 times as

large as those of the thin films, respectively. The comparison implies that the nature of the morphological orientation (perpendicular vs. parallel) does have an effect on the magnetic properties. The close relation between the exhibited magnetic properties and the film morphology is confirmed.

The second investigated hybrid film system consists of PS-*b*-PMMA DBC and maghemi te NPs. Here, an external magnetic field has been applied aiming at implementing better highly ordered nano/micro magnetic NPs orientations. The morphology of the films was fully characterized as function of incorporated NP concentrations and the applied external magnetic fields during the film preparation using a solution-casting method. Highly oriented, wire-shaped NP aggregates embedded in the DBCs with different widths, lengths, and neighboring spacing were well fabricated via a simple, low cost, and high-throughput method. So far, the preparation of such nano/micro wires of magnetic NPs required high temperature, high energy consumption, or high voltage conditions. This novel film preparation, performed at room temperature, without any requirement on an external energy source, is successfully introduced in the current thesis. The wire-shaped NP aggregates impart strong magnetic shape anisotropy of the hybrid film. The highly anisotropic structures, both on the microscale as well as on the nanoscale, benefit the potential applications requiring superparamagnetic features and pronounced magnetic shape anisotropy.

The third NPs-DBC hybrid film system is based on a different type of DBC, PS-*b*-PNIPAM, consisting of a hydrophobic PS block and a hydrophilic PNIPAM block. The PNIPAM polymer is one of the most explored thermo-responsive polymers. A precise arrangement of NPs inside the PNIPAM block of the DBC film was achieved. It is the first time that combination of magnetic NPs with the PNIPAM based DBC in dry film regime was shown. The morphological evolution of the hybrid films is comprehensively presented as a function of the embedded NP concentration. The cylinder-forming composition of the pristine DBC showed a transition from parallel to perpendicular orientation (with respect to the film surface) upon incorporation of small amount of NPs. The order of the cylindrical morphology was further enhanced with increasing NP concentration up to a critical concentration. From previous related studies, the perfect perpendicular cylindrical structure is mostly found in case of sophisticated, special treated substrates, or when thin films are confined with the film thickness smaller than the periodic distance D of DBC. However, in the current study, a simple and highly reproducible spin coating method was used without any prior or post-treatment steps. Films with thicknesses around 10 times larger than the periodic distance D of the employed DBC resulted in a perpendicular cylindrical morphology. At concentrations larger than a critical concentra-

tion, an enriched layer of NP-aggregates was established on the top surface of the hybrid film. The presence of the enriched NPs layer on the film surface resulted in a correlated interface roughness, waveguide property. Such special structure is as well useful in the fields of thermo-responsive magnetic devices.

To conclude, this thesis presents several possible morphological architectures composed of NPs-DBC hybrid films. The combination of inorganic maghemite NPs and the DBCs is found to be an efficient approach for making hybrid films for many different applications, by tuning of the preparation conditions, NP concentration and possible external magnetic fields. So far, the optimal structures of the hybrid films are most likely established with the inclusion of a small amount of NPs (0.5 wt%) rather than high NP concentrations.

As an outlook, closely following the current investigation, several ideas would be interesting to pursue. For instance, in case of thermo-responsive DBC system, the effect of an external stimulus such as humidity on the morphology of the final hybrid film can be tailored. The high swelling capability of the thermo-responsive block of the DBC, would allow tuning the effective volume fraction of the PNIPAM block in the hybrid film, resulting in a possible phase transition between different distinct morphologies. The humidity-dependent magnetic properties of the hybrid film system due to the thermoresponsivity of the PNIPAM block of the DBC is an interesting subject for further investigations. Based on selective incorporation of NPs in DBC scaffolds, polymer degradation methods, such as plasma etching or acid etching, could be applied subsequently with the aim to create metal-oxide nanopatterns. Such type of patterns with perpendicularly aligned magnetic nano-wires is considered to be developed for future storage devices.

Bibliography

[1] A. M. Budgin, Y. A. Kabachii, Z. B. Shifrina, P. M. Valetsky, S. S. Kochev, B. D. Stein, A. Malyutin, and L. M. Bronstein, "Functionalization of magnetic nanoparticles with amphiphilic block copolymers: self-assembled thermoresponsive submicrometer particles," *Langmuir*, vol. 28, no. 9, pp. 4142–4151, 2012.

[2] F. Caruso, R. A. Caruso, and H. Möhwald, "Nanoengineering of inorganic and hybrid hollow spheres by colloidal templating," *Science*, vol. 282, no. 5391, pp. 1111–1114, 1998.

[3] H. Chen, X. Wu, H. Duan, Y. A. Wang, L. Wang, M. Zhang, and H. Mao, "Biocompatible polysiloxane-containing diblock copolymer PEO-b-PγMPS for coating magnetic nanoparticles," *ACS applied materials & interfaces*, vol. 1, no. 10, pp. 2134–2140, 2009.

[4] J. H. Choi, F. T. Nguyen, P. W. Barone, D. A. Heller, A. E. Moll, D. Patel, S. A. Boppart, and M. S. Strano, "Multimodal biomedical imaging with asymmetric single-walled carbon nanotube/iron oxide nanoparticle complexes," *Nano Letters*, vol. 7, no. 4, pp. 861–867, 2007.

[5] J. Gao, H. Gu, and B. Xu, "Multifunctional magnetic nanoparticles: Design, synthesis, and biomedical applications," *Accounts of Chemical Research*, vol. 42, no. 8, pp. 1097–1107, 2009.

[6] E. Han, M. Leolukman, M. Kim, and P. Gopalan, "Resist free patterning of non-preferential buffer layers for block copolymer lithography," *ACS nano*, vol. 4, no. 11, pp. 6527–6534, 2010.

[7] D. H. Kim, A. Wei, and Y.-Y. Won, "Preparation of super-stable gold nanorods via encapsulation into block copolymer micelles," *ACS applied materials & interfaces*, vol. 4, no. 4, pp. 1872–1877, 2012.

[8] S. Krishnamoorthy, S. Krishnan, P. Thoniyot, and H. Y. Low, "Inherently reproducible fabrication of plasmonic nanoparticle arrays for SERS by combining nanoimprint and copolymer lithography," *ACS applied materials & interfaces*, vol. 3, no. 4, pp. 1033–1040, 2011.

[9] F. E. Kruis, H. Fissan, and A. Peled, "Synthesis of nanoparticles in the gas phase for electronic, optical and magnetic applications—review," *Journal of Aerosol Science*, vol. 29, no. 5, pp. 511–535, 1998.

[10] H.-C. Liao, C.-S. Tsao, T.-H. Lin, M.-H. Jao, C.-M. Chuang, S.-Y. Chang, Y.-C. Huang, Y.-T. Shao, C.-Y. Chen, and C.-J. Su, "Nanoparticle-tuned self-organization of a bulk heterojunction hybrid solar cell with enhanced performance," *ACS nano*, vol. 6, no. 2, pp. 1657–1666, 2012.

[11] P. A. Mistark, S. Park, S. E. Yalcin, D. H. Lee, O. Yavuzcetin, M. T. Tuominen, T. P. Russell, and M. Achermann, "Block-copolymer-based plasmonic nanostructures," *ACS nano*, vol. 3, no. 12, pp. 3987–3992, 2009.

[12] S. P. Mornet, S. b. Vasseur, F. Grasset, and E. Duguet, "Magnetic nanoparticle design for medical diagnosis and therapy," *Journal of Materials Chemistry*, vol. 14, no. 14, pp. 2161–2175, 2004.

[13] R. N. Patel, A. T. Heitsch, C. Hyun, D.-M. Smilgies, A. De Lozanne, Y.-L. Loo, and B. A. Korgel, "Printed magnetic FePt nanocrystal films," *ACS applied materials & interfaces*, vol. 1, no. 6, pp. 1339–1346, 2009.

[14] M. Rawolle, M. A. Niedermeier, G. Kaune, J. Perlich, P. Lellig, M. Memesa, Y.-J. Cheng, J. S. Gutmann, and P. Müller-Buschbaum, "Fabrication and characterization of nanostructured titania films with integrated function from inorganic-organic hybrid materials," *Chemical Society Reviews*, vol. 41, no. 15, pp. 5131–5142, 2012.

[15] S. Ren, L.-Y. Chang, S.-K. Lim, J. Zhao, M. Smith, N. Zhao, V. Bulovic, M. Bawendi, and S. Gradecak, "Inorganic-organic hybrid solar cell: Bridging quantum dots to conjugated polymer nanowires," *Nano Letters*, vol. 11, no. 9, pp. 3998–4002, 2011.

[16] D. A. Rider, K. Liu, J.-C. Eloi, L. Vanderark, L. Yang, J.-Y. Wang, D. Grozea, Z.-H. Lu, T. P. Russell, and I. Manners, "Nanostructured magnetic thin films from organometallic block copolymers: pyrolysis of self-assembled polystyrene-block-poly (ferrocenylethylmethylsilane)," *ACS nano*, vol. 2, no. 2, pp. 263–270, 2008.

[17] B. Sahoo, K. S. P. Devi, R. Banerjee, T. K. Maiti, P. Pramanik, and D. Dhara, "Thermal and PH responsive polymer-tethered multifunctional magnetic nanoparticles for targeted delivery of anticancer drug," *ACS applied materials & interfaces*, vol. 5, no. 9, pp. 3884–3893, 2013.

[18] R. Sknepnek, J. A. Anderson, M. H. Lamm, J. Schmalian, and A. Travesset, "Nanoparticle ordering via functionalized block copolymers in solution," *ACS nano*, vol. 2, no. 6, pp. 1259–1265, 2008.

[19] I. I. Slowing, B. G. Trewyn, S. Giri, and V.-Y. Lin, "Mesoporous silica nanoparticles for drug delivery and biosensing applications," *Advanced Functional Materials*, vol. 17, no. 8, pp. 1225–1236, 2007.

[20] A. Sukhov and J. Berakdar, "Local control of ultrafast dynamics of magnetic nanoparticles," *Physical Review Letters*, vol. 102, no. 5, p. 057204, 2009. PRL.

[21] Q. Wei, Y. Lin, E. R. Anderson, A. L. Briseno, S. P. Gido, and J. J. Watkins, "Additive-driven assembly of block copolymer-nanoparticleanoparticle hybrid materials for solution processable floating gate memory," *ACS nano*, vol. 6, no. 2, pp. 1188–1194, 2012.

[22] F. L. Yap, P. Thoniyot, S. Krishnan, and S. Krishnamoorthy, "Nanoparticle cluster arrays for high-performance SERS through directed self-assembly on flat substrates and on optical fibers," *ACS nano*, vol. 6, no. 3, pp. 2056–2070, 2012.

[23] J. Yoon, W. Lee, and E. L. Thomas, "Self-assembly of block copolymers for photonic-bandgap materials," *MRS bulletin*, vol. 30, no. 10, pp. 721–726, 2005.

[24] L. Zhao, D. A. Loy, and K. J. Shea, "Photodeformable spherical hybrid nanoparticles," *Journal of the American Chemical Society*, vol. 128, no. 44, pp. 14250–14251, 2006.

[25] B. H. Sohn and R. E. Cohen, "Processible optically transparent block copolymer films containing superparamagnetic iron oxide nanoclusters," *Chemistry of Materials*, vol. 9, no. 1, pp. 264–269, 1997.

[26] A. H. Lu, E. E. Salabas, and F. Schüth, "Magnetic nanoparticles: synthesis, protection, functionalization, and application," *Angewandte Chemie International Edition*, vol. 46, no. 8, pp. 1222–1244, 2007.

[27] M. Bockstaller, R. Mickiewicz, and E. Thomas, "Block copolymer nanocomposites: perspectives for tailored functional materials," *Advanced Materials*, vol. 17, no. 11, pp. 1331–1349, 2005.

[28] I. W. Hamley, *Developments in Block Copolymer Science and Technology*. Developments in Block Copolymer Science and Technology, West Sussex, England: John Wiley & Sons, Ltd, 2004.

[29] T. N. Hoheisel, K. Hur, and U. B. Wiesner, "Block copolymer-nanoparticle hybrid self-assembly," *Progress in Polymer Science*, vol. 40, no. 0, pp. 3–32, 2015.

[30] S. Darling, N. Yufa, A. Cisse, S. Bader, and S. Sibener, "Self-organization of FePt nanoparticles on photochemically modified diblock copolymer templates," *Advanced Materials*, vol. 17, no. 20, pp. 2446–2450, 2005.

[31] S. B. Darling and S. D. Bader, "A materials chemistry perspective on nanomagnetism," *Journal of Materials Chemistry*, vol. 15, no. 39, pp. 4189–4195, 2005.

[32] K. Schlage, S. Couet, S. V. Roth, U. Vainio, R. Röffer, M. M. Abul Kashem, P. Müller-Buschbaum, and R. Röhlsberger, "The formation and magnetism of iron nanostructures on ordered polymer templates," *New Journal of Physics*, vol. 14, no. 4, p. 043007, 2012.

[33] Y. Jiao and P. Akcora, "Assembly of polymer-grafted magnetic nanoparticles in polymer melts," *Macromolecules*, vol. 45, no. 8, pp. 3463–3470, 2012.

[34] Z. Varga, G. Filipcsei, A. Szilgyi, and M. Zrinyi, "Electric and magnetic field-structured smart composites," *Macromolecular Symposia*, vol. 227, no. 1, pp. 123–134, 2005.

[35] V. Tomer, C. A. Randall, G. Polizos, J. Kostelnick, and E. Manias, "High-and low-field dielectric characteristics of dielectrophoretically aligned ceramic/polymer nanocomposites," *Journal of Applied Physics*, vol. 103, no. 3, pp. 034115–034117, 2008.

[36] W. X. Fang, Z. H. He, X. Q. Xu, Z. Q. Mao, and H. Shen, "Magnetic-field-induced chain-like assembly structures of Fe_3O_4 nanoparticles," *Europhysics Letters*, vol. 77, no. 6, p. 68004, 2007.

[37] J. E. Martin, E. Venturini, J. Odinek, and R. A. Anderson, "Anisotropic magnetism in field-structured composites," *Physical Review E*, vol. 61, no. 3, p. 2818, 2000.

[38] G. Filipcsei, I. Csetneki, A. Szilágyi, and M. Zrínyi, *Magnetic field-responsive smart polymer composites*, vol. 206, book section 104, pp. 137–189. Berlin,Heidelberg: Springer, 2007.

[39] J. Y. Lee, R. B. Thompson, D. Jasnow, and A. C. Balazs, "Effect of nanoscopic particles on the mesophase structure of diblock copolymers," *Macromolecules*, vol. 35, no. 13, pp. 4855–4858, 2002.

[40] H. Fan and Z. Jin, "Selective swelling of block copolymer nanoparticles: size, nanostructure, and composition," *Macromolecules*, vol. 47, no. 8, pp. 2674–2681, 2014.

[41] Y. Lin, A. Böker, J. He, K. Sill, H. Xiang, C. Abetz, X. Li, J. Wang, T. Emrick, S. Long, Q. Wang, A. Balazs, and T. P. Russell, "Self-directed self-assembly of nanoparticle/copolymer mixtures," *Nature*, vol. 434, no. 7029, pp. 55–59, 2005.

[42] G. Herzog, G. Benecke, A. Buffet, B. Heidmann, J. Perlich, J. F. H. Risch, G. Santoro, M. Schwartzkopf, S. Yu, W. Wurth, and S. V. Roth, "In situ grazing incidence small-angle x-ray scattering investigation of polystyrene nanoparticle spray deposition onto silicon," *Langmuir*, vol. 29, no. 36, pp. 11260–11266, 2013.

[43] E. Metwalli, I. Krisch, I. Markovits, M. Rawolle, M. A. Ruderer, S. Guo, S. Wyrzgol, A. Jentys, J. Perlich, J. A. Lercher, and P. Müller-Buschbaum, "Polymer-coated PtCo nanoparticles deposited on diblock copolymer templates: Chemical selectivity versus topographical effects," *ChemPhysChem*, vol. 15, no. 11, pp. 2236–2239, 2014.

[44] Y. Zhao, K. Thorkelsson, A. J. Mastroianni, T. Schilling, J. M. Luther, B. J. Rancatore, K. Matsunaga, H. Jinnai, Y. Wu, D. Poulsen, J. M. J. Fréchet, A. P. Alivisatos, and T. Xu, "Small-molecule-directed nanoparticle assembly towards stimuli-responsive nanocomposites," *Nature materials*, vol. 8, no. 12, pp. 979–985, 2009.

[45] S. B. Darling, "Mechanism for hierarchical self-assembly of nanoparticles on scaffolds derived from block copolymers," *Surface Science*, vol. 601, no. 13, pp. 2555–2561, 2007.

[46] C.-T. Lo, B. Lee, V. G. Pol, N. L. Dietz Rago, S. Seifert, R. E. Winans, and P. Thiyagarajan, "Effect of molecular properties of block copolymers and nanoparticles on the morphology of self-assembled bulk nanocomposites," *Macromolecules*, vol. 40, no. 23, pp. 8302–8310, 2007.

[47] A.-S. Robbes, J. Jestin, F. Meneau, F. Dalmas, O. Sandre, J. Perez, F. Boué, and F. Cousin, "Homogeneous dispersion of magnetic nanoparticles aggregates in a PS nanocomposite: Highly reproducible hierarchical structure tuned by the nanoparticles' size," *Macromolecules*, vol. 43, no. 13, pp. 5785–5796, 2010.

[48] C. Xu, K. Ohno, V. Ladmiral, and R. J. Composto, "Dispersion of polymer-grafted magnetic nanoparticles in homopolymers and block copolymers," *Polymer*, vol. 49, no. 16, pp. 3568–3577, 2008.

[49] N. J. Fernandes, H. Koerner, E. P. Giannelis, and R. A. Vaia, "Hairy nanoparticle assemblies as one-component functional polymer nanocomposites: opportunities and challenges," *MRS Communications*, vol. 3, no. 01, pp. 13–29, 2013.

[50] E. Metwalli, V. Körstgens, K. Schlage, R. Meier, G. Kaune, A. Buffet, S. Couet, S. V. Roth, R. Röhlsberger, and P. Müller-Buschbaum, "Cobalt nanoparticles growth on a block copolymer thin film: A time-resolved GISAXS study," *Langmuir*, vol. 29, no. 21, pp. 6331–6340, 2013.

[51] R. J. Hickey, A. S. Haynes, J. M. Kikkawa, and S.-J. Park, "Controlling the self-assembly structure of magnetic nanoparticles and amphiphilic block-copolymers: from micelles to vesicles," *Journal of the American Chemical Society*, vol. 133, no. 5, pp. 1517–1525, 2011.

[52] V. Raman, A. Bose, B. D. Olsen, and T. A. Hatton, "Long-range ordering of symmetric block copolymer domains by chaining of superparamagnetic nanoparticles in external magnetic fields," *Macromolecules*, vol. 45, no. 23, pp. 9373–9382, 2012.

[53] C.-T. Lo, Y.-C. Chang, S.-C. Wu, and C.-L. Lee, "Effect of particle size on the phase behavior of block copolymer/nanoparticle composites," *Colloids and Surfaces, A: Physicochemical and Engineering Aspects*, vol. 368, no. 1, pp. 6–12, 2010.

[54] Q. Zhang, S. Gupta, T. Emrick, and T. P. Russell, "Surface-functionalized CdSe nanorods for assembly in diblock copolymer templates," *Journal of the American Chemical Society*, vol. 128, no. 12, pp. 3898–3899, 2006.

[55] C.-T. Lo and W.-T. Lin, "Effect of rod length on the morphology of block copolymer/magnetic nanorod composites," *The Journal of Physical Chemistry B*, vol. 117, no. 17, pp. 5261–5270, 2013.

[56] U. W. Gedde, *Polymer Physics*. Chapman & Hall, 1st ed., 1995.

[57] P. Appl.Chem. in *Macromolecular division*, vol. 68, p. 2287, 1996.

[58] A. D. Jenkins, P. Kratochvil, R. F. Stepto, and U. Suter, "Glossary of basic terms in polymer science," *Pure and applied chemistry*, vol. 68, no. 12, pp. 2287–2311, 1996.

[59] G. Strobl, *The physics of polymers*. Springer-Verlag Berlin Heidelberg, 3rd ed., 2007.

[60] http://www.doitpoms.ac.uk/tlplib/polymerbasics/printall.php, *Dissemination of IT for the Promotion of Materials Science*. University of Cambridge, 2004-2015.

[61] http://www.doitpoms.ac.uk/tlplib/glass transition/conformation.php, *Dissemination of IT for the Promotion of Materials Science*. University of Cambridge, 2004-2015.

[62] D. I. Bower, *An introduction to polymer physics*. Cambridge university press cambridge, 2004.

[63] T. G. Fox, "Influence of diluent and of copolymer composition on the glass temperature of a polymer system," *Bull Am Phys Soc*, vol. 1, no. 123, pp. 22060–6218, 1956.

[64] M. L. Huggins, "Thermodynamic properties of solutions of long-chain compounds," *Annals of the New York Academy of Sciences*, vol. 43, no. 1, pp. 1–32, 1942.

[65] P. J. Flory, "Thermodynamics of high polymer solutions," *The Journal of chemical physics*, vol. 10, no. 1, pp. 51–61, 1942.

[66] M. Rawolle, *Structuring and filling of titania films for applications in photovoltaics*. PhD thesis, Technische Universität München, München, Germany, 2013.

[67] Y.-C. Tseng and S. B. Darling, "Block copolymer nanostructures for technology," *Polymers*, vol. 2, no. 4, pp. 470–489, 2010.

[68] T. Wu, K. Efimenko, and J. Genzer, "Preparing high-density polymer brushes by mechanically assisted polymer assembly," *Macromolecules*, vol. 34, no. 4, pp. 684–686, 2001.

[69] F. S. Bates and G. H. Fredrickson, "Block copolymer thermodynamics: theory and experiment," *Annual Review of Physical Chemistry*, vol. 41, no. 1, pp. 525–557, 1990.

[70] M. W. Matsen and F. S. Bates, "Unifying weak-and strong-segregation block copolymer theories," *Macromolecules*, vol. 29, no. 4, pp. 1091–1098, 1996.

[71] L. Leibler, "Theory of microphase separation in block copolymers," *Macromolecules*, vol. 13, no. 6, pp. 1602–1617, 1980.

[72] S. Ma, *Modern theory of critical phenomena*. No. 46, Da Capo Press, 2000.

[73] G. H. Fredrickson, "Surface ordering phenomena in block copolymer melts," *Macromolecules*, vol. 20, no. 10, pp. 2535–2542, 1987.

[74] S. A. Brazovskii, "Phase transition of an isotropic system to a nonuniform state," *JETP*, vol. 41, p. 85, 1975.

[75] K. Binder, "Theory of first-order phase transitions," *Reports on progress in physics*, vol. 50, no. 7, p. 783, 1987.

[76] T. Ohta and K. Kawasaki, "Equilibrium morphology of block copolymer melts," *Macromolecules*, vol. 19, no. 10, pp. 2621–2632, 1986.

[77] A. N. Semenov, "Contribution to the theory of microphase layering in block-copolymer melts," *Journal of Experimental and Theoretical Physics*, vol. 61, no. 4, pp. 733–742, 1985.

[78] D. G. Walton, G. J. Kellogg, A. M. Mayes, P. Lambooy, and T. P. Russell, "A free energy model for confined diblock copolymers," *Macromolecules*, vol. 27, no. 21, pp. 6225–6228, 1994.

[79] K. R. Shull, "Mean-field theory of block copolymers: bulk melts, surfaces, and thin films," *Macromolecules*, vol. 25, no. 8, pp. 2122–2133, 1992.

[80] J. D. Vavasour and M. D. Whitmore, "Self-consistent mean field theory of the microphases of diblock copolymers," *Macromolecules*, vol. 25, no. 20, pp. 5477–5486, 1992.

[81] J. L. Barrat and G. H. Fredrickson, "Diffusion of a symmetric block copolymer in a periodic potential," *Macromolecules*, vol. 24, no. 24, pp. 6378–6383, 1991.

[82] A. M. Mayes and M. O. de la Cruz, "Concentration fluctuation effects on disorder–order transitions in block copolymer melts," *The Journal of chemical physics*, vol. 95, no. 6, pp. 4670–4677, 1991.

[83] H. Fried and K. Binder, "The microphase separation transition in symmetric diblock copolymer melts: A monte carlo study," *The Journal of chemical physics*, vol. 94, no. 12, pp. 8349–8366, 1991.

[84] K. Almdal, J. H. Rosedale, F. S. Bates, G. D. Wignall, and G. H. Fredrickson, "Gaussian-to stretched-coil transition in block copolymer melts," *Physical review letters*, vol. 65, no. 9, p. 1112, 1990.

[85] M. D. Foster, M. Sikka, N. Singh, F. S. Bates, S. K. Satija, and C. F. Majkrzak, "Structure of symmetric polyolefin block copolymer thin films," *The Journal of chemical physics*, vol. 96, no. 11, pp. 8605–8615, 1992.

[86] G. Hadziioannou and A. Skoulios, "Molecular weight dependence of lamellar structure in styrene isoprene two-and three-block copolymers," *Macromolecules*, vol. 15, no. 2, pp. 258–262, 1982.

[87] H. Hasegawa, H. Tanaka, K. Yamasaki, and T. Hashimoto, "Bicontinuous microdomain morphology of block copolymers. 1. tetrapod-network structure of polystyrene-polyisoprene diblock polymers," *Macromolecules*, vol. 20, no. 7, pp. 1651–1662, 1987.

[88] T. Hashimoto, M. Shibayama, and H. Kawai, "Domain-boundary structure of styrene-isoprene block copolymer films cast from solution. 4. molecular-weight dependence of lamellar microdomains," *Macromolecules*, vol. 13, no. 5, pp. 1237–1247, 1980.

[89] A. N. Semenov, "Theory of block copolymer interfaces in the strong segregation limit," *Macromolecules*, vol. 26, no. 24, pp. 6617–6621, 1993.

[90] M. M. Abul kashem, *Magnetic particle in supported Polymer Nanostructures*. PhD thesis, Technische Universität München, München, Germany, 2008.

[91] R. W. Richards and J. Thomason, "Small-angle neutron scattering study of block copolymer morphology," *Macromolecules*, vol. 16, no. 6, pp. 982–992, 1983.

[92] G. H. Fredrickson, "Noncircular wigner-seitz cells in strongly segregated block copolymers," *Macromolecules*, vol. 26, no. 16, pp. 4351–4355, 1993.

[93] E. Helfand, "Block copolymer theory. III. statistical mechanics of the microdomain structure," *Macromolecules*, vol. 8, no. 4, pp. 552–556, 1975.

[94] R. C. Ball, J. F. Marko, S. T. Milner, and T. A. Witten, "Polymers grafted to a convex surface," *Macromolecules*, vol. 24, no. 3, pp. 693–703, 1991.

[95] H. Li and T. A. Witten, "Polymers grafted to convex surfaces: a variational approach," *Macromolecules*, vol. 27, no. 2, pp. 449–457, 1994.

[96] F. S. Bates, R. E. Cohen, and C. V. Berney, "Small-angle neutron scattering determination of macrolattice structure in a polystyrene-polybutadiene diblock copolymer," *Macromolecules*, vol. 15, no. 2, pp. 589–592, 1982.

[97] D. A. Hajduk, P. E. Harper, S. M. Gruner, C. C. Honeker, G. Kim, E. L. Thomas, and L. J. Fetters, "The gyroid: A new equilibrium morphology in weakly segregated diblock copolymers," *Macromolecules*, vol. 27, no. 15, pp. 4063–4075, 1994.

[98] N. F. Henry and K. Lonsdale, *International tables for X-ray crystallography*. Kynoch Press, 1952.

[99] H. Fried and K. Binder, "Non-Gaussian conformational behaviour in diblock copolymer melts: is the RPA valid?," *Europhysics Letters*, vol. 16, no. 3, p. 237, 1991.

[100] A. N. Semenov, "Microphase separation in diblock-copolymer melts: ordering of micelles," *Macromolecules*, vol. 22, no. 6, pp. 2849–2851, 1989.

[101] P. D. Olmsted and S. T. Milner, "Strong-segregation theory of bicontinuous phases in block copolymers," *Physical review letters*, vol. 72, no. 6, p. 936, 1994.

[102] S. T. Milner, "Strongly stretched polymer brushes," *Journal of Polymer Science Part B: Polymer Physics*, vol. 32, no. 16, pp. 2743–2755, 1994.

[103] A. E. Likhtman and A. N. Semenov, "Stability of the obdd structure for diblock copolymer melts in the strong segregation limit," *Macromolecules*, vol. 27, no. 11, pp. 3103–3106, 1994.

[104] A. K. Khandpur, S. Foerster, F. S. Bates, I. W. Hamley, A. J. Ryan, W. Bras, K. Almdal, and K. Mortensen, "Polyisoprene-polystyrene diblock copolymer phase diagram near the order-disorder transition," *Macromolecules*, vol. 28, no. 26, pp. 8796–8806, 1995.

[105] S. H. Anastasiadis, T. P. Russell, S. K. Satija, and C. F. Majkrzak, "Neutron reflectivity studies of the surface-induced ordering of diblock copolymer films," *Physical Review Letters*, vol. 62, no. 16, p. 1852, 1989.

[106] A. Menelle, T. P. Russell, S. H. Anastasiadis, S. K. Satija, and C. F. Majkrzak, "Ordering of thin diblock copolymer films," *Physical review letters*, vol. 68, no. 1, p. 67, 1992.

[107] R. A. Segalman, "Patterning with block copolymer thin films," *Materials Science and Engineering: R: Reports*, vol. 48, no. 6, pp. 191–22, 2005.

[108] Y. Yao, E. Metwalli, M. A. Niedermeier, M. Opel, C. Lin, J. Ning, J. Perlich, S. V. Roth, and P. Müller-Buschbaum, "Nano- and microstructures of magnetic field-guided maghemite nanoparticles in diblock copolymer films," *ACS Applied Materials & Interfaces*, vol. 6, no. 7, pp. 5244–5254, 2014.

[109] Y. Yao, E. Metwalli, B. Su, V. Körstgens, D. Moseguí González, A. Miasnikova, A. Laschewsky, M. Opel, G. Santoro, S. V. Roth, and P. Müller-Buschbaum, "Arrangement of maghemite nanoparticles via wet chemical self-assembly in PS-b-PNIPAM diblock copolymer films," *ACS Applied Materials & Interfaces*, vol. 7, no. 23, pp. 13080–13091, 2015.

[110] Y. Yao, E. Metwalli, J.-F. Moulin, B. Su, M. Opel, and P. Müller-Buschbaum, "Self-assembly of diblock copolymer-maghemite nanoparticle hybrid thin films," *ACS Applied Materials & Interfaces*, vol. 6, no. 20, pp. 18152–18162, 2014.

[111] I. I. Potemkin, "Lamellar orientation in thin, supported diblock copolymer films: strong segregation theory," *Macromolecules*, vol. 37, no. 9, pp. 3505–3509, 2004.

[112] T. L. Morkved and H. M. Jaeger, "Thickness-induced morphology changes in lamellar diblock copolymer ultrathin films," *Europhysics Letters*, vol. 40, no. 6, p. 643, 1997.

[113] M. J. Fasolka, P. Banerjee, A. M. Mayes, G. Pickett, and A. C. Balazs, "Morphology of ultrathin supported diblock copolymer films: theory and experiment," *Macromolecules*, vol. 33, no. 15, pp. 5702–5712, 2000.

[114] T. P. Russell, A. Menelle, S. H. Anastasiadis, S. K. Satija, and C. F. Majkrzak, "Unconventional morphologies of symmetric, diblock copolymers due to film thickness constraints," *Macromolecules*, vol. 24, no. 23, pp. 6263–6269, 1991.

[115] G. Coulon, T. P. Russell, V. R. Deline, and P. F. Green, "Surface-induced orientation of symmetric, diblock copolymers: a secondary ion mass-spectrometry study," *Macromolecules*, vol. 22, no. 6, pp. 2581–2589, 1989.

[116] G. Coulon, D. Ausserre, and T. P. Russell, "Interference microscopy on thin diblock copolymer films," *Journal de physique*, vol. 51, no. 8, pp. 777–786, 1990.

[117] T. P. Russell, G. Coulon, V. R. Deline, and D. C. Miller, "Characteristics of the surface-induced orientation for symmetric diblock PS/PMMA copolymers," *Macromolecules*, vol. 22, no. 12, pp. 4600–4606, 1989.

[118] W. H. Tang, "Confinement of symmetric diblock copolymer thin films," *Macromolecules*, vol. 33, no. 4, pp. 1370–1384, 2000.

[119] J.-U. Sommer, A. Hoffmann, and A. Blumen, "Block copolymer films between neutral walls: A monte carlo study," *The Journal of chemical physics*, vol. 111, no. 8, pp. 3728–3732, 1999.

[120] G. Coulon, J. Daillant, B. Collin, J. J. Benattar, and Y. Gallot, "Time evolution of the free surface of ultrathin copolymer films," *Macromolecules*, vol. 26, no. 7, pp. 1582–1589, 1993.

[121] P. Müller-Buschbaum, E. Bauer, O. Wunnicke, and M. Stamm, "The control of thin film morphology by the interplay of dewetting, phase separation and microphase separation," *Journal of Physics: Condensed Matter*, vol. 17, no. 9, p. S363, 2005.

[122] C. Davis, K. Beers, A. M. Forster, C. Stafford, A. Smith, C. Harrison, W. Zhang, A. Karim, and E. Amis, "Polymer science at the NIST combinatorial methods center," *Polymeric Materials: Science & Engineering*, vol. 88, pp. 386–387, 2003.

[123] A. Knoll, A. Horvat, K. S. Lyakhova, G. Krausch, G. J. Sevink, A. V. Zvelindovsky, and R. Magerle, "Phase behavior in thin films of cylinder-forming block copolymers," *Physical review letters*, vol. 89, no. 3, p. 035501, 2002.

[124] H. P. Huinink, J. C. Brokken-Zijp, M. A. Van Dijk, and G. J. Sevink, "Asymmetric block copolymers confined in a thin film," *The Journal of Chemical Physics*, vol. 112, no. 5, pp. 2452–2462, 2000.

[125] S. Burke, H. Shen, and A. Eisenberg, "Multiple vesicular morphologies from block copolymers in solution," *Macromolecular Symposia*, vol. 175, no. 1, pp. 273–284, 2001.

[126] D. C. Jiles, *Introduction to magnetism and magnetic materials*. CRC press, 1998.

[127] H. C. Oersted, "Electricity and magnetic needles," *Philosophy*, vol. 16, no. 4, pp. 273–276, 1820.

[128] P. Weiss, "L'hypothèse du champ moléculaire et la propriété ferromagnétique," *J. Phys. Rad.*, vol. 6, pp. 661–690, 1907.

[129] R. O' Handley, *Modern Magnetic Materials: Principles and Applications*. New York: John Wiley & Sons, 2000.

[130] D. Givord, Q. Lu, and M. Rossignol, *coercivity in hard magnetic materials*, book section 5, pp. 635–656. New York, London: Plenum Press, 1991.

[131] B. D. Cullity, *Introduction to magnetic materials*. John Wiley & Sons, 2000.

[132] S. Bedanta and W. Kleemann, "Supermagnetism," *Journal of Physics D: Applied Physics*, vol. 42, no. 1, p. 013001, 2009.

[133] L. Néel, "Théorie du traínage magnétique des ferromagnétiques en grains fins avec applications aux terres cuites," *Ann. Géophys*, vol. 5, pp. 99–136, 1949.

[134] S. Bedanta, *Supermagnetism in magnetic nanoparticle systems*. PhD thesis, Physik Fachbereich, Universität Duisburg-Essen, 2006.

[135] E. Katelhon and R. G. Compton, "Nanoparticles in sensing applications: on what timescale do analyte species adsorb on the particle surface?," *Analyst*, vol. 139, pp. 2411–2415, 2014.

[136] S. Park, D. H. Lee, J. Xu, B. Kim, S. W. Hong, U. Jeong, T. Xu, and T. P. Russell, "Macroscopic 10-terabit-per-square-inch arrays from block copolymers with lateral order," *Science*, vol. 323, no. 5917, pp. 1030–1033, 2009.

[137] G. Kortaberria, P. Arruti, A. Jimeno, I. Mondragon, and M. Sangermano, "Local dynamics in epoxy coatings containing iron oxide nanoparticles by dielectric relaxation spectroscopy," *Journal of Applied Polymer Science*, vol. 109, no. 5, pp. 3224–3229, 2008.

[138] A. Horechyy, N. E. Zafeiropoulos, B. Nandan, P. Formanek, F. Simon, A. Kiriy, and M. Stamm, "Highly ordered arrays of magnetic nanoparticles prepared via block copolymer assembly," *Journal of Materials Chemistry*, vol. 20, no. 36, pp. 7734–7741, 2010.

[139] B. Reddy, *Advances in Diverse Industrial Applications of Nanocomposites*. Oxford University Press: New York, 2002.

[140] M. Tolan, *X-ray scattering from soft-matter thin films*. Springer, 1999.

[141] P. Müller-Buschbaum, *Polymer Surfaces and Interfaces: Characterization, Modification and Applications*. Springer-Verlag Berlin Heidelberg, 2008.

[142] H. Dosch, B. Batterman, and D. Wack, "Depth-controlled grazing-incidence diffraction of synchrotron x-radiation," *Physics Review Letters*, vol. 56, no. 11, p. 1144–1147, 1986.

[143] A. Duparre, J. Ferre-Borrull, S. Gliech, G. Notni, J. Steinert, and J. M. Bennett, "Surface characterization techniques for determining the root-mean-square roughness and power spectral densities of optical components," *Appl. Opt.*, vol. 41, pp. 154–171, Jan 2002.

[144] L. Nevot and P. Croce, "Characterization of surfaces by grazing x-ray reflection–application to the study of polishing of some silicate glasses," *Rev. Phys. Appl.*, vol. 15, p. 761, 1980.

[145] H. Kiessig, "Interferenz von röntgenstrahlen an dünnen schichten," *Ann. Phys*, vol. 10, p. 769–788, 1931.

[146] G. Renaud, R. Lazzari, and F. Leroy, "Probing surface and interface morphology with grazing incidence small angle x-ray scattering," *Surf. Sci. Rep.*, vol. 64, p. 255–380, 2009.

[147] J. Lekner, "Reflection theory and the analysis of neutron reflection data," *Physica B*, vol. 173, p. 99–111, 1991.

[148] M. A. Ruderer and P. Müller-Buschbaum, "Morphology of polymer-based bulk heterojunction films for organic photovoltaics," *Soft Matter*, vol. 7, no. 12, p. 5482–5493, 2011.

[149] R. Lazzari, "IsGISAXS: a program for grazing-incidence small-angle x-ray scattering analysis of supported islands," *Journal of applied crystallography*, vol. 35, no. 4, p. 406–421, 2002.

[150] P. Müller-Buschbaum, *A basic introduction to grazing incidence small angle x-ray scattering*. Springer, Berlin, 2009.

[151] S. K. Sinha, E. B. Sirota, S. Garoff, and H. B. Stanley, "X-ray and neutron scattering from rough surfaces," *Phys. Rev. B*, vol. 38, p. 2297–2311, 1988.

[152] V. Holý and T. Baumbach, "Nonspecular x-ray reflection from rough multilayers," *Phys. Rev. B*, vol. 49, p. 10668–10676, 1994.

[153] Y. Yoneda, "Anomalous surface reflection of x-rays," *Physical review*, vol. 131, pp. 2010–2013, 1963.

[154] M. A. Niedermeier, *Novel structuring routines of titania films for application in photovoltaics*. PhD thesis, Technische Universität München, München, Germany, 2013.

[155] P. Müller-Buschbaum, "Grazing incidence small-angle neutron scattering: challenges and possibilities," *Polymer Journal*, vol. 45, no. 1, pp. 34–42, 2013.

[156] A. Naudon, D. Babonneau, D. T. Andrére, and S. Lequien., "Grazing-incidence small-angle x-ray scattering applied to the characterization of aggregates in surface regions," *Physica B*, vol. 283, p. 69–74, 2000.

[157] R. Hosemann, W. Vogel, D. Weick, and F. J. Baltá-Calleja, "Novel aspects of the real paracrystal," *Acta Cryst.*, vol. A37, p. 85–91, 1981.

[158] M. Rauscher, T. Salditt, and H. Spohn, "Small-angle x-ray scattering under grazing incidence: The cross section in the distorted-wave born approximation.," *Phys. Rev. B*, vol. 52, p. 16855–16863, 1995.

[159] E. W. Weisstein, "Gaussian function." From MathWorld - A Wolfram Web Resource. Last access on 26.10.2012.

[160] P. Müller-Buschbaum, E. Metwalli, J.-F. Moulin, V. Kudryashov, M. Haese-Seiller, and R. Kampmann, "Time of flight grazing incidence small angle neutron scattering," *The European Physical Journal Special Topics*, vol. 167, no. 1, pp. 107–112, 2009.

[161] P. Müller-Buschbaum, "Grazing incidence small-angle x-ray scattering: an advanced scattering technique for the investigation of nanostructured polymer films," *Analytical and bioanalytical chemistry*, vol. 376, no. 1, pp. 3–10, 2003.

[162] L. Reimer and P. W. Hawkes, *Scanning Electron Microscopy: Principles of Image formation and Microanalysis*. springer Berlin Heidelberg, 2nd ed., 1998.

[163] L. Spiess, R. Schwarzer, H. Behnken, and G. Teichert, *Modern Röntgenbeugung: Röntgendiffraktometrie für Materialwissenschaftler, Physiker under Chemiker*. Teubner, 1st ed., 2005.

[164] L. Parratt, "Surface studies of solids by total reflection of x-rays," *Physical review*, vol. 95, no. 2, pp. 359–369, 1954.

[165] B. Ingham, H. Li, E. L. Allen, and M. F. Toney, "SAXSFit: A program for fitting small-angle x-ray and neutron scattering data," *arXiv preprint arXiv:0901.4782*, 2009.

[166] M. Rawolle, V. Körstgens, M. A. Ruderer, E. Metwalli, S. Guo, G. Herzog, G. Benecke, M. Schwartzkopf, A. Buffet, and J. Perlich, "Note: Comparison of grazing incidence small angle x-ray scattering of a titania sponge structure at the beamlines BW4 (Doris III) and P03 (Petra III)," *Rev. Scien. Instr.*, vol. 83, p. 106104, 2012.

[167] A. Buffet, A. Rothkirch, R. Dohrmann, V. Körstgens, M. M. Abul Kashem, J. Perlich, G. Herzog, M. Schwartzkopf, R. Gehrke, and P. Müller-Buschbaum, "P03, the microfocus and nanofocus x-ray scattering (MiNaXS) beamline of the PETRA III storage ring: the microfocus endstation," *Journal of Synchrotron Radiation*, vol. 19, no. 4, pp. 647–653, 2012.

[168] J. Perlich, J. Rubeck, S. Botta, R. Gehrke, S. V. Roth, M. A. Ruderer, S. M. Prams, M. Rawolle, Q. Zhong, V. Körstgens, and P. Müller-Buschbaum, "Grazing incidence wide angle x-ray scattering at the wiggler beamline BW4 of HASYLAB," *Review of scientific instruments*, vol. 81, no. 10, p. 105105–1–7, 2010.

[169] S. V. Roth, R. Döhrmann, M. Dommach, M. Kuhlmann, I. Kröger, R. Gehrke, H. Walter, C. Schroer, B. Lengeler, and P. Müller-Buschbaum, "Small-angle options of the upgraded ultrasmall-angle x-ray scattering beamline BW4 at HASYLAB," *Review of scientific instruments*, vol. 77, no. 8, pp. 085106–1–7, 2006.

[170] R. Kampmann, M. Haese-Seiller, V. Kudryashov, V. Deriglazov, V. Syromiatnikov, M. Tristl, B. Toperverg, A. Okorokov, A. Schreyer, and E. Sackmann, "Perspectives for polarised reflectometry at the novel reflectometer REFSANS at FRM-II in Munich/Germany," *Physica B: Condensed Matter*, vol. 335, no. 1, pp. 274–277, 2003.

[171] R. Kampmann, M. Haese-Seiller, V. Kudryashov, V. Deriglazov, M. Tristl, C. Daniel, B. Toperverg, A. Schreyer, and E. Sackmann, "The potential of the horizontal reflectometer REFSANS/FRM-II for measuring low reflectivity and diffuse surface scattering," *Physica B: Condensed Matter*, vol. 350, no. 1, pp. E763–E766, 2004.

[172] R. Kampmann, M. Haese-Seiller, V. Kudryashov, B. Nickel, C. Daniel, W. Fenzl, A. Schreyer, E. Sackmann, and J. Raedler, "Horizontal TOF-neutron reflectometer REFSANS at FRM-II Munich/Germany: First tests and status," *Physica B: Condensed Matter*, vol. 385, pp. 1161–1163, 2006.

[173] R. Kampmann, M. Haese-Seiller, M. Marmotti, J. Burmester, V. Deriglazov, V. Syromiatnikov, A. Okorokov, F. Frisius, M. Tristl, and E. Sackmann, "The novel reflectometer REFSANS for analyses of liquid and soft surfaces at the new research reactor FRM-II in Munich, Germany," *Applied Physics A: Materials Science & Processing*, vol. 74, no. 1, pp. s249–s251, 2002.

[174] G. Kaune, M. Haese-Seiller, R. Kampmann, J.-F. Moulin, Q. Zhong, and P. Müller-Buschbaum, "TOF-GISANS investigation of polymer infiltration in mesoporous TiO_2 films for photovoltaic applications," *Journal of Polymer Science Part B: Polymer Physics*, vol. 48, no. 14, pp. 1628–1635, 2010.

[175] B. D. Josephson, "Possible new effects in superconductive tunnelling," *Physics letters*, vol. 1, no. 7, pp. 251–253, 1962.

[176] Q. Design, *Magnetic Property Measurement System MPMS XL Hardware Reference Manual*. San Diege, CA, 1996.

[177] L. H. Bennett and R. Watson, *Magnetic multilayers*. World Scientific, 1994.

[178] T. Mansfeldt, S. Schuth, W. Häusler, F. E. Wagner, S. Kaufhold, and M. Overesch, "Iron oxide mineralogy and stable iron isotope composition in a gleysol with petrogleyic properties," *Journal of Soils and Sediments*, vol. 12, no. 1, pp. 97–114, 2012.

[179] J. Rieger, "The glass transition temperature of polystyrene: results of a round robin test," *Journal of Thermal Analysis and Calorimetry*, vol. 46, no. 3-4, pp. 965–972, 1996.

[180] M. F. Ashby, *Materials Selection in Mechanical Design*. Elsevier, 3rd ed., 2005.

[181] K. Tauer, D. Gau, S. Schulze, A. Völkel, and R. Dimova, "Thermal property changes of poly(N-isopropylacrylamide) microgel particles and block copolymers," *Colloid Polym Sci*, vol. 287, pp. 299–312, 2009.

[182] K. Skrabania, A. Miasnikova, A. M. Bivigou-Koumba, D. Zehm, and A. Laschewsky, "Examining the UV-vis absorption of RAFT chain transfer agents and their use for polymer analysis," *Polymer Chemistry*, vol. 2, no. 9, pp. 2074–2083, 2011.

[183] K. Troll, A. Kulkarni, W. Wang, C. Darko, A. M. Bivigou Koumba, A. Laschewsky, P. Müller-Buschbaum, and C. M. Papadakis, "The collapse transition of poly(styrene-b-(N-isopropyl acrylamide)) diblock copolymers in aqueous solution and in thin films," *Colloid and Polymer Science*, vol. 286, no. 8-9, pp. 1079–1092, 2008.

[184] W. Wang, K. Troll, G. Kaune, E. Metwalli, M. A. Ruderer, K. Skrabania, A. Laschewsky, S. V. Roth, C. M. Papadakis, and P. Müller-Buschbaum, "Thin films of poly(N-isopropylacrylamide) end-capped with n-Butyltrithiocarbonate," *Macromolecules*, vol. 41, no. 9, pp. 3209–3218, 2008.

[185] J. Adelsberger, A. Kulkarni, A. Jain, W. Wang, A. M. Bivigou-Koumba, P. Busch, V. Pipich, O. Holderer, T. Hellweg, A. Laschewsky, P. Müller-Buschbaum, and C. M. Papadakis, "Thermoresponsive PS-b-PNIPAM-b-PS micelles: Aggregation behavior, segmental dynamics, and thermal response," *Macromolecules*, vol. 43, no. 5, pp. 2490–2501, 2010.

[186] V. Cabuil, N. Hochart, R. Perzynski, and P. J. Lutz, *Synthesis of cyclohexane magnetic fluids through adsorption of end-functionalized polymers on magnetic particles*, vol. 97 of *Progress in Colloid & Polymer Science*, book section 15, pp. 71–74. New York: Springer-Verlag, 1994.

[187] J. Wu, H. Li, S. Wu, G. Huang, W. Xing, M. Tang, and Q. Fu, "Influence of magnetic nanoparticle size on the particle dispersion and phase separation in an ABA triblock copolymer," *The Journal of Physical Chemistry B*, vol. 118, no. 8, pp. 2186–2193, 2014.

[188] P. Müller-Buschbaum, N. Hermsdorf, S. V. Roth, J. Wiedersich, S. Cunis, and R. Gehrke, "Comparative analysis of nanostructured diblock copolymer films. spectrochimica," *Acta Part B*, vol. 59, p. 1789, 2004.

[189] C. Lawrence, "The mechanics of spin coating of polymer-films," *Physics of fluids*, vol. 31, no. 10, p. 2786–2795, 1988.

[190] D. W. Schubert, "Spin coating as a method for polymer molecular weight determination," *Pol. Bull.*, vol. 38, p. 117, 1997.

[191] D. W. Schubert and T. Dunkel, "Spin coating from a molecular point of view: its concentration regimes, influence of molar mass and distribution," *Mat.Res. Innovat.*, vol. 7, p. 314, 2003.

[192] E. Metwalli, J.-F. Moulin, M. Rauscher, G. Kaune, M. A. Ruderer, U. Van Burck, M. Haese-Seiller, R. Kampmann, and P. Müller-Buschbaum, "Structural investigation of thin diblock copolymer films using time-of-flight grazing-incidence small-angle neutron scattering," *Journal of Applied Crystallography*, vol. 44, no. 1, pp. 84–92, 2010.

[193] H.-C. Kim and W. D. Hinsberg, "Surface patterns from block copolymer self-assembly," *Journal of Vacuum Science & Technology A*, vol. 26, no. 6, pp. 1369–1382, 2008.

[194] G. Vignaud, A. Gibaud, G. Grübel, S. Joly, D. Ausserre, J. F. Legrand, and Y. Gallot, "Ordering of diblock PS-PBMA thin films: An x-ray reflectivity study," *Physica B: Condensed Matter*, vol. 248, no. 1, pp. 250–257, 1998.

[195] J. A. Ramos, L. H. Espósito, R. Fernndez, I. Zalakain, S. Goyanes, A. Avgeropoulos, N. E. Zafeiropoulos, G. Kortaberria, and I. Mondragon, "Block copolymer concentration gradient and solvent effects on nanostructuring of thin epoxy coatings modified with epoxidized styrene-butadiene-styrene block copolymers," *Macromolecules*, vol. 45, no. 3, pp. 1483–1491, 2012.

[196] S. O. Kim, H. H. Solak, M. P. Stoykovich, N. J. Ferrier, J. J. de Pablo, and P. F. Nealey, "Epitaxial self-assembly of block copolymers on lithographically defined nanopatterned substrates," *Nature*, vol. 424, no. 6947, pp. 411–414, 2003.

[197] G. J. Kellogg, D. G. Walton, A. M. Mayes, P. Lambooy, T. P. Russell, P. D. Gallagher, and S. K. Satija, "Observed surface energy effects in confined diblock copolymers," *Physical Review Letters*, vol. 76, no. 14, pp. 2503–2506, 1996. PRL.

[198] W. A. Lopes and H. M. Jaeger, "Hierarchical self-assembly of metal nanostructures on diblock copolymer scaffolds," *Nature*, vol. 414, no. 6865, pp. 735–738, 2001.

[199] R. A. L. Jones, *Soft condensed matter*. New York: Oxford University Press, 2002.

[200] J. E. Mark, K. L. Ngai, W. W. Graessley, L. Mandelkern, E. T. Samulski, J. L. Koenig, and W. G. D., *Physical properties of polymers*. Cambridge: Cambridge University Press, 2004.

[201] J. J. Chiu, B. J. Kim, E. J. Kramer, and D. J. Pine, "Control of nanoparticle location in block copolymers," *Journal of the American Chemical Society*, vol. 127, no. 14, pp. 5036–5037, 2005.

[202] V. Lauter-Pasyuk, H. Lauter, G. Gordeev, P. Müller-Buschbaum, B. P. Toperverg, W. Petry, M. Jernenkov, A. Petrenko, and V. Aksenov, "Parallel and perpendicular lamellar phases in copolymer-nanoparticle multilayer structures," *Physica B: Condensed Matter*, vol. 350, no. 1, pp. E939–E942, 2004.

[203] S.-W. Yeh, K.-H. Wei, Y.-S. Sun, U.-S. Jeng, and K. S. Liang, "CdS nanoparticles induce a morphological transformation of poly (styrene-b-4-vinylpyridine) from hexagonally packed cylinders to a lamellar structure," *Macromolecules*, vol. 38, no. 15, pp. 6559–6565, 2005.

[204] R.-M. Ho, T. Lin, M.-R. Jhong, T.-M. Chung, B.-T. Ko, and Y.-C. Chen, "Phase transformation in self-assembly of the gold/poly(4-vinylpyridine)-b-poly (ε -caprolactone) hybrid system," *Macromolecules*, vol. 38, no. 21, pp. 8607–8610, 2005.

[205] B. J. Kim, J. J. Chiu, G. Yi, D. J. Pine, and E. J. Kramer, "Nanoparticle-induced phase transitions in diblock-copolymer films," *Advanced Materials*, vol. 17, no. 21, pp. 2618–2622, 2005.

[206] J. Huh, V. V. Ginzburg, and A. C. Balazs, "Thermodynamic behavior of particle/diblock copolymer mixtures: Simulation and theory," *Macromolecules*, vol. 33, no. 21, pp. 8085–8096, 2000.

[207] P. Müller-Buschbaum, G. Kaune, M. Haese-Seiller, and J.-F. Moulin, "Morphology determination of defect-rich diblock copolymer films with time-of-flight grazing-incidence small-angle neutron scattering," *Journal of Applied Crystallography*, vol. 47, no. 4, pp. 1228–1237, 2014.

[208] P. Müller-Buschbaum, E. Maurer, E. Bauer, and R. Cubitt, "Surface versus confinement induced morphology transition in triblock copolymer films: a grazing incidence small angle neutron scattering investigation," *Langmuir*, vol. 22, no. 22, pp. 9295–9303, 2006.

[209] P. Müller-Buschbaum, L. Schulz, E. Metwalli, J.-F. Moulin, and R. Cubitt, "Lateral structures of buried interfaces in ABA-type triblock copolymer films," *Langmuir*, vol. 24, no. 15, pp. 7639–7644, 2008.

[210] M. Rawolle, K. Sarkar, M. A. Niedermeier, M. Schindler, P. Lellig, J. S. Gutmann, J.-F. Moulin, M. Haese-Seiller, A. S. Wochnik, C. Scheu, and P. Müller-Buschbaum, "Infiltration of polymer hole-conductor into mesoporous titania structures for solid-state dye-sensitized solar cells," *ACS applied materials & interfaces*, vol. 5, no. 3, pp. 719–729, 2013.

[211] G. Kaune, M. Haese-Seiller, R. Kampmann, J.-F. Moulin, Q. Zhong, and P. Müller-Buschbaum, "TOF-GISANS investigation of polymer infiltration in mesoporous TiO_2 films for photovoltaic applications," *Journal of Polymer Science Part B: Polymer Physics*, vol. 48, no. 14, pp. 1628–1635, 2010.

[212] M. A. Niedermeier, D. Magerl, Q. Zhong, A. Nathan, V. Körstgens, J. Perlich, S. V. Roth, and P. Müller-Buschbaum, "Combining mixed titania morphologies into a complex assembly thin film by iterative block-copolymer-based sol-gel templating," *Nanotechnology*, vol. 23, no. 14, p. 145602, 2012.

[213] V. Lauter-Pasyuk, H. J. Lauter, D. Ausserre, Y. Gallot, V. Cabuil, E. I. Kornilov, and B. Hamdoun, "Effect of nanoparticle size on the internal structure of copolymer-nanoparticles composite thin films studied by neutron reflection," *Physica B: Condensed Matter*, vol. 241-243, pp. 1092–1094, 1998.

[214] V. Weith, A. Krekhov, and W. Zimmermann, "Stability and orientation of lamellae in diblock copolymer films," *The Journal of Chemical Physics*, vol. 139, no. 5, p. 054908, 2013.

[215] X. Xia, E. Metwalli, M. A. Ruderer, V. Körstgens, P. Busch, P. Böni, and P. Müller-Buschbaum, "Nanostructured diblock copolymer films with embedded magnetic nanoparticles," *Journal of Physics: Condensed Matter*, vol. 23, no. 25, p. 254203, 2011.

[216] S. Blundell, *Magnetism in condensed matter*. New York: Oxford University Press, 2001.

[217] C. P. Bean and I. S. Jacobs, "Magnetic granulometry and super-paramagnetism," *Journal of Applied Physics*, vol. 27, no. 12, pp. 1448–1452, 1956.

[218] L. Schulz, W. Schirmacher, A. Omran, V. R. Shah, P. Böni, W. Petry, and P. Müller-Buschbaum, "Elastic torsion effects in magnetic nanoparticle diblock-copolymer structures," *Journal of Physics: Condensed Matter*, vol. 22, no. 34, p. 346008, 2010.

[219] P. Busch, M. Rauscher, D.-M. Smilgies, D. Posselt, and C. M. Papadakis, "Grazing-incidence small-angle x-ray scattering from thin polymer films with lamellar structures - the scattering cross section in the distorted-wave born approximation," *Journal of Applied Crystallography*, vol. 39, no. 3, pp. 433–442, 2006.

[220] P. Busch, M. Rauscher, J.-F. Moulin, and P. Müller-Buschbaum, "Debye-scherrer rings from block copolymer films with powder-like order," *Journal of Applied Crystallography*, vol. 44, no. 2, pp. 370–379, 2011.

[221] K. Theis-Bröhl, D. Mishra, B. P. Toperverg, H. Zabel, B. Vogel, A. Regtmeier, and A. Hütten, "Self organization of magnetic nanoparticles: A polarized grazing incidence small angle neutron scattering and grazing incidence small angle x-ray scattering study," *Journal of Applied Physics*, vol. 110, no. 10, p. 102207, 2011.

[222] W. F. J. Brown, "Thermal fluctuations of a single-domain particle," *Physical Review*, vol. 130, no. 5, p. 1677, 1963.

[223] M. M. Abul Kashem, J. Perlich, A. Diethert, W. Wang, M. Memesa, J. S. Gutmann, E. Majkova, I. Capek, S. V. Roth, W. Petry, and P. Müller-Buschbaum, "Array of magnetic nanoparticles via particle co-operated self-assembly in block copolymer thin film," *Macromolecules*, vol. 42, no. 16, pp. 6202–6208, 2009.

[224] M. M. Abul Kashem, J. Perlich, L. Schulz, S. Roth, W. Petry, and P. Müller-Buschbaum, "Maghemite nanoparticles on supported diblock copolymer nanostructures," *Macromolecules*, vol. 40, no. 14, pp. 5075–5083, 2007.

[225] H. Singh, P. E. Laibinis, and T. A. Hatton, "Synthesis of flexible magnetic nanowires of permanently linked core-shell magnetic beads tethered to a glass surface patterned by microcontact printing," *Nano letters*, vol. 5, no. 11, pp. 2149–2154, 2005.

[226] R. Sheparovych, Y. Sahoo, M. Motornov, S. Wang, H. Luo, P. N. Prasad, I. Sokolov, and S. Minko, "Polyelectrolyte stabilized nanowires from Fe_3O_4 nanoparticles via magnetic field induced self-assembly," *Chemistry of materials*, vol. 18, no. 3, pp. 591–593, 2006.

[227] M. Klokkenburg, C. Vonk, E. M. Claesson, J. D. Meeldijk, B. H. Erné, and A. P. Philipse, "Direct imaging of zero-field dipolar structures in colloidal dispersions of synthetic magnetite," *Journal of the American Chemical Society*, vol. 126, no. 51, pp. 16706–16707, 2004.

[228] E. M. Furst, C. Suzuki, M. Fermigier, and A. P. Gast, "Permanently linked monodisperse paramagnetic chains," *Langmuir*, vol. 14, no. 26, pp. 7334–7336, 1998.

[229] P. Y. Keng, M. M. Bull, I.-B. Shim, K. G. Nebesny, N. R. Armstrong, Y. Sung, K. Char, and J. Pyun, "Colloidal polymerization of polymer-coated ferromagnetic Cobalt nanoparticles into Pt-Co_3O_4 nanowires," *Chemistry of Materials*, vol. 23, no. 5, pp. 1120–1129, 2011.

[230] J. J. Benkoski, J. L. Breidenich, O. M. Uy, A. T. Hayes, R. M. Deacon, H. B. Land, J. M. Spicer, P. Y. Keng, and J. Pyun, "Dipolar organization and magnetic actuation of flagella-like nanoparticle assemblies," *Journal of Materials Chemistry*, vol. 21, no. 20, pp. 7314–7325, 2011.

[231] V. Q. Nguyen and R. Ramanujan, "Novel coiling behavior in magnet -polymer composites," *Macromolecular Chemistry and Physics*, vol. 211, no. 6, pp. 618–626, 2010.

[232] Z. Varga, G. Filipcsei, and M. Zrínyi, "Magnetic field sensitive functional elastomers with tuneable elastic modulus," *Polymer*, vol. 47, no. 1, pp. 227–233, 2006.

[233] W. Kim, C.-Y. Suh, S.-W. Cho, K.-M. Roh, H. Kwon, K. Song, and I.-J. Shon, "A new method for the identification and quantification of magnetite-maghemite mixture using conventional x-ray diffraction technique," *Talanta*, vol. 94, pp. 348–352, 2012.

[234] Y.-k. Sun, M. Ma, Y. Zhang, and N. Gu, "Synthesis of nanometer-size maghemite particles from magnetite," *Colloids and Surfaces A: Physicochemical and Engineering Aspects*, vol. 245, no. 1, pp. 15–19, 2004.

[235] S. Chikazumi and S. H. Charap, *Physics of magnetism*. Malabar: FL: RE Krieger Publishing Company, 1978.

[236] E. C. Stoner and E. P. Wohlfarth, "A mechanism of magnetic hysteresis in heterogeneous alloys," *Philosophical Transactions of the Royal Society of London. Series A. Mathematical and Physical Sciences*, pp. 599–642, 1948.

[237] P. Müller-Buschbaum and M. Stamm, "Correlated roughness, long-range correlations, and dewetting of thin polymer films," *Macromolecules*, vol. 31, no. 11, pp. 3686–3692, 1998.

[238] M. R. Scheinfein, K. E. Schmidt, K. R. Heim, and G. G. Hembree, "Magnetic order in two-dimensional arrays of nanometer-sized superparamagnets," *Physical review letters*, vol. 76, no. 9, pp. 1541–1544, 1996.

[239] A. Sugawara and M. R. Scheinfein, "Room-temperature dipole ferromagnetism in linear-self-assembling mesoscopic Fe particle arrays," *Physical Review B*, vol. 56, no. 14, pp. R8499–R8502, 1997.

[240] H. G. Schild, "Poly(N-isopropylacrylamide): experiment, theory and application," *Progress in Polymer Science*, vol. 17, no. 2, pp. 163–249, 1992.

[241] T. Tanaka, "Collapse of gels and the critical endpoint," *Physical Review Letters*, vol. 40, no. 12, pp. 820–823, 1978. PRL.

[242] M. A. C. Stuart, W. T. S. Huck, J. Genzer, M. Müller, C. Ober, M. Stamm, G. B. Sukhorukov, I. Szleifer, V. V. Tsukruk, M. Urban, F. Winnik, S. Zauscher, I. Luzinov, and S. Minko, "Emerging applications of stimuli-responsive polymer materials," *Nat Mater*, vol. 9, no. 2, pp. 101–113, 2010. 10.1038/nmat2614.

[243] W. Wang, G. Kaune, J. Perlich, C. M. Papadakis, A. M. Bivigou Koumba, A. Laschewsky, K. Schlage, R. Röhlsberger, S. V. Roth, R. Cubitt, and P. Müller-Buschbaum, "Swelling and switching kinetics of gold coated end-capped poly(N-isopropylacrylamide) thin films," *Macromolecules*, vol. 43, no. 5, pp. 2444–2452, 2010.

[244] R. Shenhar, T. B. Norsten, and V. M. Rotello, "Polymer-mediated nanoparticle assembly: Structural control and applications," *Advanced Materials*, vol. 17, no. 6, pp. 657–669, 2005.

[245] T. Shinjo, T. Okuno, R. Hassdorf, K. Shigeto, and T. Ono, "Magnetic vortex core observation in circular dots of permalloy," *Science*, vol. 289, no. 5481, pp. 930–932, 2000.

[246] R. P. Cowburn, D. K. Koltsov, A. O. Adeyeye, M. E. Welland, and D. M. Tricker, "Single-domain circular nanomagnets," *Physical Review Letters*, vol. 83, no. 5, pp. 1042–1045, 1999. PRL.

[247] R. P. Cowburn, "Property variation with shape in magnetic nanoelements," *Journal of Physics D: Applied Physics*, vol. 33, no. 1, pp. R1–R16, 2000.

[248] G. Coulon, T. P. Russell, V. R. Deline, and P. F. Green, "Surface-induced orientation of symmetric, diblock copolymers: a secondary ion mass-spectrometry study," *Macromolecules*, vol. 22, no. 6, pp. 2581–2589, 1989.

[249] M. Ramanathan, E. Nettleton, and S. B. Darling, "Simple orientational control over cylindrical organic–inorganic block copolymer domains for etch mask applications," *Thin Solid Films*, vol. 517, no. 15, pp. 4474–4478, 2009.

[250] M. A. Ojeda-Lopez, D. J. Needleman, C. Song, A. Ginsburg, P. A. Kohl, Y. Li, H. P. Miller, L. Wilson, U. Raviv, M. C. Choi, and C. R. Safinya, "Transformation of taxol-stabilized microtubules into inverted tubulin tubules triggered by a tubulin conformation switch," *Nat Mater*, vol. 13, no. 2, pp. 195–203, 2014.

[251] Y. Tsori, E. Sivaniah, D. Andelman, and T. Hashimoto, "Orientational transitions in symmetric diblock copolymers on rough surfaces," *Macromolecules*, vol. 38, no. 16, pp. 7193–7196, 2005.

[252] G. Kaune, M. A. Ruderer, E. Metwalli, W. Wang, S. Couet, K. Schlage, R. Röhlsberger, S. V. Roth, and P. Müller-Buschbaum, "In situ GISAXS study of gold film growth on conducting polymer films," *ACS Applied Materials & Interfaces*, vol. 1, no. 2, pp. 353–360, 2008.

[253] M. M. Abul Kashem, J. Perlich, L. Schulz, S. V. Roth, and P. Müller-Buschbaum, "Correlated roughness in polymer films containing maghemite nanoparticles," *Macromolecules*, vol. 41, no. 6, pp. 2186–2194, 2008.

[254] D. Babonneau, S. Camelio, D. Lantiat, L. Simonot, and A. Michel, "Waveguiding and correlated roughness effects in layered nanocomposite thin films studied by grazing-incidence small-angle x-ray scattering," *Physical Review B*, vol. 80, no. 15, p. 155446, 2009. PRB.

[255] P. Müller-Buschbaum, J. S. Gutmann, C. Lorenz, T. Schmitt, and M. Stamm, "Decay of interface correlation in thin polymer films," *Macromolecules*, vol. 31, no. 26, pp. 9265–9272, 1998.

List of publications

Publications related to the dissertation

- Y. Yao, E. Metwalli, M. A. Niedermeier, M. Opel, C. Lin, J. Ning, J. Perlich, S. V. Roth, and P. Müller-Buschbaum, "Nano- and microstructures of magnetic field-guided maghemite nanoparticles in diblock copolymer films", *ACS Applied Materials & Interfaces*, **2014**, *6*, 5244-5254.

- Y. Yao, E. Metwalli, J.-F. Moulin, B. Su, M. Opel and P. Müller-Buschbaum, "Self-assembly of diblock copolymer–maghemite nanoparticle hybrid thin films", *ACS Applied Materials & Interfaces*, **2014**, *6*, 18152-18162.

- Y. Yao, E. Metwalli, B. Su, V. Körstgens, D. M. González, A. Miasnikova, A. Laschewsky, M. Opel, G. Santoro, S. V. Roth and P. Müller-Buschbaum, "Arrangement of maghemite nanoparticles via wet chemical self-assembly in PS-*b*-PNIPAM diblock copolymer films", *ACS Applied Materials & Interfaces*, **2015**, *7*, 13080-13091.

- Y. Yao, E. Metwalli, M. Opel, M. Haese, J.-F. Moulin, K. Rodewald, B. Rieger and P. Müller-Buschbaum, "Lamellar diblock copolymer films with embedded maghemite nanoparticles", *Advanced Materials Interfaces*, **2016**, DOI: 10.1002/admi.201500712.

Further publications

- D. M. González, V. Körstgens, Y. Yao, L. Song, G. Santoro, S. V. Roth, and P. Müller-Buschbaum, "Improved power conversion efficiency of P3HT:PCBM organic solar cells by strong spin–orbit coupling-induced delayed fluorescence", *Adv. Energy Mater.*, **2015**, *5*, 1401770.

- S. Guo, J. Ning, V. Körstgens, Y. Yao, E. M. Herzig, S. V. Roth, and P. Müller-Buschbaum, "The effect of fluorination in manipulating the nanomorphology in PTB7:PC71BM bulk heterojunction systems", *Adv. Energy Mater.*, **2015**, *5*, 1401315.

- L. Song, W. Wang, V. Körstgens, D. M. González, Y. Yao, N. Minar, H. Feckl, K. Peters, T. Bein, D. Fattakhova, G. Santoro, S. V. Roth, and P. Müller-Buschbaum, "Spray deposition of titania films with incorporated crystalline nanoparticles for allsolid-state dye-sensitized solar cells using P3HT", *Adv. Funct. Mater.*, *accepted*.

- Y. Xiao, S. You, Y. Yao, T. Zheng, C. Lin, S. V. Roth, P. Müller-Buschbaum, W. Steffen, L.-D. Sun, C.-H. Yan, J. S. Gutmann, M. Yin, J. Fu, and Y.-J. Cheng, "Generalized synthesis of mesoporous rare earth oxide thin films through amphiphilic ionic block copolymer templating", *Eur. J. Inorg. Chem.*, **2013**, *8*, 1251-1257.

- N. Paul, E. Metwalli, Y. Yao, M. Schwartzkopf, S. Yu, S. V. Roth, P. Müller-Buschbaum, A. Paul, "Templating growth of gold nanostructures with a CdSe quantum dot array", *Nanoscale*, **2015**, *7*, 9703-9714.

- S. Yu, G. Santoro, Y. Yao, D. Babonneau, M. Schwartzkopf, P. Zhang, S. K. Vayalil, S. V. Roth, P. Wessels, R. Döhrmann, M. Drescher, P. Müller-Buschbaum, and S. V. Roth, "Following the island growth in real time: Ag nanocluster layer on Alq3 thin film", *J. Phys. Chem. C*, **2015**, *119*, 4406-4413.

- Y. Xiao, X. Wang, Y. Xia, Y. Yao, E. Metwalli, Q. Zhang, R. Liu, B. Qiu, M. Rasool, Z. Liu, J.-Q. Meng, L.-D. Sun, C.-H. Yan, P. Müller-Buschbaum, and Y.-J. Cheng, "Green facile scalable synthesis of Titania/Carbon nanocomposites: new use of old dental resins", *ACS Applied Materials & Interfaces*, **2014**, *6*, 18461-18468.

- Y. Xiao, X. Wang, Y. Xia, T. Wagner, J. Thiel, Y. Yao, Y. Lin, E. Metwalli, R. Liu, Q. Zhang, R. Liu, H. J. Butt, P. Müller-Buschbaum, J.-Q. Meng, L. Chen, L.-D. Sun, C.-H. Yan, and Y.-J. Cheng, "Solvothermal synthesis of hierarchical Eu_2O_3 nanostructures templated by PS-*b*-PMAA: morphology control via simple variation of water contents", *J. Mater. Chem. A*, **2015**, *3*, 5789-5793.

- M. Philipp, V. Körstgens, D. Magerl, C. Heller, Y. Yao, W. Wang, G. Santoro, S. V. Roth and P. Müller-Buschbaum, "Sorption of water and initial stages of swelling of thin PNIPAM films using in situ GISAXS microfluidics", *Langmuir*, **2015**, *31*, 9619-9627.

- M. Schwartzkopf, G. Santoro, C. J. Brett, A. Rothkirch, O. Polonskyi, A. Hinz, E. Metwalli, Y. Yao, T. Strunskus, F. Faupel, P. Müller-Buschbaum and S. V. Roth, "Real-time monitoring of morphology and optical properties during sputter deposition for tailoring metal–polymer interfaces", *ACS Applied Materials & Interfaces*, **2015**, *7*, 13547-13556.

- S. V. Roth, G. Santoro, J. F. H. Risch, S. Yu, M. Schwartzkopf, T. Boese, R. Döhrmann, P. Zhang, B. Besner, P. Bremer, D. Rukser, M. A. Rübhausen, N. J. Terrill, P. A. Staniec, Y. Yao, E. Metwalli, and P. Müller-Buschbaum and "Patterned diblock co-polymer thin films as templates for advanced anisotropic metal nanostructures", *ACS Applied Materials & Interfaces*, **2015**, *7*, 12470-12477.

- V. Körstgens, S. Proller, T. Buchmann, D. M. González, L. Song, Y. Yao, W. Wang, J. Werhahn, G. Santoro, S. V. Roth, H. Iglev, R. Kienberger and P. Müller-Buschbaum, "Laser-ablated titania nanoparticles for aqueous processed hybrid solar cells", *Nanoscale*, **2015**, *7*, 2900-2904.

- X. Wang, J.-Q. Meng, M. Wang, Y. Xiao, R. Liu, Y. Xia, Y. Yao, E. Metwalli, Q. Zhang, B. Qiu, Z. Liu, J. Pan, L.-D. Sun, C.-H. Yan, P. Müller-Buschbaum, and Y.-J. Cheng, "Facile scalable synthesis of TiO_2/Carbon nanohybrids with ultrasmall TiO_2 nanoparticles homogeneously embedded in carbon matrix", *ACS Applied Materials & Interfaces*, **2014**, *7*, 24247-24255.

Scientific reports

- Y. Yao, E. Metwalli, J.-F. Moulin, B. Su, and P. Müller-Buschbaum, "Morphology investigation of diblock copolymer-maghemite nanoparticle hybrid thin films fabricated via self-assembly", *Lehrstuhl für Funktionelle Materialien, Annual Report*, 2014.

- Y. Yao, E. Metwalli, B. Su, V. Körstgens, D. M. González, L. Song, G. Santoro, S. V. Roth and P. Müller-Buschbaum, "Arrangement of maghemite nanoparticles in P(S-*b*-NIPAM) diblock copolymer films", *Lehrstuhl für Funktionelle Materialien, Annual Report*, 2013.

- Y. Yao, E. Metwalli, J.-F. Moulin, M. Haese-Seiller and P. Müller-Buschbaum, "Depth-dependent morphology investigation of diblock copolymer films using TOF-GISANS", *FRM II Annual Report*, 2012.

- Y. Yao, E. Metwalli, H. Choe, M. Opel, S. V. Roth, and P. Müller-Buschbaum, "Magnetic nanoparticles in thin block copolymer films", *HASYLAB Annual Report*, 2011.
- Y. Yao, E. Metwalli, H. Choe, S. V. Roth, M. Opel, and P. Müller-Buschbaum, "Magnetic nanoparticles in thin block copolymer films", *Lehrstuhl für Funktionelle Materialien, Annual Report*, 2011.
- Y. Yao, E. Metwalli, H. Choe, P. Busch, and P. Müller-Buschbaum, "Effect of external magnetic field on the alignment of metal-polymer nanocomposites", *Lehrstuhl für Funktionelle Materialien, Annual Report*, 2010.

Conference talks

- Y. Yao, and R. Wang, "Block copolymer films", *E13 Summer School*, Obertauern (Austria), 24.–27.06.2014.
- Y. Yao, E. Metwalli, J. -F. Moulin, M. Haese-Seiller, and P. Müller-Buschbaum, "Structure investigation of polymer-metal nanocomposite films using time-of-flight grazing incidence small angle neutron scattering", *DPG Frühjahrstagung*, Regensburg (Germany), 10.–15.03.2013.
- Y. Yao, E. Metwalli, V. Körstgens, E. M. Herzig, W. Wang, A. Buffet, S. V. Roth, and P. Müller-Buschbaum, "Magnetic nanoparticles in thin block copolymer films", *3rd TUM-HASYLAB Colloquium*, Garching (Germany), 10.–11.09.2012.
- Y. Yao, and Q. Zhong, "Block copolymer films", *E13 Summer School*, Rudolfshütte (Austria), 12.–15.06.2012.

Conference poster presentations

- Y. Yao, E. Metwalli, J. -F. Moulin, B. Su, M. Opel, and P. Müller-Buschbaum, "Maghemite nanoparticles embedded in thin block copolymer films", *2nd internal biennial science meeting of the MLZ*, Grainau (Germany), 15.-18.06.2015.
- Y. Yao, E. Metwalli, J. -F. Moulin, B. Su, M. Opel, and P. Müller-Buschbaum, "Morphology investigation of self-assembly of metal oxide-diblock copolymer nanocomposite films", *DPG Frühjahrstagung*, Berlin (Germany), 15.-20.03.2015.

- Y. Yao, E. Metwalli, B. Su, V. Körstgens, D. M. Gonzalez, G. Santoro, S. V. Roth, M. Opel, and P. Müller-Buschbaum, "Maghemite nanoparticles embedded in thin block copolymer flms", *DPG Frühjahrstagung*, Dresden (Germany), 30.03-04.04.2014.

- Y. Yao, E. Metwalli, J. -F. Moulin, and P. Müller-Buschbaum, "Maghemite nanoparticles in thin block copolymer films", *DPG Frühjahrstagung*, Berlin (Germany), 25.-30.03.2012.

- Y. Yao, E. Metwalli, J. -F. Moulin, and P. Müller-Buschbaum, "Magnetic nanoparticles embedded in thin block copolymer films", *FRM II User Meeting*, Garching (Germany), 23.03.2012.

- Y. Yao, E. Metwalli, H. Choe, M. Opel,and P. Müller-Buschbaum, "Alignment of magnetic nanoparticles in diblock copolymer films under external magnetic fields", *5th FRM II Science Meeting*, Burg Rothenfels (Germany), 06.-09.06.2011.

- Y. Yao, E. Metwalli, H. Choe, P. Busch, and P. Müller-Buschbaum, "Alignment of magnetic nanoparticles in diblock copolymer films under external magnetic fields", *DPG Frühjahrstagung*, Dresden (Germany), 13.-18.03.2011.

Acknowledgments

First of all, I would like to thank Prof. Dr. Peter Müller-Buschbaum for giving me the opportunity to work in the interesting topic of magnetic NPs-DBC hybrid film. I am grateful for his scientific guidance, deep insight, inspiration and fruitful advice in many research fields. Particularly, his abundant experience on scattering techniques and polymer physics greatly helped me throughout my Ph.D. period. Additional, I appreciate his trust in me so I have the chance to participate in reviewing scientific publications and lead a group in external beamtime measurements.

I would like to thank Dr. Ezzeldin Metwalli for advising me during my Ph.D. time. We have fruitful scientific discussion on many aspects of difficult points. His plentiful advice for designing experiments, utilizing characterization techniques, as well as writing on the publications and the dissertation greatly helped me.

I would like to thank all the partners during the external beamtimes. The successful scattering results presented in my publications and this thesis are attributed to the excellent teamwork in every beamtime measurement. It is very honored to be in a team with Dr. Ezzeldin Metwalli, Dr. Volker Körstgens, Dr. Martin A. Niedermeier, Dr. Kuhu Sarkar, Weijia Wang, Dr. Eva Maria Ruderer, Dr. Monika Rawolle, Daniel Moseguí González, Chen Lin, Jing Ning, Wei Liu, and Lin Song. Local support at beamline is as well quite important. I would like to thank all the beamline scientists Dr. Stephan V. Roth, Dr. Adeline Buffet, Dr. Jan Perlich and Dr. Gonzalo Santoro from DESY, and Dr. Jean-Francois Moulin and Dr. Martin Haese-Seiller from HZG.

Several experiments would be impossible performed without the instruments from external collaborations. I would like to thank Dr. Matthias Opel from Walther-Meissner-Institut for the magnetic property measurements, Peter Weiser and Prof. Dr. Alexander Holleitner for the chance to perform SEM. In addition, I would like to thank Prof. Dr. André Laschewsky and Dr. Anna Miasnikova from Institut für Chemie of Universität Potsdam for providing custom synthesized DBC.

Furthermore, I am indebted to all the people who proofread and helped me to improve my thesis: Dr. Ezzeldin Metwalli, Dr. Volker Körstgens, Dr. Martine Philipp, Daniel Moseguí González, Johannes Schlipf, Nitin Saxena, Franziska Löhrer, Bo Su, Lin Song,

Senlin Xia, Jiaxin Zheng and Lukas Oesinghaus. Great thanks also come to Jiaxin Zheng, Bo Su, and Yuzhe Ding, who helped me solving programming problems during the thesis writing. Special thanks go to Senlin Xia for his generous help in submission process of my thesis when I was in China.

I enjoy my stay at the Lehrstuhl für Funktionelle Materialen very much. I truly feel that my abilities in all aspects, especially related to the scientific research are improved a lot via learning and discussing among the group. I would like to thank all my office mates for making such excellent working atmosphere and colorful leisure time. Besides the scientific work, I enjoy all the group activities we did together, including summer and winter hiking days, conference trips, summer school, Go-Kart race, B2run, Christmas parties, Oktoberfest and Nockherberg visits. I will always remember the great fun we had together in my heart. With this, I am grateful for all the former and current E13 team members, who, I have not mentioned so far, contributed to the very nice atmosphere: Prof. Dr. Christine M. Papadakis, Dr. Alexander Diethert, Dr. Jianqi Zhang, Dr. Neelima Paul, Claudia Palumbiny, Dr. Robert Meier, Dr. Anatoly Berezkin, Lorenz Bießmann, Dr. Konstantinos Raftopoulos, Dr. Konstantinos Kyriakos, Margarita Dyakonova, David Magerl, Shuai Guo, Biye Cao, Yichuan Rui, Majid Rasool, Edoardo Barabino, Anna Naumann, Nuri Hohn, Felipe Martinez, Christoph J. Schaffer, Natalya Vishnevetskaya, and Xiaohan Zhang.

I am very grateful for all the support from our warm heart secretaries Susanna Fink, Marion Waletzki, and Petra Douglas. They have done so much to help me go through many complicated documents and visa issues.

I would like to give my sincere thanks to all my friends both, in Germany and in China. Thank Dr. Martin A. Niedermeier for his promised dinner, which encouraged me to finish my thesis finally. I thank Wei Wei, Chen Liu, Lin Liu, Yingyang Huo and Xiyang Zhang for the joy, the fun, the great sunny days we lived together. Particularly, thank Xiyang Zhang and Bo Su for accommodating me and cheering me up in my depression time, I will never forget your generous help and companionship. I am very grateful to Shasha Xu and Wei Wang. Although we live in different countries, you always listen to me, talk to me and support me whenever I have a frustrated time. I deeply appreciate the good time we spent together and the shining days imprint on my mind. My dear friends, I love you all. I wish all the best for you.

Additionally, financial support by CSC scholarship is greatly acknowledged.

Lastly, I want to apologize to my deeply loved parents. I have spent such a long time in a foreign country so far away during the past years. I do not have enough time to accompany with you. I am grateful for your eternal love, unconditional support, long-term understanding and massive encouragement. I want to give my deepest thank-you to my

family! Without the faith you give to me, I can never reach all the achievements. I wish you live a happy and healthy life. I dedicate my thesis to you, the most precious people to me in the world.